Spinor Condensates in Optical Superlattices

Inauguraldissertation

zur Erlangung der Würde eines Doktors der Philosophie
vorgelegt der Philosophisch-Naturwissenschaftlichen Fakultät
der Universität Basel

von

Andreas Wagner,

aus Konstanz, Deutschland

UNI
BASEL
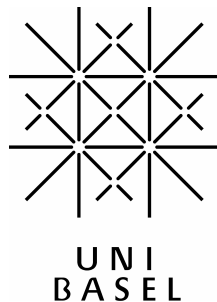
Basel, 2012

Genehmigt von der Philosophisch-Naturwissenschaftlichen Fakultät auf Antrag von

Prof. Dr. Christoph Bruder

Prof. Dr. Dieter Jaksch

Basel, den 16. Oktober 2012,   Prof. Dr. Jörg Schibler, Dekan

Summary

In this thesis we study various aspects of spinor Bose-Einstein condensates in optical superlattices using a Bose-Hubbard Hamiltonian that takes spin effects into account. We decouple the unit cells of the superlattice via a mean-field approach and take into account the dynamics within the unit cell exactly. In this way we derive the ground-state phase diagram of spinor bosons in superlattices. The system supports Mott-insulating as well as superfluid phases. The transitions between these phases are second-order for spinless bosons and second- or first-order for spin-1 bosons. Antiferromagnetic interactions energetically penalize high-spin configurations and elongate all Mott lobes, especially the ones corresponding to an even atom number on each lattice site. We find that the quadratic Zeeman effect lifts the degeneracy between different polar superfluid phases leading to additional metastable phases and first-order phase transitions. A change of magnetic fields can drive quantum phase transitions in the same way as a change in the tunneling amplitude does.

Furthermore we study the physics of spin-1 atoms in superlattices deep in the Mott insulating phase when the superlattice decomposes into isolated double-well potentials. Assuming that a small number of spin-1 bosons is loaded in an optical double-well potential, we study single-particle tunneling that occurs when one lattice site is ramped up relative to a neighboring site. Spin-dependent effects modify the tunneling events in a qualitative and quantitative way. Depending on the asymmetry of the double well different types of magnetic order occur, making the system of spin-1 bosons in an optical superlattice a model for mesoscopic magnetism with an unprecedented control of the parameters. Homogeneous and inhomogeneous magnetic fields are applied and the effects of the linear and the quadratic Zeeman shifts are examined. We generalize the concept of bosonic staircases to connected double-well potentials. We show that an energy offset between the two sites of the unit cell in an extended superlattice induces a staircase of single-atom resonances in the same way as in isolated double well. We also examine single-atom resonances in the superfluid regime and find clear fingerprints of them in the superfluid density.

We also investigate the bipartite entanglement between the sites and construct states of maximal entanglement. The entanglement in our system is due to both orbital and spin degrees of freedom. We calculate the contribution of orbital and spin entanglement and show that the sum of these two terms gives a lower bound for the total entanglement.

Kurzfassung

In der vorliegenden Dissertation werden verschiedene Aspekte von Bose-Einstein-Kondensaten aus Spin-1-Atomen in optischen Supergittern studiert. Dazu wird ein Bose-Hubbard-Modell verwendet, das spinabhängige Wechselwirkungen berücksichtigt. Zunächst werden die Einheitszellen des Supergitters duch eine Molekularfeld-Näherung entkoppelt, wobei die Dynamik innerhalb der Einheitszelle exakt behandelt wird. Mit Hilfe dieser Näherung wird das Phasendiagramm von spinlosen, bosonischen Atomen und Spin-1-Atomen in Supergittern berechnet. Das System unterstützt Mott-isolierende sowie superfluide Phasen. Die Übergänge zwischen diesen Phasen sind zweiter Ordnung für spinlose Bosonen und zweiter oder erster Ordnung für Spin-1-Bosonen.

Antiferromagnetische Wechselwirkungen verursachen eine Verlängerung der Mott-Inseln hin zu grösseren Tunnelamplituden und bevorzugen allgemein niedrige Spin-Konfigurationen. Die Mott-Inseln, die einer geraden Anzahl von Atomen pro Gitterplatz entsprechen, werden besonders vergrössert, da eine gerade Anzahl von Spin-1-Atomen immer Spin-Singletts bilden können. Es werden verschiedene superfluide Phasen beschrieben und herausgestellt, dass durch schwache magnetische Felder die Entartung der verschiedenen polaren superfluiden Phasen aufgehoben wird, was zu zusätzlichen metastabilen Phasen führt. Phasenübergange lassen sich durch Veränderung des Magnetfeldes ebenso wie durch eine Veränderung der Wechselwirkungsstärke verursachen.

Weiterhin wird die Physik von Spin-1-Atomen in Supergittern tief in der Mott-Phase studiert, wenn das Supergitter in isolierte Doppelmuldenpotentiale zerfällt. Es folgt eine Untersuchung der Besetzungwahrscheinlichkeit in asymmetrischen Doppelmulden für eine geringe Anzahl von Atomen. Für diese Systeme können Einteilchen-Resonanzen festgestellt werden. Diese Einteilchen-Resonanzen werden durch spinabhängige Wechselwirkungen qualitativ und quantitativ verändert. Abhängig von der Asymmetrie der Doppelmulde treten verschiedene magnetische Ordnungen auf; dadurch wird das System von Spin-1-Atomen in optischen Supergittern zu einem Modell für mesoskopischen Magnetismus, wobei in diesem Modell alle Parameter mit einem sehr hohen Grad der Kontrolle verändert werden können. Es wird die Wirkung von homogenen und inhomogenen Magnetfeldern untersucht, wobei der lineare und quadratische Zeeman Effekt berücksichtigt wird. Weiter wird das Konzept der Einteilchen-Resonanzen auf Supergitter verallgemeinert und gezeigt, dass eine Asymmetrie in den Einheitszellen des Supergitters ebenso Einteilchen-Resonanzen verursacht. Im Anschluss werden Einteilchen-Resonanzen in dem su-

perfluiden Regime untersucht und festgestellt, dass diese auch in der superfluiden Dichte sichtbar sind.

Im letzten Kapitel dieser Dissertation werden Verschränkungseigenschaften zwischen Gitterplätzen untersucht und maximal verschränkte Zustände konstruiert. Die Verschränkung in dem System von Spin-1-Atomen resultiert aus orbitalen und Spin-Freiheitsgraden. Es werden die Beiträge beider untersucht und argumentiert, dass die Summe beider eine untere Grenze für die gesamte Verschränkung ist.

Acknowledgments

First, I want to express my gratitude to my advisor, Christoph Bruder. It has been great to be part of his group. I really enjoyed working under his supervision, he was always available for discussions and I benefited a lot from his friendliness, knowledge and experience. I also would like to thank Andreas Nunnenkamp for his energy, his ability to motivate me and highly valuable input. Of course, I also need to thank all current and former members of the theory group in Basel: My office-mates Thomas Schmidt, Ying-Dan Wang, Samuel Aldana, Grégory Strübi and Patrick Hofer, but also every other member of the group, especially Stefano Chesi, Daniel Becker, Mathias Duckheim, Jan Fischer, Verena Koerting, Roman Riwar, Beat Röthlisberger, Manuel Schmidt, Dimitrije Stepanenko, Mircea Trif, Oleksandr Tsyplyatyev, Kevin van Hoogdalem, Robert Zak, Gerson Ferreira, Diego Rainis, Peter Stano, Vladimir M. Stojanovic, Rakesh Tiwari, James Wootton, Adrian Hutter, Jelena Klinovaja, Christoph Klöffel, Viktoriia Kornich, Franziska Maier, Christoph Orth, Fabio Pedrocchi, Luka Trifunovic and Robert Zielke.

Throughout my doctoral studies, I also benefited a lot from the discussions with other scientists. Specifically, I would like to thank Eugene Demler, Rosario Fazio and Daniel Burgarth.

All this support would count nothing without my family. I want to thank my wife Beata for her love, encouragement and unconditional backing. I also want to thank Julius. He did not really help, he was even a source of permanent distraction. Nevertheless, he was my main source of motivation.

Contents

Chapter 1

Introduction

In 1995, atomic gases were cooled down to such low temperatures that a large number of atoms occupied a single quantum state and formed a Bose-Einstein condensate.[1] That was the first experimental realization of this novel state of matter predicted by Albert Einstein[2] following the quantum statistics of bosons suggested by Satyendranath Bose.[3] A Bose-Einstein condensate in an atomic cloud is formed when the de Broglie wavelength of the (bosonic) atoms is of the order of the mean inter-atomic distance; at such low temperatures the atoms are called ultracold. Ultracold atomic gases are quantum liquids in which macroscopic characteristics of the liquid derive directly from quantum coherences. Thus, ultracold atomic gases offer the possibility to observe quantum effects on a macroscopic scale. In this thesis we will discuss ultracold spinless and spin-1 atoms in optical superlattices.

For atoms trapped in a magneto-optical trap the spin degree of freedom is frozen and the atoms become effectively spinless. If, however, the quantum gas is trapped by purely optical means, the atoms keep their spin degree of freedom and the order parameter describing the superfluid phase becomes a spinor. The spinor degree of freedom in optically trapped alkaline gases corresponds to the manifold of degenerate Zeeman hyperfine levels. Spinor Bose-Einstein condensates possess an internal degree of freedom, similar to quantum liquids such as d-wave and p-wave superconductors or superfluid ^{3}He. It is therefore tempting to use spinor condensates as a quantum simulator for these quantum liquids which still lack a thorough theoretical understanding. This idea dates back to a proposal of R. Feynman to create quantum simulators which are controllable quantum systems that can model the behavior of more complicated systems.[4]

Nevertheless, spinor condensates are also interesting in their own right. The interaction between the external and internal degrees of freedom leads to a number of phenomena unfamiliar from studies of scalar quantum liquids. The experimental examination of spinor condensates started in 1998 with experiments on ultra-cold

---

[1] [Anderson *et al.*(1995), Bradley *et al.*(1995), Davis *et al.*(1995)], see also [Ketterle(2002)]

[2] [Einstein(1925)]

[3] [Bose(1924)]

[4] [Feynman(1982), Buluta and Nori(2009)]

sodium[1] and rubidium.[2] Seminal theoretical work on the ground-state properties of spinor Bose-Einstein condensates in single traps has been done soon afterwards by T. Ho and Ohmi *et al.*.[3] Experimentally, long-lived alkali spinor gases have been explored in the $F = 1$ manifold both of ^{23}Na (by D. Stamper-Kurn *et al.*(1998)[4]) and ^{87}Rb (by M. Barrett *et al.*(2001)[5]) and the higher energy $F = 2$ manifold of ^{87}Rb.[6] Further experiments on spinor condensates in harmonic traps highlighting spin dynamics, spin textures and properties of the superfluid order parameter have been performed in the following.[7]

Atoms can be trapped via the ac-Stark effect in optical lattices, which are created by counter-propagating laser-beams; in case there are only a few atoms per site, they build up so-called "optical crystals" or "artificial solids". In a typical natural solid, electrons are moving in a lattice generated by the periodic array of atom cores. This can be simulated with ultracold neutral atoms moving in an optical lattice.[8] Ultracold atoms in optical latices offer the unique opportunity to study quantum many-body effects in an extremely clean and well-controlled environment. In contrast to most condensed matter systems they are characterized by the absence of disorder and other imperfections. Ultracold atoms in optical lattices offer robust quantum coherence, a unique controllability and powerful read-out tools like time-of-flight measurements[9] or *in situ* imaging.[10] Experiments with cold atoms in optical lattices were done already at the beginning of the 1990's in the micro-kelvin range.[11] But not until realization of Bose-Einstein Condensates, when much colder temperatures became possible, the field started to become such an interesting and lively field of research.

One of the most prominent examples illustrating how cold atoms in optical lattices can be used to study genuine many-body phenomena is the quantum phase transition between a Mott-insulating and a superfluid phase. In 1998 Jaksch *et al.*[12] worked out that ultracold bosonic atoms in deep optical lattices are an essentially perfect realization of the Bose-Hubbard model. The fermionic Hubbard model is one of the most prominent models of a solid in a condensed-matter physics.[13] The Bose-

---

[1] [Stenger *et al.*(1998)]

[2] [Hall *et al.*(1998)b, Hall *et al.*(1998)a, Matthews *et al.*(1998)]

[3] [Ho(1998), Ohmi and Machida(1998)]

[4] [Stamper-Kurn *et al.*(1998)]

[5] [Barrett *et al.*(2001)]

[6] [Chang *et al.*(2004), Kuwamoto *et al.*(2004), Schmaljohann *et al.*(2004)]

[7] [Chang *et al.*(2005), Black *et al.*(2007), Vengalattore *et al.*(2008), Liu *et al.*(2009), Vengalattore *et al.*(2010), Bookjans *et al.*(2011), Guzman *et al.*(2011)], see also Refs. in [Ueda and Kawaguchi(2010), Stamper-Kurn and Ueda(2012)].

[8] [Lewenstein *et al.*(2007), Bloch *et al.*(2008), Bloch *et al.*(2012), Lewenstein *et al.*(2012)]

[9] [Pedri *et al.*(2001), Gerbier *et al.*(2008)]

[10] [Sherson *et al.*(2010)]

[11] [Grynberg *et al.*(1993), Hemmerich *et al.*(1995)]

[12] [Jaksch *et al.*(1998)]

[13] [Hubbard(1963), Bruus and Flensberg(2004)]

Hubbard model is the simplest Hamiltonian which contains the essential features of strongly interacting Bose systems, namely the competition between the kinetic and the interaction energy. Thus, for ultracold atoms in deep optical lattices there are only two relevant energy scales, the on-site interaction of the atoms and the tunneling amplitude between adjacent lattice sites (the tunneling amplitudes are given by the kinetic energy of the atoms). Optical lattices allow to tune the kinetic energy of the atoms; strong optical lattices significantly reduce the kinetic energy and therefore drive the tunneling amplitudes to zero. The Bose-Hubbard model with repulsive interactions displays a generic quantum phase transition at zero temperature.[1] For large tunneling amplitudes the kinetic energy overcomes the on-site repulsion and the bosons are delocalized over the lattice. However, at commensurate filling (i.e. if the the total particle number is an integer multiple of the number of lattice sites) the system looses its coherent nature when the ratio of the on-site interaction over the tunneling amplitude exceeds a critical value and the atoms become localized. The Bose-Hubbard model was known to display this generic quantum phase transition and so Jaksch *et al.* proposed that this Mott insulating-superfluid transition is observable in ultracold atom experiments. In 2002 Greiner *et al.*[2] demonstrated this transition experimentally in 3D lattices and proved the coherent nature of the dynamics of atoms; later the superfluid to Mott-insulator transition has been observed in 1D and 2D lattices, too.[3]

Due to their spin-dependent interactions spinor quantum gases in optical lattices offer the possibility study magnetic quantum systems with an unprecedented control of the parameters and provide therefore simulators for mesoscopic magnetism. They are well described by the Bose-Hubbard model, but the spin-dependent effects alter the system in a qualitative and quantitative way.[4] The Bose-Hubbard model for spin-1 atoms contains an additional term that incorporates spin-dependent interactions. This term penalizes high-spin configurations on individual lattice sites in the case of antiferromagnetic interactions between the atoms (e.g. for ^{23}Na) and low-spin configuration in the case of ferromagnetic interactions (e.g. for ^{87}Rb). The phase boundaries between superfluid and a Mott-insulating phases are shifted for spin-1 atoms compared to the spinless case, and for certain atomic configurations the phase transition is no longer second- but first-order. This is a consequence of the additional spin-dependent on-site interaction. If this interaction is antiferromagnetic, atomic singlets are energetically favored and the Mott-insulating phase is stable in some parameter ranges where the system is superfluid for spinless atoms. The occurrence of first-order phase transitions comes along with metastable phases and hysteretic behavior.

In this thesis we investigate ultracold bosons loaded into optical period-2 super-lattices. Scalar quantum gases in optical superlattices have already been studied

---

[1] [Fisher *et al.*(1989), Sachdev(2001)]

[2] [Greiner *et al.*(2002)a, Greiner *et al.*(2002)b]

[3] [Köhl *et al.*(2005), Spielman *et al.*(2007)]

[4] [Imambekov *et al.*(2003), Tsuchiya *et al.*(2004), Krutitsky and Graham(2004), Kimura *et al.*(2005), Krutitsky *et al.*(2005), Pai *et al.*(2008)]
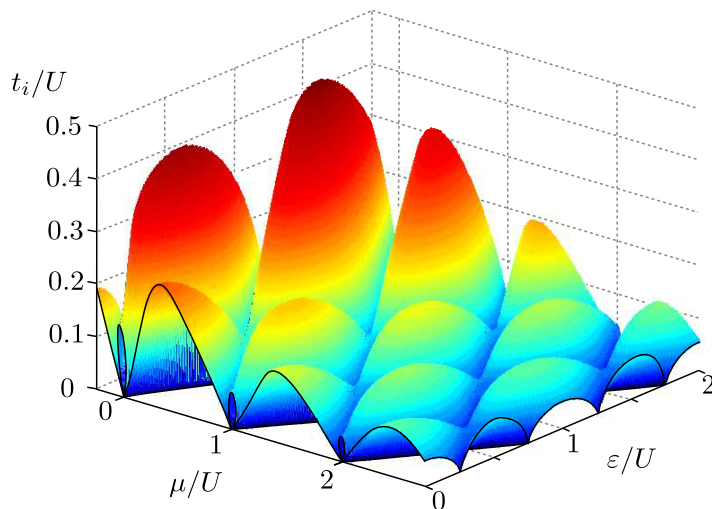
Figure 1.1: Phase diagram of spinless bosons in a two-dimensional superlattice (described by the Hamiltonian given in Eq. (3.38) in Chapter 3). We plot the critical internal tunneling amplitude t_i as a function of chemical potential μ and energy offset ε for $t_i = 10t_e$, where t_e is the tunneling between neighboring double wells. In the region above the plotted surface the system is superfluid, below the surface the system is Mott insulating. Each of the bumps corresponds to a different Mott phase (see Sec. 3.3). The edge at $\varepsilon = 0$ of the phase diagram reveals the contraction of Mott lobes to loops at integer values of μ/U.

theoretically[1] and experimentally.[2] An optical period-2 superlattices is an optical lattice that is formed by overlapping two standing-wave laser fields with a commensurate wavelength ratio of 2. The resulting lattice is an array of optical micro-traps with a double-well structure. By introducing a phase shift between the two laser fields the double wells become asymmetric and an energy offset between the two sites emerges. This energy offset causes the atom number distribution within the double well to be asymmetric and allows us to tune several quantum phases (see Fig. 1.1). The Bose-Hubbard model describing atoms in deep period-2 superlattices contains two different tunneling amplitudes. In our mean-field appproach we take into account the dynamics in the double wells exactly and include the tunneling between neighboring unit cells via a mean-field ansatz. The system supports Mott-insulating phases as well as superfluid phases.[3] The former are characterized by a fixed number of atoms per unit cell. In agreement with previous studies, we find a contraction of Mott lobes to loops for specific values of the energy offset.

In the case of spin-1 atoms in superlattices the mean-field Hamiltonian shows

[1] [Rey *et al.*(2007)]

[2] [Sebby-Strabley *et al.*(2006), Anderlini *et al.*(2007), Fölling *et al.*(2007), Lee *et al.*(2007), Trotzky *et al.*(2008)]

[3] [Buonsante *et al.*(2005), Chen *et al.*(2010)]
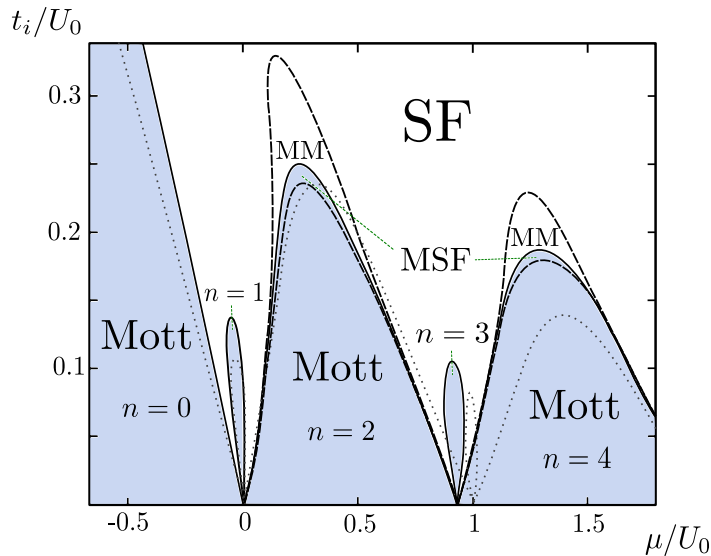
Figure 1.2: Phase diagram for antiferromagnetic spin-1 atoms in optical two-dimensional period-2 superlattices with symmetric unit cells (compare Sec. 3.4). The shaded regions denote Mott-insulating phases, the white ones superfluid phases. The dashed lines are the phase boundaries for metastable phases and the dotted lines are the phase boundaries for the spinless case. The regions in which a metastable Mott phase coexists beside the superfluid [SF] phase is marked with MM; MSF denotes regions where metastable superfluid phases exist alongside the Mott [Mott] phase. The Mott lobes are labeled according to the total atom number per double well.

a much richer quantum phase diagram (see Fig. 1.2) than in the case of spinless bosons. For antiferromagnetic interactions all Mott lobes are elongated towards higher tunneling amplitudes. Mott lobes with an even number of atoms at each lattice site are especially favored because their atomic spins can couple to form spin singlets. For spin-1 atoms we find that some of the phase transitions become first order similar to the case of usual period-1 lattices.[1]

We take the effects of magnetic fields into account by using an effective Hamiltonian which includes a quadratic Zeeman shift. For antiferromagnetic interactions magnetic fields break the degeneracy between different polar superfluid phases. This leads to new classes of metastable phases and changes the phase boundaries significantly. Thus, we can drive quantum phase transitions by applying a magnetic field as well as by varying the lattice depth. In the ferromagnetic case magnetic fields cause first-order phase transitions and metastable phases. These results apply to spin-1 atoms in superlattices as well as in usual lattices.

Furthermore, we study the physics of spin-1 atoms deep in the Mott-insulating phase, thus, in isolated double-well potentials. In this regime the atoms are described by a two-site Bose-Hubbard model. The two-site Bose-Hubbard model for spinless

---

[1] [Krutitsky *et al.*(2005)]
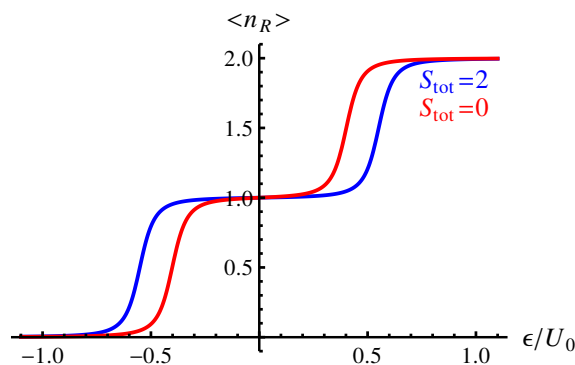
Figure 1.3: Two spin-1 bosons with antiferromagnetic ordering in a double-well potential. Here n_R is the occupation number of the right well, and ϵ characterizes the energy offset between the two wells. Depending on the total spin of the system, bosonic staircase transitions occur at different bias voltages. Note that both the states with $S_{tot} = 0$ and $S_{tot} = 2$ have symmetric orbital wave functions. The difference in the occupation numbers arises due to spin-dependent interactions and not due to a different orbital symmetry of the states. Thus, a measurement of the spin-dependent bosonic staircases provides a demonstration of mesoscopic magnetism.

bosons can be used to describe the transfer of single Cooper pairs in small Josephson junctions, i.e., the physics of "Cooper-pair staircases".[1] With ultracold atoms in optical superlattices this model has been realized and was shown to give rise to a "single-atom staircase" or "bosonic staircase"; for isolated double-well potentials these bosonic staircases were theoretically predicted[2] and experimentally detected.[3] This is achieved by monitoring the particle number in either of the wells for different values of the energy offset. In the case of small tunneling strength, the difference in the number of atoms in the two wells does not change smoothly when the energy offset is varied, but is characterized by a step-like behavior. Jumps from one plateau to the next signal the tunneling of a single atom.

In this thesis, such single-atom staircases are examined for spinor condensates. We examine the case when each double-well potential is filled with a small number of spin-1 bosons. Depending on the energy bias, different types of magnetic order occur, and the system of spin-1 bosons in an optical superlattice becomes a model for mesoscopic magnetism. A specific example of how this mesoscopic magnetism can be observed in experiments is presented in Fig. 1.3. This figure shows the difference between bosonic staircases for two spin-1 bosons for configurations with different total spins. If the total spin is $S_{tot} = 2$, the spins of the two atoms are parallel and for antiferromagnetic interactions (as in the case of ^{23}Na) being in the

---

[1] [Averin *et al.*(1985), Lafarge *et al.*(1991), Lafarge *et al.*(1993)]

[2] [Gati and Oberthaler(2007), Averin *et al.*(2008), Ferrini *et al.*(2008), Rinck and Bruder(2011)]

[3] [Cheinet *et al.*(2008)]

same well costs extra energy. Therefore the $S_{tot} = 2$ configuration switches later (i.e., at a higher energy offset) to the state with both atoms in the same well. In the ferromagnetic case (such as ^{87}Rb), the curves for $S_{tot} = 0$ and $S_{tot} = 2$ will be exchanged. We also examine single-atom tunneling resonances in superlattices. We find clear fingerprints of single-atom resonances in the density of condensed bosons, too.

Spinor gases in optical lattices can also be used to engineer strongly correlated, entangled states for quantum information processing.[1] Entanglement lies at the heart of quantum mechanics since it incorporates its non-local nature.[2] Thus, entanglement, a generic quantum correlation, is a main feature of quantum mechanical systems and understanding entanglement deepens our understanding of quantum mechanics. Moreover, entanglement is a resource for quantum computation and correlates separated systems stronger than all classical correlations can do. Spin-1 atoms allow stronger quantum correlations between the wells compared with the case of spinless bosons. For spinless bosons it has been noted that particle fluctuations between the left and the right well lead to entanglement between the wells.[3] In addition to this orbital entanglement, spin-1 atoms allow spinor entanglement. In this thesis, the quantum correlations between the wells are examined for different values of the energy offset and different ratios of the tunneling strength relative to the on-site interaction. We give a lower bound for the entanglement between the wells by estimating the amount of orbital and spinor entanglement separately. At this point, we consider entanglement mainly as a theoretical characterization of the many-body state of the system.

[1] [Widera *et al.*(2005)]

[2] [Einstein *et al.*(1935)]

[3]see e.g., Refs. [Mazzarella *et al.*(2011),Dell'Anna(2012)] and references therein

Thesis Overview

The thesis is organized as follows. In Chapter 2 we review some basics regarding trapping ultracold atoms, interactions between atoms and optical lattices. We introduce spinor condensates and derive a Bose-Hubbard Hamiltonian that takes spin effects into account.

In Chapter 3 we discuss quantum phase transitions in the Bose-Hubbard model. In Sec. 3.1 we use a mean-field decoupling approach to derive the ground-state phase diagram for spinless bosons in conventional optical lattices. We discuss various methods to treat the Bose-Hubbard model and review the concept of time-of-flight measurements. In Sec. 3.2 we examine spin-1 atoms in usual lattices and discuss the different superfluid phases and first-order phase transitions. In Sec. 3.3 we introduce the mean-field Hamiltonian for spinless bosons in optical superlattices. We discuss methods to treat this Hamiltonian and present the phase diagram. In Sec. 3.4 we generalize the Bose-Hubbard Hamiltonian of Sec. 3.3 by including spin-dependent interactions and examine the phase diagram of spin-1 atoms in optical superlattices. We include magnetic fields in Sec. 3.4 which enhance spin-dependent effects and lead to additional metastable phases.

In Chapter 4 we present our studies of single-atom resonances in spinor condensates in optical superlattices. First we study isolated double-well potentials. In Sec. 4.2 we give the explicit form of the Bose-Hubbard Hamiltonian for small atom numbers. In Sec. 4.3 we present bosonic staircases of spin-1 atoms and explain why this system is a model for mesoscopic magnetism. In Sec. 4.5 the effect of magnetic fields is included. In the second part of this chapter we extend our studies of single-atom resonances to extended superlattices. Section 4.6.1 treats the phenomenon of single-atom resonances for spinless atoms in optical superlattices. In Sec. 4.6.2 we examine bosonic staircases for spin-1 atoms in superlattices.

In Chapter 5 the bipartite entanglement for the two-site Bose-Hubbard model is examined. The total entanglement between the sites depends on orbital and spin degrees of freedom. We obtain a lower bound of the total entanglement, which is given by the sum of the orbital entanglement and the spin entanglement.

Parts of this thesis have been published. Chapter 3 is based on Reference A.Wagner, A. Nunnenkamp and C. Bruder (2012)[1] and Chapter 4 and Chapter 5 are based on Reference A.Wagner, E. Demler and C. Bruder (2011).[2]

---

[1] [Wagner *et al.*(2012)]

[2] [Wagner *et al.*(2011)]

Chapter 2

Ultracold Atoms in Optical Lattices

In this chapter we review the trapping of ultracold atoms in optical dipole traps and the interactions in dilute quantum gases. We examine the physics of ultracold atoms in optical lattices and explain why the Bose-Hubbard model is applicable to this system. We introduce spinor condensates and derive a Bose-Hubbard model which takes spin-dependent interactions into account. In the last part of this review chapter we examine how ultracold atoms in lattices are experimentally probed.

Cooling and Trapping

It is quite challenging to trap neutral atoms because they must be very cold before they can be trapped. Ions are much easier to trap due to the strong Coulomb force; the forces which can be exerted on neutral atoms are much weaker than the Coulomb force.[1] At room temperature the average speed of atoms is 300 m/s; the speed of the atoms just above condensation is 150 m/s for N_2 and 90 m/s for He. Thus, neutral atoms must be highly dilute to avoid condensing and very cold, before we can trap them.

The three most common classes of traps for neutral atoms are magnetic, radiation-pressure and optical dipole traps. The first type of traps - magnetic traps - employ inhomogeneous magnetic fields which exert a state-dependent force on magnetic dipole moments.[2] The second and third type of traps exploit the fact that light can exert a radiative force on an atom because photons carry momentum. This process happens either incoherently by absorption and emission of photons as in radiation-pressure traps or coherently as in optical dipole traps. Incoherent interaction exerts the "scattering force": Light strikes an object and is scattered in random directions. In radiation-pressure traps one uses three orthogonal standing wave laser beams to

---

[1] [Chu(1991), Phillips(1998), Metcalf and der Straten(1999), Pethick and Smith(2008)]

[2] [Migdall *et al.*(1985), Bergeman *et al.*(1987)]

create an optical molasses, which is used to cool down the atoms.[1] The narrower the atomic resonance the better the red detuned standing laser beam can cool the atoms. These traps cause naturally very strong dissipation, thus cool quite effectively, but lead to unstable trap dynamics.

The third kind of traps for neutral atoms are optical dipole traps.[2] Here, one uses coherent interactions of the atoms with far detuned laser light. The laser field polarizes the atom and the polarized atom experiences a force in the inhomogeneous electromagnetic field of the incident light field. The atom induces a redistribution (or lensing) of the incident field. In these traps the potential is nearly conservative with only very weak influence from spontaneous photon scattering.

2.1   Optical Dipole Traps

The optical dipole force is generated by the dispersive interaction of the induced atomic dipole moment with the intensity gradient of the light field. The interaction is dispersive because the ground state of the atom is shifted by a frequency dependent term, which is called the alternating current (AC) Stark shift.

To examine the AC Stark effect of an oscillating electric field on an atom we use a semiclassical approach and assume the atom has got only two energy levels, an excited state $|e\rangle$ and a ground state $|g\rangle$.[3] The energy difference between these states is $\hbar\omega_0$, where ω_0 is the transition frequency of the system. When one sets the energy scale such that the energy of the ground state is zero, the unperturbed Hamiltonian of the atom may be written as $\hat{H}_0 = \hbar\omega_0|e\rangle\langle e|$.

Suppose the atom is placed at $x = 0$ in an oscillating electric field of frequency ω_L, given by $\mathbf{E}(x,t) = \mathbf{E}(x)\cos(\omega_L t)$. Under the assumption that the wavelength of the applied light is large compared to the size of the atom (which is called the dipole approximation), the interaction Hamiltonian can be expressed as $\hat{H}_I = -\hat{\mathbf{d}}\cdot\mathbf{E}$, where $\hat{\mathbf{d}}$ is the dipole moment operator of the atom. The total Hamiltonian for the atom-light system is therefore $\hat{H} = \hat{H}_0 + \hat{H}_I$. The dipole moments of the energy eigenstates of the system vanish, i.e. $\langle e|\hat{\mathbf{d}}|e\rangle = \langle g|\hat{\mathbf{d}}|g\rangle = 0$, therefore, the Hamiltonian can be written as

$$\hat{H} = \hbar\omega_0|e\rangle\langle e| - \hbar\cos(\omega_L t)\Omega_R(x)\left(|e\rangle\langle g| + |g\rangle\langle e|\right) ,$$

where $\Omega_R(x) \equiv \langle e|\hat{\mathbf{d}}|g\rangle \cdot \mathbf{E}(x)/\hbar$ is the Rabi frequency. The Rabi frequency determines the frequency at which the occupation of the ground state oscillates, which is given by $\Omega = \sqrt{\Omega_R^2 + \omega_\delta^2}$, where $\omega_\delta \equiv \omega_0 - \omega_L$ is the detuning of the laser. In the next step we write the Hamiltonian in the interaction picture. The unitary

---

[1] [Pritchard *et al.*(1986), Raab *et al.*(1987)]

[2] [Chu *et al.*(1986)]

[3] [Jessen and Deutsch(1996), Metcalf and der Straten(1999), Grimm *et al.*(2000), Pethick and Smith(2008), Foot(2010)]

transformation we need to do this is given by $\hat{U} = e^{i\hat{H}_0 t/\hbar} = |g\rangle\langle g| + e^{i\omega_0 t}|e\rangle\langle e|$. The transformed interaction part of the Hamiltonian becomes

$$\hat{U}\hat{H}_I\hat{U}^\dagger = -\frac{\hbar\Omega_R}{2}\left(e^{i(\omega_0+\omega_L)t} + e^{i(\omega_0-\omega_L)t}\right)|e\rangle\langle g| - \frac{\hbar\Omega_R}{2}\left(e^{-i(\omega_0+\omega_L)t} + e^{-i(\omega_0-\omega_L)t}\right)|g\rangle\langle e|.$$

The incoming laser light ω_L is usually far detuned, but still of the order of the atomic transition frequency ω_0. The terms containing $\omega_0 + \omega_L$ oscillate therefore much more rapidly than the terms with the detuning ω_δ and can be neglected. This is called the rotating wave approximation.[1] The full Hamiltonian in the Schrödinger picture is then given by

$$\hat{H} \approx \hbar\omega_0|e\rangle\langle e| - \frac{\hbar\Omega_R}{2}e^{-i\omega_L t}|e\rangle\langle g| - \frac{\hbar\Omega_R}{2}e^{i\omega_L t}|g\rangle\langle e|.$$

Finally, we can apply an additional unitary transformation into the frame rotating with the laser frequency $\hat{U} = e^{i\omega_L t}$ and obtain the stationary Hamiltonian

$$\hat{H} \approx \hbar\omega_\delta|e\rangle\langle e| - \frac{\hbar\Omega_R}{2}\left(|e\rangle\langle g| + |g\rangle\langle e|\right).$$

We assume the laser to be far detuned from the atomic transition, hence the population of the ground state is not significantly reduced through optical excitations. Thus, the Rabi frequency is smaller than the detuning, i.e. $\omega_\delta \gg \Omega_R$, and we can treat the oscillating electric field as a perturbation. The first-order contribution vanishes because the perturbation is purely off-diagonal. Second-order perturbation theory leads to a non-vanishing energy shift of the ground state due to the laser field which is given by

$$\Delta E_0 = \frac{|\langle e|\hat{H}_I|g\rangle|^2}{E_0 - E_e} = \frac{\hbar\Omega_R^2(x)}{4(\omega_L - \omega_0)} = -\frac{1}{2}\alpha(\omega_L)|\mathbf{E}(x)|^2, \tag{2.1}$$

where the perturbing part of the Hamiltonian is $\hat{H}_I = -\frac{\hbar\Omega_R}{2}\left(|e\rangle\langle g| + |g\rangle\langle e|\right)$ and we introduced the polarizability

$$\alpha(\omega_L) = \frac{|\langle e|\hat{\mathbf{d}}|g\rangle|^2}{\hbar(\omega_0 - \omega_L)}.$$

The energy shift in Eq. (2.1) is positive for blue-detuned laser light, i.e. $\omega_L > \omega_0$, and in this case the atom is repelled by the points of maximal field intensity. For red-detuned laser light, i.e. $\omega_L < \omega_0$, the atom is attracted toward the points of maximal light intensity (See Fig. 2.1). The approximation (2.1) is valid when the population transfer to the excited level by the laser is small; because the laser light is far off resonance (or far detuned) this is the case (the population transfer[2] is proportional to $|\Omega_R|^2/\omega_\delta^2$). In the above calculations we considered only coherent

---

[1] [Barnett and P.M. Radmore(2002)]

[2] [Metcalf and der Straten(1999)]
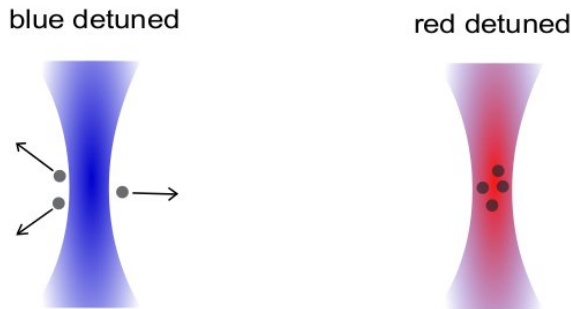
Figure 2.1: Blue and red detuned optical dipole traps.

light-matter interations and we can treat the energy shift as a conservative potential. From this potential one can derive a force,

$$\mathbf{F}(x) = \frac{1}{2}\alpha(\omega_L)\nabla|\mathbf{E}(x)|^2 \, , \tag{2.2}$$

which drives atoms into the regions of maximal light intensity for red detuned lasers and away from these regions for blue detuned lasers (see Fig. 2.1).

Until now we assumed that the lifetime of the excited state is infinite, i.e. we did not include the possibility of spontaneous emissions of photons. In this way we obtained a real polarizability and a conservative potential (2.2). However, spontaneous emission events of photons lead to a finite effective decay rate Γ_{eff} of the excited state. We can include this finite decay rate in the interaction Hamiltonian $\hat{H}_I$ and deduce that the perturbed ground state energy becomes a complex quantity. Equivalently we can say that the polarizability becomes a complex number with a non-vanishing imaginary part (compare Eq. (2.1)). Within the two-level approximation one obtains a modified energy shift[1]

$$\Delta E_0 = \frac{\hbar\Omega_R^2(x)}{4(\omega_L - \omega_0)} + i \, \Gamma_{\text{eff}} \, \frac{\hbar}{8} \left(\frac{\Omega_R(x)}{\omega_\delta} \right)^2 \, ,$$

which leads to a loss rate of atoms (i.e. random scattering) from the ground state given by

$$\Gamma_{sc}(r) \propto \left(\frac{\Omega_R(x)}{\omega_\delta} \right)^2 \, . \tag{2.3}$$

This shows that incoherent light-matter interactions and energy dissipation are negligible when the detuning is large ($\Omega_R(x) \ll \omega_\delta$). Since the loss rate increases with the laser intensity the loss rate in blue detuned traps is smaller than in red detuned ones: In red detuned traps the atoms are attracted toward regions with high light intensity, contrary to blue detuned ones. But for typical ultracold atoms experiments the loss rate is quite small for both traps and the atoms emit photons on a time

---

[1] [Grimm *et al.*(2000), Rey(2004), Foot(2010)]

scale of minutes,[1] which is much longer than the duration of a usual experiment, which takes some seconds.

The optical dipole force Eq. (2.2) can be used to generate a harmonic trap from a focused laser beam. The intensity profile of a Gaussian laser beam along the z direction is given by

$$I(r,z) = \frac{2P}{\pi w^2(z)} \exp\left(-\frac{2r^2}{w^2(z)}\right), \tag{2.4}$$

where P is the power of the laser beam, $w(z) = w_0\sqrt{1 + z^2/z_R^2}$ is the $1/e^2$ radius (w_0 is the beam waist and the Rayleigh length is $z_R = \pi w_0^2/\lambda$) and r is the radial component. Typical values for z_R are in the millimeter range and for $w_0 \approx 100\mu$m. For a red-detuned laser the intensity maximum at $z = r = 0$ corresponds to a potential minimum. We can expand the potential around this point and obtain a harmonic dipole trap,

$$V_{dip}(r,z) \approx -\frac{2P}{\pi \omega_0^2}\left(1 - \left(\frac{z}{z_R}\right)^2 - 2\left(\frac{r}{\omega_0}\right)^2\right). \tag{2.5}$$

2.2 Interactions between Ultracold Atoms

Ultracold atom experiments are usually performed by creating first a Bose-Einstein condensate of an atom cloud. Thus, the de Broglie wavelength of the atoms is of the order of the inter-atomic distance d; for dilute atom gases d is of the order of hundreds of nanometers. This is much larger than the range of the inter-atomic interactions for ultracold gases. The interactions between ultracold atoms are determined by s-wave scattering,[2] and vice-versa, the regime where s-wave scattering dominates defines the regime of ultracold atoms.

A typical s-wave scattering length a_S of ultracold atom collisions is a few nanometers. This is much shorter than the average inter-atomic distance which implies that the most relevant interactions are due to two-body encounters and that the exact interaction potential can be replaced by an effective contact interaction,

$$V(\vec{x}_1, \vec{x}_2) = g\delta(\vec{x}_1 - \vec{x}_2). \tag{2.6}$$

We can relate the quantity g to the physical parameter a_S by demanding that the interaction potential (2.6) reproduces the correct two-body scattering of ultracold atoms.

The scattering amplitude is given by

$$f(\vec{k}', \vec{k}) = \frac{m}{4\pi\hbar^2} \int d^3x' e^{i\vec{k}'\cdot\vec{x}'} V(x')\psi_{\vec{k}}(\vec{x}').$$

---

[1] [Jaksch and Zoller(2005)]

[2] [Bloch *et al.*(2008), Dalibard(1998), Pethick and Smith(2008), Gribakin and Flambaum(1993), Fetter(1998)]

In the low energy limit ($|\vec{k}| \to 0$) the scattering amplitude becomes constant and is equal to the scattering length

$$\lim_{|\vec{k}|=|\vec{k}'|\to 0} f(\vec{k}', \vec{k}) = -a_S .$$

The scattering amplitude can be expressed via the Fourier transform of the interaction potential and can be calculated iteratively

$$-f(\vec{k}', \vec{k}) \approx \frac{m}{4\pi\hbar^2} V_{\vec{k}'-\vec{k}} = \frac{m}{4\pi\hbar^2} g ,$$

where we used that the Fourier transform of the effective interaction potential (2.6) is $V(\vec{k}) = g$. We obtain the result, that the constant g is (in lowest order) related to the scattering length via the simple equation

$$g \approx \frac{4\pi\hbar^2 a_S}{m} . \tag{2.7}$$

The scattering length a_S can be negative as well as positive;[1] the effective interactions can therefore be attractive or repulsive although the interactions between ultracold atoms are dominated by attractive van-der-Waals interactions.

The interactions in a cloud of ultracold atoms are very weak and quantum-statistical effects are predominant. This can be seen by estimating the ratio of the interaction energy to the kinetic energy for a Bose gas with the density n,

$$\gamma = \frac{\epsilon_{int}}{\epsilon_{kin}} = \frac{gd^{-3}}{\hbar^2 d^2/m} \approx \frac{a_S}{d} , \tag{2.8}$$

where $d = n^{-1/3}$ is the average inter-particle spacing and we used that the de Broglie wavelength is of the order of d. The scattering length a_S is usually much shorter than d; a_S is a few nanometers and the atom density n is so small that d is a few hundred nanometers.

2.3   Optical Lattices

In this section we discuss how we can use the optical dipole force Eq. (2.2) to create a optical lattices by standing laser beams. Standing laser beams are created by superimposing two counter-propagating laser beams. Say, one laser beam is traveling in x-direction, $E(x) = E_0 \exp(ik_L x)$, with amplitude E_0, wave number k_L and wave length $\lambda = 2\pi/k$. By adding a second laser beam running in the $-x$-direction with same amplitude and wave number one obtains an optical potential $V(x) = V_0 \cos^2(k_L x)$ with periodicity $a = \lambda/2$ and strength V_0. The strength V_0 depends upon the amplitude E_0 and the polarizability of the atoms. By applying

---

[1] [Bloch *et al.*(2008)]
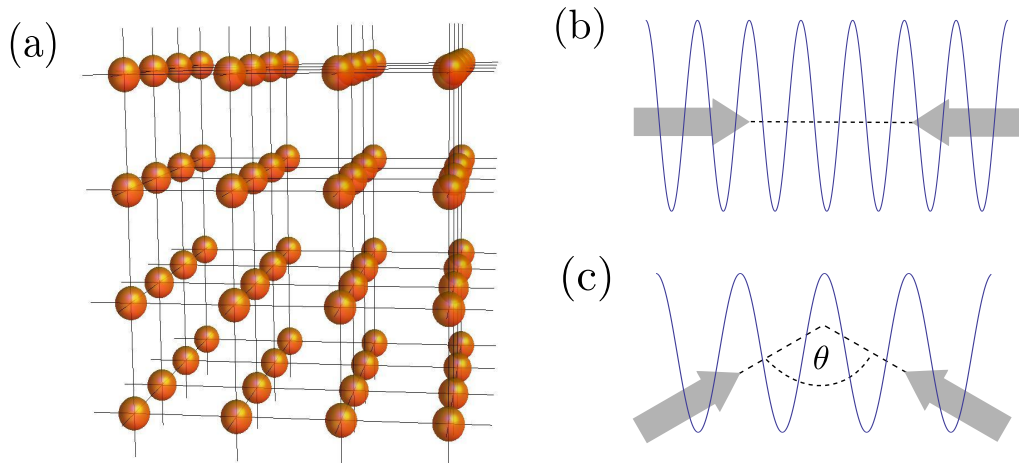
Figure 2.2: (a) Three-dimensional optical lattice, (b) one-dimensional optical lattice created from counter-propagating laser beams and (c) one dimensional lattice from two laser beams enclosing an angle θ.

two additional pairs of laser beams propagating in y- and z-direction, respectively, one obtains a 3D optical lattice

$$V_L(x) = V_{0x} \sin^2(k_L^{(x)} x) + V_{0y} \sin^2(k_L^{(y)} y) + V_{0z} \sin^2(k_L^{(z)} z) \,, \tag{2.9}$$

which creates a periodic array of microtraps and thereby an optical crystal (see Fig. 2.2a). When two laser beams interfere under an angle of 180° the lattice has a lattice constant of $\lambda/2 = \pi/k$; when the angle is smaller than 180°, one can also realize lattices with larger lattice constants (see Fig. 2.2b and 2.2c).

The strength of the trapping potential V_0 is usually given in terms of the recoil energy $E_r = \hbar^2 k_L^2 / 2m$, which is the energy an atom receives when it absorbs one photon of the optical lattice. However, the scattering of atoms with photons from the optical lattice is negligible and the potential (2.9) is nearly conservative, because the laser light is usually chosen far off resonance (see Eq. (2.3)). A typical value of the lattice constant is in the range of hundreds of nanometers and the recoil energies are in the few kilohertz range. The lattice potential might have a strength up to 100 kHz.

It is possible to create more sophisticated optical lattices by using additional standing laser beams, these are called optical superlattices.[1] E.g., we can add on top of the 1D potential $V_L(x) = V_0 \cos^2(kx)$ a second one with half the wavelength and obtain the period-2 superlattice potential

$$V_{SL}(x) = V_s \cos^2(4\pi x/\lambda - \varphi) + V_0 \cos^2(2\pi x/\lambda) \,, \tag{2.10}$$

see Fig. 2.3. The phase shift φ induces an off-set between the two sites of the unit cells of the superlattices. In Fig. 2.3 we choose $\varphi = 0$ and the unit cells are therefore degenerate.

---

[1] [Sebby-Strabley *et al.*(2006)]
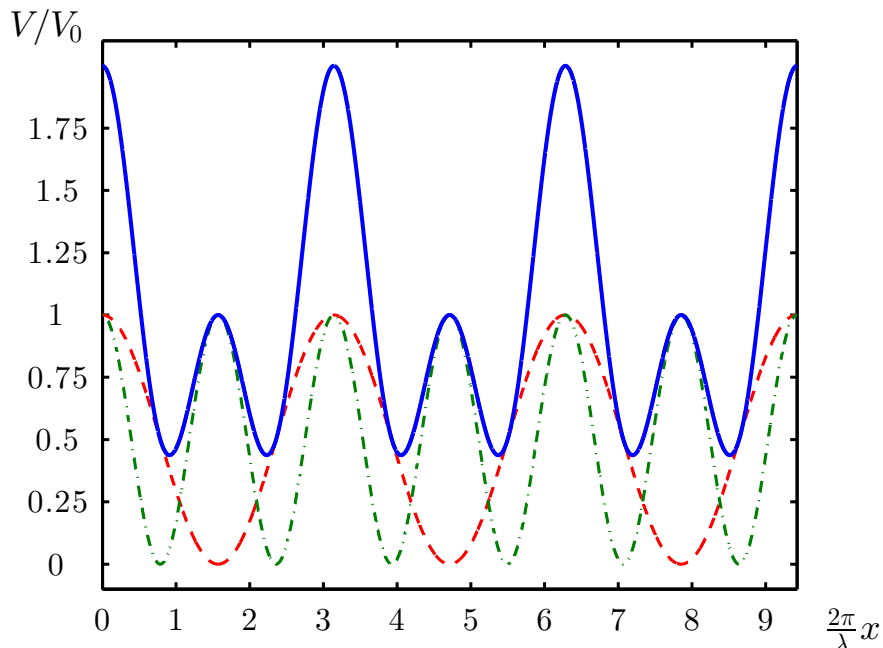
Figure 2.3: Optical superlattice created by superimposing two standing laser beams according to Eq. (2.10) with $V_0 = V_s$ and $\varphi = 0$. One laser beam corresponds to the green dashed-dotted line, the other one with half the wavelength of the first one to the red dashed line and the superposition of both, the superlattice, is painted as blue solid line.

For sufficiently strong optical lattices it is possible to approximate the lattice sites by harmonic potentials.[1] Around $x = 0$ we can use the approximation $V_0 \sin^2(kx) \approx V_0 k^2 x^2$ and obtain the Hamiltonian of a harmonic oscillator,

$$\hat{H} = \frac{\hat{p}^2}{2m} + \frac{m\omega_{ho}^2}{2}\hat{x}^2 \; , \tag{2.11}$$

where $\hbar\omega_{ho} = \sqrt{2k^2 V_0/m} = 2\sqrt{E_r V_0}$. When V_0 is much larger than E_r, each well supports a number of vibrational levels that are separated by $\hbar\omega_{ho}$.

Single Atoms in Optical Lattices

In this section we examine the spectrum of a single atom in a 1D optical lattice. The Hamiltonian of this system is given by

$$\hat{H} = \frac{\hat{p}^2}{2m} + V_L(x) \; , \tag{2.12}$$

where $V_L(x) = V_0 \sin^2(kx)$ is a periodic potential ($V_L(x) = V_L(x + a)$). The Bloch theorem states that the eigenfunctions of this Hamiltonian can be written as Bloch

---

[1] [Jaksch *et al.*(1998)]
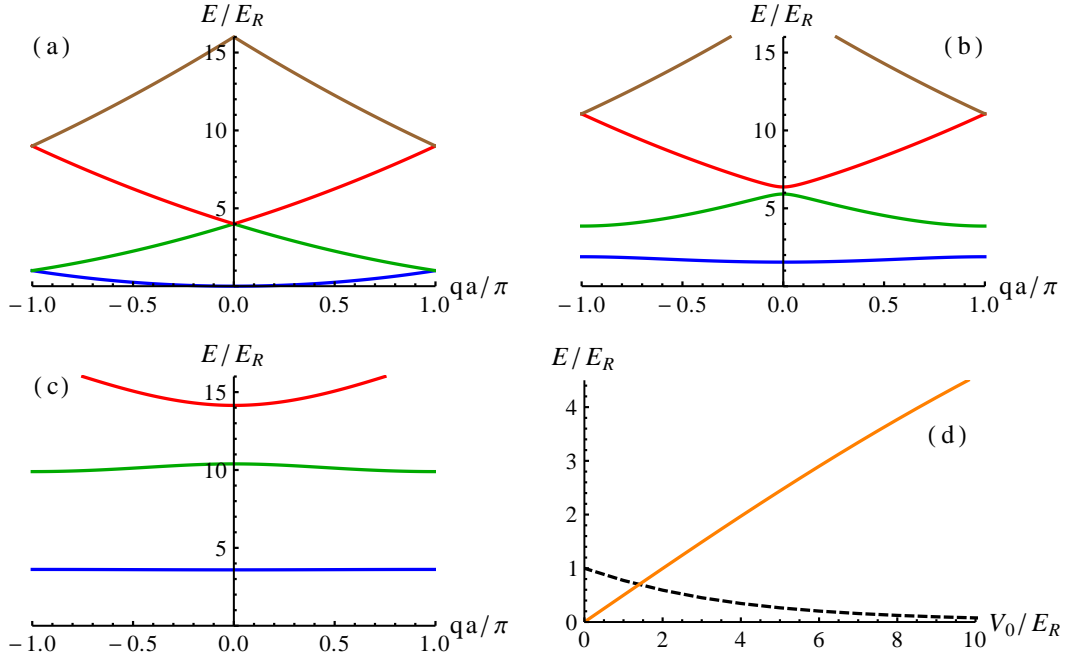
Figure 2.4: Band structure for a single atom in an optical lattice (a) $V_0/E_R = 0$, (b) $V_0/E_R = 4$, (c) $V_0/E_R = 15$ and (d) the bandwidth of the lowest band (black dashed line) and the band gap between the lowest and first energy band (orange line).

functions $\phi_q^{(n)}(x) = e^{iqx}u_q^{(n)}(x)$; here n is a band index, the $u_q^{(n)}$'s have the same periodicity as the optical potential and q is the quasi-momentum confined to the first Brillouin zone $[-\pi/a, \pi/a]$. We perform a Fourier expansion over reciprocal lattice points $G_l = 2\pi l/a$ for the potential and the Bloch functions,

$$V_L(x) = \frac{1}{\sqrt{2\pi}} \sum_{l=-\infty}^{\infty} V_l e^{iG_l x}, \quad u_q(x) = \frac{1}{\sqrt{2\pi}} \sum_{l=-\infty}^{\infty} u_q^l e^{iG_l x}, \tag{2.13}$$

where we omitted the band index (n). The Fourier coefficients of the optical potential are easily obtained because $V_L(x) = V_0 \sin^2(kx) = V_0(1/2 + e^{iG_1 x}/4 + e^{-iG_1 x}/4)$. We can now perform the Fourier transform of the Schrödinger equation $\hat{H}\phi_q(x) = E_q\phi_q(x)$ and obtain a system of algebraic equations for the Fourier coefficients u_q^l,

$$\frac{\hbar^2}{2m} (q + G_l)^2 u_q^l + \sum_m V_{l-m}u_q^m = E_q\, u_q^l. \tag{2.14}$$

We can solve these equations numerically for a finite lattice. In the case of L lattice sites there are L quasi-momenta evenly distributed in the first Brillouin zone. We can then rephrase the Eqs. (2.14) into a finite dimensional eigenvalue problem $H_q\vec{u}_q = E_q\vec{u}_q$, where the corresponding Hamiltonian H_q is tridiagonal. The diagonal elements are given by $H_{ll} = E_R (qa/\pi + 2l)^2$ ($E_R = \hbar^2 k_L^2/2M = \hbar^2\pi^2/2Ma^2$) and

the only non-vanishing off-diagonal elements are $H_{lm} = V_0/4$ for $|l - m| = 1$. In Fig. 2.4 the lowest four eigenvalues of each quasi-momentum $q \in [-\pi/a, \pi/a]$ are plotted for different lattice strengths. For finite lattice strengths the energy bands are separated by energy gaps. The band gaps vanish for a vanishing optical potential and increase when the optical potential is increased.

It is important to note that the gap between the first and the second energy band increases quite rapidly (see Fig. 2.4d). For sufficiently low temperatures only the lowest vibrational levels at each lattice site are populated. It is therefore a good approximation to assume that only the first energy band is populated; this is called the single-band approximation.

Bloch functions depend on the quasi-momentum q and describe particles which are spread out over the whole lattice. An alternative single-particle basis is provided by Wannier functions.[1] They are designed to be centered around single lattice sites x_i,

$$w_n(x, x_i) = \sqrt{\frac{a}{2\pi}} \int_{BZ} dq \; e^{-iqx_i} \phi_q^{(n)}(x) \tag{2.15}$$

with BZ indicating the first Brillouin zone. Note that due to the periodicity of the Bloch functions $\phi_q^{(n)}(x)$, the Wannier functions depend only on the distance $x - x_i$, i.e., $w_n(x, x_i) = w_n(x - x_i)$. One can use Wannier functions to derive explicit formulas for the wavefunctions of atoms in optical lattices.[2] The definition (2.15) does not lead to a unique set of Wannier states, but leaves a gauge freedom due to the possibility to multiply each Bloch function with a phase, $\phi_q^{(n)} \rightarrow e^{\theta(q,n)} \phi_q^{(n)}$. This gauge freedom preserves the centers of the Wannier functions but alters their spatial spread $\Delta^2 = \langle x^2 \rangle - \langle x \rangle^2$. To obtain maximally localized Wannier functions in a regular lattice one minimizes the spread and creates thereby exponentially decaying wave functions.[3] For superlattices it is not sufficient to use conventional Wannier functions but one needs to introduce generalized Wannier functions[4] that mix Bloch states of different bands.

Tight-Binding Single-Particle Hamiltonian

To describe non-interacting atoms in a 3D optical potential in second quantization we rewrite the Hamiltonian (2.12),

$$\hat{H} \; = \; \int d^3\vec{x} \; \hat{\psi}^\dagger(\vec{x}) \left(-\frac{\hbar^2}{2m} \; \vec{\nabla}^2 + V_L(\vec{x}) \right) \hat{\psi}(\vec{x}) , \tag{2.16}$$

where $\hat{\psi}(\vec{x})$ is a bosonic field operator for atoms in a given internal atomic state satisfying the canonical commutation relations and $V_L(\vec{x})$ the optical lattice potential.

---

[1] [Bruus and Flensberg(2004)]

[2] [Kohn(1959), Marzari and Vanderbilt(1997), Modugno and Pettini(2012)]

[3] [Kohn(1959)]

[4] [Marzari and Vanderbilt(1997), Modugno and Pettini(2012)]

We can expand the field operators in terms of the complete orthonormal Wannier basis,

$$\hat{\psi}(\vec{x}) = \sum_{i,\vec{n}} w_{\vec{n}}(\vec{x} - \vec{x}_i)\hat{b}_{\vec{n},i} \, ,$$

where $\hat{b}_{\vec{n},i}$ is the bosonic annihilation operator for the Wannier state $w_{\vec{n}}(\vec{x} - \vec{x}_i) = w_{n_x}(x - x_i)w_{n_y}(y - y_i)w_{n_z}(z - z_i)$. This product ansatz of 1D Wannier wave functions is possible for a simple cubic lattice geometry. For more complicated lattices the Wannier functions need to be modified.[1] Using Eq. (2.15) we obtain

$$
\begin{aligned}
\hat{H} &= \int d^3\vec{x} \left(\int_{BZ} d^3q \sum_{i,\vec{n}} e^{i\vec{q}\cdot\vec{x}_i}\phi_{\vec{q}}^{*(\vec{n})}(\vec{x})\hat{b}_{\vec{n},i}^\dagger \right) \left(-\frac{\hbar^2}{2m}\,\nabla^2 + V_L(\vec{x}) \right) \\
&\quad \times \left(\int_{BZ} d^3q' \sum_{j,\vec{n}'} e^{-i\vec{q}'\cdot\vec{x}_j}\phi_{\vec{q}'}^{(\vec{n}')}(\vec{x})\hat{b}_{\vec{n}',j} \right) \\
&= \sum_{i,j,\vec{n}} t_{\vec{n}}\left(\vec{x}_i - \vec{x}_j \right) \hat{b}_{\vec{n},i}^\dagger \hat{b}_{\vec{n},j} \, ,
\end{aligned}
$$

where $t_{\vec{n}}\left(\vec{x}_i - \vec{x}_j \right) = \langle w_{\vec{n},i}|\hat{H}|w_{n,j}\rangle$ contains the hopping amplitude between a particle being in the Wannier state in the band n at $\vec{x}_i$ and the Wannier state at $\vec{x}_j$. Note that due to the orthogonality of the Bloch functions $\phi_{\vec{q}}^{(\vec{n})}(\vec{x}) = \phi_{q_x}^{(n_x)}(x)\phi_{q_y}^{(n_y)}(y)\phi_{q_z}^{(n_z)}(z)$ only transitions within the same band and hopping in the direction of the lattice axes are allowed.[2]

Now we can use the result from the band structure calculation, that the band gap between the lowest and the first energy band increases for deep lattices quite rapidly and that ultracold atoms populate only the lowest energy band. Furthermore, since the Wannier functions decay within one lattice site it is justified to neglect any tunneling amplitudes other than nearest-neighbor ones.[3] This leads to a tight-binding Hamiltonian

$$\hat{H} = -\sum_{\langle i,j \rangle} t\,\hat{b}_i^\dagger \hat{b}_j \, , \tag{2.17}$$

where $\langle i, j \rangle$ denotes the summation over neighboring lattice sites and we omitted all band indexes since we assume $n = 0$. We subtracted the diagonal contribution in Eq. (2.17) (the on-site energy) because it merely shifts the position of the lowest energy band. We can express the real space operators $\hat{b}_{n,j}$ in terms of quasi-momentum operators and derive

$$\hat{H} = \sum_q \epsilon_q\,\hat{b}_q^\dagger \hat{b}_q \, ,$$

[1] [Modugno and Pettini(2012)]

[2] [Blakie and Clark(2004)]

[3] [Jaksch *et al.*(1998)]
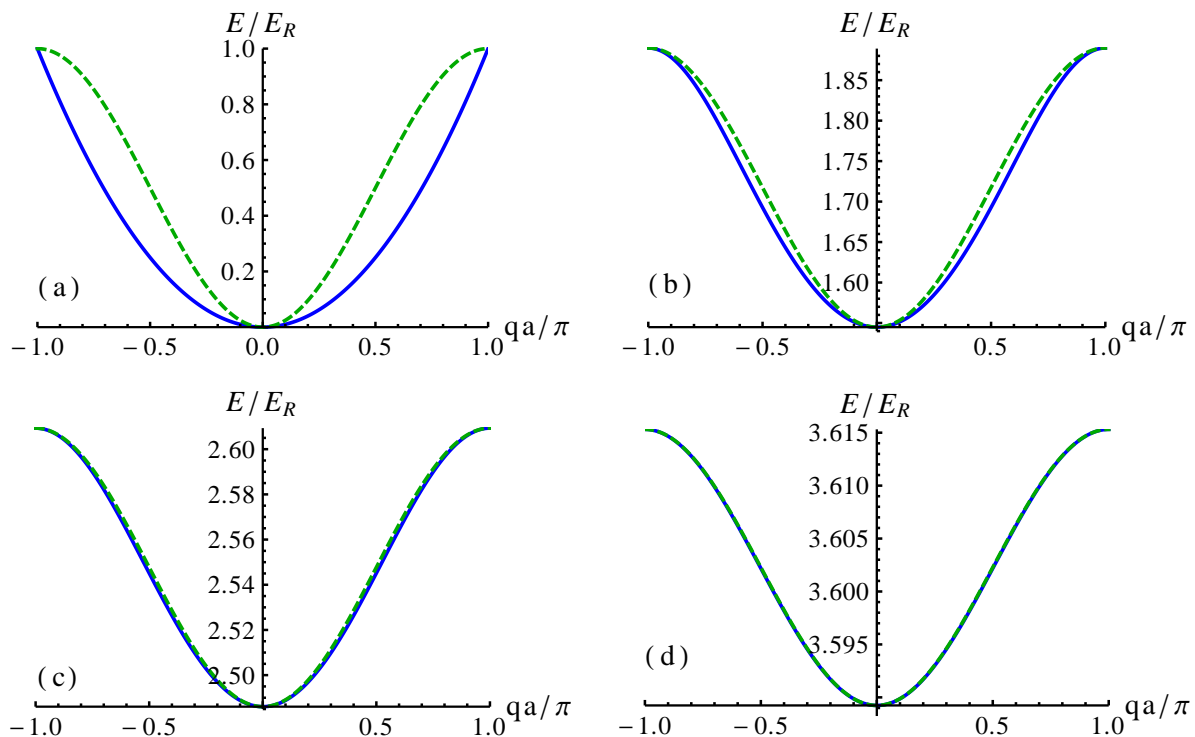
Figure 2.5: Comparison of the exact band structure (blue solid line) of the lowest Bloch band of a single atom in an optical lattice with the tight-binding band structure (green dashed line) (a) $V_0/E_R = 0$, (b) $V_0/E_R = 4$, (c) $V_0/E_R = 15$ and (d) $V_0/E_R = 15$.

where $\epsilon_q = -zt\cos(qa)$ (z is the number of neighboring lattice sites) and q lies within the first Brillouin zone. Note that the tunneling amplitude is a quarter of the bandwidth of the tight-binding band for one-dimensional lattices. This bandwidth decreases with increasing lattice strength (see Fig. 2.4d). In Fig. 2.5 the tight-binding dispersion relation is compared with the exact shape of the lowest Bloch band. We see that even for shallow lattices the exact solution is quite well approximated by the tight-binding approach and for lattice strengths above $V_0 \approx 10E_r$ the tight-binding dispersion relation is nearly exact.

It is possible to solve Eq. (2.16) exactly by mapping it onto the Mathieu equation.[1] From the width of the lowest energy band one can derive an exact value for the tunneling amplitude,

$$t = \frac{4}{\sqrt{\pi}}\left(\frac{V_0}{E_r}\right)^{3/4}\exp\left[-2\left(\frac{V_0}{E_r}\right)^{1/2}\right]E_r, \qquad (2.18)$$

which is the gain in the kinetic energy due to nearest-neighbor tunneling. The tunneling amplitude decays exponentially with increasing lattice strength (compare Fig. 2.4d).

---

[1] [Abramowitz and Stegun(1964), Büchler *et al.*(2003)]

2.4   The Bose-Hubbard Model

In this section we combine our knowledge about interactions between ultracold atoms and the behaviour of single atoms in optical lattices. We obtain the full many-body Hamiltonian in second quantisation for ultracold atoms by adding a term containing the effective contact interaction to the single-particle Hamiltonian (2.16),

$$
\begin{aligned}
\hat{H} &= \int d^3\vec{x}\ \hat{\psi}^\dagger(\vec{x})\left(-\frac{\hbar^2}{2m}\ \nabla^2 + V_L(\vec{x})\right)\hat{\psi}(\vec{x}) \\
&+ \frac{1}{2}\frac{4\pi a_s\hbar^2}{m}\int d^3x\ \hat{\psi}^\dagger(\vec{x})\hat{\psi}^\dagger(\vec{x})\hat{\psi}(\vec{x})\hat{\psi}(\vec{x}),
\end{aligned}
\tag{2.19}
$$

where $\hat{\psi}(\vec{x})$ is a bosonic field operator for atoms in a given internal atomic state satisfying the canonical commutation relations, $V_L(\vec{x})$ is an optical lattice potential (e.g., Eq. (2.9)), a_s is the s-wave scattering length (compare Eqs. (2.6) and (2.7)) and m is mass of the atoms (see Eq. 2.6). For the sake of simplicity we omitted the harmonic trapping potential. Following Sec. 2.3 we expand the atom operators $\psi(\vec{x})$ in terms of Wannier operators,

$$
\hat{\psi}(\vec{x}) = \sum_j w_0(\vec{x} - \vec{x}_j)\hat{b}_j,
\tag{2.20}
$$

where $\hat{b}_i$ is the bosonic annihilation operator for an atom at site $\vec{x}_i$. We included only the Wannier functions belonging to the lowest Bloch band, because the atom cloud is so cold that only the lowest energy band is populated and so dilute, that the interactions are too weak to excite the atoms to higher bands;[1] that means we apply a single-band approximation. Performing the expansion of Eq. (2.19) in terms of Wannier functions leads to

$$
\hat{H} = -\sum_{i,j} t_{ij}\hat{b}_j^\dagger\hat{b}_i + \frac{1}{2}\sum_{ijkl} U_{ijkl}\hat{b}_i^\dagger\hat{b}_j^\dagger\hat{b}_k\hat{b}_l,
$$

where the coefficients U_{ijkl} and t_{ij} are defined in terms of overlap integrals of Wannier functions. The kinetic energy is contained in

$$
t_{ij} = -\int d^3x\ w_0^*(\vec{x} - \vec{x}_i)\left(-\frac{\hbar^2}{2m}\ \nabla^2 + V_L(\vec{x})\right)w_0(\vec{x} - \vec{x}_j)
\tag{2.21}
$$

and the interaction between the atoms in

$$
U_{ijkl} = \frac{4\pi a_s\hbar^2}{m}\int d^3x\ w_0^*(\vec{x} - \vec{x}_i)w_0^*(\vec{x} - \vec{x}_j)w_0(\vec{x} - \vec{x}_k)w_0(\vec{x} - \vec{x}_l).
\tag{2.22}
$$

For sufficiently deep optical lattices, the Wannier functions decay within one lattice site and the overlap of neighboring Wannier functions is very small. We can restrict

---

[1] [Jaksch *et al.*(1998), Jaksch and Zoller(2005)]
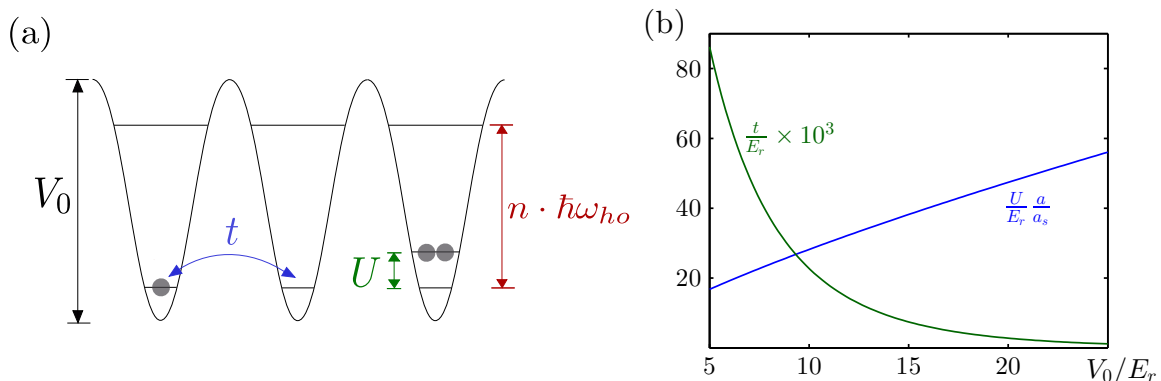
Figure 2.6: (a) Sketch of the Bose-Hubbard parameters given in Eq. (2.23) with repulsive on-site interactions. The optical wells support a number of vibrational levels (indicated with $n \cdot \hbar\omega_{ho}$). (b) Lattice strength dependence of the on-site interaction U (blue line, we used the harmonic approximation given in Eq. (2.24) to calculate U) and lattice strength dependence of the tunneling amplitude t (green line), which is orders of magnitude smaller than the on-site interaction.

the tunneling to nearest neighbor tunneling ($t_{ij} = t$) and the interactions to on-site interactions ($U_{0000} = U$).[1] We obtain the standard tight-binding Bose-Hubbard Hamiltonian,[2]

$$\hat{H} = -t \sum_{<i,j>} \hat{b}_j^\dagger \hat{b}_i + \mu \sum_i \hat{n}_i + \frac{U}{2} \sum_i \hat{n}_i(\hat{n}_i - 1), \qquad (2.23)$$

where $\hat{n}_i = \hat{b}_i^\dagger \hat{b}_i$ and the operators $\hat{b}_i$ satisfy boson commutation relations. We included a term containing the chemical potential μ to tune the particle number. The Bose-Hubbard model describes Bose particles on a lattice with on-site interaction, so that only particles occupying the same site interact, while tunneling is allowed between adjacent sites. The tunneling parameter t corresponds to the gain in kinetic energy during a tunneling event and the strength of the on-site interaction is given by U (compare Fig. 2.6a). Repulsive interactions result in a positive U and attractive interactions in a negative U.

We can use the harmonic approximation (2.11) to obtain an expression for the on-site interaction. The Wannier wave-function in a lattice site is then replaced by $\psi_{ho}(x) = (\sqrt{\pi}a_{ho})^{-1/2} \exp[-x^2/2a_{ho}^2]$ where $a_{ho} = \sqrt{\hbar/m\omega_{ho}}$ and $\hbar\omega_{ho} = 2\sqrt{E_r V_0}$. The on-site interaction in the harmonic approximation is then

$$U^{(ho)} = \frac{4\pi a_s \hbar^2}{m} \cdot \left(\frac{1}{\sqrt{2\pi}a_{ho}}\right)^3 = \sqrt{8\pi}\frac{a_s}{a}\left(\frac{V_0}{E_r}\right)^{3/4} E_r, \qquad (2.24)$$

where a is the lattice spacing and we used $\hbar^2/m = 2E_r a^2/\pi^2$. Thus, the strength of the repulsive interaction increases with V_0 (due to tighter squeezing of the wavefunc-

---

[1] [Jaksch *et al.*(1998)]

[2] [Hubbard(1963), Fisher *et al.*(1989)]

22

tions $w_0(\vec{x} - \vec{x_i})$). Using the harmonic approximation and the tunneling amplitude given in Eq. (2.18) we see that it is possible to tune the ratio

$$\frac{U}{t} \approx \frac{a_s}{a} \exp\left[2\sqrt{\frac{V_0}{E_r}}\right] \qquad (2.25)$$

from the regime of weak to strong interactions by tuning the laser strength V_0 (see Fig. 2.6b). The kinetic energy of the atoms in a lattice decreases exponentially when optical lattice gets stronger; in the same time the on-site interactions increases only polynomially with the lattice strength. We see that the ratio $\gamma = \frac{\epsilon_{int}}{\epsilon_{kin}}$ (compare Eq. (2.8)) is changed because of the optical lattice. Even if the atom density in the microtraps is still small, the weakly interacting condensate is transformed into a strongly interacting system. The lattice does not increase the interaction energies much but reduces the kinetic energy a lot. Alternatively, one can say that the lattice increases the effective mass of the atoms exponentially.

The Bose-Hubbard model contains the essential features of interacting Bose systems in a minimal way, namely the competition between kinetic and potential energy. Because the parameters in the Bose-Hubbard model can be controlled by external laser fields, one can consider the system as a toolbox, with which one can create plenty of different Hamiltonians. There are many theoretical tools to examine the Bose-Hubbard model, some will be presented in Chapter 3. Nonetheless, the Bose-Hubbard model is not exactly solvable, not even in one dimension, where the corresponding continuum model (the Lieb-Liniger model) is exactly solvable (on the contrary, the fermionic Hubbard model is solvable in one dimension via the Bethe ansatz). This makes ultracold quantum gases in optical lattices an ideal paradigm for quantum simulations, in the sense that we can use a physical system to simulate a theoretical model or another physical system which is approximated by this theoretical model. Physical realizations of strongly interacting Bose systems include Josephson junction arrays, granular and short-correlation-length superconductors and flux lattices in type-II superconductors.

2.5 Spinor Condensates

Trapping ultracold atoms in conventional magnetic traps leads to frozen spin degrees of freedom, i.e., all atoms are in the same internal hyperfine state, such that the atoms behave effectively as spinless particles.[1] If the atoms are trapped by optical means only, the atoms keep the extra spin degree of freedom and the Bose-Einstein condensate becomes a spinor condensate.[2] The spinor degree of freedom on alkaline gases corresponds to the manifold of degenerate Zeeman hyperfine levels. Experimentally, long-lived alkali spinor gases have been explored in the $F = 1$ manifold

---

[1] [Stamper-Kurn and Ketterle(2000)]

[2] [Stamper-Kurn *et al.*(1998), Stenger *et al.*(1998)]

both of ^{23}N (by D. Stamper-Kurn *et al.*(1998)) and ^{87}Rb (by Barrett *et al.*(2001)[1])
and the higher energy $F = 2$ manifold of ^{87}Rb.[2] The ground-state properties of
spinor Bose-Einstein condensates in single traps were theoretically investigated by
T. Ho and Ohmi *et al.*.[3] There are review articles about spinor quantum gases writ-
ten by M. Lewenstein *et al.*,[4] Ma. Ueda and Y. Kawaguchi[5] and D. Stamper-Kurn
et al..[6]

Atoms can be bosons or fermions, depending on the total angular momentum
they carry. The total atomic angular momentum **F** is the result of the coupling of
the orbital angular momentum of the electrons **L**, the electronic spins **S** and the
nuclear spin **I**. The alkali-metal atoms ^{23}Na and ^{87}Rb carry no electronic orbital
angular momentum, the electron spin $1/2$ and the nuclear spin $3/2$; their total
angular momentum is therefore 1 or 2 and the atoms are Bosons. The Rubidium
isotope ^{85}Rb carries nuclear spin $5/2$ and its total spin is therefore 2 or 3. The alkali-
metal atoms ^{133}Cs carry nuclear spin $7/2$ and their hyperfine quantum number is 3
or 4.

In this section we want to describe spin-1 atoms. Instead of a scalar wavefunction
we use a three-component wavefunction to describe the atoms,

$$\vec{\psi}(\vec{r}) = \begin{pmatrix} \psi_1(\vec{r}) \\ \psi_0(\vec{r}) \\ \psi_{-1}(\vec{r}) \end{pmatrix}, \tag{2.26}$$

where the subscripts of ψ_m refer to the spin projection on the quantization axes,
$m_F \in \{-1, 0, 1\}$. The wavefunction transforms as a vector and this vectorial char-
acter has a pronounced effect on the inter-atomic interactions, which we will see
when we examine the symmetry constraints of our model in detail.

To include interactions between the atoms we follow Sec. (2.2). The only relevant
interactions are two-body contact interactions. The atoms can therefore be modeled
by a generalized version of Eq. (2.19),

$$\hat{H} = \int d^3r \left\{ \hat{\psi}_m^\dagger \left(-\frac{\hbar^2}{2m} \nabla^2 + V_{ext} \right) \hat{\psi}_m + \frac{g_{ij,kl}}{2} \hat{\psi}_i^\dagger \hat{\psi}_j^\dagger \hat{\psi}_k \hat{\psi}_l \right\}, \tag{2.27}$$

where $\hat{\psi}_m$ ($\hat{\psi}_m^\dagger$) is a field operator that annihilates (or creates) an atom in the m-th
hyperfine state ($m \in \{-1, 0, 1\}$) at point r and we sum over repeated indexes.
The interaction term describes the annihilation of two atoms in the hyperfine states
k and l and the creation of two atoms in the states i and j. There are $3^4 = 81$
possible coefficients $g_{ij,kl}$ but fundamental symmetries restrict the number of allowed
interactions and independent parameters.

---

[1] [Barrett *et al.*(2001)]

[2] [Chang *et al.*(2004), Kuwamoto *et al.*(2004), Schmaljohann *et al.*(2004)]

[3] [Ho(1998), Ohmi and Machida(1998)]

[4] [Lewenstein *et al.*(2007), Lewenstein *et al.*(2012)]

[5] [Ueda and Kawaguchi(2010)]

[6] [Stamper-Kurn and Ketterle(2000), Stamper-Kurn and Ueda(2012)]

The particle exchange symmetry, which holds in this case due to the indistinguishability of the bosons, states that it does not make a difference if particle A collides with B or particle B with A, i.e., $g_{ij,kl} = g_{ji,kl}$. There are six possible tuples ij for three different hyperfine states ($ij \in [11, 10, 1-1, 00, 0-1, -1-1]$). Furthermore the system is time reversal invariant, i.e., $g_{ij,kl} = g_{kl,ij}$, which reduces the number of independent interaction parameters $g_{ij,kl}$ to $\binom{6+2-1}{2} = 21$.

Another symmetry restricts the interactions considerably, namely rotational symmetry. Without an external magnetic field there is no preferred direction in a system of spin-1 atoms and the system is therefore invariant under rotations. This leads to the conservation of the total angular momentum and there is only a small number of independent interaction parameters left. The contact interaction for spin-1 atoms can be written in terms of scattering channels according to the total spin. For indistinguishable spin-1 bosons the interaction reads

$$\hat{V}(r_1, r_2) = \sum_{S=0,2} g_S \ \hat{P}_S \ \delta(r_1 - r_2), \tag{2.28}$$

where $g_S = \frac{4\pi\hbar^2 a_S}{m}$ is the interaction strength for every channel, a_S is the respective scattering length and the sum is over $S = 0$ and $S = 2$ only, because of the particle-exchange symmetry. Here we speak of channels, but the $\hat{P}$ are just projection operators, i.e. $\hat{\mathbb{1}} = \hat{P}_0 + \hat{P}_2$. The different a_S will lead to distinct magnetic ordering. To see this, it is convenient to rewrite the contact potential in terms of spin operators,

$$(\mathbf{F}_1 \cdot \mathbf{F}_2)|\phi\rangle = (\mathbf{F}_1 \cdot \mathbf{F}_2)(\hat{P}_0 + \hat{P}_2)|\phi\rangle = (-2\hat{P}_0 + \hat{P}_2)|\phi\rangle,$$

because the P's project onto eigenstates of $\mathbf{F}_1 \cdot \mathbf{F}_2$. This leads to

$$\hat{V}(r_1, r_2) = \left(\frac{g_0 + 2g_2}{3} + \frac{g_2 - g_0}{3} \mathbf{F}_1 \cdot \mathbf{F}_2 \right) \delta(r_1 - r_2). \tag{2.29}$$

The difference between the scattering lengths a_0 and a_2 is usually small such that the spin-independent part $\frac{g_0 + 2g_2}{3}$ of the interaction potential dominates. Nevertheless, the spin ordering leads to a ferromagnetic phase when $a_0 > a_2$ (e.g. Rubidium) and to a antiferromagnetic phase when $a_0 < a_2$ (e.g. Sodium).

We can plug in the interaction potential (2.29) into the Hamiltonian (2.27) and obtain[1]

$$
\begin{aligned}
\hat{H} &= \int d^3r \left[\hat{\psi}_m^\dagger \left(-\frac{\hbar^2}{2M}\nabla^2 + V_{ext} \right) \hat{\psi}_m + \frac{c_0}{2} \hat{\psi}_m^\dagger \hat{\psi}_j^\dagger \hat{\psi}_j \hat{\psi}_m \right. \\
&\quad + \left. \frac{c_2}{2} \hat{\psi}_m^\dagger (F_\nu)_{mj} \hat{\psi}_j \cdot \hat{\psi}_l^\dagger (F_\nu)_{lk} \hat{\psi}_k \right],
\end{aligned}
\tag{2.30}
$$

where

$$c_0 = \frac{g_0 + 2g_2}{3} = 4\pi\hbar^2 \frac{a_0 + 2a_2}{3m} \tag{2.31}$$

---

[1] [Ho(1998), Ohmi and Machida(1998)]

and

$$c_2 = \frac{g_2 - g_0}{3} = 4\pi\hbar^2 \frac{a_2 - a_0}{3m} \ . \tag{2.32}$$

Thus, we can use the angular momentum conservation to express the interaction parameters $g_{ij,kl}$ by scattering lengths, which are well known physical parameters. The repeated indexes in Eq. (2.30) are summed over and F_ν with $\nu = x, y, z$ are the spin-1 matrices,

$$F_x = \frac{1}{\sqrt{2}} \begin{pmatrix} 0 & 1 & 0 \\ 1 & 0 & 1 \\ 0 & 1 & 0 \end{pmatrix}, \ F_y = \frac{i}{\sqrt{2}} \begin{pmatrix} 0 & -1 & 0 \\ 1 & 0 & -1 \\ 0 & 1 & 0 \end{pmatrix}, \ F_z = \begin{pmatrix} 1 & 0 & 0 \\ 0 & 0 & 0 \\ 0 & 0 & -1 \end{pmatrix}. \tag{2.33}$$

It is instructive to write down the interaction terms in detail,

$$c_0 \hat{\psi}_m^\dagger \hat{\psi}_j^\dagger \hat{\psi}_j \hat{\psi}_m + c_2 \ \hat{\psi}_m^\dagger (F_\nu)_{mj} \hat{\psi}_j \cdot \hat{\psi}_l^\dagger (F_\nu)_{lk} \hat{\psi}_k =$$

$$
\begin{aligned}
& (c_0 + c_2) \hat{\psi}_1^\dagger \hat{\psi}_1^\dagger \hat{\psi}_1 \hat{\psi}_1 + c_0 \hat{\psi}_0^\dagger \hat{\psi}_0^\dagger \hat{\psi}_0 \hat{\psi}_0 + (c_0 + c_2) \hat{\psi}_{-1}^\dagger \hat{\psi}_{-1}^\dagger \hat{\psi}_{-1} \hat{\psi}_{-1} \\
+ \ & 2(c_0 + c_2) \hat{\psi}_1^\dagger \hat{\psi}_0^\dagger \hat{\psi}_1 \hat{\psi}_0 + 2(c_0 + c_2) \hat{\psi}_{-1}^\dagger \hat{\psi}_0^\dagger \hat{\psi}_{-1} \hat{\psi}_0 + 2(c_0 - c_2) \hat{\psi}_1^\dagger \hat{\psi}_{-1}^\dagger \hat{\psi}_1 \hat{\psi}_{-1} \\
+ \ & 2c_2 \hat{\psi}_0^\dagger \hat{\psi}_0^\dagger \hat{\psi}_1 \hat{\psi}_{-1} + 2c_2 \hat{\psi}_1^\dagger \hat{\psi}_{-1}^\dagger \hat{\psi}_0 \hat{\psi}_0.
\end{aligned}
$$

$$\tag{2.34}$$

The comparison with Eq. (2.27) shows that we expressed the interaction coefficients with the two independent physical parameters a_0 and a_2. Only eight interaction terms remain, three self-scattering (first three terms one the right side of Eq. (2.34)), three cross-scattering (next three terms of Eq. (2.34)) and two spin relaxation terms (last row of Eq. (2.34). We can now make a clear distinction between usual multi-component condensates and spinor condensates. A usual multi-component condensate consists for example out of ^{87}Rb atoms in a conventional magneto-optical trap. For certain magnetic field strengths the singlet and the triplet scattering length are practically equal allowing simultaneous magnetic trapping of more than one hyperfine component.[1] These multi-component ultracold gases are also called pseudo-spin systems. The spin-relaxation terms are the result of the rotational symmetry in spinor condensates and do not appear in pseudo-spin multi-component condensates. In these condensates the atom number of each component is conserved; spin relaxation leads to trap loss for them. In spinor quantum gases the population transfer between different hyperfine components is only subjected to conservation of the total number of atoms and the total magnetization.

The simplification of the interaction is only strictly valid in the absence of magnetic fields. In the presence of a non-vanishing magnetic field the hyperfine spin is not a good quantum number anymore and the collisional properties will be more complicated. The strongest deviations from the rotationally symmetric case occur at Feshbach resonances where a closed scattering channel is coupled to an open one via a certain magnetic field. Nevertheless, away from Feshbach resonances and for weak magnetic fields the zero-field description is a good approximation.

---

[1] [Myatt et al.(1997)]

Meanfield Ansatz for a Weakly Interacting Spinor Condensate

In this section we examine a spin-1 quantum gas trapped in a shallow harmonic trap without an optical lattice.[1] For a weakly interacting spinor quantum gas we can replace the bosonic field operators $\hat{\vec{\psi}}$ by their expectation values, $\hat{\vec{\psi}} = \vec{\phi}$, where $\vec{\phi} = (\phi_1, \phi_0, \phi_{-1})$ is a vector of c-numbers. Using this in Eq. (2.30) we obtain the energy functional $E[\vec{\phi}] = \langle \hat{H} - \mu \hat{N} \rangle$,

$$E[\vec{\phi}] = \int d^3 r \left\{ \frac{\hbar^2}{2m} \left(\nabla \sqrt{n} \right)^2 + \frac{\hbar^2}{2m} \left(\nabla \vec{\xi} \right)^2 n + (V_{ext} - \mu) + \frac{n^2}{2} \left(c_0 + c_2 \langle \vec{F} \rangle^2 \right) \right\} ,$$

(2.35)

where we introduced a spinor $\vec{\xi}$ such that

$$\vec{\phi} = \sqrt{n} \vec{\xi}.$$

(2.36)

The spinor is normalized $|\vec{\xi}|^2 = 1$, n is the atomic density and $\langle \vec{F} \rangle = \sum_{kl} \xi_k^* \vec{F}_{kl} \xi_l$. All spinors that are related to each other by gauge transformations $\vec{\xi} \to e^{i\varphi} \vec{\xi}$ and spin rotations $\vec{\xi} \to \mathcal{U}(\alpha, \beta, \gamma) \vec{\xi}$, where $\mathcal{U}(\alpha, \beta, \gamma) = e^{-i\alpha F_z} e^{-i\beta F_y} e^{-i\gamma F_z}$ and $\{\alpha, \beta, \gamma\}$ are the Euler angles, lead to degenerate values of $E[\vec{\phi}]$. The ground state of the system is found by minimizing the energy functional. The value of the spin-independent interaction parameter c_0 must be positive, otherwise the condensate collapses. Depending on the sign of of the spin-dependent interaction parameter c_2 there are two distinct mean-field phases.

Ferromagnetic phase: For ferromagnetic spin interactions, i.e. $c_2 < 0$, the system is minimized for $\langle \vec{F} \rangle^2 = 1$. The ground state in this case corresponds to all possible rotations of the state $(1, 0, 0)^T$, such as

$$\vec{\xi} = e^{i\varphi} \mathcal{U}(\alpha, \beta, \gamma) \begin{pmatrix} 1 \\ 0 \\ 0 \end{pmatrix} = e^{i(\varphi - \gamma)} \begin{pmatrix} e^{-i\alpha} \cos^2(\beta/2) \\ \sqrt{2} \cos(\beta/2) \sin(\beta/2) \\ e^{i\alpha} \sin^2(\beta/2) \end{pmatrix}.$$

This state is called ferromagnetic state. The symmetry group of this phase is SO(3). Given that the square of the order parameter is just the atom number we can ask for the positive, real values of $\vec{\xi}$. For $\beta = \pi/2$, $\alpha = 0$ and $0 < \theta = \gamma \le 2\pi$ we obtain

$$\vec{\xi} = \frac{1}{2} \begin{pmatrix} 1 \\ \sqrt{2} \\ 1 \end{pmatrix}.$$

(2.37)

Ferromagnetic spin interactions occur for ^{87}Rb in the $F = 1$ manifold.

---

[1] [Ho(1998), Ohmi and Machida(1998)]

Polar phase: For antiferromagnetic spin interactions, i.e. $c_2 > 0$, the system is minimized for $\langle \vec{F} \rangle^2 = 0$. The ground state spinor in this case is given by

$$\vec{\xi} = e^{i\varphi} \mathcal{U}(\alpha, \beta, \gamma) \begin{pmatrix} 0 \\ 1 \\ 0 \end{pmatrix} = e^{i\varphi} \begin{pmatrix} -\frac{1}{\sqrt{2}} e^{-i\alpha} \sin(\beta) \\ \cos(\beta) \\ \frac{1}{\sqrt{2}} e^{i\alpha} \sin(\beta) \end{pmatrix}$$

and the ground state is called polar. Here the spinor $\vec{\xi}$ is independent of the Euler angle γ and the symmetry group is $U(1) \times S^2$, where S^2 consists of all vectors pointing at the surface of a unit sphere. Again we can use gauge invariance to obtain a real, positive order parameter. One possible tuple $\{\varphi, \alpha, \beta\}$ to generate a real order parameters is $\beta = \pm \pi/2$ and $\varphi \pm \alpha = 0, \pi, \ldots$, which leads to

$$\vec{\xi} = \frac{1}{\sqrt{2}} \begin{pmatrix} 1 \\ 0 \\ 1 \end{pmatrix}, \tag{2.38}$$

which is called the transverse polar state.[1] There is another possibility to obtain a real, positive order parameter, namely $\varphi = 0, \pi, \ldots$ and $\alpha = 0, \pi, \ldots$, which leads to

$$\vec{\xi} = \begin{pmatrix} 0 \\ 1 \\ 0 \end{pmatrix}. \tag{2.39}$$

This state is called longitudinal polar. Thus, in the antiferromagnetic case there are two possible spinors. antiferromagnetic interactions are present for ^{23}Na and ^{85}Rb in the $F = 1$ manifold.

Ultracold Spin-1 Atoms in Optical Lattices

In this section we want to derive a Hubbard type lattice model similar to Eq. (2.30) for spinor gases in optical lattices. We expand the field operators (2.26) in the Wannier basis analogous to Eq. (2.20),

$$\hat{\psi}(\vec{x}) = \sum_{i,\sigma} \hat{b}_{i\sigma} w_0(\vec{x} - \vec{x}_i), \tag{2.40}$$

where we included only the lowest vibrational states (see above) and assumed that the Wannier functions are independent of the hyperfine quantum number σ. The bosonic operators $\hat{b}_{i,\sigma}$ ($\hat{b}_{i,\sigma}^\dagger$) annihilate (create) an atom in the lowest Bloch band localized at site i in the hyperfine state σ. The operators $\hat{b}_{i,\sigma}$ obey the canonical

---

[1] [Stamper-Kurn and Ueda(2012)]

commutation relations $[\hat{b}_{i,\sigma}, \hat{b}^\dagger_{j,\sigma'}] = \delta_{ij}\delta_{\sigma\sigma'}$ and $[\hat{b}^\dagger_{i,\sigma}, \hat{b}^\dagger_{j,\sigma'}] = [\hat{b}_{i,\sigma}, \hat{b}_{j,\sigma'}] = 0$. Using this expansion in Eq. (2.30) we can derive a Hubbard-type tight-binding Hamiltonian[1]

$$\hat{H} = -t \sum_{\langle i,j \rangle, \sigma} \hat{b}^\dagger_{\sigma i}\hat{b}_{\sigma j} + \frac{U_0}{2} \sum_i \hat{n}_i(\hat{n}_i - 1) + \mu \sum_i \hat{n}_i + \frac{U_2}{2} \sum_i \left(\hat{\vec{S}}_i^2 - 2\hat{n}_i \right), \quad (2.41)$$

where $\hat{n}_i = \sum_\sigma \hat{b}^\dagger_{\sigma i}\hat{b}_{\sigma i}$ is the atom number operator of site i and $\langle i, j \rangle$ denotes nearest neighbors. The first term in Eq. (2.41) contains the spin-symmetric tunneling between the wells and t is the hopping matrix element between the lattice sites. The amplitude t can be calculated via overlap integrals of Wannier functions similar to Eq. (2.21). The on-site repulsive interaction is described by two terms. The first one, which is parameterized by U_0, is independent of the spin of the atoms. The term proportional to U_2 describes spin-dependent interactions: it penalizes nonzero spin configurations on individual lattice sites in the case of antiferromagnetic interactions ($U_2 > 0$, e.g. ^{23}Na) and favors high-spin configurations in the case of ferromagnetic interactions ($U_2 < 0$, e.g. ^{87}Rb). The values of the on-site interaction parameters are given in terms of overlap integrals,

$$\begin{aligned}
U_0 &= \frac{4\pi\hbar^2}{3m}(a_0 + 2a_2) \int d^3x\ w_0^*(\vec{x} - \vec{x}_i)w_0^*(\vec{x} - \vec{x}_j)w_0(\vec{x} - \vec{x}_k)w_0(\vec{x} - \vec{x}_l) \\
U_2 &= \frac{4\pi\hbar^2}{3m}(a_2 - a_0) \int d^3x\ w_0^*(\vec{x} - \vec{x}_i)w_0^*(\vec{x} - \vec{x}_j)w_0(\vec{x} - \vec{x}_k)w_0(\vec{x} - \vec{x}_l),
\end{aligned}$$

where we can choose any value for i, because the on-site interaction is assumed to be site-independent (compare Eq. (2.22)). The operators

$$\hat{\vec{S}}_i = \sum_{\sigma\sigma'} \hat{b}^\dagger_{i,\sigma}\vec{F}_{\sigma\sigma'}\hat{b}_{i,\sigma'} \tag{2.42}$$

correspond to the total spin at site i, with F denoting the spin-1 matrices given in Eq. (2.33). The components of the spin operator are given by

$$\begin{aligned}
\hat{S}_{ix} &= \frac{1}{\sqrt{2}} \left(\hat{b}^\dagger_{1i}\hat{b}_{0i} + \hat{b}^\dagger_{0i}\hat{b}_{1i} + \hat{b}^\dagger_{-1i}\hat{b}_{0i} + \hat{b}^\dagger_{0i}\hat{b}_{-1i} \right) \\
\hat{S}_{iy} &= \frac{i}{\sqrt{2}} \left(-\hat{b}^\dagger_{1i}\hat{b}_{0i} + \hat{b}^\dagger_{0i}\hat{b}_{1i} + \hat{b}^\dagger_{-1i}\hat{b}_{0i} - \hat{b}^\dagger_{0i}\hat{b}_{-1i} \right) \\
\hat{S}_{iz} &= \hat{b}^\dagger_{1i}\hat{b}_{1i} - \hat{b}^\dagger_{-1i}\hat{b}_{-1i}.
\end{aligned} \tag{2.43}$$

and obey the usual angular momentum commutation relations $[\hat{S}_{ik}, \hat{S}_{il}] = i\epsilon_{klm}\hat{S}_{im}$ with $\{k, l, m\} = \{x, y, z\}$.

The parameters Eq. (2.41) can be controlled by adjusting the intensity of the laser beams; it is possible to move from regimes of strong tunneling ($U_0 \ll t$) to regimes of very weak tunneling ($t \ll U_0$). We can check this by calculating the ratio U_0/t in the harmonic approximation (compare Eq. (2.25)),

$$\frac{t}{U_0} \approx \frac{3a}{a_0 + 2a_2} \exp\left[-2\sqrt{\frac{V_0}{E_r}} \right], \tag{2.44}$$

---

[1] [Jaksch *et al.*(1998), Imambekov *et al.*(2003)]

where a is the lattice spacing and E_r is the recoil energy. Whereas the ratio of t/U_0 can be changed, the ratio U_0/U_2 is fixed for all lattice geometries,

$$\frac{U_2}{U_0} = \frac{a_2 - a_0}{a_0 + 2a_2} \, , \tag{2.45}$$

because the scattering lengths a_0 and a_2 do not depend on the trapping potentials. The optical dipole force depends on the hyperfine state of the atoms, but only weakly. Let ω_δ be the detuning of the laser light from the atomic transition frequency, then the spin-independent energy shift is proportional to $1/\omega_\delta$ (compare Eq. (2.1)) and the spin-dependent is proportional to as $1/\omega_\delta^2$.[1] An estimated ratio of U_2/U_0 is 0.04 for ^{23}Na and -0.005 for ^{87}Rb.[2]

Effects of Magnetic Fields

In this section we want to examine the effect of weak magnetic fields on spinor condensates. Spinor Bose-Einstein condensates are realized in optical traps, because strong magnetic traps would break the degeneracy of the different hyperfine levels and align the atom spins, thus creating a condensate of effectively spinless bosons. Nevertheless it is interesting to include weak magnetic fields in the calculations (also because magnetic shielding is needed but can be done only to a certain degree).

The most obvious contribution from a weak homogeneous magnetic field is the linear Zeeman shift. The linear Zeeman energy caused by a homogeneous magnetic field $\vec{B} = (0, 0, B_0)$ chosen along the z-axis (which is our quantization axis) is given by

$$E_{lin} = -p \int d^3x \; n \; \langle F_z \rangle \tag{2.46}$$

and is minimized by placing all atoms in the strong-field seeking $|m_F = 1\rangle$ state. Here $p = g\mu_B B_0$ where g is the Landé factor, μ_B is the Bohr magneton and n is the mean-field atomic density (compare Eq. (2.35)). The linear Zeeman shift for the Bose-Hubbard model for spin-1 bosons (2.41) is given by

$$\hat{H}_{\mathrm{lin}} = p \sum_{i,\sigma} m_{i\sigma} \hat{n}_{i\sigma} = p \; \hat{S}_z^{tot}, \tag{2.47}$$

where $\hat{n}_{i\sigma}$ is the particle number operator for the ith site that gives the number of bosons in the mth hyperfine state. The linear Zeeman energy splitting is much larger than the spin-dependent interactions energy scale already at magnetic fields of tens of μG.[3] Thus, under the application of even very weak magnetic fields exothermic

---

[1] see [Stamper-Kurn and Ueda(2012)], Sec. IV.A "Experimental Realities".

[2] [Burke $et\ al.$(1998), Imambekov $et\ al.$(2003), Black $et\ al.$(2007), Stamper-Kurn and Ueda(2012)]

[3] [Stamper-Kurn and Ketterle(2000)]

(a)

(b)
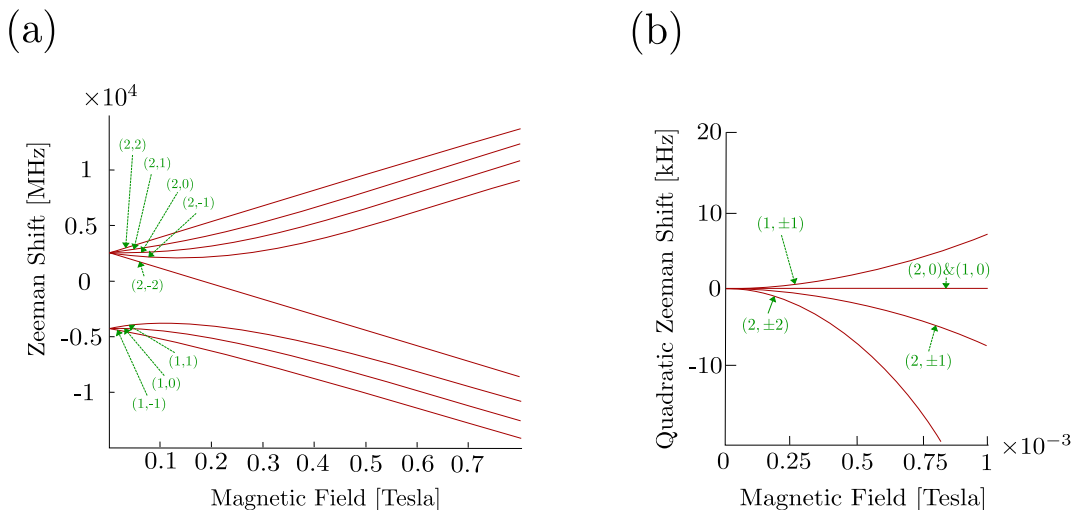
Figure 2.7: Sketch of the magnetic field dependence of the hyperfine (F, m_F) levels of ^{87}Rb. This rubidium isotope has a nuclear spin of $I = 3/2$ and therefore a total angular momentum of $F = 1$ or $F = 2$. The $F = 1$ and $F = 2$ spin manifolds are separated by the hyperfine interaction. In (a) the Zeeman splitting of the hyperfine levels is shown. For small magnetic fields F is a good quantum number. In (b) the zero-field hyperfine splitting and the linear Zeeman shift are subtracted. The quadratic Zeeman shift is positive for the $(F = 1, m_F = \pm 1)$ levels and negative for the $(F = 2, m_F = \pm 2)$ and $(F = 2, m_F = \pm 1)$ levels.

dipolar relaxation collisions might drive the spinor condensate into a scalar condensate where all atoms are spin-aligned. However, these spin-relaxation collisions are quite rare and the magnetization of the spinor gas is on the time scale of seconds a conserved quantity. All experiments take place on a shorter timescale and we can therefore ignore the linear Zeeman effect.[1] One can include spin conservation via a Lagrange multiplier;[2] the parameter p in Eq. (2.46) can be chosen as the Lagrange multiplier and the linear Zeeman shift can be gauged away.

However, the Zeeman shift of hyperfine spin states at weak magnetic fields is not strictly linear (see Fig. 2.7). For alkali atoms the shift of the energy levels can be calculated by the Breit-Rabi Hamiltonian[3] and the quadratic Zeeman shift to Eq. (2.35) is given by

$$E_{quad} = q \int d^3r \ n \ \langle F_z^2 \rangle, \tag{2.48}$$

where $q = q_0 B^2$ and $q_0 = h \times 390$ Hz/G^2 for the $(F = 1, \ m_F = \pm 1)$ states of sodium.[4] The quadratic Zeeman effect for spin-1 atoms in optical lattices can be

---

[1] [Stenger *et al.*(1998), Rodriguez *et al.*(2011), Stamper-Kurn and Ueda(2012)]

[2] [Stenger *et al.*(1998)]

[3] [Breit and Rabi(1931)]

[4] [Stenger *et al.*(1998)]
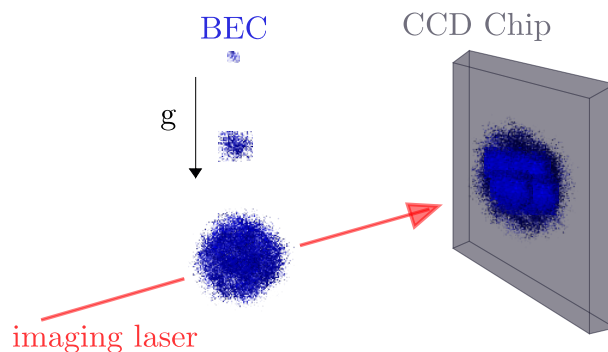
Figure 2.8: Time-of-flight absorption imaging. After some time-of-flight in which the Bose-Einstein condensate (BEC) expands freely only subjected to the gravitational force an imaging laser is used to take a picture of the expanded cloud on a CCD chip.

incorporated in the Hamiltonian (2.41) by adding the term

$$\hat{H}_{\text{QZ}} = q \sum_{i,\sigma} m_{i\sigma}^2 \hat{n}_{i\sigma}, \qquad (2.49)$$

where $\hat{n}_{i\sigma}$ counts the number of atoms in the m_ith hyperfine spin. Only for small magnetic fields the hyperfine quantum number is conserved and therefore a good quantum number.

2.6 Probing Ultracold Atoms

Ultracold atoms offer the possibility to prepare, manipulate and detect quantum states with a very high degree of perfection. In this section we review some methods to probe ultracold atoms experimentally.

Time of Flight Measurements

In time-of-flight measurements trapping potentials are switched off and the expanding cloud of atoms is probed via an absorption image[1] (see Fig. 2.8). There are two possibilities how to switch off the trapping potentials. One can either switch off the laser fields abruptly, which is called sudden release, or release the atom cloud slowly by an adiabatic shutoff. After a sudden release the quasi-momentum distribution is abruptly transformed into momentum space and after some time of flight this momentum distribution is experimentally detectable as spatial distribution.[2] By

---

[1] [Pedri *et al.*(2001), Isacsson and Girvin(2005), Bloch *et al.*(2008), Gerbier *et al.*(2008)]

[2] [Roth and Burnett(2003), Toth *et al.*(2008)]

removing the lattice in an adiabatic manner it is also possible to map out the quasi-momentum distribution and thereby visualize the occupation within the Brillouin zone.[1]

To examine the mechanism of time of flight measurements we assume that the atom cloud trapped in the lattice is in the many body state $|\Phi\rangle$. After switching off the trapping potentials the interactions vanish and the system evolves freely,[2] i.e., the propagator is given by $\hat{U}(t) = \exp(-i\hat{H}t/\hbar)$ with $\hat{H} = \int d^3x \hat{\psi}^\dagger(x)\hat{p}^2/(2m)\hat{\psi}(x)$. This propagator describes the ballistic expansion of the atom cloud, i.e., given an atom with momentum $\vec{p}$ its position $\vec{x}$ after some time t is $\vec{x}(t) = \hbar t \vec{p}/m$. The spatial density of the atom cloud after some time of flight t is given by

$$\langle n(\vec{x})\rangle_t = \langle\Phi|U^\dagger(t)\hat{n}(\vec{x})U(t)|\Phi\rangle$$

We can expand the density distribution in terms of momentum components,

$$\langle n(\vec{x})\rangle_t = \int \frac{d\vec{k}_1}{(2\pi)^3} \int \frac{d\vec{k}_2}{(2\pi)^3} e^{-i(\vec{k}_1\cdot\vec{x})} e^{i(\vec{k}_2\cdot\vec{x})} e^{-i\hbar t|\vec{k}_1|^2/2m} e^{-i\hbar t|\vec{k}_2|^2/2m} \langle\Phi|\hat{\psi}^\dagger_{\vec{k}_1}\hat{\psi}_{\vec{k}_2}|\Phi\rangle$$

$$= \int \frac{d\vec{k}_1}{(2\pi)^3} \int \frac{d\vec{k}_2}{(2\pi)^3} e^{-i(\vec{k}_1-\vec{k}_2)\cdot[\vec{x}-(\hbar t/2m)(\vec{k}_1+\vec{k}_2)]} \langle\Phi|\hat{\psi}^\dagger_{\vec{k}_1}\hat{\psi}_{\vec{k}_2}|\Phi\rangle \qquad (2.50)$$

For long t we can make a far-field approximation which uses the fact that the size of the expanded cloud is much larger than the size L of the atom cloud before the traps are switched off. Thus, we use $\hbar t \gg mL^2$ and make a stationary-phase approximation to calculate the integral in Eq. (2.50). Let the phase be $\varphi(\vec{k}_1, \vec{k}_2)$. For the sake of simplicity we consider a 1D integral; the points of stationary phase are at $\frac{\partial\varphi}{\partial k_1} = \frac{\partial\varphi}{\partial k_2} = 0$, which leads to $k_1 = k_2 = \frac{mx}{\hbar t}$. From this we can calculate the full integral, obtaining

$$\langle\hat{n}(\vec{x})\rangle_t \approx \left(\frac{m}{ht}\right)^3 \langle\Phi|\hat{n}_{\vec{k}(\vec{x})}|\Phi\rangle, \qquad (2.51)$$

where $\hat{n}_{\vec{k}} = \hat{\psi}^\dagger_{\vec{k}}\hat{\psi}_{\vec{k}}$ and $\vec{k}(\vec{x}) = m\vec{x}/\hbar t$ relates the in situ momentum $\hbar\vec{k}$ to the final observation position $\vec{x}$. Measuring the the density of atoms after a long time of flight t at a point $\vec{x}$ thus corresponds to a measurement of momentum distribution at $\vec{k} = m\vec{x}/\hbar t$ of the state $|\Phi\rangle$ prior to trap release.

Time-of-flight experiments also allow the detection of higher order correlations by noise measurements.[3] Similar to the density distribution, the density-density correlation function after some time-of-flight mirrors the momentum correlations of the trapped system,

$$\langle\hat{n}(\vec{x}_1)n(\vec{x}_2)\rangle_t \propto \langle\Phi|\hat{n}_{\vec{k}_1}\hat{n}_{\vec{k}_2}|\Phi\rangle,$$

---

[1] [Greiner *et al.*(2001)]

[2] [Kupferschmidt and Müller(2010)]

[3] [Altman *et al.*(2004)]

where t denotes the time of free expansion and $|\Phi\rangle$ is the quantum state in the trap. The method allows to distinguish many different phases of proposed phase diagrams.[1]

In order to probe spinor atoms a combination of Stern-Gerlach experiments[2] and time-of flight measurements can be used. During the time-of-flight a magnetic field gradient is applied to separate atoms in different magnetic hyperfine states in different spatial regions. Here, the magnetic field is switched on adiabatically during the expansion to obtain a projective measurement of the distribution of atoms among the Zeeman sublevels in the trap. The population of each different sublevel has been measured by several groups with sub-poissonian measurement uncertainty.[3] However, until now experiments with spinor condensates and Stern-Gerlach time-of-flight mapping have been performed only with conventional traps and not with optical lattices.[4]

Single-Site Measurements

It is possible to probe quantum gases in optical lattice with single site accuracy.[5] These *in situ* images allow to go beyond the analysis of the momentum distribution and of the coherence properties of trapped atoms. In single-site fluorescence imaging near-resonant light is used, such that the atoms start fluorescing. This laser-induced fluorescence is captured by a high resolution microscope and imaged onto a low-noise CCD camera. To achieve sufficiently high scattering rates the atoms are constantly cooled to keep the temperature below the lattice depth and at the same time the lattice depth is increased to hold the atoms at their position. Because the imaging laser is near resonant atom pairs are expelled out of the trap by light-induced collisions;[6] the imaged occupation in the lattice reflects therefor the parity of the atom number per site. Another *in situ* detection method is absorption imaging.[7]

Quantum Polarization Spectroscopy

In quantum polarization spectroscopy the quantum Faraday effect is used to detect magnetic ordering of ultracold atoms in optical lattices.[8] The quantum Faraday effect describes the rotation of the polarization of light when it is propagating inside a magnetic medium. The method is non-demolishing and can be used with a very high spatial resolution.

---

[1] [Greiner *et al.*(2005), Fölling *et al.*(2005), Rom *et al.*(2006), Greif *et al.*(2011)]

[2] [Gerlach and Stern(1924)]

[3] [Bookjans *et al.*(2011), Gross *et al.*(2011), Lücke *et al.*(2011), Hamley *et al.*(2012)]

[4] e.g., [Liu *et al.*(2009)]

[5] [Nelson *et al.*(2007), Sherson *et al.*(2010), Bakr *et al.*(2010), Weitenberg *et al.*(2011)]

[6] [DePue *et al.*(1999)]

[7] [Gemelke *et al.*(2009), Hung *et al.*(2010), Zimmermann *et al.*(2011)]

[8] [Julsgaard(2003), Eckert *et al.*(2008), Roscilde *et al.*(2009), Hammerer *et al.*(2010), De Chiara and Sanpera(2011), De Chiara *et al.*(2011)]

Bragg Spectroscopy

Two-photon Bragg spectroscopy allows to detect the low-energy excitations and thereby reveals fundamental properties of the quantum state of the system. The Bragg spectroscopy provides a direct measure of the dynamic structure factor, i.e., the Fourier transform of the density-density correlation function. By means of Bragg spectroscopy one can probe the band structure of the excitation spectrum in the presence of a periodic potential.[1] Bragg spectroscopy allows also to detect the magnetic order in an atomic gas because appropriately tuned light couples differently to the different spin components of the sample.[2]

---

[1] [Stöferle *et al.*(2004), Köhl *et al.*(2005), Fabbri *et al.*(2009), Clément *et al.*(2009), Clément *et al.*(2010)] and references therein.

[2] [Partridge *et al.*(2006), Shin *et al.*(2006)]

Chapter 3

Quantum Phase Transitions in the Bose-Hubbard Model

In this chapter we discuss the Mott-superfluid quantum phase transition of ultracold atoms in optical lattices. The Bose-Hubbard model represents an excellent model of these systems[1] and is known to display this phase transition.[2] In Sec. 3.1 we examine the two limiting cases of the Bose-Hubbard model (vanishing tunneling and vanishing interactions), present some methods to treat the model for finite interactions and discuss Gutzwiller mean-field methods in detail. In Sec. 3.1.1 we present the phase diagram of spinless bosons in optical lattices. In Sec. 3.2 we discuss spin-1 atoms in optical lattices, in Sec. 3.3 spinless bosons in optical superlattices and in Sec. 3.4 spin-1 atoms in optical superlattices.

Quantum Phase Transitions

Quantum phase transitions occur at zero temperature. They are not driven by thermal fluctuations (like classical phase transitions), but by quantum fluctuations. Quantum phase transitions are based on an abrupt qualitative change of the ground state of the many body system.

In a classical system at finite temperature the thermal equilibrium is reached when the free energy,

$$F = E - TS, \tag{3.1}$$

is minimal (E is the internal energy, T the temperature and S the entropy). The system can lower the free energy in two ways: The state of the system can be chosen such that the internal energy is minimized, or one chooses a configuration such that the entropy is maximal. The temperature determines which of the two possibilities leads to a smaller free energy. Let us consider a three-dimensional array of spins

---

[1] [Jaksch *et al.*(1998)]

[2] [Fisher *et al.*(1989)]

with nearest-neighbor, ferromagnetic interactions, e.g., an Ising ferromagnet. This system has its minimal internal energy when all spins are aligned, but the entropy is minimal in this state as well. In order to maximize its entropy all spins must be in disorder, although the internal energy is maximal in this configuration. The temperature T then decides which of the two states is realized. For high temperatures the free energy is minimal for high entropy and the spins are in disorder. Below a critical temperature T_c the advantage of a high entropy does not compensate the disadvantage of a higher internal energy anymore and all the spins are aligned, which is then the stable equilibrium state of the system.

Classical phase transitions are a result of two competing elements while minimizing the free energy. For $T = 0$ no classical phase transition is possible anymore because the free energy is equal to the internal energy and the classical entropy vanishes. But at this temperature quantum phase transitions may occur; they are driven by competing terms in the ground-state energy. These phase transitions can only be accessed by varying a physical parameter, such as magnetic field or interaction properties.[1]

3.1 The Mott-Superfluid Quantum Phase Transition

We can use the Bose-Hubbard model to describe ultra-cold atoms in deep optical lattices (see Sec. 2.4). For low temperatures and sufficiently strong lattices the thermal and interaction energies are much smaller than the band-gap between the first and second energy band, and the Wannier functions decay inside a single lattice site. The Bose-Hubbard model of such a system is given by

$$\hat{H} = -t \sum_{<i,j>} \hat{b}_i^\dagger \hat{b}_j - \mu \sum_i \hat{n}_i + \frac{U}{2} \sum_i \hat{n}_i(\hat{n}_i - 1), \tag{3.2}$$

where $\hat{b}_i^\dagger$ creates an atom at the site i, $\hat{n}_i = \hat{b}_i^\dagger \hat{b}_i$ counts the atoms at each site, U gives the strength of the on-site interaction and t corresponds to the tunneling amplitude between neighboring lattice sites (compare Eq. 2.23).

The Bose-Hubbard model with repulsive interactions supports two prominent quantum phases[2] at $T = 0$. For small on-site interactions ($U \ll t$) the wave functions of the atoms superimpose coherently and a finite fraction of the bosons is condensed. In this regime the system is in the superfluid quantum phase which is characterized by long-range correlations, a gapless excitation spectrum and a finite compressibility. When the on-site interactions dominate ($U \gg t$) and the filling is commensurate,

---

[1] [Sachdev(2001)]

[2] [Fisher *et al.*(1989), Rokhsar and Kotliar(1991), Krauth *et al.*(1992), Bruder *et al.*(1993), Zwerger(2003), Jaksch and Zoller(2005)]

the system is called Mott-insulating. In this quantum phase there is no long-range order, the excitation spectrum has a gap, and the system is incompressible.

Although the Bose-Hubbard model is so simple it contains the essential features of strongly interacting Bose systems, namely the competition between kinetic and interaction energy. Similar to Eq. (3.1), where for each given temperature one of the two terms dominates, for each ratio of t/U either the kinetic or the potential energy determines the quantum phase of the system. Thus, the Bose-Hubbard model provides one of the simplest realizations of a quantum phase transition.[1]

Limit of Strong Tunneling

In the limit of vanishing on-site interactions ($U = 0$) the Hamiltonian Eq. (3.2) can be trivially diagonalized by a discrete Fourier transform into the space of quasi-momentum. Assuming a regular lattice with L sites, we replace the operators $\hat{b}^\dagger$ creating an atom at a specific site by

$$\hat{c}_{\vec{k}}^\dagger = \frac{1}{\sqrt{L}} \sum_i \hat{b}_i^\dagger e^{-i\vec{k}\cdot\vec{r}_i}, \tag{3.3}$$

which create atoms with a certain quasi-momentum $\vec{k}$, which is discretized over the first Brillouin zone. When we substitute this quasi-momentum operators into the Hamiltonian (3.2), we find

$$\hat{H} = \sum_k \left(\epsilon_{\vec{k}} - \mu\right) \hat{c}_{\vec{k}}^\dagger \hat{c}_{\vec{k}} + \frac{U}{2L} \sum_{k_1,\ldots,k_4} \hat{c}_{\vec{k}_1}^\dagger c_{\vec{k}_2}^\dagger c_{\vec{k}_3} c_{\vec{k}_4} \delta_{\vec{k}_1 + \vec{k}_2} \delta_{\vec{k}_3 + \vec{k}_4} \tag{3.4}$$

where

$$\epsilon_{\vec{k}} = -2t \sum_{d=1}^{D} \cos(k_d a) \tag{3.5}$$

is the free-particle dispersion relation in a cubic lattice with lattice spacing a and dimension D. For small lattice spacings and small velocities, the dispersion relation is quadratic and describes the dynamics of free particles. For vanishing interactions all atoms are Bose-condensed in the zero momentum state and the ground state of N atoms is given by

$$\Psi_{SF} = \frac{\left(\hat{c}_0^\dagger\right)^N}{\sqrt{N!}} |0\rangle = \frac{1}{\sqrt{N!}} \left(\frac{1}{\sqrt{L}} \sum_{j=1}^{L} \hat{b}_j^\dagger\right)^N |0\rangle,$$

where $|0\rangle$ denotes the vacuum state. Thus, for vanishing interactions the atoms are totally delocalized over the lattice, which minimizes the overall kinetic energy. This quantum phase is called superfluid.[2] In the superfluid phase the wave functions

---

[1] [Sachdev(2001)]

[2] The fraction of condensed atoms is in general not the same as the fraction of superfluid atoms (see [Yukalov(2009)]).

of the ultracold atoms superpose coherently to a macroscopic wavefunction; in the thermodynamic limit (i.e., $N, L \to \infty$ at a fixed density $\bar{n} = N/L$) the superfluid wave function can be written as a product of coherent states,

$$\Psi_{SF} = \prod_i^L |\psi_i\rangle, \quad \text{where} \quad |\psi_i\rangle = e^{-|\phi_i|^2/2} \sum_{n=0}^\infty \frac{\phi_i^n}{\sqrt{n!}} |n\rangle_i, \tag{3.6}$$

where $|n\rangle_i$ is the Fock state with n atoms on site i. For vanishing interactions $|\phi_i| = |\langle \hat{b}_i \rangle| = \sqrt{N/L} = \sqrt{\bar{n}}$ and the atom number distribution in each site is Poissonian, i.e., the probability to find n atoms in a lattice site is $p(n) = \frac{\bar{n}^n e^{-\bar{n}}}{n!}$.

Atomic Limit

The atomic limit is the limit of vanishing tunneling amplitudes, i.e., $t = 0$. The Hamiltonian in this limit decomposes into a sum over single-site operators,

$$\hat{H}_0 = -\sum_i \mu \hat{n}_i + \frac{U}{2} \sum_i \hat{n}_i(\hat{n}_i - 1), \tag{3.7}$$

where $\hat{n}_i = \hat{b}_i^\dagger \hat{b}_i$ is the particle number operator on each site. Since there is no tunneling in the lattice and the interactions are predominant the atoms do not move and the system is a Mott insulator. The ground state of the system for $t = 0$ is simply a product of on-site Fock states with no correlations,

$$\Psi_{Mott} \propto \prod_{i=1}^L |\bar{n}\rangle_i, \tag{3.8}$$

where the filling of each lattice site $N/L = \bar{n}$ is an integer. Here we assume that the chemical potential is constant over the lattice and the filling is the same in each site. In the atomic limit all atoms are localized and the compressibility

$$\kappa = \frac{\partial \langle \hat{n} \rangle}{\partial \mu}$$

vanishes for non-integer values of μ/U (see below). As we will see there are islands in the phase diagram nearby $t = 0$ of fixed particle number and vanishing compressibility. These islands are called Mott lobes.

To excite the ground state of the system described in Eq. (3.7) at a constant particle number, one has to move one atom to another site, thereby producing one site with $n-1$ atoms and one with $n+1$ atoms. For vanishing tunneling, the energy difference between the ground state and the first excited state is

$$\Delta E = \frac{U}{2} \left[(n+1)^2 + (n-1)^2 - 2n^2 \right] = U. \tag{3.9}$$

Consequently, there is an energy gap between the ground state and the first excited states. This energy gap characterizes the Mott-insulating phase and can be probed by Bragg spectroscopy.[1]

---

[1] [Stöferle *et al.*(2004), Köhl *et al.*(2005)]

Finite Interactions

For ultracold atoms in optical lattices we can tune the ratio of of the interactions over the tunneling amplitudes (U/t) over many orders of magnitude (compare Eq. (2.25)). In this section we want to mention some methods to describe the properties of the Bose-Hubbard model for finite ratios of U/t.

Starting from the limit of vanishing interactions, increasing interactions will gradually remove atoms from the condensate even at zero temperature, a phenomenon called quantum depletion. We can describe this process with a **Bogoliubov approach**.[1] For small interactions we replace the annihilation and creation operators of the zero momentum state (in which the vast majority of atoms still is) in the Hamiltonian (3.4) by their mean values plus a fluctuation,

$$\hat{c}_0^\dagger \;\to\; \sqrt{N_0} + \delta\hat{c}_0^\dagger \;\; \text{and} \;\; \hat{c}_0 \;\to\; \sqrt{N_0} + \delta\hat{c}_0,$$

where N_0 is the number of condensed atoms. The approximation consists of neglecting higher order correlations of the deviations from the condensate (or equivalently, interactions between the quasi-particles). This approach does predict a gapless spectrum in the thermodynamic limit;[2] it is therefore not suited to examine the quantum phase transition. Nevertheless, it works well for small interactions and gives the correct dispersion relation of the atom cloud when the kinetic energy of the atoms dominates.

Corrections to the limiting case of vanishing tunneling amplitudes can be included via the **strong coupling expansion**.[3] This approximation examines the corrections within the Mott-insulating phase due to weak tunneling; it is a perturbative expansion of Eq. (3.2) in t/U. Increased tunneling is due to lowering the strength of the lattice potential. In first order the ground-state wave function is given by

$$\Psi_{Mott}^{(1)} = \Psi_{Mott} + \frac{t}{U} \sum_{<i,j>} \hat{b}_i^\dagger \hat{b}_j \Psi_{Mott}, \tag{3.10}$$

where $<i,j>$ denotes the summation over adjacent lattice sites. Equation (3.10) states that small tunneling $t \ll U$ adds adjacent particle-hole excitations to the state Ψ_{Mott} of completely localized atoms. When the tunneling amplitudes increases higher order excitations appear as well, i.e., additional particle-hole excitations and particle-hole pairs which are separated further apart. Once the kinetic energy of the atoms (approximately t) becomes of the order of the interaction energy U, the gain in kinetic energy outweighs the repulsion and the atoms will be delocalized over the whole lattice and the strong coupling expansion breaks down. The strong-coupling expansion has been performed up to 13th order and is used as a benchmark for other approximations. Nevertheless it is analytically and numerically quite involved

---

[1] [Bogoliubov(1947), van Oosten *et al.*(2001)]

[2] [Hugenholtz and Pines(1959)]

[3] [Freericks and Monien(1996), Elstner and Monien(1999), Rey *et al.*(2005)]

and the much simpler mean-field approach also predicts important features of the Bose-Hubbard model.

The **Gutzwiller mean-field**[1] approach is able to predict a quantum phase transition for the Bose-Hubbard model. In this approach we reduce the Hamiltonian (3.2) to a single-site Hamiltonian by neglecting correlations of neighboring deviation operators,

$$
\begin{aligned}
\hat{b}_i^\dagger \hat{b}_j &= (\hat{b}_i^\dagger - \langle \hat{b}_i^\dagger \rangle)(\hat{b}_j - \langle \hat{b}_j \rangle) + \hat{b}_i^\dagger \langle \hat{b}_j \rangle + \hat{b}_j \langle \hat{b}_i^\dagger \rangle - \langle \hat{b}_i^\dagger \rangle \langle \hat{b}_j \rangle \\
&\xrightarrow{MF} \hat{b}_i^\dagger \langle \hat{b}_j \rangle + \hat{b}_j \langle \hat{b}_i^\dagger \rangle - \langle \hat{b}_i^\dagger \rangle \langle \hat{b}_j \rangle.
\end{aligned}
\tag{3.11}
$$

The result is the zero-dimensional mean-field Hamiltonian

$$
\hat{H}_{MF} = \sum_i \left[-\mu \hat{n}_i + \frac{U}{2} \hat{n}_i(\hat{n}_i - 1) - zt(\phi^* \hat{b}_i + \phi\, \hat{b}_i^\dagger) + zt|\phi|^2 \right],
\tag{3.12}
$$

where z denotes the number of neighbors of each lattice site; for 1D lattices $z = 2$, for 2D $z = 4$ and for 3D $z = 6$. The superfluid order parameter is given by

$$
\langle b_j \rangle = \phi,
\tag{3.13}
$$

since it is connected to its conjugate "field"[2] zt by

$$
\phi = -\frac{\partial \langle \hat{H}_{MF} \rangle}{\partial(zt)}\ .
$$

In the Mott phase the expectation value of $\hat{b}$ (and $\hat{b}^\dagger$) vanishes, since the Mott wave function is a product of Fock-states (see Eq. (3.8)). In the superfluid phase the expectation value of $\hat{b}$ is given by $\langle \hat{b} \rangle = \sqrt{n_{\mathrm{sf}}}$ where n_{sf} is the number of condensed atoms per site. The decoupling mean-field approach is equivalent to decomposing the many-particle wave function of the lattice into a product of single site contributions,

$$
|\Psi_{MF}\rangle = \prod_j |\psi\rangle_j \quad \text{with} \quad |\psi\rangle_j = \sum_{n=0}^\infty \alpha_n^{(j)} |n\rangle_j,
$$

where $|n\rangle_j$ denotes the Fock state of n atoms at the j-th site and $\left|\alpha_n^{(j)}\right|^2$ corresponds to the probability of having n atoms at the j-th site. For a homogeneous Bose-Hubbard model as in Eq. (3.2) these probabilities do not depend on the site index j. The strength of the Gutzwiller approach is that it includes the correct wave function for the non-interacting limit Eq. (3.6) as well as for the limit of vanishing tunneling Eq. (3.8),[3] which are both product states of single-site wave functions. In this chapter we will use a decoupling mean-field approach to model ultracold atoms in deep optical lattices.

---

[1] [Gutzwiller(1963), Sheshadri *et al.*(1993), van Oosten *et al.*(2001)]

[2] [Huang(1987)]

[3] [Zwerger(2003)]

Before we discuss the mean-field ansatz in detail we want mention the numerical methods to treat the Bose-Hubbard Hamiltonian. **Quantum Monte Carlo** (QMC) simulations have been used shortly after the seminal paper of Fisher *et al.* and reproduced important features of it;[1] improved computational resources have led to greatly enhanced QMC simulations.[2] **DMRG** (density matrix renormalization group) methods were also used highly successfully for 1D systems (and less successfully for 2D systems).[3] Both QMC and DMRG calculations are used as very reliable tools to obtain quantitative results but also to obtain qualitative insights as for example the importance of entanglement to reproduce the correct many body state in 1D lattices.[4]

3.1.1 Gutzwiller Mean-Field Approximation

In this chapter we analyze Bose-Hubbard models via a mean field approach. The most simple model we examine is given in Eq. (3.2) and its single-site mean-field approximation is given in Eq. (3.12). The Hamiltonian (3.12) must be solved self-consistently, i.e., one has to find the value of the mean-field parameter ϕ such that

$$\phi = \langle \psi_\phi^{(0)} | \hat{b} | \psi_\phi^{(0)} \rangle \equiv \langle \hat{b} \rangle_\phi,$$

where $|\psi_\phi^{(0)}\rangle$ denotes the ground state of the Hamiltonian Eq. (3.12) for a given ϕ. The self-consistent value of ϕ can be found in an iterative procedure,

$$\phi_{i+1} = \langle \hat{b} \rangle_{\phi_i}, \tag{3.14}$$

which defines a map $\phi_i \to \phi_{i+1}$. When $\phi_{i+1} \approx \phi_i$ with some satisfying accuracy, the value of ϕ is said to be self-consistent; the self-consistent values of ϕ are stable fixed points of the map (3.14). These fixed points correspond to the extrema of the energy functional

$$E[\phi] = \langle \psi_\phi^{(0)} | \hat{H} | \psi_\phi^{(0)} \rangle. \tag{3.15}$$

This can be seen by analyzing the energy functional

$$E[\phi] = \langle \hat{H}_0 \rangle_\phi - zt \left(\phi^* \langle \hat{b} \rangle_\phi + \phi \langle \hat{b}^\dagger \rangle_\phi - |\phi|^2 \right),$$

where $\hat{H}_0 = \sum_i [U/2 \hat{n}_i (\hat{n}_i - 1) - \mu \hat{n}_i]$. The extrema of this functional are determined by demanding that

$$\frac{\partial E[|\phi|]}{\partial |\phi|} = -zt \left(\langle \hat{b} \rangle_\phi + \langle \hat{b}^\dagger \rangle_\phi - 2|\phi| \right) \stackrel{!}{=} 0,$$

---

[1] [Batrouni *et al.*(1990), Scalettar *et al.*(1991)]

[2] see e.g. [Prokof'ev *et al.*(1998), Batrouni *et al.*(2002), Alet *et al.*(2006), Capogrosso-Sansone *et al.*(2007), Trotzky *et al.*(2010), Trefzger and Sengupta(2011)] and references therein.

[3] see for example [White(1992), Rommer and Östlund(1997), Orús and Vidal(2008)] and references therein.

[4] [Pino *et al.*(2012)]
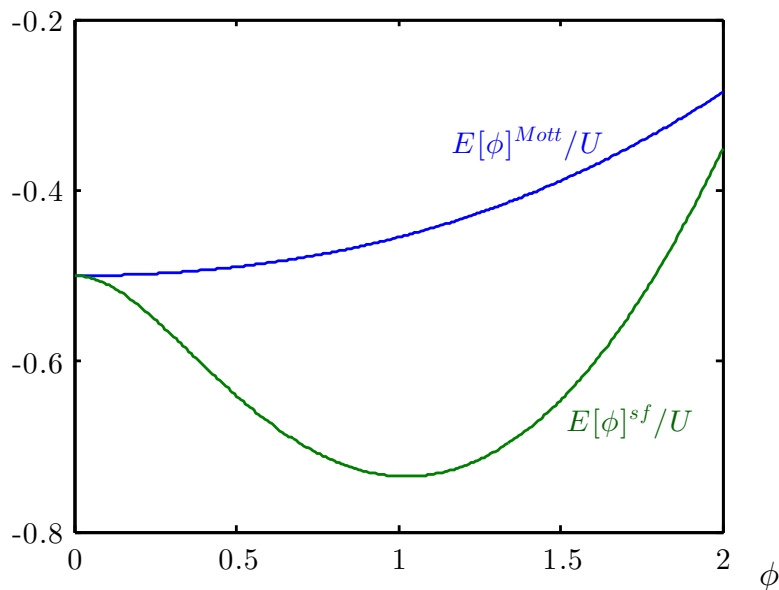
Figure 3.1: Ground-state energy $E[\phi]$ of the Hamiltonian (3.2) as a function of the order parameter ϕ. The green line $E[\phi]^{\text{sf}}$ corresponds to the parameters $t/U = 0.5$ and $\mu/U = 0.5$ and signals a non-vanishing order parameter ϕ. The blue line $E[\phi]^{Mott}$ corresponds to the parameters $t/U = 0.1$ and $\mu/U = 0.5$ and the Mott-insulating phase.

where we used the Hellmann-Feynman theorem[1] and $\partial \hat{H}_0/\partial \phi = 0$. Thus, the energy functional has an extremum when $\langle \hat{b} \rangle_\phi = \phi$, which is equivalent to the self-consistency equation. Therefore, each fixed point of the map (3.14) corresponds to an extremum of $E[\phi]$. The stable fixed points correspond to the local minima of $E[\phi]$ given in Eq. (3.15), the unstable ones to the local maxima.[2] It is therefore equivalent to find the minima of the energy functional $E[\phi]$ or to use an iterative procedure to find the mean field ground state of the system. In the following two sections we will study both approaches.

Analysis of the Ground-State Energy Functional

The Hamiltonian (3.12) is so simple that it generates only two classes of energy functionals (see Fig. 3.1). The first type of energy functionals are qualitatively equivalent to $E[\phi]^{\text{sf}}$ in Fig. 3.1 which has its minimum at $\phi \neq 0$. Such energy functionals correspond to a values of t/U and μ/U for which the system is superfluid. The other class of energy functionals is equivalent to $E[\phi]^{Mott}$ in Fig. 3.1; here the only self-consistent value of ϕ is zero and the energy functional has only one local

---

[1] [Cohen-Tannoudji *et al.*(1992)]

[2] [Bruus and Flensberg(2004)]

extremum.

For each given set of parameters $\{U, t, \mu\}$ we can analyze the energy functional with a Landau procedure, i.e., we calculate $E[\phi]$ up to second order in ϕ,

$$E[\phi] = const. + \beta|\phi|^2 + \mathcal{O}(|\phi|^4). \tag{3.16}$$

The coefficient β depends on the parameters $\{U, t, \mu\}$. When two of these parameters are fixed and β changes its sign when the third one is varied, one crosses a phase boundary. This sign change of β marks a phase transition because it signals that the ground-state energy functional changes its character from one class to the other. This can be seen by approximating $E[\phi]$ with a symmetric fourth-order polynomial, which is sufficient to interpolate the energy functionals given in Fig. 3.1. The polynomial $f(x) = ax^4 + bx^2 + c$ has one extremum at $x = 0$ and two at $x = \pm\sqrt{-2b/(4a)}$. The coefficient a corresponds to the fourth order coefficient in Eq. (3.16); it is always positive. The coefficient b corresponds to β and c is the constant in Eq. (3.16). Thus, $E[\phi]$ has only one extremum for $\beta > 0$ and an additional extremum for $\beta < 0$. It is straightforward to calculate $E[\phi]$ in second order perturbation theory. We use the following perturbative ansatz for the Hamiltonian (3.12),

$$\hat{H} = \hat{H}^{(0)} + \phi \, \hat{V} , \tag{3.17}$$

where $\hat{H}^{(0)} = -\mu\hat{n} + \frac{U}{2}\hat{n}(\hat{n}-1) + zt|\phi|^2$, $\hat{V} = -zt(\hat{b} + \hat{b}^\dagger)$. The perturbation couples states with an atom number difference of one, thus the second order shift of the ground state energy is given by

$$E_0^{(2)} = \frac{|\langle\bar{n}+1|zt\hat{b}^\dagger|\bar{n}\rangle|^2}{E_{\bar{n}} - E_{\bar{n}+1}} + \frac{|\langle\bar{n}-1|zt\hat{b}|\bar{n}\rangle|^2}{E_{\bar{n}} - E_{\bar{n}-1}} = \frac{z^2t^2(\bar{n}+1)}{\mu - U\bar{n}} + \frac{z^2t^2\bar{n}}{U(\bar{n}-1) - \mu},$$

where $\bar{n}$ is an integer and corresponds to the filling of each lattice site. Because the unperturbed Hamiltonian $\hat{H}^{(0)}$ contains a term with $|\phi|^2$, the second order coefficient of the Landau expansion is given by

$$\beta = \beta(\mu, t, U) = E_0^{(2)} + zt.$$

The condition that this coefficient must vanish translates into

$$\frac{z^2t^2(\bar{n}+1)}{\mu - U\bar{n}} + \frac{z^2t^2\bar{n}}{U(\bar{n}-1) - \mu} + zt = 0,$$

and we obtain the phase boundary for a given chemical potential

$$\mu/U = \frac{1}{2}\left[2\bar{n} - 1 - \frac{zt}{U} + \sqrt{1 - 2(2\bar{n}+1)\frac{zt}{U} + \left(\frac{zt}{U}\right)^2}\right]. \tag{3.18}$$

Stability Analysis Approach

Instead of examining the ground state energy functional we can also analyze the map given in Eq. (3.14). The map changes its qualitative features for different values of t, U and μ. The self-consistent values of the order parameter are the positions of the stable fixed points of this map. The $\phi = 0$ point is always a fixed point; when it is a stable one the system is in the Mott insulating phase, when it is an unstable fixed point the system is superfluid. Hence, due to the simple structure of the energy functionals given in Fig. (3.1) it is sufficient to analyze if $\phi = 0$ is a stable fixed point or an unstable one to distinguish the two quantum phases.

We can linearize the map around the $\phi = 0$ fixed point,

$$\phi_{i+1} \approx \frac{d\langle \hat{b} \rangle_\phi}{d\phi} \bigg|_{\phi=0} \phi_i + \mathcal{O}\left(\phi^2\right) \approx c\,\phi_i.$$

The absolute value of the coefficient c determines if the fixed point is stable or not:[1] If it is smaller than 1, the fixed point is stable (the Lyapunov exponent is negative), when it is larger than 1, the fixed point is unstable (the Lyapunov exponent is positive). To obtain the value of c we rewrite the Hamiltonian (3.12),

$$\hat{H} = \hat{H}^{(0)} + t\,\hat{V},$$

where $\hat{V} = -z\phi(\hat{b} + \hat{b}^\dagger)$ and $\hat{H}^{(0)} = -\mu\hat{n} + \frac{U}{2}\hat{n}(\hat{n}-1) + zt|\phi|^2$ (compare Eq. (3.17)). Let $|\psi_0\rangle$ be the ground state of $\hat{H}^{(0)}$. The first order approximation for the ground state is $|\psi\rangle = |\psi_0\rangle + t\,|\psi_1\rangle$ where $|\psi_1\rangle = \sum_{i\neq0} \frac{\langle \psi_i|\hat{V}|\psi_0\rangle}{E_0-E_i}|\psi_i\rangle$. It follows that

$$\langle \hat{b} \rangle_{\phi_i} \approx t\langle \psi_0|\hat{b}|\psi_1\rangle + t\langle \psi_1|\hat{b}|\psi_0\rangle = t\langle \psi_0|b + b^\dagger|\psi_1\rangle = c\,\phi_i$$

where

$$c = t\sum_{i\neq0} \frac{z|\langle \psi_i|\hat{b} + \hat{b}^\dagger|\psi_0\rangle|^2}{E_i - E_0} \tag{3.19}$$

It is much easier to check for each point (μ, t) if $c < 1$ or $c > 1$ than to do the complete iterative procedure and actually determine the order parameter. Furthermore, Eq. (3.19) enables us to give an analytical expression for the phase boundary in the same way as in Eq. (3.18) since the coefficient c is linear in t. The phases boundary is at $c = 1$ which leads to

$$t_c = \frac{1}{\sum_{i\neq0} \frac{z|\langle \psi_i|\hat{b}+\hat{b}^\dagger|\psi_0\rangle|^2}{E_i-E_0}}. \tag{3.20}$$

In Fig. 3.2 we give a graphical analysis of the map (3.14). On the ordinate axes of Fig. 3.2 the change of the order parameter

$$\delta\phi = \frac{\phi_{i+1}}{\phi_i}$$

---

[1] [Abraham and Shaw(1992)]
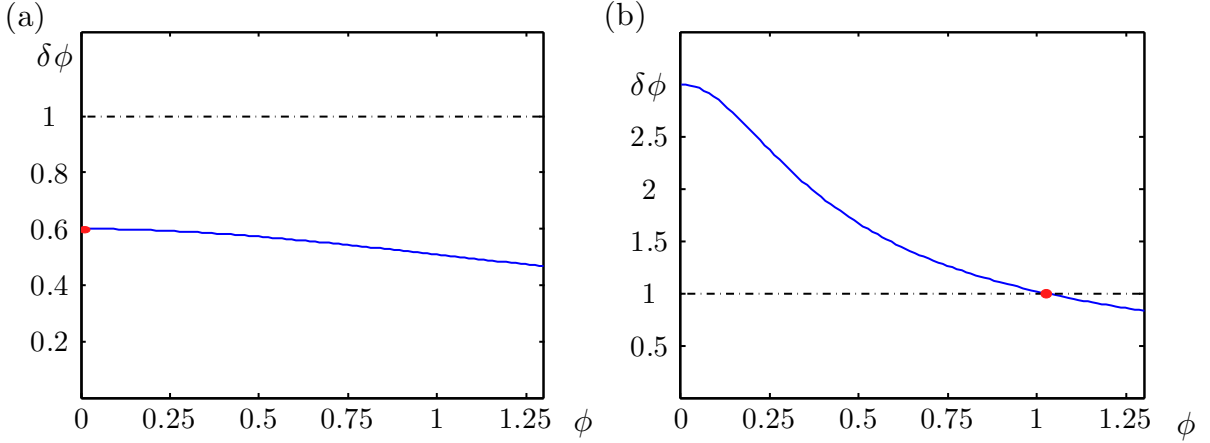
Figure 3.2: Graphical analysis of the map $\phi_i \rightarrow \phi_{i+1}$ given in Eq. (3.14): $\delta\phi$ denotes ϕ_{i+1}/ϕ_i. The parameters are the same as in Fig. 3.1: In (a) $\mu = 0.5$ and $t/U = 0.1$ (compare $E[\phi]^{Mott}$) and in (b) $\mu = 0.5$ and $t/U = 0.5$ (compare $E[\phi]^{\text{sf}}$). The red dots denote the stable fixed points of the maps and correspond to the local minima in Fig. 3.1.

is plotted. If $\delta\phi$ is larger than one, the order parameter increases during an iteration starting with the given ϕ, if $\delta\phi < 0$ the order parameter decreases. All values of ϕ which correspond to $\delta\phi = 1$ are to fixed points. When the functions $\delta\phi$ cross the $\delta\phi = 1$ line with a positive slope the crossing denotes an unstable fixed point, when the slope is negative the crossing corresponds to a stable fixed point (red dots in Fig. 3.2). In Fig. 3.2a we choose the same parameters as in $E[\phi]^{Mott}$ in Fig. 3.1 and in Fig. 3.2b the same parameters as in $E[\phi]^{\text{sf}}$ in Fig. 3.1. In Fig. 3.2a there is a stable fixed point at $\phi = 0$, because ϕ cannot be smaller than zero (by definition) and $\delta\phi$ is smaller than one at this point, thus any order parameter above zero will be driven to zero. In Fig. 3.2b the point $\phi = 0$ is above $\delta\phi = 1$ and the stable fixed point is at $\phi = 1.02$.

The Phase Diagram

The phase diagram calculated with the Gutzwiller mean-field procedure is plotted in Fig. 3.3. The calculations are presented in Appendix A.1. The areas of fixed integer filling build up Mott lobes (light blue regions in Fig. 3.3). For any noninteger filling the ground state of the homogeneous Bose-Hubbard model given in Eq. (3.2) contains a superfluid fraction even for very small tunneling amplitudes. This can be seen by considering a filling which is slightly larger than one, $\langle \hat{n} \rangle = 1 + \varepsilon$ (see red line Fig. 3.3). At this filling the atoms are delocalized over the whole lattice for large tunneling amplitudes and the situation is hardly different from the case of integer filing. However, for small tunneling the red line in Fig. 3.3 remains in the superfluid region.

In the non-interacting limit all atoms condense in the $\vec{k} = 0$ quasi-momentum
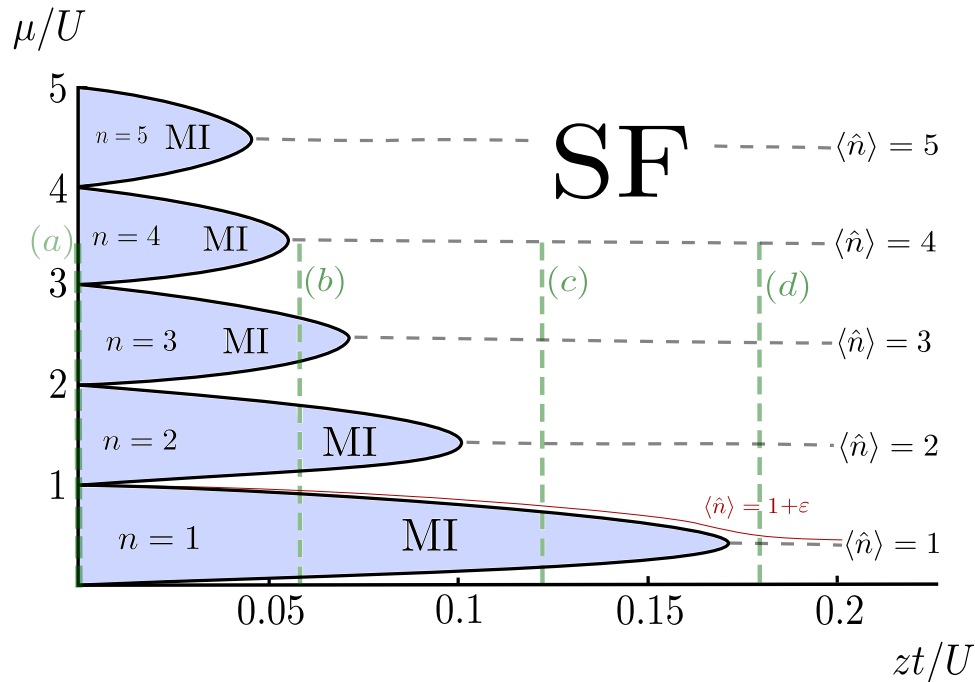
Figure 3.3: Mean-field phase diagram for the Bose-Hubbard model given in Eq. (3.2). The Mott-insulating phases (MI) are painted in light blue. The surrounding parameter region is superfluid (SF). The grey dashed lines depict lines of constant integer density which hit the Mott lobes at their tip. The red line denotes a contour of constant density slightly above 1, i.e. $\langle \hat{n} \rangle = 1 + \varepsilon$. The green dashed lines display the parameter curves for different strengths of the optical lattice when the surrounding harmonic trap and the particle density is chosen such that $\mu/U = 3.5$ in the center of the trap (see Fig. 3.4).

state with every particle having an energy $-zt$ (compare Eq. (3.5)). If the chemical potential is smaller than $-zt$, the system is empty since it costs energy to add a particle. For fixed on-site interaction U and chemical potential $\mu > -zt$ the density in in the lattice goes to infinity for $t \to \infty$ because every additional atom reduces the energy of the system; thus, the contours with fixed particle number in Fig. 3.3 have negative slope once t is large enough.[1] For large $t \gg U$ we can deduce from the Bogoliubov theory that the contours follow the straight lines

$$\mu = Un_0 - zt, \tag{3.21}$$

where n_0 is the superfluid density.[2] We can derive Eq. (3.21) from physical arguments since the chemical potential is the energy needed to add one particle to the system. If there are n_0 atoms at each site (for large t the number of condensed atoms is equal to the total number of atoms) the energy of the system increases by Un_0 when one particle is added. In the same time there is an energy decrease per added

---

[1] [Elstner and Monien(1999)]

[2] [van Oosten et $al.$(2001)]
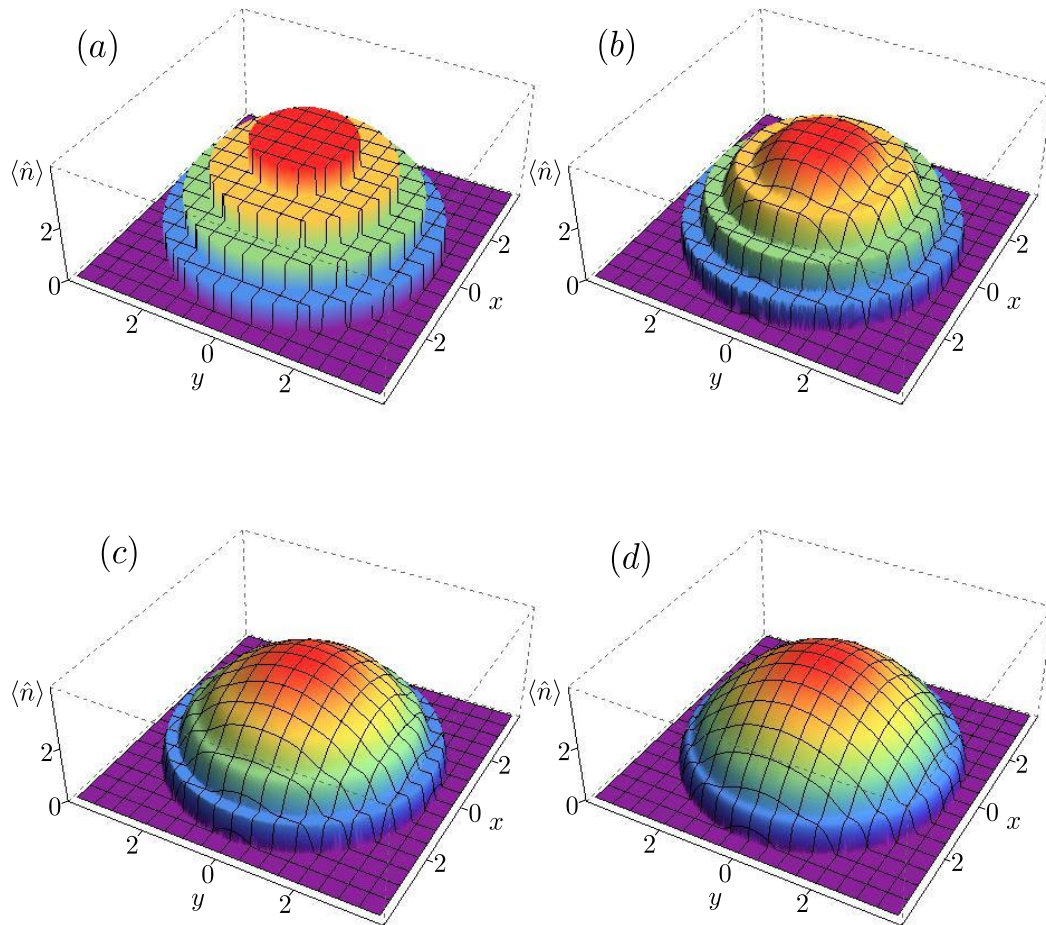
Figure 3.4: Atomic density inside a harmonic trap according to the Bose-Hubbard Hamiltonian (3.2) in mean-field approximation. The four "weddingcakes" correspond to four different lattice strengths (a) $t = 0$, (b) $t/U = 0.6$, (c) $t/U = 1.2$ and (d) $t/U = 1.8$ (compare green dashed lines in Fig. 3.3).

particle since the kinetic energy of each particle is negative due to the hopping to z neighbors.

The contours corresponding to a constant integer filling hit the Mott lobes at their tip (see dashed grey lines in Fig. 3.3); this must be the case because otherwise the compressibility $\frac{\partial n}{\partial \mu}$ would be negative around the tip breaking a fundamental thermodynamic law. The transitions at the tips are therefore different from any other point on the lobe boundary. At the tips the density remains commensurate during the quantum phase transition whereas elsewhere a commensurately filled Mott phase changes into an incommensurate filled superfluid phase. Fisher *et al*[1] developed a scaling theory for the tips and showed that the phase transition there are in the universality class of the $(d+1)$-dimensional XY model, whereas the transitions at the other points are described by mean-field critical exponents in any dimension.

The mean-field approximation is exact in infinite dimensions. For a 2D and

---

[1] [Fisher *et al.*(1989)]

3D lattice the mean-field approach gives a very good approximation for the phase diagram. However, it fails to generate some important features of the phase diagram for 1D systems. At the tip of the Mott lobes the 1D system does not show a phase transition but a Kosterlitz-Thouless transition[1] (like the 2D XY model, see above). This is because the the energy gap separating the Mott-insulating phase from excitations closes exponentially slowly. Since the width of the Mott lobes along the μ-direction is equal to the energy gap the Mott lobes change their shape in 1D: They are no longer round but sharp. Furthermore the Mott lobes show a reentrance behavior.[2]

In a weak harmonic trap of the type given in Eq. (2.5) the chemical potential is not constant over the whole lattice. Instead the slowly varying external potential causes a spatially varying chemical potential

$$\mu(r) = \mu(0) - \varepsilon(r), \qquad (3.22)$$

where r denotes the distance from the trap center and we set $\varepsilon(0) = 0$. The atoms occupy the region around the trap center up to the distance where $\mu(0) = \varepsilon(r)$. In this way all the different quantum phases which exist for given t/U below $\mu(0)$ are present simultaneously, although at different positions of the trap. In Fig. 3.4 we show the spatial distribution of the atomic density for four different lattice strengths t/U; in each plot we choose $\mu(0) = 3.5$. The realized chemical potentials are drawn in Fig. 3.3 as green dashed lines. In Fig. 3.4a the tunneling amplitude is chosen to be zero and the Mott plateaus corresponding to $n = 4$, $n = 3$, $n = 2$ and $n = 1$ are clearly visible. In Fig. 3.4b the Mott plateau $n = 4$ is "melting"; in Fig. 3.4c the chemical potential curve in Fig. 3.3 cuts only the $n = 1$ Mott lobe and correspondingly only the $n = 1$ Mott plateau is clearly visible. In Fig. 3.4d there are no Mott plateaus anymore and the density distribution reflects already the shape of the harmonic trap; thus, we enter the regime where Eq. (3.21) is valid and the atomic density is equal to

$$n = \frac{\mu(r) + zt}{U}\,,$$

where $\mu(r)$ is given by Eq. (3.22).

Detection of the Mott-Superfluid Phase Transitions

In 2002 Greiner *et al.*[3] experimentally demonstrated the Mott-superfluid phase transition (see Fig. 3.5). In their experiments time-of-flight measurements were used. In order to understand how time-of-flight experiments provide a direct evidence of the Mott-superfluid transition we examine the idealized situation of a lattice

---

[1] [Kosterlitz and Thouless(1973)]

[2] [Kashurnikov *et al.*(1996), Kühner and Monien(1998), Elstner and Monien(1999), Kühner *et al.*(2000), Pino *et al.*(2012)]

[3] [Greiner *et al.*(2002)a]
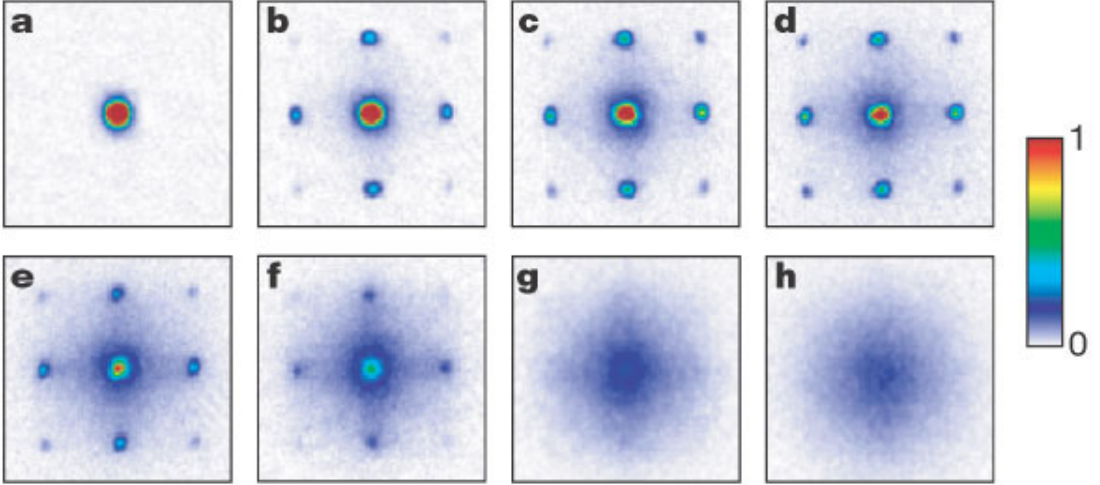
Figure 3.5: Density distributions of ultracold atoms released from an optical lattice after time-of-flight expansion as measured by Greiner *et al.*(2002). The different pictures correspond to different lattice depths V_0 (V_0 is the amplitude of the spatially varying optical potential and is given in units of the recoil energy E_r, compare Sec. 2.3); (a) $V_0 = 0$, (b) $V_0 = 3E_r$, (c) $V_0 = 7E_r$, (d) $V_0 = 10E_r$, (e) $V_0 = 13E_r$, (f) $V_0 = 14E_r$, (g) $V_0 = 16E_r$ and (h) $V_0 = 20E_r$ (Taken from Reference [Greiner *et al.*(2002)a]).

without a harmonic trap. In these experiments the spatial distribution of an atom cloud after some time of flight is probed: This distribution gives evidence of the momentum distribution prior to trap release, $\langle \hat{n}(\vec{x}) \rangle_t \approx \left(\frac{m}{\hbar t} \right)^3 \langle \Phi | \hat{n}_{\vec{k}(\vec{x})} | \Phi \rangle$ where $\vec{k}(\vec{x}) = m\vec{x}/\hbar t$ relates the in situ momentum $\hbar \vec{k}$ to the final observation position $\vec{x}$ (compare Eq. (2.51)). The momentum distribution can be expressed in terms of the exact one-particle density matrix $\rho_1(\vec{x}) = \langle \hat{b}_{\vec{x}}^\dagger \hat{b}_0 \rangle$,

$$\langle \Phi | n_{\vec{k}(\vec{x})} | \Phi \rangle = n \ |w(\vec{k}(\vec{x}))|^2 \sum_{\vec{x}} e^{i\vec{k}\cdot\vec{x}} \langle \hat{b}_{\vec{x}}^\dagger \hat{b}_0 \rangle, \qquad (3.23)$$

where the summation is over all lattice vectors which are integer multiples of the three primitive vectors of the lattice, Φ is the many-body state of the atom cloud in the lattice prior to trap release, n is the density and $w(\vec{k})$ the Fourier transform of the Wannier function $w_0(\vec{x})$.

In the superfluid regime the one-particle density matrix converges to a finite value,

$$\lim_{|\vec{x}| \to \infty} \langle \hat{b}_{\vec{x}}^\dagger \hat{b}_0 \rangle = \frac{n_0}{n},$$

which defines the superfluid density n_0. For vanishing interactions, i.e. $U \ll t$, all atoms become superfluid and $n_0 = n$. The existence of this off-diagonal long-range order in dilute atomic gases has been verified by experiments of Bloch *et*

al. in 2000.[1] When $\langle \hat{b}_{\vec{x}}^{\dagger} \hat{b}_0 \rangle$ takes a constant value we see from Eq. (3.23) that the momentum distribution has peaks at reciprocal lattice vectors $\vec{q} = \vec{G}$, where $\vec{G} \cdot \vec{x} = 2\pi$. These peaks in the momentum distribution are observable as peaks in the spatial distribution (see Fig. 3.5). We can also say that within the superfluid phase the wave packets from different lattice sites interfere coherently an lead to diffraction peaks in the spatial resolution. In the strongly interacting limit all phase coherences are lost, the one-particle density matrix decreases exponentially fast and the spatial resolution reflects only the Fourier transform of the Wannier functions (see Fig. 3.5h).

In conclusion, time-of-flight measurements give a possibility to determine the one-particle density matrix; the interference pattern of the spatial resolution is directly related to the existence of off-diagonal long-range order in $\langle \hat{b}_i^{\dagger} \hat{b}_j \rangle$. To compare the measured momentum distribution with the theory we need to take the finite size of the atom cloud and the co-existence of several Mott and superfluid phases into account.[2]

A second possibility to detect the Mott-superfluid transition is to probe if there is a finite energy gap separating the ground state from excited states. Deep in the Mott phase this gap is U (compare Eq. (3.9)). For larger tunneling amplitudes the gap closes, which has been experimentally detected.[3] Furthermore *in situ* imaging of the Mott-superfluid phase transition has become possible.[4]

---

[1] [Bloch *et al.*(2000)]

[2] [Kashurnikov *et al.*(2002), Roth and Burnett(2003)]

[3] [Stöferle *et al.*(2004)]

[4] [Gemelke *et al.*(2009), Hung *et al.*(2010), Sherson *et al.*(2010), Bakr *et al.*(2010)]

3.2 Ultracold Spin-1 Atoms in Optical Lattices

In this section we examine spin-1 bosons in optical lattices in mean-field approximation. Ultracold spin-1 bosons in deep optical lattices are well described by a Bose-Hubbard model given Eq. (2.41). We transform this Hamiltonian to a single-site mean-field Hamiltonian similar to Eq. (3.12) using Eq. (3.11),

$$\hat{H}_{MF} = -\mu\hat{n} + \frac{U_0}{2}\hat{n}(\hat{n}-1) + \frac{U_2}{2}\left(\hat{\vec{S}}^2 - 2\hat{n}\right) - zt\sum_\sigma(\phi_\sigma^*\hat{b}_\sigma + \phi_\sigma\hat{b}_\sigma^\dagger) + zt|\vec{\phi}|^2\,,$$

(3.24)

where we introduced

$$\vec{\phi} = \begin{pmatrix} \phi_1 \\ \phi_0 \\ \phi_{-1} \end{pmatrix}$$

(3.25)

with $\phi_\sigma \equiv \langle\hat{b}_\sigma\rangle$ (compare Eq. (2.36)); thus, the order parameter is in the case of spin-1 atoms no longer a simple scalar but a vector. The chemical potential is given by μ, the hopping matrix element is t and $\hat{n} = \sum_\sigma \hat{b}_{\sigma}^\dagger\hat{b}_{\sigma i}$ is the atom number operator. Because the tunneling term in Eq. (2.41) includes only spin symmetric tunneling the mth-component of the order parameter couples only to the mth-component of the annihilation and creation operators. The on-site interaction is described by a spin-independent term with U_0 and a spin-dependent one parametrized by U_2.

The term proportional to U_2 describes spin-dependent contact interactions; it penalizes non-zero spin configurations for antiferromagnetic atoms (e.g. ^{23}Na) while it favors high-spin configurations in the case of ferromagnetic interactions (e.g. ^{87}Rb). Whereas the ratio t/U_0 can be controlled with the intensity of the laser beams (compare Eq. (2.44)), the ratio U_2/U_0 depends on the spin-2 and spin-0 scattering lengths of the spin-1 atoms (compare Eq. (2.45)).

Due to the spinor nature of the order parameter additional properties of the superfluid phases arise. For antiferromagnetic interactions ($U_2 > 0$) the bosons form a polar superfluid,[1] i.e. the spin-dependent interaction energy is minimized by $\langle\hat{\vec{S}}\rangle = 0$. There are two different classes of polar order parameters,[2] one is the transverse polar state

$$\begin{pmatrix} \phi_1 \\ \phi_0 \\ \phi_{-1} \end{pmatrix} = \sqrt{n^{\mathrm{sf}}}\,\frac{1}{\sqrt{2}}\begin{pmatrix} 1 \\ 0 \\ 1 \end{pmatrix}$$

(3.26)

(compare Eq. (2.38)) the other one the longitudinal polar state

$$\begin{pmatrix} \phi_1 \\ \phi_0 \\ \phi_{-1} \end{pmatrix} = \sqrt{n^{\mathrm{sf}}}\begin{pmatrix} 0 \\ 1 \\ 0 \end{pmatrix}\,,$$

(3.27)

---

[1] [Ho(1998)]

[2] [Pai $et\ al.$(2008), Stamper-Kurn and Ueda(2012)]

(compare Eq. (2.39)) where $\sqrt{n^{\text{sf}}}$ is the number of condensed atoms per site. In the ferromagnetic case $(U_2 < 0)$ there is only one superfluid order parameter, which is given by

$$\begin{pmatrix} \phi_1 \\ \phi_0 \\ \phi_{-1} \end{pmatrix} = \sqrt{n^{\text{sf}}} \, \frac{1}{2} \begin{pmatrix} 1 \\ \sqrt{2} \\ 1 \end{pmatrix}, \tag{3.28}$$

(compare Eq. (2.37)).

Note that due to the symmetries discussed in Sec. 2.5 (which determine the superfluid order parameter given in Eqs. (3.27) and (3.26)) ϕ_1 is always equal to ϕ_{-1}, when one uses the gauge freedom in the absence of vortexes and chooses the order parameter real.

In Fig. 3.6 we plot the energy functional $E[\vec{\phi}]$ as a function of the order parameter $\vec{\phi}$. Because $\phi_1 = \phi_{-1}$ we use ϕ_1 and ϕ_0 as x- and y-axes, respectively. In Fig. 3.6a we assume antiferromagnetic interactions. The parameters are chosen such that the system is in the superfluid regime ($t/U_0 = 0.25, \mu/U_0 = 0.7$ and $U_2/U_0 = 0.04$). There are two minima clearly visible: One corresponding to a transverse polar superfluid at $\vec{\phi} = \{0.6208, 0, 0.6208\}^T$ and the other one corresponding to a longitudinal polar superfluid at $\vec{\phi} = \{0, 0.8782, 0\}^T$. Because superfluid density is the same in each minimum the two positions are connected via $0.8782 \approx \sqrt{2} \cdot 0.6208$ (compare Eqs. (3.26) and (3.27)). The two minima at a non-vanishing order parameter are degenerate because both correspond to $\langle \hat{\vec{S}} \rangle = 0$ and therefore suffer the same spin-dependent energy shift of the on-site interaction. Due to the special form of the two superfluid phases given in Eqs. (3.26) and (3.27) the superfluid minima are always on the $\phi_1 = 0$ and the $\phi_0 = 0$ axes, respectively.

In Fig. 3.6b the spin interactions are ferromagnetic and the parameters ($t/U_0 = 0.18, \mu/U_0 = 0.7$ and $U_2/U_0 = -0.04$) are chosen such that the system is superfluid. In accordance with Eq. (3.28) there is only one minimum at $\vec{\phi} = \{0.3829, 0.5413, 0.3829\}^T$, where indeed $\phi_1 \cdot \sqrt{2} = \phi_0$ and $\phi_1 = \phi_{-1}$.

In Fig. 3.6c we set the spin-dependent interactions to zero ($U_2/U_0 = 0$). The energy functional is rotationally symmetric around $\phi_1 = \phi_0 = 0$; thus, the spin-dependent interaction changes the symmetry of the energy functional $E[\vec{\phi}]$ in the ϕ_0-ϕ_1 plane. In Fig. 3.6d we choose the parameters such that the system is Mott insulating ($t/U_0 = 0.08, \mu/U_0 = 0.5$ and $U_2/U_0 = -0.04$).
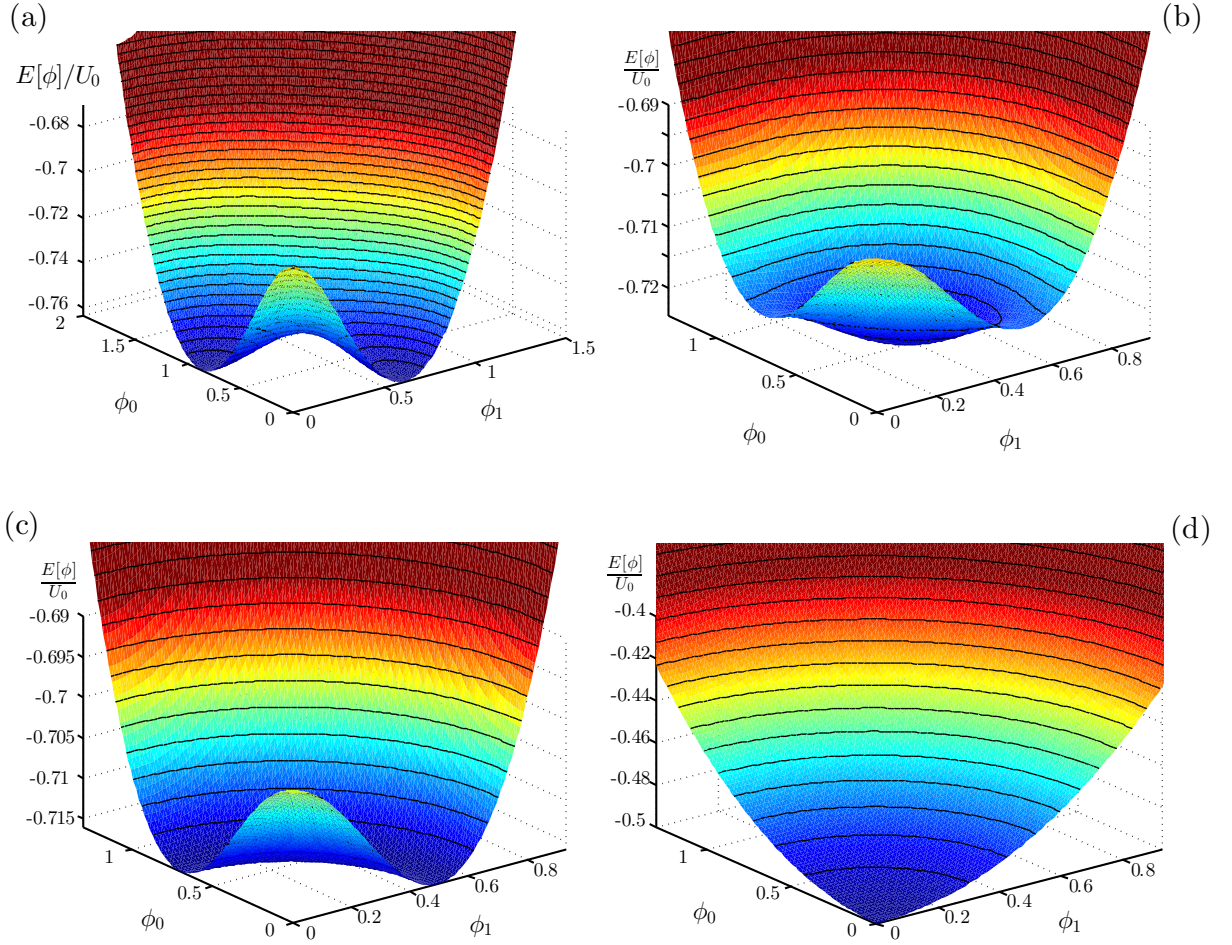
Figure 3.6: Ground-state energy $E[\vec{\phi}]$ of the Hamiltonian (3.2) as a function of the order parameter $\vec{\phi}$. (a) $E[\vec{\phi}]$ for antiferromagnetic spin interactions in the superfluid regime ($t/U_0 = 0.25, \mu/U_0 = 0.7$ and $U_2/U_0 = 0.04$). There are two degenerate minima at $\vec{\phi} = \{0.6208, 0, 0.6208\}^T$ and $\vec{\phi} = \{0, 0.8782, 0\}^T$. (b) $E[\vec{\phi}]$ for ferromagnetic interactions in the superfluid regime with one minimum at $\vec{\phi} = \{0.3829, 0.5413, 0.3829\}^T$ ($t/U_0 = 0.18, \mu/U_0 = 0.7$ and $U_2/U_0 = -0.04$). (c) Superfluid phase for vanishing spin-dependent interactions and ($t/U_0 = 0.08, \mu/U_0 = 0.5$ and $U_2/U_0 = -0$) (d) $E[\vec{\phi}]$ in the Mott-insulating regime ($t/U_0 = 0.08, \mu/U_0 = 0.5$ and $U_2/U_0 = -0.04$) with one minimum at $\vec{\phi} = \{0, 0, 0\}^T$.

First Order Quantum Phase Transitions

The energy functionals in Fig 3.6 are more complicated and have a richer structure than the energy functionals for spinless atoms shown in Fig. 3.1 but they do not show qualitatively different features: They correspond either to superfluid or to Mott-insulating phases. In addition to those shown in Fig. 3.6, two qualitatively different classes of energy functionals arise in certain parameter regimes for antiferromagnetic spin interactions ($U_2 > 0$), see Fig. 3.7. For these figures, we plot only the cuts of $E[\vec{\phi}]$ at the $\phi_0 = 0$ axes and the $\phi_1 = 0$ axes because all local minima of the full energy functional are on these axes (see Eqs. (3.26) and (3.27) and compare Fig. 3.6). The ground-state energy functionals in Fig. 3.7 display additional local minima. For each of these functionals the global minimum determines the stable quantum phase of the system; the other one at a higher energy corresponds to a meta-stable phase.
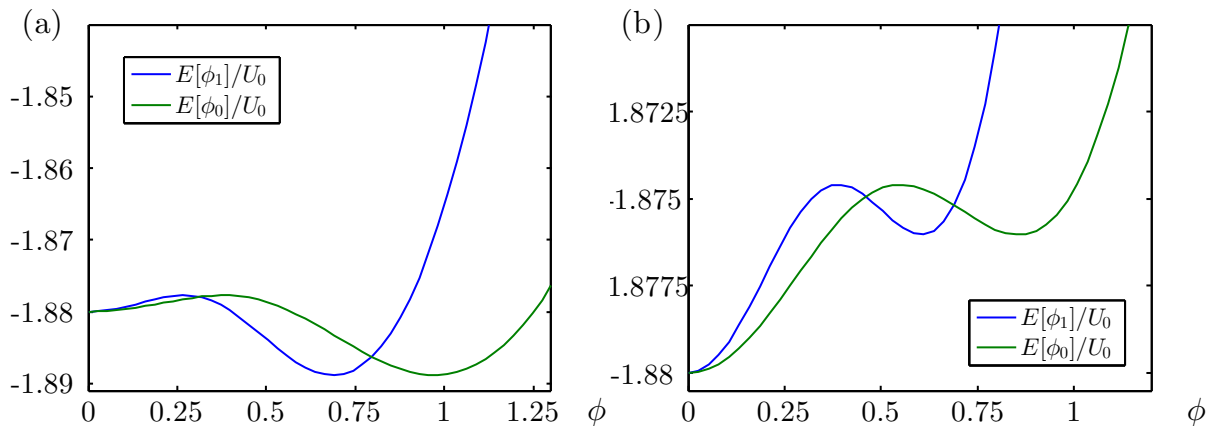
Figure 3.7: Energy functionals $E[\vec{\phi}]$ for (a) $t/U_0 = 0.2$, $\mu/U_0 = 1.4$ and $U_2/U_0 = 0.04$ and (b) $t/U_0 = 0.185$, $\mu/U_0 = 1.4$ and $U_2/U_0 = 0.04$. The blue lines $E[\phi_1]$ denote the energy functionals with $\phi_0 = 0$ and the green lines $E[\phi_0]$ the energy functionals for $\phi_1 = \phi_{-1} = 0$. The energy functionals in (a) signal meta-stable Mott insulating phases and the energy functionals in (b) metastable superfluid phases.

In Fig. 3.7a there is one local minimum of $E[\vec{\phi}]$ at $\vec{\phi} = \vec{0}$ and two energetically lower minima at $\vec{\phi} \neq \vec{0}$; thus, the stable quantum phase in this case is superfluid but there exists also a meta-stable Mott-insulating quantum phase. In Fig. 3.7b there exists beside a stable Mott phase a meta-stable superfluid one. Metastable phases cause first order phase transition;[1] to see what this means we plot in Fig. 3.8 the order parameter ϕ_0 as a function of the tunneling amplitude t/U. In Fig. 3.8a the order parameter itself changes discontinuously its value at t_c/U and not only its

---

[1] [Huang(1987)]
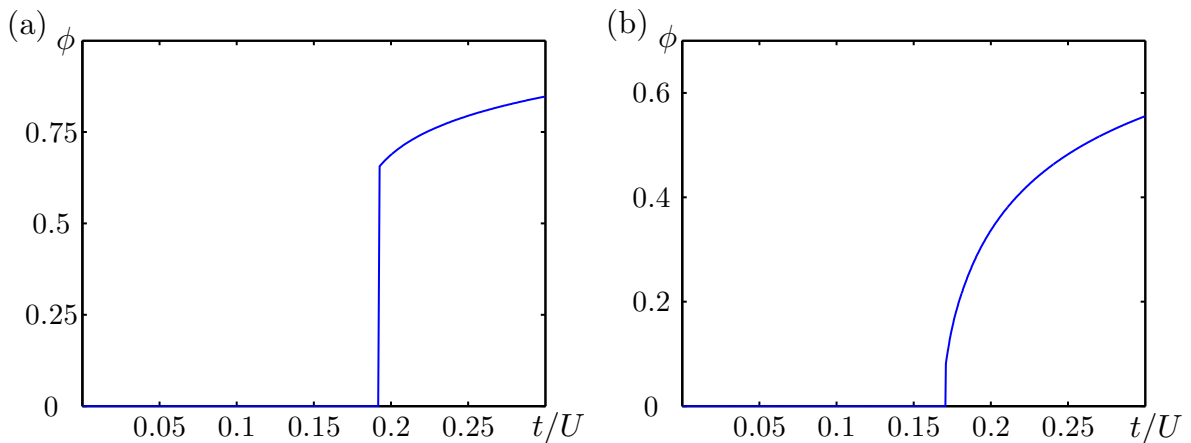
Figure 3.8: Second and first order phase transitions: Superfluid order parameter $\phi_0 = \langle \hat{b}_0 \rangle$ as a function of the tunneling amplitude t for fixed on-site interaction U and antiferromagnetic spin interactions $U_2/U_0 = 0.04$. In (a) the chemical potential is $\mu/U = 1.4$ and the phase transition is a first order one; in (b) the chemical potential is $\mu/U = 0.4$ and the phase transition is of second order.

first derivative as in Fig. 3.8b. Thus, the system undergoes in Fig. 3.8a a first order phase transition and in Fig. 3.8b a second order transition.

In conclusion, the Bose-Hubbard model for spin-1 atoms with antiferromagnetic interactions gives rise to metastable quantum phases and therefore to first-order phase transitions and hysteretic behavior of the system.[1] The additional local minimum for certain parameter regimes are a result of a "spin barrier": For a vanishing order parameter the spin fluctuations and therefore the spin-dependent energy penalty in Eq. (3.24) are minimal. An increased order parameter leads to higher spin configurations and an increased ground state energy, hence the barrier at a small order parameter. In the ferromagnetic case, the spin-dependent interaction in Eq. (3.24) has the same sign as the tunneling term and therefore does not create metastable quantum phases.

Analysis of the Ground-State Energy Functional

Next we analyze the ground-state energy functionals of the Hamiltonanian (3.24) with a Landau procedure. The qualitative features of the functionals given in Fig. 3.7 can be described by even sixth order polynomials,

$$E[\phi] = \frac{1}{2}a\phi^2 + \frac{1}{4}b\phi^4 + \frac{1}{6}c\phi^6, \tag{3.29}$$

---

[1] [Krutitsky *et al.*(2005), Kimura *et al.*(2005)]
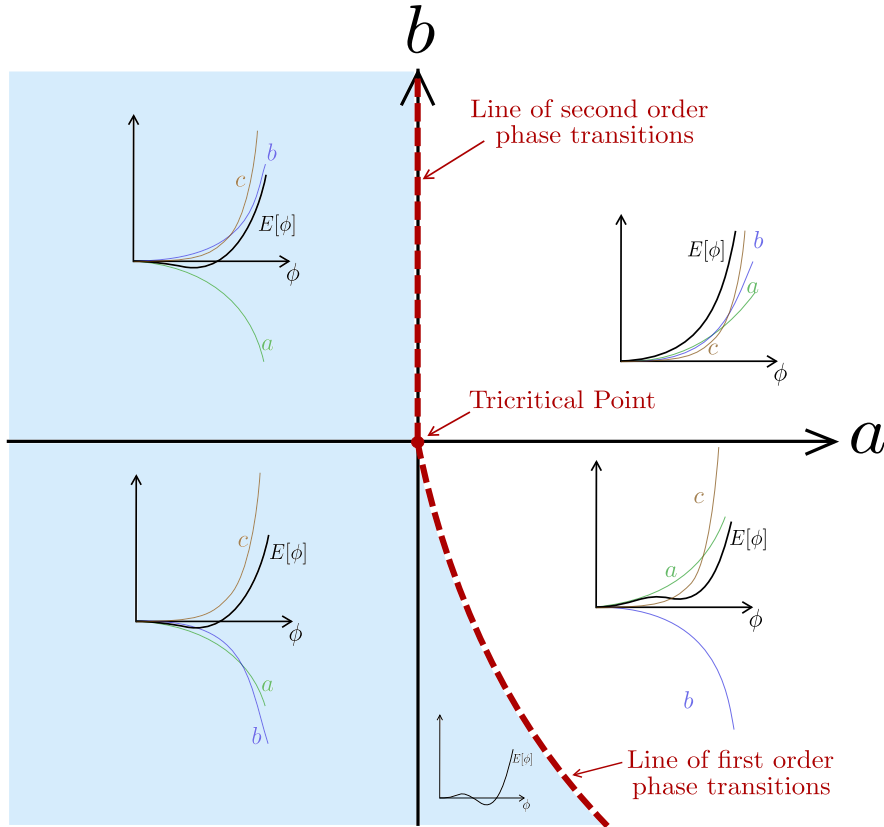
Figure 3.9: Graphical analysis of the Landau ground-state energy fucntional given in Eq. (3.29). The coefficient of ϕ^6 is c; it is always positive. The coefficient of ϕ^2 is a and of ϕ^4 is b; these coefficients can be negative or positive. The shaded parameter region is superfluid, the other one Mott insulating (see text for details). Along the line of second order phase transitions the minima of $E[\phi]$ are degenerate; along the line of first order phase transitions the energy functional has only one minimum. (after [Huang(1987)])

where we set $E[0] = 0$. For simplicity we consider a scalar order parameter; ϕ can be either ϕ_1, ϕ_{-1} or ϕ_0. The sixth order coefficient is always positive, i.e. $c > 0$, whereas a and b can be negative as well as positive. The derivatives of $E[\phi]$ are given by

$$E'[\phi] = a\phi + b\phi^3 + c\phi^5 \tag{3.30}$$

$$E''[\phi] = a + 3b\phi^2 + 5c\phi^4 . \tag{3.31}$$

The the function (3.29) has got maximally five extrema; the extremum at $\phi = 0$ is a minimum according to Eq. (3.31) when $a > 0$. Other possible minima of (3.29) are at

$$\phi_{sf} = \pm\sqrt{\sqrt{\frac{b^2}{4c^2} - \frac{a}{c}} - \frac{b}{2c}}. \tag{3.32}$$
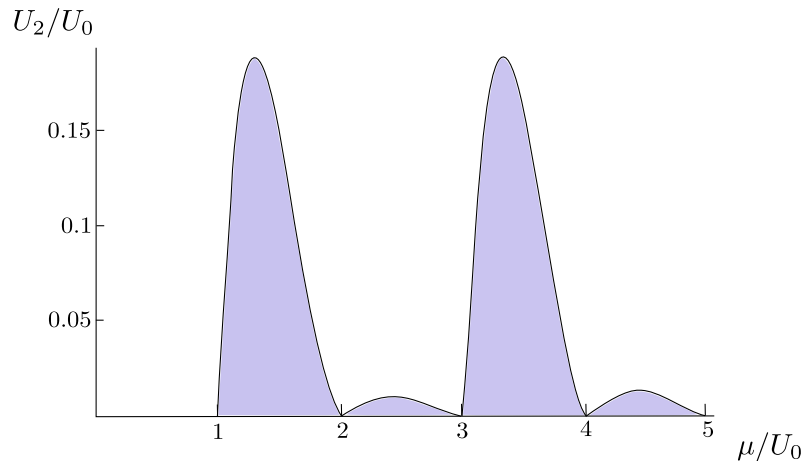
Figure 3.10: The shaded regions denote areas where the ground-state energy functional $E[\vec{\phi}]$ has two local minima. In these regions the Mott-superfluid phase transition is of first order, in the the remaining region it is second order. (Plot appeared first in Reference [Krutitsky *et al.*(2005)].)

The other extrema are (if they exist) maxima. In Fig. 3.9 we give a graphical overview over the qualitative features of the functional (3.29). We discriminate between the four possible choices for the signs of $\{a, b\}$ and included for each one a sketch of the terms containing a, b and c as well as the sum $E[\phi]$ of these. For $a < 0$ (the left side of Fig. 3.9) the functional has a maximum at $\phi = 0$ and the Mott insulating is not stable, thus the system is superfluid and the value of the order parameter is given by the absolute value of Eq. (3.32). When both a and b are positive (top right corner of Fig. 3.9) the functional has a minimum at $\phi = 0$ and only there because the Eq. (3.32) returns an imaginary number. The region $a > 0$ and $b < 0$ is special (bottom right corner of Fig. 3.9): Here the functional has three minima. This quadrant decomposes into two regions, one where the minimum at $\phi = 0$ is the global minimum and one where the minimum given by Eq. (3.32) determines the stable quantum phase.

Thus, there are two qualitatively different ways to cross from the superfluid to the Mott insulating region. When $b > 0$ the energy functional has always only one local minimum and $a = 0$ marks a line of second order phase transitions (compare Fig. 3.8b). For $b < 0$ the energy functional has for $a < 0$ only one local minimum but at $a = 0$ a second local minimum emerges. For a certain range of a the minimum at a non-vanishing order parameter is still the global minimum; but at a certain point this changes and the order parameter jumps to zero signaling a first order phase transition (compare Fig. 3.8a). The point where the line of first and second order transitions meet and thus the minima coincide is called tricritical point.[1] Along the line of first order phase transitions the minima of the energy functional are degenerate. We can calculate this line from

$$E[\phi_{sf}] = 0 \,, \tag{3.33}$$

_____

[1] [Huang(1987)]
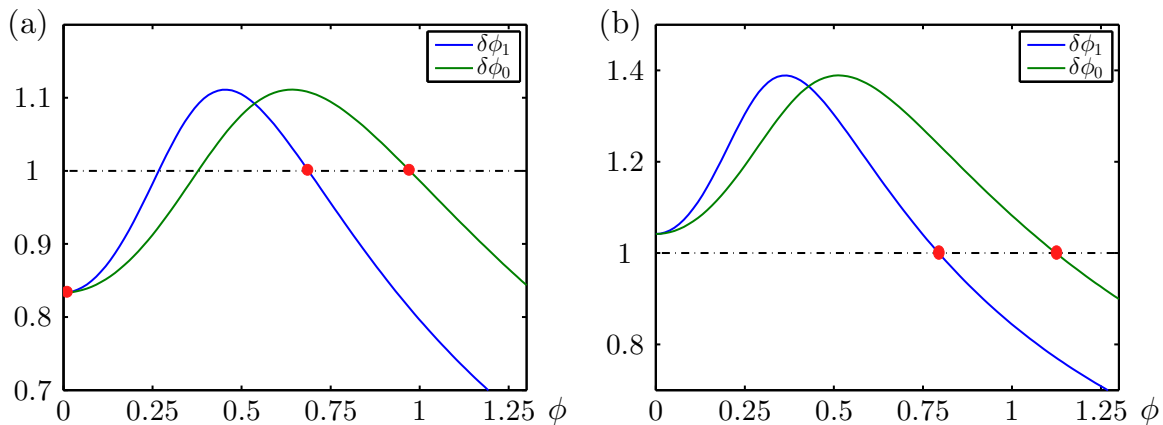
Figure 3.11: Plot of the map $\vec{\phi}_i \to \vec{\phi}_{i+1}$: $\delta\phi_1$ denotes $(\phi_1)_{i+1}/(\phi_1)_i$ and $\delta\phi_0$ denotes $(\phi_0)_{i+1}/(\phi_0)_i$. In (a) the parameters are chosen such that the point lies within the region of three stable fixed points (the red dots denote the stable fixed points, $\mu = 1.4$, $t/U_0 = 0.2$ and $U_2/U_0 = 0.04$). In (b) the point $\vec{\phi} = 0$ is above the $\delta\phi_m = 1$ line and is therefore no longer a stable fixed point ($\mu = 1.4$, $t/U_0 = 0.25$ and $U_2/U_0 = 0.04$).

since the minimum at $\phi = 0$ is at $E[0] = 0$. This leads to

$$b = -4\sqrt{\frac{ca}{3}},$$

as the line of first order phase transitions, which we indicated in Fig. 3.9. We can now calculate the fourth order expansion coefficient of the ground-state energy functional of Eq. (3.24) and determine its sign.[1] In Fig. 3.10 the regions with negative fourth order coefficients and therefore first order phase transitions are displayed.

The energy functionals in Fig. 3.7 have two local minima and an iterative procedure similar to the one described in Sec. 3.1.1 does not lead to an unique value of the order parameter but depends on the starting point. When the starting point of the iterative procedure is chosen close to zero, one finds the minimum at $\vec{\phi} = \vec{0}$. If one starts at a value beyond the maximum separating the two minima one obtains the second minimum corresponding to a superfluid phase. Thus, for spin-1 atoms it is no longer sufficient to determine the stability of the $\vec{\phi} = \vec{0}$ fixed point of the iterative map as it is for spinless bosons (compare Sec. 3.1.1). To see this more clearly we examine the map defined by the iterative procedure

$$\vec{\phi}_{i+1} = \langle \hat{\vec{b}} \rangle_{\vec{\phi}}, \tag{3.34}$$

where $\langle \cdot \rangle_{\vec{\phi}}$ denotes the expectation value in the ground state of Hamiltonian (3.24) for a given $\vec{\phi}$ (compare Eq. (3.14)) and $\hat{\vec{b}} = (\hat{b}_1, \hat{b}_0, \hat{b}_{-1})^T$. In Fig. 3.11 we give a

---

[1] [Krutitsky *et al.*(2005)]

60

graphical analysis of the map (3.34). On the ordinate axes of Fig. 3.11 the changes of the components of the order parameter

$$\delta\phi_m = \frac{(\phi_m)_{i+1}}{(\phi_m)_i}$$

are plotted. If $\delta\phi_m$ is larger than one, the component of the order parameter increases during an iteration starting with the given $\vec{\phi}$, if $\delta\phi_m < 0$ the order parameter decreases. All values of $\vec{\phi}$ which correspond to $\delta\phi_m = 1$ correspond to fixed points. When the functions $\delta\phi_m$ cross the $\delta\phi_m = 1$ line with a positive slope the crossing denotes an unstable fixed point, when the slope is negative the crossing corresponds to a stable fixed point (red dots in Fig. 3.11).[1] There is an additional stable fixed point at $\vec{\phi} = 0$ in Fig. 3.11a because $\vec{\phi}$ cannot be smaller than zero by definition and $\delta\vec{\phi}$ is smaller than one at this point. In Fig. 3.11b the point $\vec{\phi} = 0$ is above $\delta\vec{\phi} = 1$, thus, $\vec{\phi}$ increases for any value of $\vec{\phi}$ close to zero. The analysis of the map (3.34) is well suited to determine all stable fixed points of the iterative procedure but does not answer the question which of the fixed points corresponds to meta-stable or stable quantum phases. This difference can only be sorted out in an analysis of the ground-state energy functional $E[\vec{\phi}]$.

The Phase Diagram

The mean-field phase diagram of antiferromagnetic spin-1 atoms in optical lattices is shown in Fig. 3.12. The familiar Mott lobes of the spinless case given in Fig. 3.3 are significantly changed.[2] The spin-dependent interactions penalize high-spin configurations in the antiferromagnetic case. This leads to an enlargement of the Mott lobes corresponding to an even number of bosons because in this case the bosons can form spin singlets and thus minimize their repulsive interactions. On the contrary, Mott lobes carrying an odd number of bosons are decreased by antiferromagnetic interactions and disappear altogether for $U_2 > 0.5\ U_0$.[3] When a Mott lobe corresponds to an odd number of bosons, the spin-1 bosons couple to a total spin 1 and the system is called nematic. Thus, the ground state in the $n = 1$ Mott lobe is a superposition of the three degenerate states $|n = 1, S = 1, S_z = 1\rangle$, $|1, 1, 0\rangle$ and $|1, 1, -1\rangle$, where S denotes the total spin per lattice site. The phase transition between the $n = 1$ Mott lobe and the superfluid phase is always second order (compare Fig. 3.10). The ground state in the Mott insulating phase with $n = 2$ contains is the state $|2, 0, 0\rangle$ and the quantum phase is therefore called singlet phase. This is a result of the mean-field approximation; however, if one takes into account the influence of higher order correlations (for example by examining a spin Hamiltonian for very weak tun-

---

[1] [Abraham and Shaw(1992)]

[2] [Tsuchiya *et al.*(2004), Krutitsky and Graham(2004), Kimura *et al.*(2005), Krutitsky *et al.*(2005)]

[3] [Demler and Zhou(2002)]
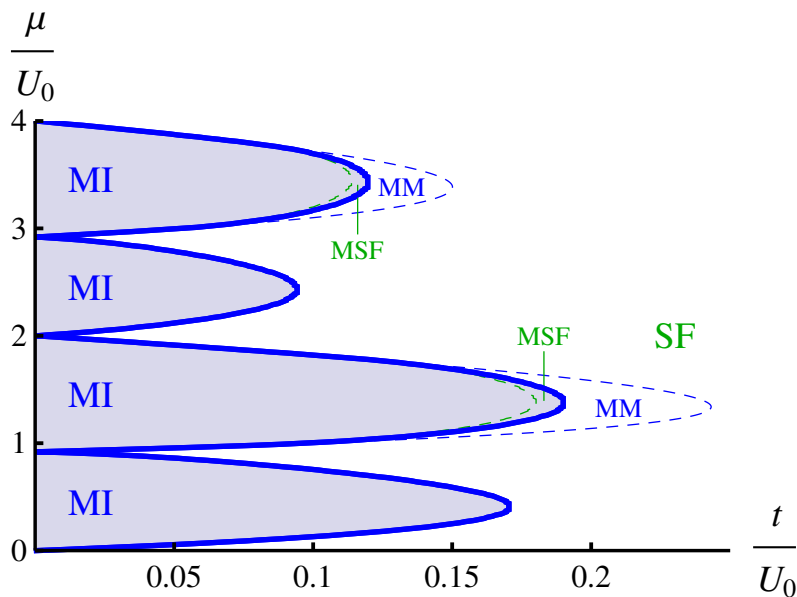
Figure 3.12: Phase boundary of the spin-1 Bose-Hubbard model with $U_2/U_0 = 0.04$. MI denotes the Mott insulating phase, MM a metastable Mott insulating phase, SF the superfluid phase and MSF a metastable superfluid phase.

neling[1]) one obtains different Mott insulating phases; the Mott lobes carrying an even number of atoms decompose into singlet and nematic regimes separated by first order phase transitions. These transitions happen when the tunneling ampliutudes are high enough to break the rotational symmetry, thus, there is an admixture of $\langle \vec{S} \rangle \neq 0$ in the ground state.

Within the mean-field theory, the $n = 3$ Mott lobe is nematic again and contains the three states $|3, 1, 1\rangle$, $|3, 1, 0\rangle$ and $|3, 1, -1\rangle$. When a Mott lobe corresponds to an even number of atoms the phase transition is first order for values $U_2/U_0 < 0.188$ (compare Fig. 3.10 and Ref. Krutitsky et $al.$(2005)[2]). For Mott lobes containing an odd number of atoms and at least three atoms the phase transition is second order if $U_2/U_0 > 0.012$ (compare Fig. 3.10 and Ref. Krutitsky et $al.$(2005)). Around the first-order phase transitions metastable phases exist.

There are several studies of the phase diagram of spin-1 atom in optical lattices using other tools than the mean-field ansatz, in the following we mention a few of them. For a complete overview see Lewenstein et $al.$(2012).[3] In 2002 E. Demler and F. Zhou[4] studied fundamental properties of the system like symmetry breaking and fractionalization. Demler et $al.$ discuss in a qualitative way the phase diagram and point out, that for strong antiferromagnetic interactions the insulating as well

[1] [Imambekov et $al.$(2003)]

[2] [Krutitsky et $al.$(2005)]

[3] [Lewenstein et $al.$(2012)]

[4] [Demler and Zhou(2002)]
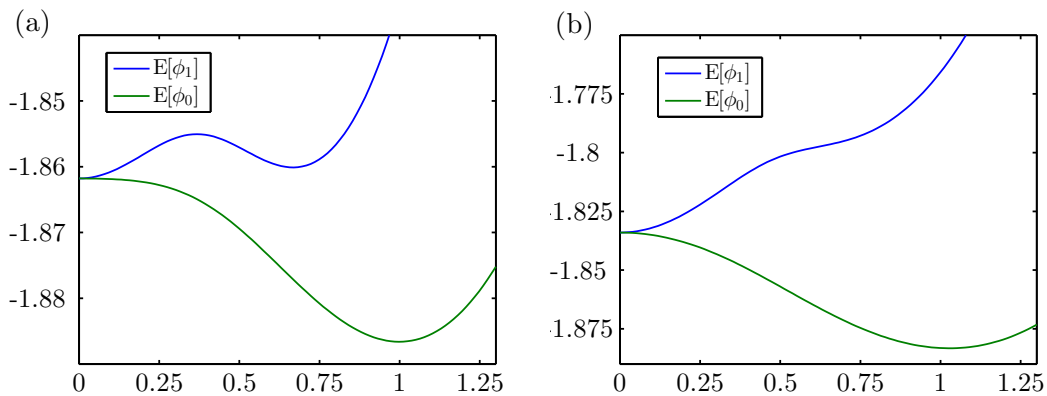
Figure 3.13: Magnetic field dependence of the ground-state energy functional $E[\vec{\phi}]$ for $\mu/U_0 = 1.4$, $t/U_0 = 0.2$ and $U_2/U_0 = 0.04$ (compare Fig. 3.7a). In (a) the parameter of the quadratic Zeeman shift is $q = 0.015$ and in (b) $q = 0.05$.

as the superfluid regime is dominated by pairs of singlets. In the superfluid phase singlet-pairs of atoms condense and in the Mott insulating phase there are only even fillings allowed. In 2003 A. Imambekov, E, Demler and M. Lukin[1] derived a spin Hamiltonian by applying a weak tunneling approximation of Eq. (2.41). They have shown that in the Mott insulating phase the system does not decompose into an array of isolated, non-interacting sites but higher order tunneling events lead to an spin ordering in the lattice. This bilinear-biquadratic spin Hamiltonian has been a topic of intensive research.[2] The 1D case has been examined by Rizzi *et al.*[3] with the help of DMRG calculations. Batrouni *et al.*[4] have used quantum Monte Carlo simulations to determine the phase diagram of 1D systems.

Effects of Magnetic Fields

The impact of magnetic fields on spinor condensates is discussed in Sec. 2.5. The linear Zeeman shift can in general be gauged away and only the quadratic Zeeman shift is relevant. We can include the quadratic Zeeman shift in our model by adding

---

[1] [Imambekov *et al.*(2003)]

[2] see [García-Ripoll *et al.*(2004), Chung and Yip(2009), Rodriguez *et al.*(2011), Leggio *et al.*(2011), Lewenstein *et al.*(2012)] and references therein.

[3] [Rizzi *et al.*(2005)]

[4] [Batrouni *et al.*(2009)]

(a)

(b)
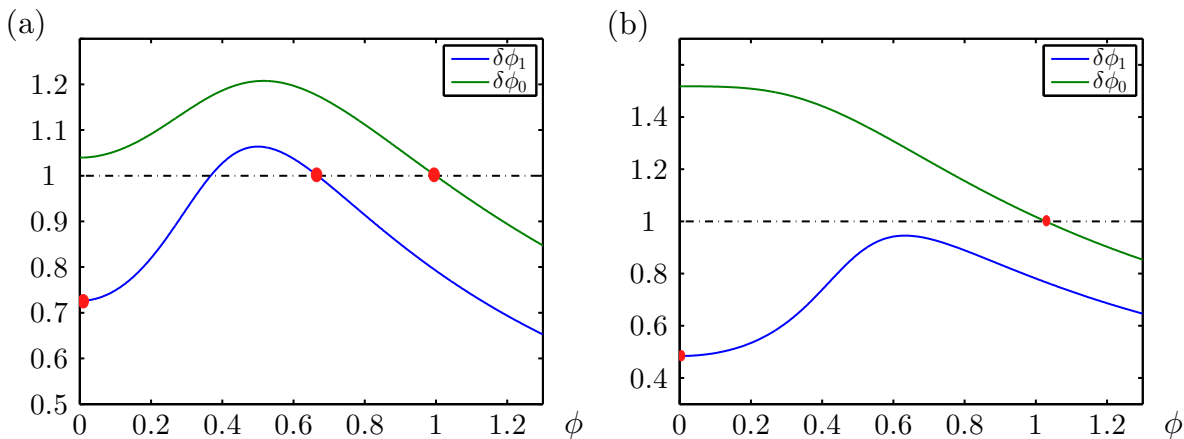
Figure 3.14: Plot of the map $\vec{\phi}_i \to \vec{\phi}_{i+1}$: $\delta\phi_1$ denotes $(\phi_1)_{i+1}/(\phi_1)_i$ and $\delta\phi_0$ denotes $(\phi_0)_{i+1}/(\phi_0)_i$. The parameters $\mu = 1.4$, $t/U_0 = 0.2$ and $U_2/U_0 = 0.04$ are the same as in Fig. 3.7 and Fig. 3.13. The red dots denote the stable fixed points. In (a) the parameter of the quadratic Zeeman shift is $q = 0.015$ and in (b) $q = 0.05$.

an energy shift given in Eq. (2.49) to the the mean-field Hamiltonian (3.24),

$$
\begin{aligned}
\hat{H}_{MF}^{\mathrm{QZ}} &= -\mu\hat{n} + \frac{U_0}{2}\hat{n}(\hat{n} - 1) + \frac{U_2}{2}\left(\hat{\vec{S}}^2 - 2\hat{n}\right) - zt\sum_{\sigma}(\phi_\sigma^*\hat{b}_\sigma + \phi_\sigma\hat{b}_\sigma^\dagger) + zt|\vec{\phi}|^2 \\
&+ q\sum_{\sigma} m_\sigma^2\hat{n}_\sigma,
\end{aligned}
\tag{3.35}
$$

where $q > 0$ because we are examining the spin-1 manifold of alkali atoms (compare Fig. 2.7). The symmetries of the ground-state energy functional are fundamentally changed due to the quadratic Zeeman shift. The notion that both minima for antiferromagnetic interactions are degenerate is no longer true (see Fig. 3.13). The quadratic Zeeman shift also drives phase transitions: In Fig. 3.13 the on-site interactions U_0 and U_2 and the tunneling amplitude t is the same as in Fig. 3.7a but the magnetic field parameter q is chosen to be $q = 0.015$ in Fig. 3.13a and $q = 0.05$ in Fig. 3.13b. In Fig. 3.13a the magnetic field increases the functional $E[\phi_1]$ such that the superfluid minimum corresponds now to a metastable phase and $E[\phi_0]$ does not show a metastable Mott-insulating phase anymore. In Fig. 3.13b the magnetic field is stronger than in Fig. 3.13a and the minimum of $E[\phi_1]$ at a non-vanishing order parameter disappears altogether leaving only a metastable Mott-insulating phase corresponding to $E[\phi_1]$ and a stable superfluid phase corresponding to $E[\phi_0]$. We can compare these energy functionals with the graphical analysis of the map (3.34) which is given in Fig. 3.14. There are three stable fixed points in Fig. 3.14a (denoted by red dots) which correspond to the three local minima in Fig. 3.13a. In Fig. 3.14b there are two stable fixed points corresponding to the two minima in Fig. 3.13b.

3.3 Spinless Bosons in Superlattices

Adapted from Phys. Rev. A **86**, 023624 (2012).

In this section we want to examine ultracold bosonic atoms in optical period-2 superlattices.[1] The unit cell of a period-2 superlattice is a double-well potential[2] (compare Eq. (2.10) and Fig. 2.3). If one neglects tunneling between neighboring unit cells the atoms in each unit cell can be described by the Hamiltonian[3]

$$\hat{H}_0 = \frac{U}{2} \sum_{k=L,R} \hat{n}_k(\hat{n}_k - 1) - t_i(\hat{L}^\dagger \hat{R} + h.c.) + \varepsilon\,(\hat{n}_L - \hat{n}_R) - \mu\,(\hat{n}_L + \hat{n}_R)\,, \quad (3.36)$$

where $\hat{L}$ ($\hat{L}^\dagger$) and $\hat{R}$ ($\hat{R}^\dagger$) are bosonic annihilation (creation) operators for atoms in the left or right well, $\hat{n}_L$ ($\hat{n}_R$) is the atom number operator at the left (right) site. U is the on-site interaction and t_i is the tunneling strength between the sites of the double well. The energy offset between the sites is given by ε and the chemical potential is μ (see Fig. 3.15). The parameters can be tuned by changing the intensity and the phase difference between the counter-propagating laser beams; it is possible to tune the system from the regime of strong tunneling ($t_i \gg U$) to the regime of weak tunneling ($t_i \ll U$).

The Hamiltonian of an array of connected double-well potentials includes tunneling between neighboring unit cells. We choose the configuration as shown in Fig. 3.16 where there are in general three different inter-well tunneling amplitudes,
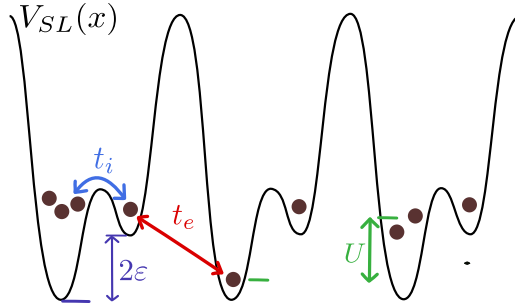
Figure 3.15: Potential landscape of an optical superlattice and parameters of the Bose-Hubbard model (3.38) for spinless ultracold atoms in optical superlattices. The dots depict the atoms in the superlattice potential $V_{SL}(x)$ given in Eq. (2.10), ε is the energy offset between the two sides of the double well, t_i (t_e) is the intra-(inter-)well tunneling amplitude and U is the strength of the on-site interaction.

---

[1] [Buonsante *et al.*(2005), Chen *et al.*(2010)]

[2] [Anderlini *et al.*(2007), Fölling *et al.*(2007), Lee *et al.*(2007), Trotzky *et al.*(2008)]

[3] [Jaksch *et al.*(1998), Vaucher *et al.*(2008)]
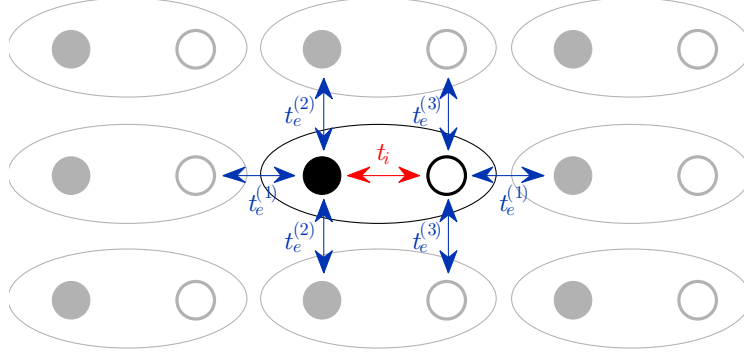
Figure 3.16: Sketch of the two-dimensional period-2 superlattice. The filled circles depict the left wells of each unit cell, the open ones the right wells. The tunneling amplitude within the unit cells is t_i. There are three different tunneling processes between neighboring unit cells, $t_e^{(1)}$, $t_e^{(2)}$, and $t_e^{(3)}$.

$t_e^{(1)}$, $t_e^{(2)}$ and $t_e^{(3)}$. It turns out that our results depend only weakly on the differences among the inter-well tunneling amplitudes. This is why we will assume

$$t_e = t_e^{(1)} = t_e^{(2)} = t_e^{(3)} \, .$$

When we focus on one double well and the the tunneling between this one and the neighboring ones we obtain the Hamiltonian

$$\hat{H} = \hat{H}_0 - t_e(\hat{L}_0^\dagger \hat{R}_1 + \hat{L}_0^\dagger \hat{L}_2 + \hat{R}_0^\dagger \hat{R}_2 + \hat{R}_0^\dagger \hat{L}_3 + \hat{L}_0^\dagger \hat{L}_4 + \hat{R}_0^\dagger \hat{R}_4 + h.c.). \qquad (3.37)$$

The operator $\hat{H}_0$ is given in Eq. (3.36) and contains the information about the internal degrees of freedom of the central unit cell in Fig. 3.16. The subscript $\{0\}$ denotes operators acting in the central unit cell and the indexes $\{1, 2, 3, 4\}$ refer to neighboring double wells according to Fig. 3.16.

To reduce the Hamiltonian (3.37) to a single double-well Hamiltonian we split the operators into their mean values and deviations from this. Next we apply a mean-field approximation, i.e., we neglect the correlations of the deviations between neighboring double wells (compare Eq. (3.11)),

$$
\begin{aligned}
\hat{L}_0^\dagger \hat{R}_N &= (\hat{L}_0^\dagger - \langle \hat{L}_0^\dagger \rangle)(\hat{R}_N - \langle \hat{R}_N \rangle) + \hat{L}_0^\dagger \langle \hat{R}_N \rangle + \hat{R}_N \langle \hat{L}_0^\dagger \rangle - \langle \hat{L}_0^\dagger \rangle \langle \hat{R}_N \rangle \\
&\xrightarrow{MF} \hat{L}_0^\dagger \langle \hat{R}_N \rangle + \hat{R}_N \langle \hat{L}_0^\dagger \rangle - \langle \hat{L}_0^\dagger \rangle \langle \hat{R}_N \rangle,
\end{aligned}
$$

where the index N refers to a neighboring site.

Using this approximation for the Hamiltonian (3.37) we obtain a single-site mean-field Hamiltonian,[1]

$$
\begin{aligned}
\hat{H} = \ &\hat{H}_0 - t_e\Big(\phi_R \hat{L}^\dagger + \phi_L \hat{R}^\dagger + 2z\phi_R \hat{R}^\dagger + 2z\phi_L \hat{L}^\dagger \\
&- \phi_R \phi_L^* - z\phi_R \phi_R^* - z\phi_L^* \phi_L + h.c.\Big),
\end{aligned} \qquad (3.38)
$$

---

[1] [Sheshadri *et al.*(1993), Buonsante *et al.*(2005)]

where we introduced the mean-field parameters $\phi_R = \langle \hat{R} \rangle$, $\phi_L = \langle \hat{L} \rangle$, and $z = 1$ for 2D lattices and $z = 2$ for 3D lattices. We suppressed all subscripts labeling the unit cells because the Hamiltonian (3.38) is a single unit-cell Hamiltonian. The Hamiltonian treats the internal degrees of freedom of each unit cell exactly and approximates the tunneling between the unit cells via a mean-field ansatz. This approach is expected to give satisfactory results if the tunneling inside the unit cells is stronger than the tunneling between the unit cells (i.e., $t_e < t_i$), otherwise correlations between neighboring double wells would be stronger than correlations within the double wells and should not be neglected.

The system is in the Mott-insulating phase if

$$\phi_L = \phi_R = 0$$

and in the superfluid phase if

$$\phi_L \neq 0 \neq \phi_R \,.$$

In the latter case the number of superfluid atoms n_L^{sf} and n_R^{sf} on the left and right site is given by

$$\vec{\phi} = \begin{pmatrix} \phi_L \\ \phi_R \end{pmatrix} = \begin{pmatrix} \sqrt{n_L^{\mathrm{sf}}} \\ \sqrt{n_R^{\mathrm{sf}}} \end{pmatrix}$$

Note that we use the symbol $\vec{\phi}$ in this section in a different way than in Eq. (3.25). Within the mean-field approximation the superlattice decomposes in the Mott-insulating into an array of isolated double-well potentials. Note that in the superfluid phase both mean-field parameters are non-zero because they are coupled to each other in Eq. (3.38) (compare also Fig. 4.15).

Similar to Sec. 3.1.1 there are two equivalent methods to treat the Hamiltonian (3.38). For a given set of parameters $\{\mu, \varepsilon, t_i, t_e, U\}$ the task is to find the self-consistent values of

$$\vec{\phi} = \begin{pmatrix} \langle \psi_{\vec{\phi}}^{(0)} | \hat{L} | \psi_{\vec{\phi}}^{(0)} \rangle \\ \langle \psi_{\vec{\phi}}^{(0)} | \hat{R} | \psi_{\vec{\phi}}^{(0)} \rangle \end{pmatrix} ,$$

where $|\psi_{\vec{\phi}}^{(0)}\rangle$ denotes the ground state of the Hamiltonian (3.38) for a given order parameter $\vec{\phi}$. On the one hand the self-consistent values are fixed points of the map

$$\vec{\phi}_{i+1} = \begin{pmatrix} \langle \hat{R} \rangle_{\vec{\phi}_i} \\ \langle \hat{L} \rangle_{\vec{\phi}_i} \end{pmatrix} \tag{3.39}$$

where the index i refers to the ith step in the iterative procedure used to find the self-consistent value of the order parameter. On the other hand the self-consistent values of $\vec{\phi}$ correspond to the local extrema of the energy functional

$$E[\phi_L, \phi_R] = \langle \psi_{\vec{\phi}}^{(0)} | \hat{H} | \psi_{\vec{\phi}}^{(0)} \rangle$$
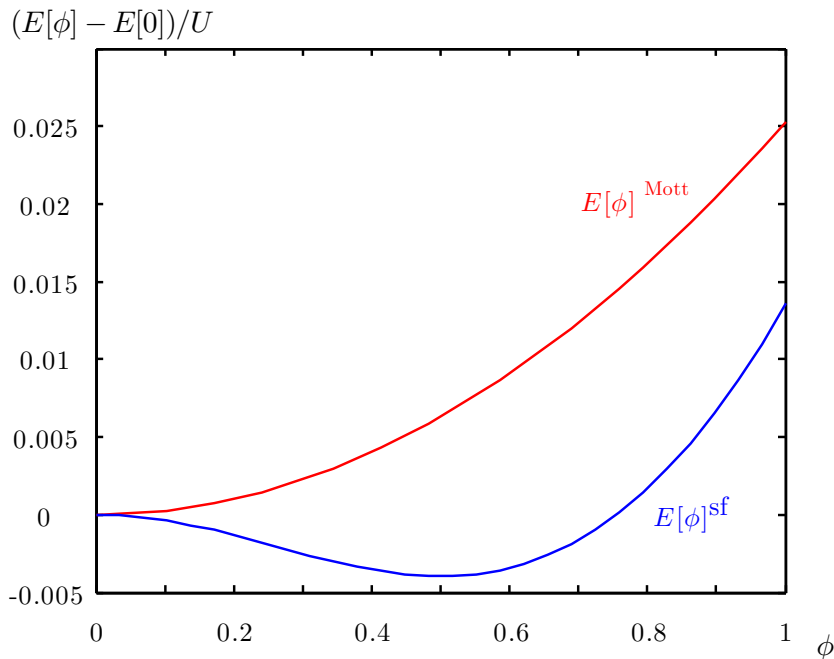
Figure 3.17: Ground-state energy $E[\phi_L, \phi_R]$ of the Hamiltonian (3.38) as a function of the order parameter $\vec{\phi} = \{\phi_L, \phi_R\}$. For a symmetric unit cell $\varepsilon = 0$, we have $\phi_L = \phi_R = \phi$. The red line $E[\phi]^{\text{Mott}}$ corresponds to the Mott-insulating phase ($\mu/U = 0.2$, $t_i/U = 0.05$, and $t_e/U = 0.005$), the blue line $E[\phi]^{\text{sf}}$ to the superfluid phase ($\mu/U = 0.5$, $t_i/U = 0.22$, and $t_e/U = 0.022$).

and its local minima correspond to stable fixed points of the map (3.39) which can be found by the iterative procedure (compare beginning of Sec. 3.1.1).

In the same way as in Sec. 3.1.1 there are only two classes of energy functionals for the Hamiltonian (3.38)(see Fig. 3.17): First, there are those with only one local extremum at $\phi_L = \phi_R = 0$ corresponding to a Mott-insulating phase. The second class are those with a second extremum at $\phi_L \neq 0 \neq \phi_R$, which is the global minimum, and which are corresponding to a superfluid phase. This enables us to distinguish the Mott and superfluid quantum phases with minimal numerical effort. We only have to calculate the ground-state energy for $\vec{\phi} = 0$ and in its proximity $\vec{\phi} \approx 0$. If $E[\vec{\phi} \approx 0] - E[\vec{\phi} = 0]$ is positive, the system is Mott-insulating; if it is negative the system is superfluid.

Stability Analysis Approach

We can use a stability analysis to calculate the phase boundary similar to Sec. 3.1.1 following Buonsante *et al.*(2005).[1] The point $\vec{\phi} = \vec{0}$ is always a fixed point of the

---

[1] [Buonsante *et al.*(2005)]

68

map (3.39). To distinguish the two quantum phases it is sufficient to examine if it is a stable fixed point or an unstable one. If this is a stable fixed point, the system is in the Mott phase. To find out, if it is stable for a given parameters μ, U, t_i and t_e we linearize the map around the fixed point,

$$
\begin{aligned}
\vec{\phi}_{i+1} &\approx \left. \frac{\partial \left(\langle \hat{L} \rangle_{\vec{\phi}}, \langle \hat{R} \rangle_{\vec{\phi}} \right)}{\partial (\phi_L, \phi_R)} \right|_{\vec{\phi}=0} \cdot \vec{\phi}_i + \mathcal{O}\left(\vec{\phi}_i^2 \right) \\
&= \mathbf{J} \cdot \vec{\phi}_i + \mathcal{O}\left(\vec{\phi}_i^2 \right).
\end{aligned}
\tag{3.40}
$$

The absolute values of the eigenvalues of the Jacobian matrix $\mathbf{J}$ determine the stability of the fixed point: If they are all smaller than 1, the fixed point is stable (the Lyapunov exponents are negative). If at least one is larger than 1, the fixed point is unstable (the Lyapunov exponents are positive). The Jacobian matrix is given by

$$
\mathbf{J} = \begin{pmatrix} \partial_{\phi_L} \langle \hat{L} \rangle_{\vec{\phi}} & \partial_{\phi_R} \langle \hat{L} \rangle_{\vec{\phi}} \\ \partial_{\phi_L} \langle \hat{R} \rangle_{\vec{\phi}} & \partial_{\phi_R} \langle \hat{R} \rangle_{\vec{\phi}} \end{pmatrix}.
$$

The two numbers $\langle \hat{L} \rangle_{\vec{\phi}}$ and $\langle \hat{R} \rangle_{\vec{\phi}}$ are in general non-linear functions of the order-parameters ϕ_L and ϕ_R. Because we are only interested in the derivative at $\vec{\phi} = \vec{0}$ it is sufficient to expand the two functions around this value and calculate only the linear term. This is equivalent to a first order perturbation theory of the Hamiltonian with a perturbation linear in the mean-field parameters,

$$
\hat{H} = \hat{H}_0 + t_e \, \hat{V},
$$

where

$$
\hat{V} = -(\phi_R \hat{L}^\dagger + \phi_R^* \hat{L} + \phi_L^* \hat{R} + \phi_L \hat{R}^\dagger)
$$

and $\hat{H}_0$ is given in Eq. (3.36). Let $|\psi_0\rangle$ be the ground state of $\hat{H}_0$. The first order correction of this is given by $|\psi\rangle = |\psi_0\rangle + t_e \, |\psi_1\rangle$ where $|\psi_1\rangle = \sum_{i \neq 0} \frac{\langle \psi_i | V | \psi_0 \rangle}{E_0 - E_i} |\psi_i\rangle$. It follows that

$$
\langle \hat{A} \rangle_{\phi_i} \approx t_e \langle \psi_0 | \hat{A} | \psi_1 \rangle + t_e \langle \psi_1 | \hat{A} | \psi_0 \rangle = t_e \langle \psi_0 | \hat{A} + \hat{A}^\dagger | \psi_1 \rangle = c_{AR} \, \phi_L + c_{AL} \, \phi_R \,,
$$

where $\hat{A} \in \{\hat{L}, \hat{R}\}$ and the coefficients c_{AR} and c_{AL} are given by

$$
c_{AB} = t_e \sum_{i \neq 0} \frac{\langle \psi_i | \hat{A} + \hat{A}^\dagger | \psi_0 \rangle \langle \psi_i | \hat{B} + \hat{B}^\dagger | \psi_0 \rangle}{E_i - E_0}.
$$

The fixed point at $\vec{\phi} = \vec{0}$ is stable if both eigenvalues of $\mathbf{J} = \begin{pmatrix} c_{LL} & c_{LR} \\ c_{RL} & c_{RR} \end{pmatrix}$ are smaller than one, i.e.,

$$
|c_{RL} \pm \sqrt{c_{RR} c_{LL}}| < 1.
$$
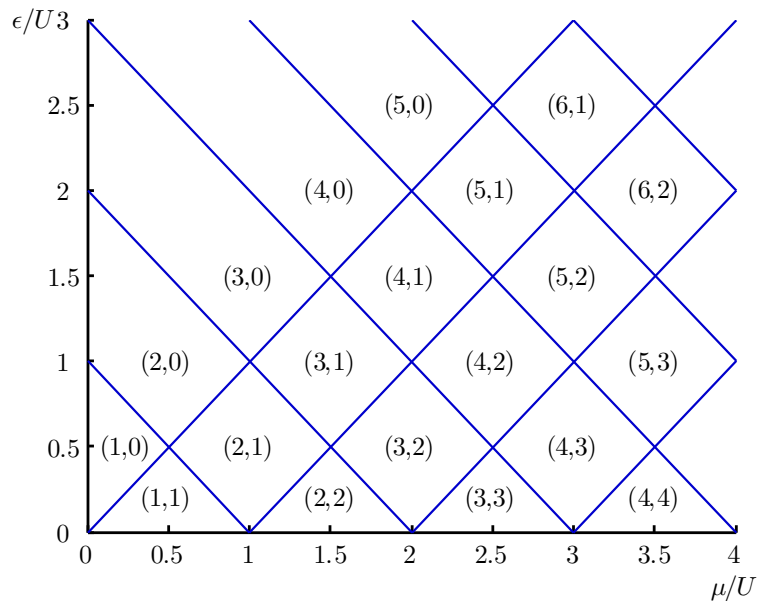
Figure 3.18: Phase diagram of spinless bosons in a superlattice described by the Hamiltonian (3.38) in the atomic limit $t_i = t_e = 0$. For $t_i = t_e = 0$ the Hamiltonian is diagonal in the Fock basis and supports only Mott-insulating phases. The blue lines mark the phase boundaries and (n_L, n_R) denotes the occupation of the left and the right site in the double well.

This stability condition enables us to calculate the phase boundary with only minimal numerical effort. To determine the eigenvalues of **J** it is sufficient to diagonalize the Hamiltonian Eq. (3.38) only once. One chooses any value for t_e and an initial value for $\vec{\phi}_s$ in the vicinity of $\vec{\phi} = \vec{0}$ and calculates $\{\langle \hat{R} \rangle_{\vec{\phi}_s}, \langle \hat{L} \rangle_{\vec{\phi}_s}\}$. The ratio $\phi_{s_L}/\langle \hat{L} \rangle_{\vec{\phi}_s}$ corresponds to the the first eigenvalue of **J**, the ratio $\phi_{s_R}/\langle \hat{R} \rangle_{\vec{\phi}_s}$ corresponds to the second. The eigenvalues are linear in t_e; because of that, the ratio of t_e and the larger of the two eigenvalues gives the critical value of t_e, i.e., at which the system turns superfluid for a given t_i, U and μ.

The Phase Diagram for Spinless Bosons in Superlattices

In this section we determine the ground-state phase diagram of the Hamiltonian (3.38). For a chemical potential μ, an energy offset ε, and a given ratio of the tunneling amplitudes t_e/t_i we calculate the critical tunneling amplitude t_e above which the system is superfluid. In the following we use the on-site interaction U as the unit of energy.

In Fig. 3.18 we plot the ground state as a function of chemical potential μ and offset ε in the atomic limit $t_i = t_e = 0$. In this case, the Hamiltonian (3.38)

state	energy	state	energy	state	energy
E_{00}	0	E_{22}	$2\,U - 4\mu$	E_{33}	$6U - 6\mu$
E_{01}	$-\mu - \varepsilon$	E_{13}	$3U - 4\mu - 2\varepsilon$	E_{24}	$7U - 2\varepsilon - 6\mu$
E_{11}	-2μ	E_{04}	$6U - 4\mu - 4\varepsilon$	E_{15}	$10U - 4\varepsilon - 6\mu$
E_{02}	$U - 2\mu - 2\varepsilon$	E_{23}	$4U - \varepsilon - 5\mu$	E_{06}	$15U - 6\varepsilon - 6\mu$
E_{12}	$U - 3\mu - \varepsilon$	E_{14}	$6U - 3\varepsilon - 5\mu$	$\ldots$	
E_{03}	$3U - 3\mu - 3\varepsilon$	E_{05}	$10U - 5\varepsilon - 5\mu$	$\ldots$	

Table 3.1: Diagonal elements of the Hamiltonian (3.38) for $t_i = t_e = 0$ in Fock space (i.e., $|n_L, n_R\rangle$) for small occupancies.

is diagonal in the Fock basis and the system supports only Mott phases (n_L, n_R) characterized by the number of atoms in the left n_L and right well n_R. The energy levels of the Hamiltonian (3.38) with $t_i = t_e = 0$ are given by

$$E(\mu, n_L, n_R, \epsilon) = \frac{U}{2}(n_L^2 - n_L + n_R^2 - n_R) + \varepsilon\,(n_L - n_R) - \mu\,(n_L + n_R)$$

The eigenstates and the eigenenergies of the system for small occupation numbers n_L and n_R can be read off the Table 3.1. For each $\mu/U \in [0, 2.5]$ and $\varepsilon/U \in [0, 3.5]$ this collection of eigenstates is sufficient to determine the ground state (compare Fig. 3.18). Each of the diamonds in Fig. 3.18 corresponds to one Fock state, i.e., a fixed particle number in the unit cell as well as a fixed particle number in the left and the right site of each unit cell. When we increase μ/U for fixed energy offset ε/U the number of particles in the unit cells increases while the ratio between left and right remains similar. When we increase ε/U for fixed chemical potential μ/U the atom number is constant but the atom distribution within the unit cells changes. Because we set the tunneling to zero this happens non-continuously. Figure 3.18 is mirror-symmetric along the $\varepsilon = 0$ axis, i.e., when $\varepsilon \to -\varepsilon$ the atom number distribution is inverted, $(n_L, n_R) \to (n_R, n_L)$.

In Fig. 3.19 we plot the critical tunneling strength t_i at which the system becomes superfluid as a function of the chemical potential μ and the offset ε for $t_i/t_e = 10$. It is convenient to pick a fixed ratio of t_i/t_e in order to obey the constraint $t_e < t_i$. For fixed energy offset ε we recover Mott lobes, which are familiar from the case of a usual lattice,[1] although the Mott phase for atoms in superlattices is characterized by a fixed integer atom number per unit cell, i.e. $n = \langle \hat{n}_L + \hat{n}_R \rangle$ where n is an integer number. When ε/U has an integer value the Mott lobes corresponding to an odd atom number per unit cell contract to Mott loops and if ε/U has an half-integer value the lobes corresponding to an even atom number contract to loops.[2] As the energy offset ε is varied, the size of the Mott lobes changes and they constitute tubes of fixed integer atom number per unit cell. The base of the plot (i.e., the $t_i = t_e = 0$ plane) shows the diamond structure given in Fig. 3.18. The nodes of the diamonds

---

[1] [Fisher *et al.*(1989)]

[2] [Buonsante *et al.*(2005)]
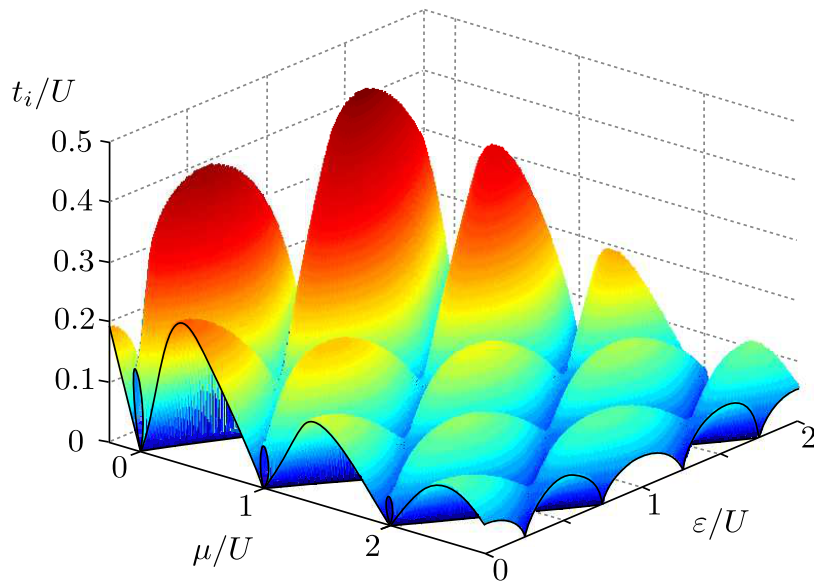
Figure 3.19: Phase diagram of spinless bosons in a two-dimensional superlattice described by the Hamiltonian (3.38). We plot the critical internal tunneling amplitude t_i as a function of chemical potential μ and energy offset ε for $t_i = 10t_e$. In Fig. 3.18 we show a cut through this 3D plot at $t_i = t_e = 0$ and in Fig. 3.20 at $t_i/U = 0.05$. The edge at $\varepsilon = 0$ of the phase diagram reveals the contraction of Mott lobes to loops at integer values of μ/U.

are special: these are the values of the energy offset ε where the lobes contract to loops, i.e. the Mott tubes touch the $t_i = t_e = 0$ plane only at one point.

Figure 3.20 presents a cut through Fig. 3.19 at $t_i/U = 0.05$, showing the Mott insulating phases in white and the superfluid phases in blue. The Mott diamonds of Fig. 3.18 are connected for non-vanishing tunneling amplitudes. This means that the quantum numbers (n_L, n_R) change continuously when ε is varied and the Mott insulating phases are characterized by one number $n = n_L + n_R$, the total number of particles per unit cell. In Fig. 3.20 the chosen tunneling amplitudes are too large to see the connections between the Mott diamonds for $n \geq 5$, nevertheless the quantum numbers (n_L, n_R) are not fixed to integer values for these Mott phases either.
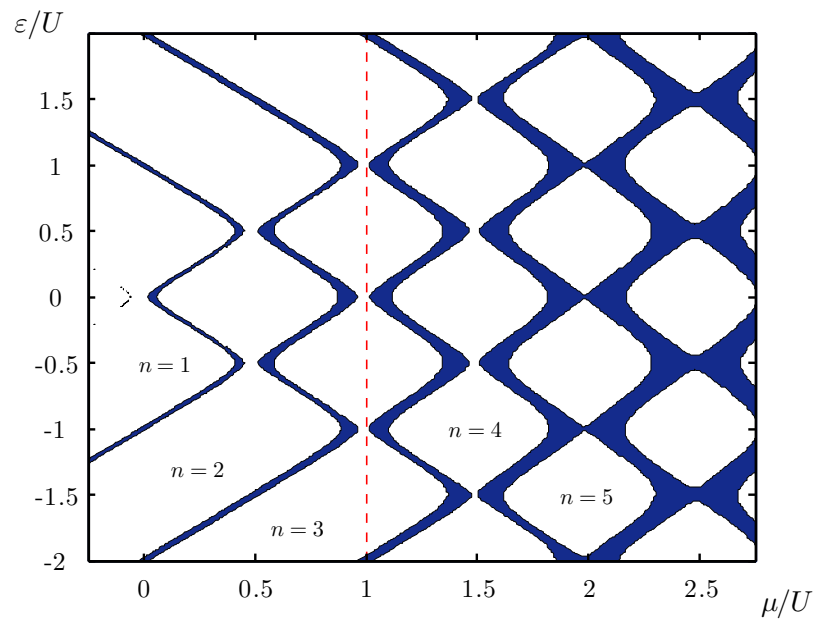
Figure 3.20: Phase diagram of spinless bosons in a two-dimensional superlattice described by the Hamiltonian (3.38) for $t_i/U = 10t_e/U = 0.05$. The blue areas depict the superfluid phase. The dashed line corresponds to the parameters chosen for Fig. 4.13.

3.4 Spin-1 Bosons in Superlattices

Adapted from Phys. Rev. A **86**, 023624 (2012).

In this section we describe spin-1 atoms in optical period-2 superlattices. We use similar to Sec. 3.3 a model which treats the dynamics within a unit cell exactly and includes the influence of the neighboring unit cells via a Gutzwiller mean-field ansatz. Spin-1 atoms in isolated double wells are described by a variant of the two-site Bose-Hubbard model,[1]

$$\hat{H}_0 = \frac{U_0}{2} \sum_{i=L,R} \hat{n}_i(\hat{n}_i - 1) - t \sum_\sigma (\hat{L}_\sigma^\dagger \hat{R}_\sigma + h.c.) + \varepsilon \left(n_L - n_R \right) + \frac{U_2}{2} \sum_{i=L,R} \left(\vec{S}_i^2 - 2n_i \right),$$

where the annihilation and creation operators $\hat{L}$, $\hat{R}$, $\hat{L}^\dagger$ and $\hat{R}^\dagger$ from Eq. (4.1) have an extra index labelling their hyperfine state $\sigma \in \{-1, 0, 1\}$ (compare Eq. (2.41). The operator $n_L = \sum_\sigma L_\sigma^\dagger L_\sigma \left(n_R = \sum_\sigma R_\sigma^\dagger R_\sigma \right)$ is the atom number operator at the left (right) site and $\vec{S}_L = \sum_{\sigma\sigma'} L_\sigma^\dagger \vec{T}_{\sigma\sigma'} L_{\sigma'}$ is the total spin on the left site and the total spin on the right site is $\vec{S}_R = \sum_{\sigma\sigma'} R_\sigma^\dagger \vec{T}_{\sigma\sigma'} R_{\sigma'}$, where $\vec{T}_{\sigma\sigma'}$ are the usual spin-1 matrices (see Eq (2.33)).

Similar to Eq. (3.38) we can include neighboring double wells via a mean-field approximation and use as in Sec. 3.2 vectors as the order parameter. The resulting Hamiltonian is

$$
\begin{aligned}
\hat{H} \quad &= \frac{U_0}{2} \sum_{k=L,R} \hat{n}_k(\hat{n}_k - 1) - t_i \left(\hat{\mathbf{L}}^\dagger \cdot \hat{\mathbf{R}} + h.c. \right) + \varepsilon \left(\hat{n}_L - \hat{n}_R \right) - \mu \left(\hat{n}_L + \hat{n}_R \right) \\
&+ \frac{U_2}{2} \sum_{k=L,R} \left(\hat{\mathbf{S}}_k^2 - 2\hat{n}_k \right) - t_e \left[\vec{\phi}_R \cdot \hat{\mathbf{L}}^\dagger + \vec{\phi}_L \cdot \hat{\mathbf{R}}^\dagger + 2z\vec{\phi}_L \cdot \hat{\mathbf{L}}^\dagger + 2z\vec{\phi}_R \cdot \hat{\mathbf{R}}^\dagger \right. \\
&- \left. \vec{\phi}_R \cdot \vec{\phi}_L^* - z\vec{\phi}_L \cdot \vec{\phi}_L^* - z\vec{\phi}_R^* \cdot \vec{\phi}_R + h.c. \right],
\end{aligned}
\tag{3.41}
$$

where we introduced a vector notation for the annihilation and creation operators. The dimensionality of the array is contained in the parameter z; for 2D lattices $z = 1$ and for 3D lattices $z = 2$. The vectors

$$
\vec{\phi}_L = \begin{pmatrix} \phi_L^{(1)} \\ \phi_L^{(0)} \\ \phi_L^{(-1)} \end{pmatrix} \quad \text{and} \quad \vec{\phi}_R = \begin{pmatrix} \phi_R^{(1)} \\ \phi_R^{(0)} \\ \phi_R^{(-1)} \end{pmatrix}
$$

contain the six mean-field parameters of the Hamiltonian (3.41). Note that the system is rotationally symmetric and $\phi_1 = \phi_{-1}$ for both $\vec{\phi}_L$ and $\vec{\phi}_R$.[2]

---

[1] [Jaksch *et al.*(1998), Imambekov *et al.*(2003)]

[2] [Ho(1998)]
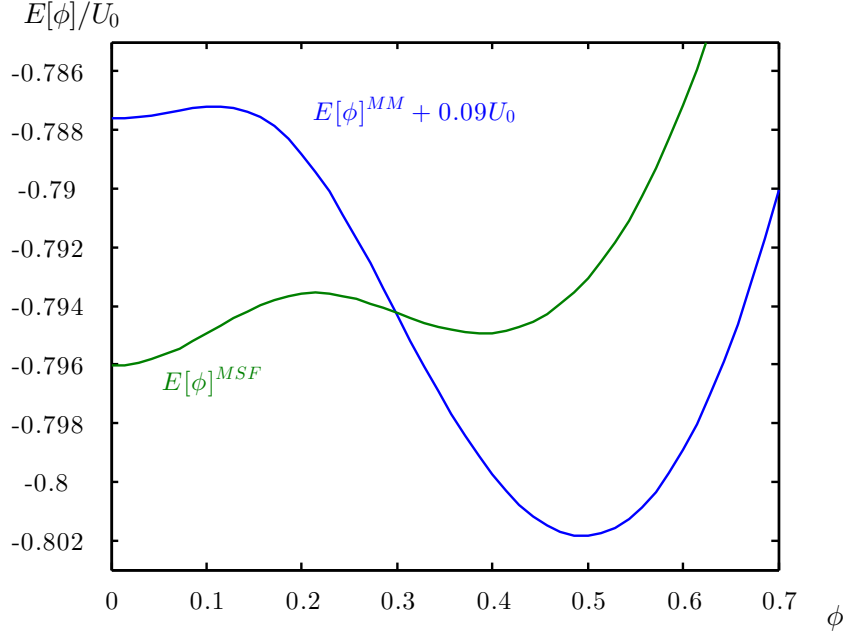
Figure 3.21: Ground-state energy $E[\vec{\phi}_L, \vec{\phi}_R]$ of the Hamiltonian (3.41) as a function of the order parameter $\vec{\phi}$. The unit cell is chosen to be symmetric $\varepsilon = 0$, i.e., we have $\vec{\phi}_L = \vec{\phi}_R = \vec{\phi}$, we have chosen $\phi_0 = 0$, and $\phi_1 = \phi_{-1}$ due to symmetry constraints. The blue line $E[\phi]^{MM}$ corresponds a point in parameter space ($\mu/U_0 = 0.25$, $t_i/U_0 = 0.35$, $t_e/U_0 = 0.035$, $U_2/U_0 = 0.04$, and $\varepsilon = 0$) where there is a metastable Mott phase in addition to the stable superfluid phase. The green line $E[\phi]^{MSF}$ corresponds a point within the metastable superfluid phase ($\mu/U_0 = 0.25$, $t_i/U_0 = 0.3$, $t_e/U_0 = 0.03$, $U_2/U_0 = 0.04$, and $\varepsilon = 0$). $E[\phi]^{MM}$ is shifted by $0.09U_0$ to show the two curves in the same plot.

The on-site interaction parametrized by U_2 describes spin-dependent contact interactions: in the case of antiferromagnetic interactions (e.g. ^{23}Na) it penalizes non-zero spin configurations while it favors high-spin configurations in the case of ferromagnetic interactions (e.g. ^{87}Rb). Whereas the ratio t/U_0 can be controlled with the intensity of the laser beams (compare Eq. (2.44)), the ratio U_2/U_0 depends on the spin-2 and spin-0 scattering lengths of the spin-1 atoms (compare Eq. (2.45)).

The Hamiltonian (3.41) has a much richer phase diagram than the Hamiltonian (3.38). In addition to Mott-insulating and superfluid quantum phases, the spin-1 Bose-Hubbard model gives rise to metastable quantum phases. This can be seen by looking at the energy functionals $E[\vec{\phi}_L, \vec{\phi}_R]$ of the Hamiltonian (3.41). In addition to those shown in Fig. 3.17, two other classes of energy functionals arise for antiferromagnetic spin interactions $U_2 > 0$, see Fig. 3.21. These energy functionals have two local minima and an iterative procedure similar to the one described in Sec. 3.1.1 does not lead to an unique value of the order parameter but depends on the starting point. When the starting point of the iterative procedure is chosen close to zero, one finds the minimum at $\vec{\phi}_L = \vec{\phi}_R = 0$. If one starts at a value
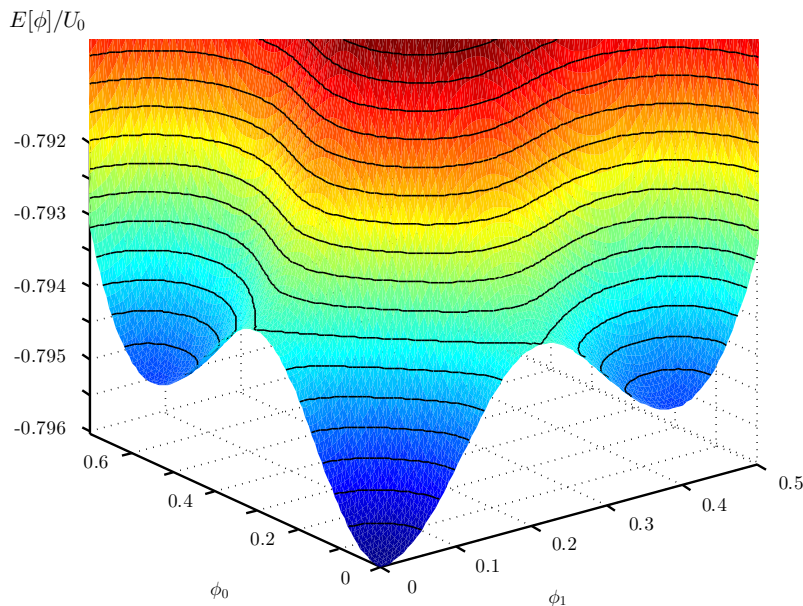
Figure 3.22: Energy functional $E[\vec{\phi}_L, \vec{\phi}_R]$ for the Hamiltonian (3.41) with antiferromagnetic interactions ($t_i/U_0 = 0.3$, $t_e/U_0 = 0.03$, $U_2/U_0 = 0.04$, $\mu/U_0 = 0.25$, $\varepsilon = 0$). Because the unit cell is chosen to be symmetric the mean-field parameters of the left and the right are equal ($\vec{\phi} = \vec{\phi}_L = \vec{\phi}_R$) and the corresponding indices are suppressed. Because of the rotational symmetry $\phi_1 = \phi_{-1}$.

beyond the maximum separating the two minima one obtains the second minimum corresponding to a superfluid phase. The global minimum of the energy functional determines the stable quantum phase of the system. The other one corresponds to a metastable phase.

Thus, energy functionals such as the ones in Fig. 3.21 signal metastable phases, first-order phase transitions and hysteric behavior of the system; they do not allow the same analysis as the spinless case. The stability analysis of the $\vec{\phi} = 0$ fixed point does not answer the question, if there is a second stable fixed point and if it is energetically lower or higher. To determine the quantum phase we numerically calculate the energy functional and analyze its local minima.

Due to the spinor nature of the order parameter additional properties of the superfluid phases arise. The spin-dependent interaction changes the symmetry of the energy functional $E[\vec{\phi}_L, \vec{\phi}_R]$ in the ϕ_0-ϕ_1 plane for $\vec{\phi}_L$ as well as $\vec{\phi}_R$. For antiferromagnetic interactions there are two different classes of polar order parameters given in Eq. (3.26) and (3.27). In the ferromagnetic case ($U_2 < 0$) there is only one superfluid order parameter which is given Eq. (3.28). In the ferromagnetic case, the spin-dependent interaction in Eq. (3.41) has the same sign as the tunneling term and therefore does not create metastable quantum phases.

In Fig. 3.22 we plot the energy functional $E[\vec{\phi}_L, \vec{\phi}_L]$ as a function of the order parameter for a symmetric unit cell and a point in parameter space at which there are

two local minima corresponding to a longitudinal and a transverse polar superfluid phase as well as a local minimum signaling a stable Mott insulating phase. Since the unit cell is chosen to be symmetric ($\varepsilon = 0$) the mean-field parameters in the left and the right site are the same ($\vec{\phi}_L = \vec{\phi}_R$). The two minima at a non-vanishing order parameter are degenerate, because both correspond to $\langle \hat{\mathbf{S}}_L \rangle = \langle \hat{\mathbf{S}}_R \rangle = 0$ and therefore suffer the same spin-dependent energy shift of the on-site interaction. Due to the special form of the two superfluid phases given in Eq. (3.26) and Eq. (3.27) the superfluid minima are always on the $\phi_1 = 0$ and the $\phi_0 = 0$ axes, respectively. This justifies why we chose $\phi_0 = 0$ in Fig. 3.21. The additional minimum in Fig. 3.22 at $\phi_0 = \phi_1 = \phi_{-1} = 0$ is the global minimum and corresponds to the Mott-insulating phase; the two degenerate minima corresponding to a non-vanishing order parameter belong therefore to two degenerate metastable phases.

The Phase Diagram

In this section we calculate the phase diagram of spin-1 atoms in superlattices. We focus on the differences to the spinless case which was discussed in Sec. 3.3.

For $t_i = t_e = 0$ the Hamiltonian (3.41) is diagonal in the Fock basis and the system supports only Mott phases. Similar to the spinless case the Mott phases are characterized by (n_L, n_R) and the boundaries between Mott phases carrying a small number of atoms can be calculated directly from the collection of eigenstates and eigenenergies in Table 3.2.

state	energy	state	energy
E_{00}	0	E_{22}	$2U_0 - 4\mu - 4U_2$
E_{01}	$-\mu - \varepsilon$	E_{13}	$3U_0 - 4\mu - 2\varepsilon - 2U_2$
E_{11}	-2μ	E_{04}	$6U_0 - 4\mu - 4\varepsilon - 4U_2$
E_{02}	$U_0 - 2\mu - 2\varepsilon - 2U_2$	E_{23}	$4U_0 - 5\mu - \varepsilon - 4U_2$
E_{12}	$U_0 - 3\mu - \varepsilon - 2U_2$	E_{14}	$6U_0 - 5\mu - 3\varepsilon - 4U_2$
E_{03}	$3U_0 - 3\mu - 3\varepsilon - 2U_2$	E_{05}	$10U_0 - 5\mu - 5\varepsilon - 4U_2$

Table 3.2: Diagonal elements of the Hamiltonian (3.41) for $t_i = t_e = 0$ in Fock space (i.e., $|n_L, n_R\rangle$). Because we are interested in ground-state properties for antiferromagnetic interactions we choose for each atom number configuration the smallest spin configuration. For ferromagnetic interactions the highest spin configuration is energetically favorable and the table is thus changed.

In Fig. 3.23 we show how the phase boundaries are shifted compared to the spinless case for antiferromagnetic interactions. Again, there is a diamond-shaped structure as in Fig. 3.18. The Mott diamonds of Fig. 3.18 increase or shrink depending on their atom number configuration. For antiferromagnetic spin interactions, the strength of the on-site interaction depends upon the parity of the atom number at
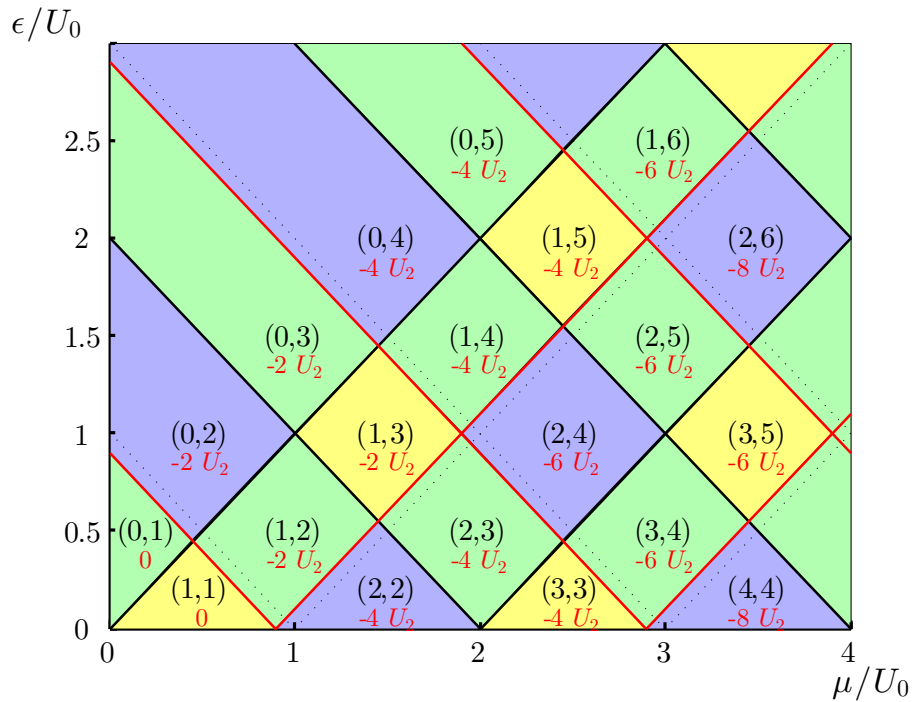
Figure 3.23: Sketch of the phase boundaries of spin-1 bosons in a two-dimensional superlattice for $t_i = t_e = 0$, described by the Hamiltonian (3.41). The red lines denote deviations in the phase boundaries relative to the spinless case (see Fig. 3.18), black solid lines to phase boundaries which are not changed and black dotted lines to shifted phase boundaries of the spinless case. Each Mott diamond is labeled by its atom number configuration (n_L, n_R) (in black) and the energy penalty due to spin-dependent interactions (in red below). The green diamonds correspond to odd-even particle number configurations, the yellow ones to odd-odd, and the blue ones to even-even configurations.

each lattice site. An even number of spin-1 atoms allows the formation of a spin singlet, i.e. vanishing total spin per site, which minimizes the on-site repulsion. Odd atom numbers are penalized, because the spin-singlet wave function is antisymmetric for an odd atom number and thereby ruled out by symmetry constraints. Diamonds corresponding to an even particle number in the left as well as the right well are favored and diamonds corresponding to an odd-odd configuration are penalized.

The boundary between two Mott diamonds is shifted only if the spin-dependent energy penalty (or bonus) is different for them (compare Table 3.2). The value of this shift depends linearly on U_2. In the antiferromagnetic case, a phase boundary is either unshifted or shifted by a constant amount. This is because at each phase boundary the atom configuration changes only by one atom and the only possible ground-state spin configurations at each lattice site are spin singlets ($\langle \hat{\mathbf{S}}^2 \rangle = 0$) and total spin equals one ($\langle \hat{\mathbf{S}}^2 \rangle = 2$). This is the reason why the straight lines in
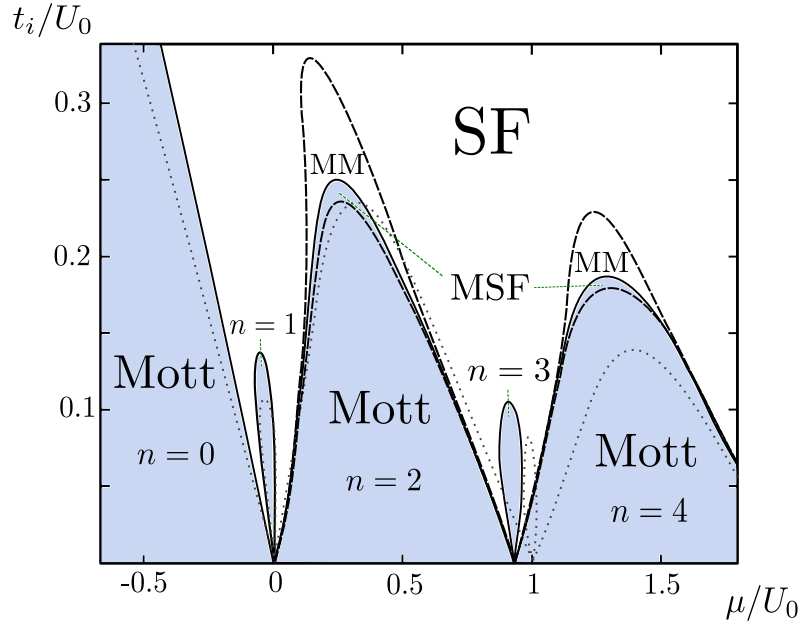
Figure 3.24: Phase diagram for spin-1 atoms in optical superlattices ($U_2/U_0 = 0.04$, $\varepsilon = 0$, and $t_i = 10t_e$). The shaded regions denote Mott-insulating phases. The dashed lines are the phase boundaries for metastable phases and the dotted lines are the phase boundaries for the spinless case $U_2 = 0$. The regions in which a metastable Mott phase coexists beside the superfluid [SF] phase is marked with MM; MSF denotes regions where metastable superfluid phases exist alongside the Mott [Mott] phase. The Mott lobes are labeled according to the total atom number n per double well.

Fig. 3.18 are preserved in case of antiferromagnetic interactions. Thus, to determine the shift of the phase boundaries it is enough to examine an example, say the phase boundary between the Mott diamonds containing one atom in the left well and the ones containing two atoms in the left well. The phase boundary follows for positive ε the path along

$$\varepsilon = -\mu + U_0 - 2U_2 \, ,$$

which can be seen by setting $E_{11} = E_{12}$ or $E_{10} = E_{20}$. The shift of the phase boundary is therefore $\Delta = \sqrt{2}U_2$. The diamonds corresponding to an odd number of atoms in the double well (green diamonds in Fig. 3.23) change their size from $1/2$ (in units of U_0^2) to $1/2 - \Delta^2/U_0^2$. Double wells carrying an even number of atoms allow even-even configurations (blue diamonds in Fig. 3.23 with area $(1/\sqrt{2} + \Delta/U_0)^2$) and odd-odd configurations (yellow diamonds in Fig. 3.23 with area $(1/\sqrt{2} - \Delta/U_0)^2$). Note that both yellow and green Mott diamonds vanish for

$$\frac{1}{2} = \frac{\Delta^2}{U_0^2} = 2\,\frac{U_2^2}{U_0^2} \, .$$

79

Thus, for $U_2 > 0.5\,U_0$ there are only Mott phases carrying even atom numbers in each lattice site.

The full ground-state phase diagram for antiferromagnetic interactions, a symmetric double well and $t_i = 10t_e$ is shown in Fig. 3.24. We choose $U_2/U_0 = 0.04$ corresponding to ^{23}Na.[1] Spin-dependent interactions lead to elongated Mott lobes. In general, the spin configuration is higher in the superfluid phase than in the Mott phase and this leads to an energy penalty (see Hamiltonian (3.41)). Whenever there is an even number of atoms in a lattice site this effect is strongest, because an even number of spin-1 bosons can form spin singlets (see above). In Fig. 3.24 the Mott lobe containing four atoms is therefore significantly enlarged, since this Mott phase corresponds to two atoms in the left as well as the right site (the unit cells are chosen to be symmetric, i.e., $\varepsilon = 0$). The Mott lobe $n = 2$ is significantly enlarged for $\varepsilon/U_0 = \pm 1$ (not contained in Fig. 3.24), because the atoms pair up on the left (or right) site and form spin singlets. The phase transitions between Mott lobes corresponding to an even number of atoms in the double well are of second order whereas the others are first-order phase transitions. For smaller values of U_2/U_0 all phase transitions become first order at a tricritical point, in contrast to spin-1 atoms in usual lattices for which the boundary of the Mott phase with one atom per site is always a second-order phase transition.[2]

Magnetic Fields

Finally, we want to examine the effect of weak magnetic fields on the phase diagram of spin-1 atoms in optical superlattices. In Sec. 2.5 we discussed the influence of magnetic fields and in Sec. 3.2 we saw how the quadratic Zeeman shift lifts the degeneracy of the two polar state and changes the qualitative features of the ground-state energy functionals. In the case of spin-1 atom in superlattices we can include the quadratic Zeeman shift by creating an effective Hamiltonian,

$$\hat{H}_{\mathrm{QZ}} \;=\; q \sum_{i=L,R} \sum_{\sigma} m_{i\sigma}^2 \hat{n}_{i\sigma}, \qquad (3.42)$$

which is added to the Hamiltonian (3.41). Here $p = g\mu_B B$ and $\hat{n}_{i\sigma}$ is the particle number operator for the ith site that gives the number of bosons in the mth hyperfine state.

The quadratic Zeeman effect affects the phase diagram considerably. The local minima of the energy functional $E[\vec{\phi}_L, \vec{\phi}_R]$ belonging to transverse and longitudinal polar superfluids are no longer degenerate in same way as in usual lattices (see Fig. 3.25). For positive q the longitudinal superfluid states are always energetically favored, for negative q the transverse ones. For antiferromagnetic spin interaction new classes of metastable quantum phases arise, see Fig. 3.26. It is important to

---

[1] [Burke *et al.*(1998)]

[2] [Krutitsky *et al.*(2005)]
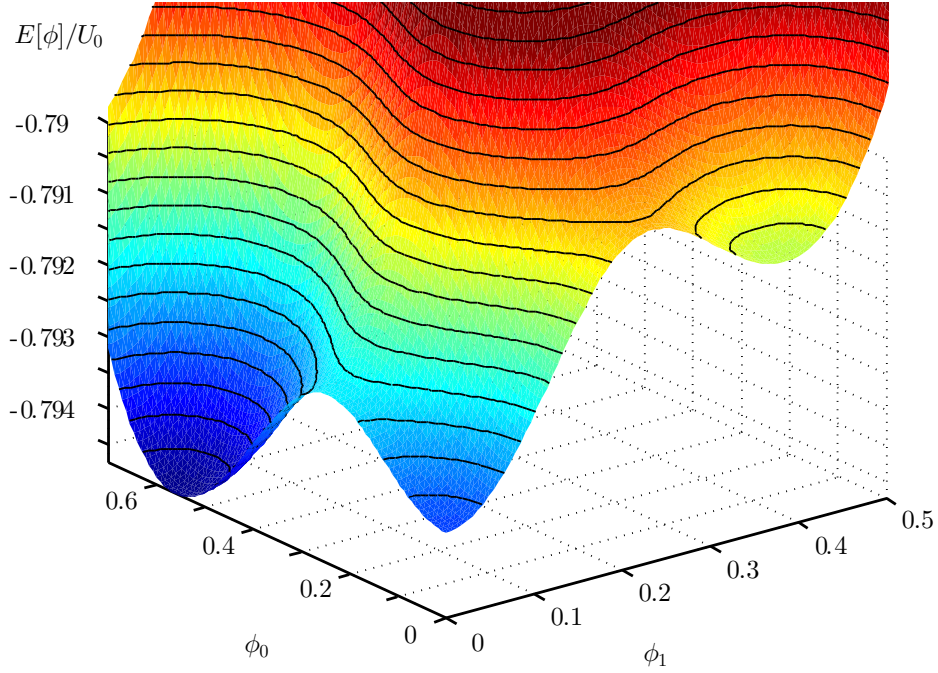
Figure 3.25: Energy functional $E[\vec{\phi}_L, \vec{\phi}_R]$ for a symmetric unit cell ($\varepsilon = 0$) and antiferromagnetic interactions $U_2/U_0 = 0.04$ in the presence of a magnetic field $q/U_0 = 0.002$. The parameters are chosen identical to Fig. 3.22 ($t_i/U_0 = 0.3$, $t_e/U_0 = 0.03$ and $\mu/U_0 = 0.25$). Because the unit cell is chosen to be symmetric the mean-field parameters of the left and the right site are equal ($\vec{\phi}_L = \vec{\phi}_R$) and the corresponding indexes are suppressed. Because of the rotational symmetry $\phi_1 = \phi_{-1}$.

notice, that even very weak magnetic fields ($q/U_0 = 0.002$ in Fig. 3.25) change the properties of the ground state energy functional substantially. In Fig. 3.26 we choose the same parameters as in Fig. 3.22 just adding a very weak magnetic field. The magnetic field causes a quantum phase transition from the superfluid phase to a Mott insulating one since the minimum at $\phi_1 = \phi_{-1} = 0$, $\phi_0 = 0.55$ is now the global one. Additionally, there are now two metastable quantum phases. The first is a metastable Mott-insulating phase at $\phi_0 = \phi_1 = \phi_{-1} = 0$. The second one is a metastable transverse polar superfluid phase at $\phi_1 = \phi_{-1} = 0.38$ and $\phi_0 = 0$.

Finally, we have also analyzed the ferromagnetic case. The presence of a magnetic field changes the energy functional of the ground state in such a way that first-order phase transitions and metastable phases are possible.
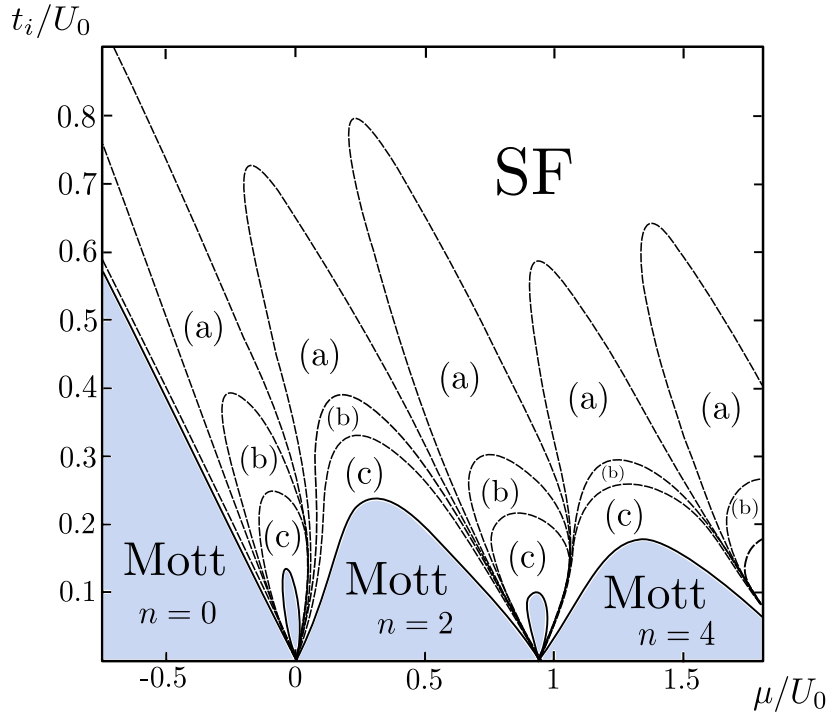
Figure 3.26: Phase diagram for spin-1 atoms in optical superlattices with a magnetic field described by the Hamiltonian (3.42) ($U_2/U_0 = 0.04$, $\varepsilon = 0$, $t_i = 10t_e$, and $q/U_0 = 0.02$). The shaded regions denote Mott-insulating phases. The dashed lines are the phase boundaries for metastable phases. There are no metastable quantum phases in the Mott-insulating region, but additional metastable phases in the superfluid one. The quantum phase (a) denotes a superfluid region where there are two metastable phases. There is a metastable superfluid phase of the transverse polar state and energetically higher a metastable Mott phase. In the quantum phase (b) there are also both metastable phases but the metastable Mott phase of the transverse polar state is energetically lower than the metastable superfluid phase. The quantum phase (c) contains only one metastable phase of the transverse polar state which is a Mott phase.

Chapter 4

Bosonic Staircases

In this chapter we examine the physics of spinless and spin-1 atoms in double-well potentials. We use a two site Bose-Hubbard model to do this. When the double-well potential is asymmetric the atom number distribution becomes asymmetric as well. Due to the finite on-site interaction the atom numbers do not change proportionally to the double well asymmetry but in steps. This step-like behavior gives rise to bosonic staircases.

For spin-1 atoms the on-site interaction and therefore the interaction blockade is spin-dependent. Thus, the system of spinor bosons in an optical superlattice becomes a model for mesoscopic magnetism; depending on the energy bias different types of magnetic order occur.

4.1 Spinless Bosons

In this section we want to review the bosonic staircases for spinless atoms. We can use a two side Bose-Hubbard model to describe ultracold, spinless bosons in a deep double-well potential,[1]

$$\hat{H} = \frac{U}{2} \sum_{i=L,R} \hat{n}_i(\hat{n}_i - 1) - t(\hat{L}^\dagger \hat{R} + \hat{R}^\dagger \hat{L}) - \varepsilon(\hat{n}_L - \hat{n}_R), \qquad (4.1)$$

where $\hat{n}_L$ ($\hat{n}_R$) is the atom number operator in the left (right) well and $\hat{L}$ ($\hat{R}$) is the particle annihilation operator in the left (right) well. The bosonic annihilation and creation operators obey the canonical commutation relations $[L, L^\dagger] = [R, R^\dagger] = 1$ and $[R, L^\dagger] = [L, R^\dagger] = 0$. The parameter U gives the strength of the on-site interaction and t the tunneling amplitude (compare Eq. (2.23)). The parameter ε incorporates the energy offset between the sites (see Fig. 4.1). The potential in Fig. 4.1 is a unit cell of the superlattice potential given in Eq. (2.10)

The Hamiltonian in Eq. (4.1) conserves the total atom number $n_L + n_R = n$ in the double-well potential. In this section we are interested in the occupancies

---

[1] [Averin *et al.*(2008)]
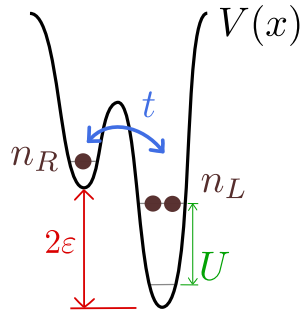
Figure 4.1:   Sketch of the parameters in the two-site Bose-Hubbard model in Eq. (4.1).   The dots depict the atoms in the double-well potential $V(x)$, ε is the energy offset between the two sides of the double well, t is the tunneling amplitude and U is the strength of the on-site interaction.

of the sites at fixed atom number n.   We calculate the Hamiltonian for a small number of bosons; we write down the Hamiltonian in the Fock basis because the terms containing the on-site interaction and the energy offset are diagonal in this basis.

As an example we study the case of five bosons in a double well. The Fock basis given by $\{n_L, n_R\} \in \{\{5,0\}, \{4,1\}, \{3,2\}, \{2,3\}, \{1,4\}, \{0,5\}\}$ and in this basis the
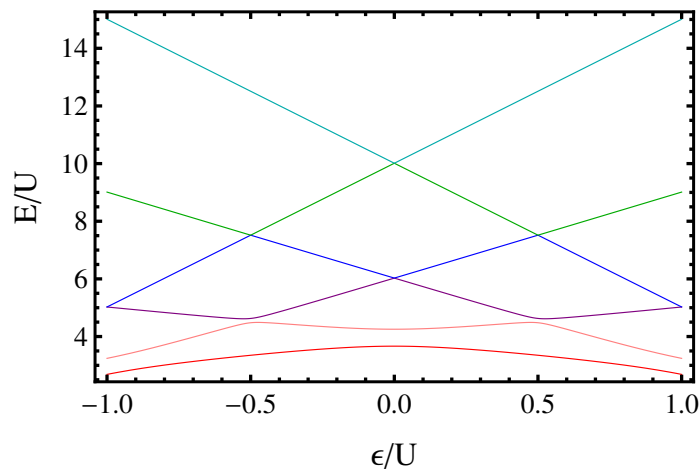
Figure 4.2:   The spectrum of 5 spinless bosons in a double well potential which are described by the Hamiltonian given in Eq. (4.2) ($t/U = 0.05$).
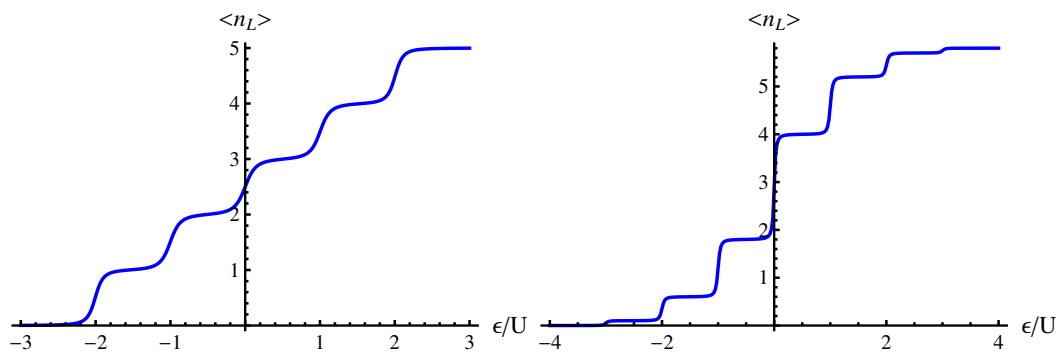
Figure 4.3: Left picture: Bosonic staircase of five bosons in an optical double-well potential ($t/U = 0.05$). Right picture: Superposition of four bosonic staircases, the bosonic staircases correspond to one, three, five and seven atoms in the double well. Such superposition are measured in experiments (compare [Cheinet *et al.*(2008)]).

Hamiltonian is given by

$$
H^{(5)} = \begin{pmatrix}
10U - 5\varepsilon & -\sqrt{5}t & 0 & 0 & 0 & 0 \\
-\sqrt{5}t & 6U - 3\varepsilon & 2 - \sqrt{2}t & 0 & 0 & 0 \\
0 & -2\sqrt{2}t & 4U - \varepsilon & -3t & 0 & 0 \\
0 & 0 & -3t & 4U + \varepsilon & -2\sqrt{2}t & 0 \\
0 & 0 & 0 & -2\sqrt{2}t & 6U + 3\varepsilon & -\sqrt{5}t \\
0 & 0 & 0 & 0 & -\sqrt{5}t & 10U + 5\varepsilon
\end{pmatrix}.
\tag{4.2}
$$

The only non-vanishing off-diagonal elements connect states with a number asymmetry of one, i.e., $|n_L - n_R| = 1$. It is fairly easy to calculate the Hamiltonian Eq. (4.2) by hand, nevertheless, we present the derivation of the Hamiltonian in Appendix B.1 with a *Mathematica* notebook to prepare ourself for the more complicated case of spinor bosons. In this *Mathematica* notebook we use algebraic tools to simplify the calculations. The spectrum of the Hamiltonian Eq. (4.2) for a range of ε is given in Fig. 4.2.

It is now easy to calculate the occupancy of one of the sites in the ground state for each parameter tuple $\{U, t, \varepsilon\}$. In the left panel of Fig. 4.3 the expectation value of the number operator of the left well is plotted. It is clearly visible that the occupancy of the left well does not change continuously but in steps. Due to the finite on-site interaction each atom has to pay a certain energy to accompany the atoms in the other site. The difference in interaction energy between one and two atoms is the same as between two and three atoms (it is always U). Thus, the steps are regular; their mutual distance is ε/U which means that atoms can only tunnel to the other site when the energy asymmetry is equal to the on-site repulsion. The single-atom staircase has been measured by Cheinet *et al.*[1] with ultra-cold ^{87}Rb atoms. In the experiments the steps are not equally spaced anymore and differ in

---

[1] [Cheinet *et al.*(2008)]

height. That is due to the fact that Cheinet *et al.* do not plot the energy off-set but the phase difference φ in Eq. (2.10) against the occupation number; furthermore, in their plots the staircases of different overall occupancies (i.e. atoms per double well) are superimposed. In the right panel of Fig. 4.3 a superposition of four staircases is plotted. The bosonic staircases correspond to one, three, five and seven atoms in the double well.

4.2 Spin-1 Atoms

Adapted from Phys. Rev. A **84**, 063636 (2011).

In this section we examine the physics of spin-1 atoms in double-well potentials. The atoms we have in mind are alkali-metal atoms, such as ^{23}Na and ^{87}Rb. When these atoms are are trapped by optical means only they keep their spin spin degree of freedom and can be used to create a spinor condensate (compare Sec. 2.5). Spin-1 bosonic atoms in a double-well potential can be described by a variant of the two-site Bose-Hubbard Hamiltonian,[1]

$$
\begin{aligned}
\hat{H}_0 &= \frac{U_0}{2} \sum_{i=L,R} \hat{n}_i(\hat{n}_i - 1) - t \sum_{\sigma} (\hat{L}_\sigma^\dagger \hat{R}_\sigma + \hat{R}_\sigma^\dagger \hat{L}_\sigma) + \varepsilon \left(n_L - n_R \right) \\
&+ \frac{U_2}{2} \sum_{i=L,R} \left(\vec{S}_i^2 - 2n_i \right),
\end{aligned}
\tag{4.3}
$$

where the operator $\hat{L}_m$ ($\hat{L}_m^\dagger$) annihilates (creates) an atom in the left site in the mth-hyperfine state (analogously $\hat{R}_m$ and $\hat{R}_m^\dagger$). The operator $n_L = \sum_\sigma L_\sigma^\dagger L_\sigma$ ($n_R = \sum_\sigma R_\sigma^\dagger R_\sigma$) is the atom number operator at the left (right) site and $\vec{S}_L = \sum_{\sigma\sigma'} L_\sigma^\dagger \vec{T}_{\sigma\sigma'} L_{\sigma'}$ is the total spin on the left site and the total spin on the right site is $\vec{S}_R = \sum_{\sigma\sigma'} R_\sigma^\dagger \vec{T}_{\sigma\sigma'} R_{\sigma'}$, where $\vec{T}_{\sigma\sigma'}$ are the usual spin-1 matrices (see Eq. (2.33)).

Two Spin-1 Bosons

Since the hopping term in Eq. (4.3) conserves the absolute value of the total spin $S_{tot} = |\vec{S}_L + \vec{S}_R|$, the Hilbert space decomposes in orthogonal subspaces which do not mix, i.e.,

$$
\mathcal{H} = \mathcal{H}(S_{tot} = 0) \oplus \mathcal{H}(S_{tot} = 1) \oplus \mathcal{H}(S_{tot} = 2).
\tag{4.4}
$$

---

[1] [Jaksch *et al.*(1998), Imambekov *et al.*(2003)]

In the case of two spin-1 bosons, the Hilbert space is seven-dimensional,

$$
\begin{aligned}
|E_1\rangle &= |\{2,0\},\{0,0\},0\rangle, & |E_2\rangle &= |\{1,1\},\{1,1\},0\rangle, \\
|E_3\rangle &= |\{0,2\},\{0,0\},0\rangle, & |E_4\rangle &= |\{1,1\},\{1,1\},1\rangle, \\
|E_5\rangle &= |\{2,0\},\{2,0\},2\rangle, & |E_6\rangle &= |\{1,1\},\{1,1\},2\rangle, \\
|E_7\rangle &= |\{0,2\},\{0,2\},2\rangle, &&
\end{aligned}
\tag{4.5}
$$

using the notation $|\{n_L, n_R\}, \{S_L, S_R\}, S_{tot}\rangle$. These basis vectors belong to three orthogonal subspaces,

$$
\mathcal{H} = \underbrace{\{E_1, E_2, E_3\}}_{S_{tot}=0} \ \oplus\ \underbrace{\{E_4\}}_{S_{tot}=1} \ \oplus\ \underbrace{\{E_5, E_6, E_7\}}_{S_{tot}=2} .
$$

To examine the ground-state properties of this system, the Hamiltonian needs to be calculated and diagonalized for each subspace separately. To calculate the off-diagonal elements of the Hamiltonian, it is necessary to write the elements of the whole system as product of the single-well wave functions, e.g.,

$$
|\{2,0\},\{2,0\},2\rangle = |n_L = 2, S_L = 2, S_{1_z} = 0\rangle \otimes |n_R = 0, S_R = 0, S_{2_z} = 0\rangle ,
$$

and

$$
\begin{aligned}
|\{1,1\},\{1,1\},2\rangle &= \sum_{m=-1,0,1} C^{(2,0)}_{(1,m),(1,-m)} |1,1,m\rangle \otimes |1,1,-m\rangle \\
&= \frac{1}{\sqrt{6}} (|1,1,1\rangle \otimes |1,1,-1\rangle + 2|1,1,0\rangle \otimes |1,1,0\rangle \\
&\quad + |1,1,-1\rangle \otimes |1,1,1\rangle) ,
\end{aligned}
$$

where we have chosen the $S_z = 0$ component for convenience, because the energy does not depend on the S_z component. The single-well wavefunctions need to be written in terms of single-particle creation operators. For two spin-1 bosons this can be done using the standard Clebsch-Gordan coefficients. The individual blocks of the Hamiltonian Eq. (4.4) are given by

$$
\mathcal{H}(S_{tot} = 0) = \begin{pmatrix} 2\varepsilon - 2U_2 + U_0 & -\sqrt{2}t & 0 \\ -\sqrt{2}t & 0 & -\sqrt{2}t \\ 0 & -\sqrt{2}t & -2\varepsilon - 2U_2 + U_0 \end{pmatrix}
$$

$$
\mathcal{H}(S_{tot} = 1) = (0)
$$

$$
\mathcal{H}(S_{tot} = 2) = \begin{pmatrix} 2\varepsilon + U_2 + U_0 & -\sqrt{2}t & 0 \\ -\sqrt{2}t & 0 & -\sqrt{2}t \\ 0 & -\sqrt{2}t & -2\varepsilon + U_2 + U_0 \end{pmatrix} .
$$

Three Spin-1 Bosons

The Hilbert space for three spin-1 bosons is given by the direct sum of the following subspaces:

$$\mathcal{H} = \underbrace{\{E_1, E_2, E_3, E_4, E_5, E_6\}}_{S_{tot}=1} \oplus \underbrace{\{E_7, E_8\}}_{S_{tot}=2} \oplus \underbrace{\{E_9, E_{10}, E_{11}, E_{12}\}}_{S_{tot}=3}.$$

The subspace $\{E_1, E_2, E_3, E_4, E_5, E_6\}$ belongs to $|\vec{S}_L+\vec{S}_R| = 1$, the subspace $\{E_7, E_8\}$ belongs to $|\vec{S}_L+\vec{S}_R| = 2$ and he subspace $\{E_9, E_{10}, E_{11}, E_{12}\}$ belongs to $|\vec{S}_L+\vec{S}_R| = 3$. The basis vectors are given by

$$
\begin{aligned}
|E_1\rangle &= |\{3,0\},\{1,0\},1\rangle, & |E_2\rangle &= |\{2,1\},\{2,1\},1\rangle, \\
|E_3\rangle &= |\{2,1\},\{0,1\},1\rangle, & |E_4\rangle &= |\{1,2\},\{1,2\},1\rangle, \\
|E_5\rangle &= |\{1,2\},\{1,0\},1\rangle, & |E_6\rangle &= |\{0,3\},\{0,1\},1\rangle,
\end{aligned}
$$

$$
\begin{aligned}
|E_7\rangle &= |\{2,1\},\{2,1\},2\rangle, & |E_8\rangle &= |\{1,2\},\{1,2\},2\rangle,
\end{aligned}
$$

$$
\begin{aligned}
|E_9\rangle &= |\{3,0\},\{3,0\},3\rangle, & |E_{10}\rangle &= |\{2,1\},\{2,1\},3\rangle, \\
|E_{11}\rangle &= |\{1,2\},\{1,2\},3\rangle, & |E_{12}\rangle &= |\{0,3\},\{0,3\},3\rangle,
\end{aligned}
$$

again using the notation $|\{n_L, n_R\}, \{S_L, S_R\}, S_{tot}\rangle$.

The Hamiltonian is block diagonal in the basis given above as in the case of two bosons. The Hamiltonians belonging to $|\vec{S}_L + \vec{S}_R| = 2$ and $|\vec{S}_L + \vec{S}_R| = 3$ are quite similar to the spinless case and the case of two spin-1 atoms. To calculate the off-diagonal elements of the Hamiltonian we need to know how three spin-1 bosons couple to a total spin $\vec{S}$ with a z-projection S_z. In order to calculate this we need to diagonalize the S^2. In Appendix B.2 we have done that and the result is shown in Table 4.1.

The Hamiltonian belonging to $|\vec{S}_L + \vec{S}_R|=2$ is given by

$$\hat{H}(S_{tot} = 2) = \begin{pmatrix} U_0 + \varepsilon + U_2 & -t \\ -t & U_0 - \varepsilon + U_2 \end{pmatrix},$$

and the Hamiltonian belonging to $|\vec{S}_L + \vec{S}_R|=3$ is given by

$$\hat{H}(S_{tot} = 3) = \begin{pmatrix} 3U_0 + 3\varepsilon + 3U_2 & -\sqrt{3}t & 0 & 0 \\ -\sqrt{3}t & U_0 + \varepsilon + U_2 & -2t & 0 \\ 0 & -2t & U_0 - \varepsilon + U_2 & -\sqrt{3}t \\ 0 & 0 & -\sqrt{3}t & 3U_0 - 3\varepsilon + 3U_2 \end{pmatrix}.$$

The Hamiltonian belonging to the Hilbert space $|\vec{S}_L + \vec{S}_R| = 1$ exhibits a richer structure and differs from the spinless case. This is because the term $-t \sum_\sigma (L_\sigma^\dagger R_\sigma +$

S	S_z	state
3	3	$\lvert 0_{-1}, 0_0, 3_1 \rangle$
3	2	$\lvert 0_{-1}, 1_0, 2_1 \rangle$
3	1	$\frac{1}{\sqrt{5}}(2 \lvert 0_{-1}, 2_0, 1_1 \rangle + \lvert 1_{-1}, 0_0, 2_1 \rangle)$
3	0	$\sqrt{\frac{2}{5}} \lvert 0_{-1}, 3_0, 0_1 \rangle + \sqrt{\frac{3}{5}} \lvert 1_{-1}, 1_0, 1_1 \rangle$
3	-1	$\frac{1}{\sqrt{5}}(2 \lvert 1_{-1}, 2_0, 0_1 \rangle + \lvert 2_{-1}, 0_0, 1_{\hat{1}} \rangle)$
3	-2	$\lvert 2_{-1}, 1_0, 0_1 \rangle$
3	-3	$\lvert 3_{-1}, 0_0, 0_1 \rangle$
1	1	$\frac{1}{\sqrt{5}}(- \lvert 0_{-1}, 2_0, 1_1 \rangle + 2 \lvert 1_{-1}, 0_0, 2_1 \rangle)$
1	0	$-\sqrt{\frac{3}{5}} \lvert 0_{-1}, 3_0, 0_1 \rangle + \sqrt{\frac{2}{5}} \lvert 1_{-1}, 1_0, 1_1 \rangle$
1	-1	$\frac{1}{\sqrt{5}}(- \lvert 1_{-1}, 2_0, 0_1 \rangle + 2 \lvert 2_{-1}, 0_0, 1_1 \rangle)$

Table 4.1: Coupling of three spin-1 particles to the total spin S with the z-projection S_z. The ket-vectors on the right are written in the basis $\lvert n_1, n_0, n_{-1} \rangle$, where n_σ denotes the number of atoms in the hyperfine state $\sigma \in \{1, 0, -1\}$.

$R_\sigma^\dagger L_\sigma$) describes tunneling between several basis vectors, e.g., between $\lvert E_1 \rangle$ and $\lvert E_2 \rangle$ as well as between $\lvert E_1 \rangle$ and $\lvert E_3 \rangle$. Because the energy does not depend on the S_z projection, we can set $S_z = 0$. The basis vector $\lvert E_1 \rangle$ is given by

$$\lvert \{3, 0\}, \{1, 0\}, 1 \rangle = \lvert 3, 1, 0 \rangle \otimes \lvert 0, 0, 0 \rangle = \left[\sqrt{\frac{2}{5}} \hat{L}_{-1}^\dagger \hat{L}_0^\dagger \hat{L}_1^\dagger - \sqrt{\frac{1}{10}} \left(\hat{L}_0^\dagger \right)^3 \right] \lvert 0 \rangle,$$

and the basis vector $\lvert E_2 \rangle$ is given by

$$\begin{aligned}
\lvert \{2, 1\}, \{2, 1\}, 1 \rangle &= \sum_{m=-2,\ldots,2} \sum_{n=-1,0,1} C^{(1,0)}_{(1,m),(1,n)} \lvert 2, 2, m \rangle \otimes \lvert 1, 1, n \rangle \\
&= \sqrt{\frac{3}{10}} \lvert 2, 1, -1 \rangle \otimes \lvert 1, 1, 1 \rangle - \sqrt{\frac{4}{10}} \lvert 2, 1, 0 \rangle \otimes \lvert 1, 1, 0 \rangle \\
&\quad + \sqrt{\frac{3}{10}} \lvert 2, 1, 1 \rangle \otimes \lvert 1, 1, -1 \rangle \\
&= \left[-\sqrt{\frac{2}{15}} \left(\hat{L}_0^\dagger \right)^2 \hat{R}_0^\dagger + \sqrt{\frac{3}{10}} \hat{L}_1^\dagger \hat{L}_0^\dagger \hat{R}_{-1}^\dagger \right. \\
&\quad \left. + \sqrt{\frac{3}{10}} \hat{L}_{-1}^\dagger \hat{L}_0^\dagger \hat{R}_1^\dagger - \sqrt{\frac{2}{15}} \hat{L}_{-1}^\dagger \hat{L}_1^\dagger \hat{R}_0^\dagger \right] \lvert 0 \rangle.
\end{aligned}$$

Now, we can calculate the corresponding non-diagonal element of the Hamiltonian,

$$\langle E_1 \rvert H \lvert E_2 \rangle = -t \langle E_1 \rvert \sum_\sigma (\hat{L}_\sigma^\dagger \hat{R}_\sigma + \hat{R}_\sigma^\dagger \hat{L}_\sigma) \lvert E_2 \rangle = -\sqrt{\frac{5}{3}} \, t \, .$$

The basis vector $|E_3\rangle$ is given by

$$|\{2,1\},\{0,1\},1\rangle = |2,0,0\rangle \otimes |1,1,0\rangle = \left[\sqrt{\frac{2}{3}}\hat{L}^\dagger_{-1}\hat{L}^\dagger_1\hat{R}^\dagger_0 - \frac{1}{\sqrt{6}}\left(\hat{L}^\dagger_0\right)^2\hat{R}^\dagger_0\right]|0\rangle,$$

and the corresponding non-diagonal element of the Hamiltonian is

$$\langle E_1|H|E_3\rangle = -\sqrt{\frac{4}{3}}\,t.$$

Note that the off-diagonal elements of the Hamiltonian depend on the spin configurations, also, the off-diagonal elements do not depend on the strength of the spin-dependent interactions U_2. Similar calculations lead to the remaining off-diagonal elements. The Hamiltonian belonging to $|\vec{S}_L + \vec{S}_R|=1$ is given by

$$\hat{H}(S_{tot}=1) = \begin{pmatrix} 3U_0+3\epsilon-2U_2 & -\frac{2t}{\sqrt{3}} & -\sqrt{\frac{5}{3}}t & 0 & 0 & 0 \\ -\frac{2t}{\sqrt{3}} & U_0+\epsilon+U_2 & 0 & -\frac{t}{3} & -\frac{2\sqrt{5}t}{3} & 0 \\ -\sqrt{\frac{5}{3}}t & 0 & U_0+\epsilon-2U_2 & -\frac{2\sqrt{5}t}{3} & -\frac{2t}{3} & 0 \\ 0 & -\frac{t}{3} & -\frac{2\sqrt{5}t}{3} & U_0-\epsilon+U_2 & 0 & -\frac{2t}{\sqrt{3}} \\ 0 & -\frac{2\sqrt{5}t}{3} & -\frac{2t}{3} & 0 & U_0-\epsilon-2U_2 & -\sqrt{\frac{5}{3}}t \\ 0 & 0 & 0 & -\frac{2t}{\sqrt{3}} & -\sqrt{\frac{5}{3}}t & 3U_0-3\epsilon-2U_2 \end{pmatrix}.$$

Four Spin-1 Bosons

Due to the conservation of the total spin the Hilbert space decomposes into the following sum,

$$\mathcal{H} = \mathcal{H}(S_{tot}=0) \oplus \mathcal{H}(S_{tot}=1) \oplus \mathcal{H}(S_{tot}=2) \oplus \mathcal{H}(S_{tot}=3) \oplus \mathcal{H}(S_{tot}=4). \quad (4.6)$$

The basis for four bosons is given by

$$
\begin{aligned}
E_1 &= |\{4,0\},\{0,0\},0\}\rangle, & E_2 &= |\{3,1\},\{1,1\},0\}\rangle, \\
E_3 &= |\{2,2\},\{2,2\},0\}\rangle, & E_4 &= |\{2,2\},\{0,0\},0\}\rangle, \\
E_5 &= |\{1,3\},\{1,1\},0\}\rangle, & E_6 &= |\{0,4\},\{0,0\},0\}\rangle,
\end{aligned}
$$

$$
\begin{aligned}
E_7 &= |\{3,1\},\{1,1\},1\}\rangle, & E_8 &= |\{2,2\},\{2,2\},1\}\rangle, \\
E_9 &= |\{1,3\},\{1,1\},1\}\rangle,
\end{aligned}
$$

$$
\begin{aligned}
E_{10} &= |\{4,0\},\{2,0\},2\}\rangle, & E_{11} &= |\{3,1\},\{3,1\},2\}\rangle, \\
E_{12} &= |\{3,1\},\{1,1\},2\}\rangle, & E_{13} &= |\{2,2\},\{2,2\},2\}\rangle, \\
E_{14} &= |\{2,2\},\{2,0\},2\}\rangle, & E_{15} &= |\{2,2\},\{0,2\},2\}\rangle, \\
E_{16} &= |\{1,3\},\{1,3\},2\}\rangle, & E_{17} &= |\{1,3\},\{1,1\},2\}\rangle, \\
E_{18} &= |\{0,4\},\{0,2\},2\}\rangle,
\end{aligned}
$$

$$
\begin{aligned}
E_{19} &= |\{3,1\},\{3,1\},3\}\rangle, & E_{20} &= |\{2,2\},\{2,2\},3\}\rangle, \\
E_{21} &= |\{1,3\},\{1,3\},3\}\rangle,
\end{aligned}
$$

$$
\begin{aligned}
E_{22} &= |\{4,0\},\{4,0\},4\}\rangle, & E_{23} &= |\{3,1\},\{3,1\},4\}\rangle, \\
E_{24} &= |\{2,2\},\{2,2\},4\}\rangle, & E_{25} &= |\{1,3\},\{1,3\},4\}\rangle, \\
E_{26} &= |\{0,4\},\{0,4\},4\}\rangle .
\end{aligned}
\tag{4.7}
$$

The coupling of four spin-1 particles is given in Table 4.2. We can now calculate the Hamilton operator in this basis. The block belonging to basis vectors with $S_{tot} = 0$ is given by

$$
\begin{pmatrix}
4\varepsilon-4U_2+6U_0 & -2t & 0 & 0 & 0 & 0 \\
-2t & 2\varepsilon-2U_2+3U_0 & -2\sqrt{\frac{2}{3}}t & -\sqrt{\frac{10}{3}}t & 0 & 0 \\
0 & -2\sqrt{\frac{2}{3}}t & 2U_2+2U_0 & 0 & -2\sqrt{\frac{2}{3}}t & 0 \\
0 & -\sqrt{\frac{10}{3}}t & 0 & -4U_2+2U_0 & -\sqrt{\frac{10}{3}}t & 0 \\
0 & 0 & -2\sqrt{\frac{2}{3}}t & -\sqrt{\frac{10}{3}}t & -2\varepsilon-2U_2+3U_0 & -2t \\
0 & 0 & 0 & 0 & -2t & -4\varepsilon-4U_2+6U_0
\end{pmatrix} .
\tag{4.8}
$$

The block belonging to $S_{tot} = 1$ is

$$
\begin{pmatrix}
2\varepsilon - 2U_2 + 3U_0 & -\sqrt{2}t & 0 \\
-\sqrt{2}t & 2U_2 + 2U_0 & -\sqrt{2}t \\
0 & -\sqrt{2}t & -2\varepsilon - 2U_2 + 3U_0
\end{pmatrix} .
\tag{4.9}
$$

S	S_z	state
4	4	$\lvert 0_{-1}, 0_0, 4_1 \rangle$
4	3	$\lvert 0_{-1}, 1_0, 3_1 \rangle$
4	2	$\dfrac{\sqrt{6}\lvert 0_{-1},2_0,2_1 \rangle + \lvert 1_{-1},0_0,3_1 \rangle}{\sqrt{7}}$
4	1	$\dfrac{\sqrt{3}\lvert 1_{-1},1_0,2_1 \rangle + 2\lvert 0_{-1},3_0,1_1 \rangle}{\sqrt{7}}$
4	0	$\dfrac{2\sqrt{2}\left(\lvert 0_{-1},4_0,0_1 \rangle + \sqrt{3}\lvert 1_{-1},2_0,1_1 \rangle\right) + \sqrt{3}\lvert 2_{-1},0_0,2_1 \rangle}{\sqrt{35}}$
4	-1	$\dfrac{\sqrt{3}\lvert 2_{-1},1_0,1_1 \rangle + 2\lvert 1_{-1},3_0,0_1 \rangle}{\sqrt{7}}$
4	-2	$\dfrac{\sqrt{6}\lvert 2_{-1},2_0,0_1 \rangle + \lvert 3_{-1},0_0,1_1 \rangle}{\sqrt{7}}$
4	-3	$\lvert 3_{-1}, 1_0, 0_1 \rangle$
4	-4	$\lvert 4_{-1}, 0_0, 0_1 \rangle$
2	2	$\dfrac{\sqrt{6}\lvert 0_0,3_1,1_{-1} \rangle - \lvert 2_0,2_1,0_{-1} \rangle}{\sqrt{7}}$
2	1	$\dfrac{2\lvert 1_0,2_1,1_{-1} \rangle - \sqrt{3}\lvert 3_0,1_1,0_{-1} \rangle}{\sqrt{7}}$
2	0	$\dfrac{2\sqrt{6}\lvert 0_0,2_1,2_{-1} \rangle + \sqrt{3}\lvert 2_0,1_1,1_{-1} \rangle - 6\lvert 4_0,0_1,0_{-1} \rangle}{3\sqrt{7}}$
2	-1	$\dfrac{2\lvert 1_0,1_1,2_{-1} \rangle - \sqrt{3}\lvert 3_0,0_1,1_{-1} \rangle}{\sqrt{7}}$
2	-2	$\dfrac{\sqrt{6}\lvert 0_0,1_1,3_{-1} \rangle - \lvert 2_0,0_1,2_{-1} \rangle}{\sqrt{7}}$
0	0	$\dfrac{2\sqrt{6}\lvert 0_0,2_1,2_{-1} \rangle - 2\sqrt{3}\lvert 2_0,1_1,1_{-1} \rangle + 3\lvert 4_0,0_1,0_{-1} \rangle}{3\sqrt{5}}$

Table 4.2: Coupling of four spin-1 particles to the total spin S with the z-projection S_z. The ket-vectors on the right are written in the basis $\lvert n_1, n_0, n_{-1} \rangle$, where n_σ denotes the number of atoms in the hyperfine state $\sigma \in \{1, 0, -1\}$.

The block corresponding to the 9 basis vectors with $S_{tot} = 2$ is given by

$$
\begin{pmatrix}
4\varepsilon-U_2+6U_0 & -\sqrt{\frac{6}{5}}t & -\sqrt{\frac{14}{5}}t & 0 & 0 & 0 & 0 & 0 & 0 \\
-\sqrt{\frac{6}{5}}t & 2\varepsilon+3U_2+3U_0 & 0 & -\sqrt{\frac{2}{5}}t & -\sqrt{\frac{14}{5}}t & 0 & 0 & 0 & 0 \\
-\sqrt{\frac{14}{5}}t & 0 & 2\varepsilon-2U_2+3U_0 & -\sqrt{\frac{14}{15}}t & -2\sqrt{\frac{2}{15}}t & -\sqrt{\frac{10}{3}}t & 0 & 0 & 0 \\
0 & -\sqrt{\frac{2}{5}}t & -\sqrt{\frac{14}{15}}t & 2U_2+2U_0 & 0 & 0 & -\sqrt{\frac{2}{5}}t & -\sqrt{\frac{14}{15}}t & 0 \\
0 & -\sqrt{\frac{14}{5}}t & -2\sqrt{\frac{2}{15}}t & 0 & -U_2+2U_0 & 0 & 0 & -\sqrt{\frac{10}{3}}t & 0 \\
0 & 0 & -\sqrt{\frac{10}{3}}t & 0 & 0 & -U_2+2U_0 & -\sqrt{\frac{14}{5}}t & -2\sqrt{\frac{2}{15}}t & 0 \\
0 & 0 & 0 & -\sqrt{\frac{2}{5}}t & 0 & -\sqrt{\frac{14}{5}}t & -2\varepsilon+3U_2+3U_0 & 0 & -\sqrt{\frac{6}{5}}t \\
0 & 0 & 0 & -\sqrt{\frac{14}{15}}t & -\sqrt{\frac{10}{3}}t & -2\sqrt{\frac{2}{15}}t & 0 & -2\varepsilon-2U_2+3U_0 & -\sqrt{\frac{14}{5}}t \\
0 & 0 & 0 & 0 & 0 & 0 & -\sqrt{\frac{6}{5}}t & -\sqrt{\frac{14}{5}}t & -4\varepsilon-U_2+6U_0
\end{pmatrix}
$$

$$(4.10)$$

The part of the Hamiltonian corresponding to $S_{tot} = 3$ is

$$
\begin{pmatrix}
2\varepsilon + 3U_2 + 3U_0 & -\sqrt{2}t & 0 \\
-\sqrt{2}t & 2U_2 + 2U_0 & -\sqrt{2}t \\
0 & -\sqrt{2}t & -2\varepsilon + 3U_2 + 3U_0
\end{pmatrix}
\qquad (4.11)
$$
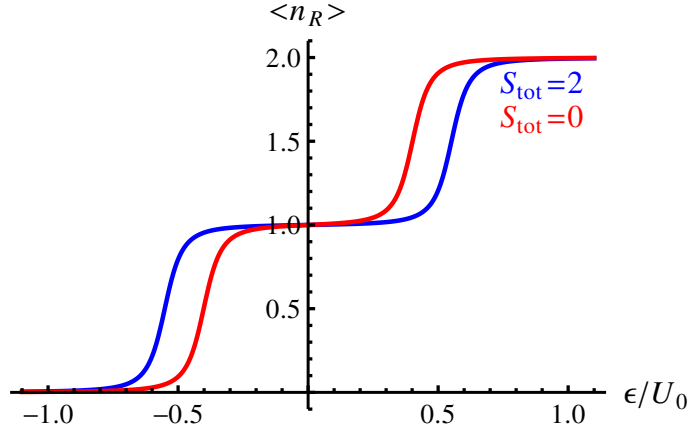
Figure 4.4: Two spin-1 bosons with antiferromagnetic ordering in a double-well potential. Here n_R is the occupation number of the right well, and ϵ characterizes the energy offset between the two wells ($t/U_0 = 0.05$ and $U_2/U_0 = 0.1$). Depending on the total spin of the system, bosonic staircase transitions occur at different bias voltages ε. Note that both the states with $S_{tot} = 0$ and $S_{tot} = 2$ have symmetric orbital wavefunctions. The difference in the occupation numbers arises due to spin-dependent interactions and not due to a different orbital symmetry of the states. Thus, a measurement of the spin-dependent bosonic staircases provides a demonstration of mesoscopic magnetism.

and the last block belonging to to $S_{tot} = 4$ is

$$
\begin{pmatrix}
4\varepsilon+6U_2+6U_0 & -2t & 0 & 0 & 0 \\
-2t & 2\varepsilon+3U_2+3U_0 & -\sqrt{6}t & 0 & 0 \\
0 & -\sqrt{6}t & 2U_2+2U_0 & -\sqrt{6}t & 0 \\
0 & 0 & -\sqrt{6}t & -2\varepsilon+3U_2+3U_0 & -2t \\
0 & 0 & 0 & -2t & -4\varepsilon+6U_2+6U_0
\end{pmatrix} . \tag{4.12}
$$

4.3 Bosonic Staircases for Spinor Atoms

In this section we present the bosonic staircases for spin-1 atoms. The Hilbert space decomposes into different subspaces according to the total spin of the system. Different subspaces are not mixed by ramping up the energy difference between the double wells and behave in a different way. In the case of two bosons this is shown in Fig. 4.4. The different widths of the steps centered at $\epsilon = 0$ corresponds to different values of total spins per site. At $\epsilon = 0.5$, the state $|\{1,1\},\{1,1\},2\rangle$ is energetically lower than the state $|\{0,2\},\{0,2\},2\rangle$, which makes the step broader for $S_{tot} = 2$. On the contrary, at $\epsilon = 0.5$ the state $|\{1,1\},\{1,1\},0\rangle$ is energetically higher than the state $|\{0,2\},\{0,0\},0\rangle$, which makes the step narrower for $S_{tot} = 0$.

This is a specific example of how this mesoscopic magnetism can be observed in experiments. If the total spin is $S_{tot} = 2$, the spins of the two atoms are parallel
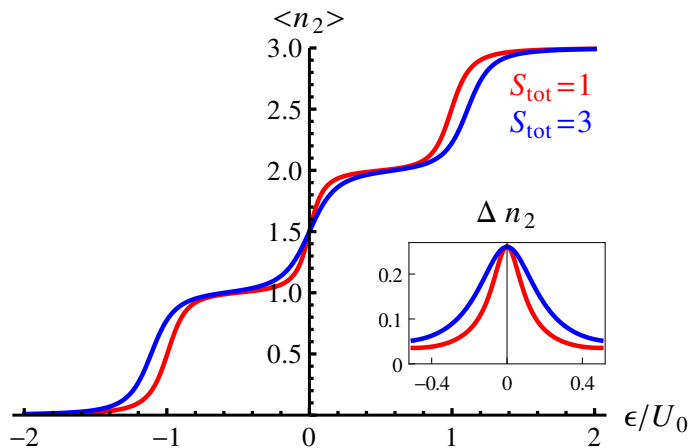
Figure 4.5: Bosonic staircase for three spin-1 bosons with antiferromagnetic ordering in a double-well potential ($t/U_0 = 0.05$ and $U_2/U_0 = 0.1$). Inset: Variance of the particle number in the left well for the step around $\epsilon = 0$.

and for antiferromagnetic interactions, as in the case of ^{23}Na, being in the same well costs extra energy. Therefore the $S_{tot} = 2$ configuration switches later (i.e. at larger energy offset) to the state with both atoms in the same well. The bosonic staircases of spinless atoms are evenly spaced (see Sec. 4.1) because the difference the in interaction energy between one and two atoms is the same as between two and three atoms (it is always U). This is not the case for spin-1 atoms, and that is the reason why the steps are not regular anymore.

In general, depending on the sign of U_2, states with high single-well angular momenta get penalized or favored. If $U_2 > 0$ (like e.g. for ^{23}Na) nonzero spin configurations get penalized. In the case of ^{87}Rb, U_2 is negative and spin-dependent interactions lead to the opposite effect: high-spin configurations are favored and the corresponding steps are broader. Therefore, in the ferromagnetic case, the curves for $S_{tot} = 0$ and S_{tot} in Fig. 4.4 will be exchanged.

The exact position of the steps can be calculated in the "atomic limit", i.e. $t = 0$. The step positions depend generally linearly on U_2. For some spin configurations, e.g. odd atom number, lowest possible total spin, and antiferromagnetic interactions, the step positions do not depend on spin-dependent interactions.

For higher boson numbers, the richer structure of the off-diagonal elements means that the variance of the particle number depends on the total spin and the energy offset. In the case of three bosons (Fig. 4.5) the step at $\epsilon = 0$ is not shifted due to symmetry reasons, whereas the steps at $\epsilon = 1$ and $\epsilon = -1$ are shifted linearly. In the same time the steps belonging to $S_{tot} = 3$ are not as sharp as the steps belonging to $S_{tot} = 1$, i.e. the curve of the variance of n_L is broader in the case of $S_{tot} = 3$.

The staircases for different total spins may be used to arrange spin-1 atoms in a two-dimensional superlattice according to their spin degrees of freedom (see Fig. 4.6).
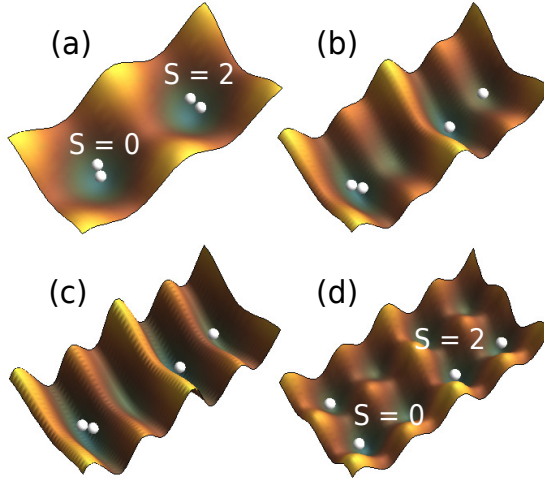
Figure 4.6: A possible way to separate the $S_{tot} = 2$ spin component from the $S_{tot} = 0$ spin component in the case of antiferromagnetic interactions between the atoms: the potentials in x- and y-direction are manipulated separately. In a first step (b), the energy offset between the double wells is lifted until the bosons combining to the total spin $S_{tot} = 0$ separate while the bosons belonging to $S_{tot} = 2$ still remain in the same site. (c) Next, the wells are separated by a large potential barrier and tunneling is suppressed. (d) An additional laser is switched on and the bosons coupling to $S_{tot} = 2$ distribute in the resulting double well. The switching is assumed to happen adiabatically such that the system can be regarded to be in the ground state at every instant.

4.4 Beyond Ground-State Analysis

The gap between the ground state and the first excited state in the energy spectrum depends strongly on the tunneling between the sites (see Fig. 4.7). For finite temperatures the density matrix describing the system is thus highly mixed for small tunneling parameters, and the ground-state behavior only dominates if tunneling is sufficiently strong.

Nonetheless, the bosonic staircases survive for small temperatures, but the spin-dependent effects are not robust. In Fig. 4.8 we include non-zero temperature bosonic staircases for two bosons with antiferromagnetic interactions ($U_2/U_0 = 0.1$) and small tunneling amplitudes ($t/U_0 = 0.05$). The thermal density matrix describing these states is given by

$$\rho(T) = \frac{1}{Z} \sum_i g_i \; e^{-\frac{E_i}{k_B T}} |\psi_i\rangle\langle\psi_i| \,,$$

where Z is the partition function and g_i denotes the degeneracy of the state $|\psi_i\rangle$.
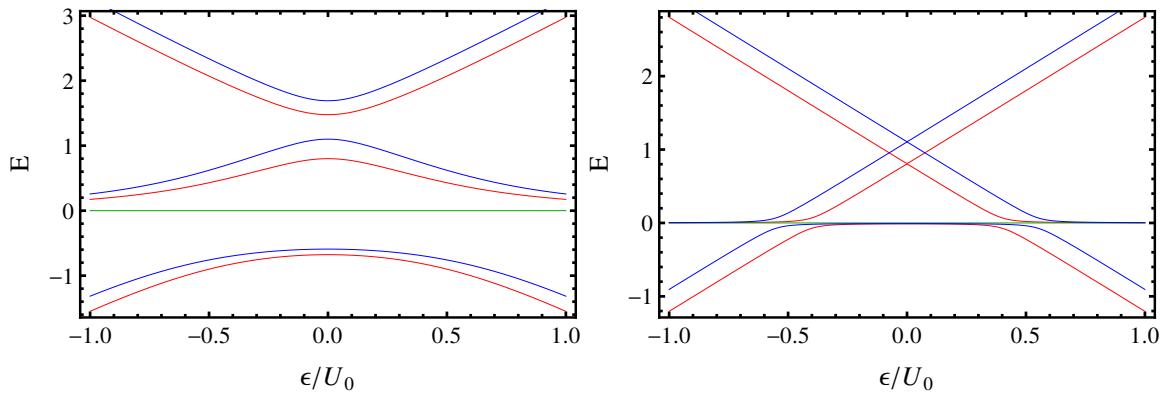
Figure 4.7: Left panel: Energy spectrum of two spin-1 bosons in a double well with strong tunneling ($t/U_0 = 0.5$ and $U_2/U_0 = 0.1$). The red energy levels belong to the $S_{tot} = 0$ subspace, the blue to $S_{tot} = 2$ and the green to $S_{tot} = 1$. Right panel: Energy spectrum of two spin-1 bosons in a double well with weak tunneling ($t/U_0 = 0.05$ and $U_2/U_0 = 0.1$).
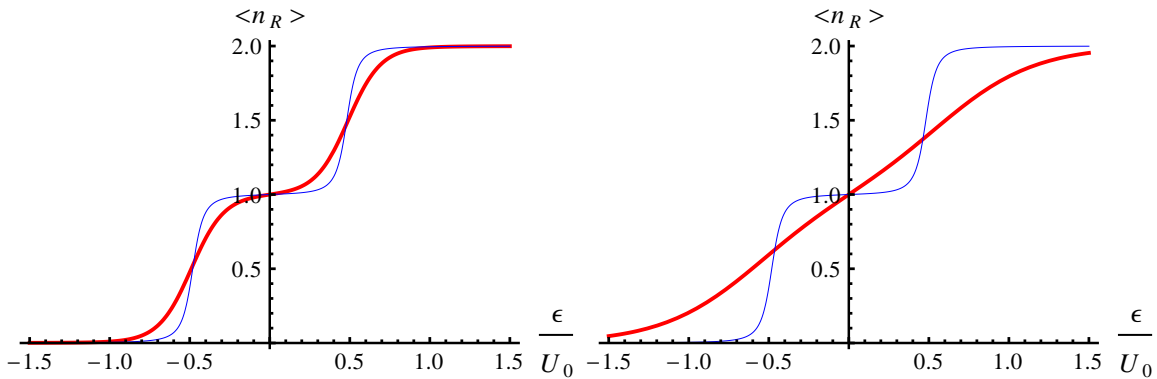
Figure 4.8: Bosonic staircases for non-zero temperatures. The thick red line denotes the expectation value of $\hat{n}_R$ at $k_BT = 0.2U_0$ (left panel) and $k_BT = 0.6U_0$ (right panel). The energies are measured in units of U_0. The thin blue line denotes the ground-state expectation value; $t/U_0 = 0.05$ and $U_2/U_0 = 0.1$ for both plots.

4.5 Effects of Magnetic Fields

The effect of a magnetic field can be included in the model (4.3) by adding a term to the Hamiltonian which describes the coupling of the spins to the magnetic field.[1] The first contribution of a magnetic field $\vec{B} = (0, 0, B)$ is a regular Zeeman shift of the energy levels:

$$H = H_0 + p \sum_{i=L,R} \sum_\sigma m_{i\sigma} \hat{n}_{i\sigma} = H_0 + p \, S_z^{tot}$$

where $p = g\mu_B B$ and $\hat{n}_{i\sigma}$ is the particle number operator for the ith site which gives the number of bosons in the mth hyperfine state. The linear Zeeman shift changes the overall state considerably. The energy eigenvalues belonging to $S_{tot} \neq 0$ split into multiplets because the hyperfine levels are no longer degenerate (see Fig. 4.9). Note that in contrast to the spectra given in Fig. 4.7 there are level crossings in the ground state in Fig. 4.9. The magnetic field couples to a conserved quantity, the magnetization S_z^{tot}, and this leads to an non-analytic behavior of the ground state properties at certain values of the energy offset.

For a given tunneling strength there is a critical magnetic field strength which leads to ground-state level crossings. Such level crossings correspond to spin-flip transitions, i.e. the ground-state energy is continuous, but the expectation values of the particle number and of the magnetization are not. This means that the overall ground state of the system does not belong to the same z-projection of the total spin for all values of the energy offset ϵ. Figure 4.10 shows the critical value of the magnetic field in the case of two bosons.
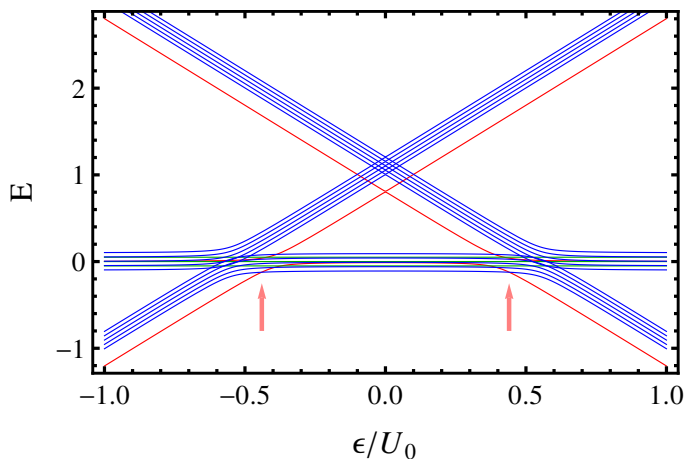
Figure 4.9: Linear Zeeman shift of the energy levels in the energy spectrum of two spin-1 bosons ($B/U_0 = 0.05$, $t/U_0 = 0.05$ and $U_2/U_0 = 0.1$). The energy levels of Fig. 4.7 split into spin multiplets. The red arrows denote ground state level crossings. Color code as in Fig. 4.7.

---

[1] [Svidzinsky and Chui(2003),Imambekov *et al.*(2004)]
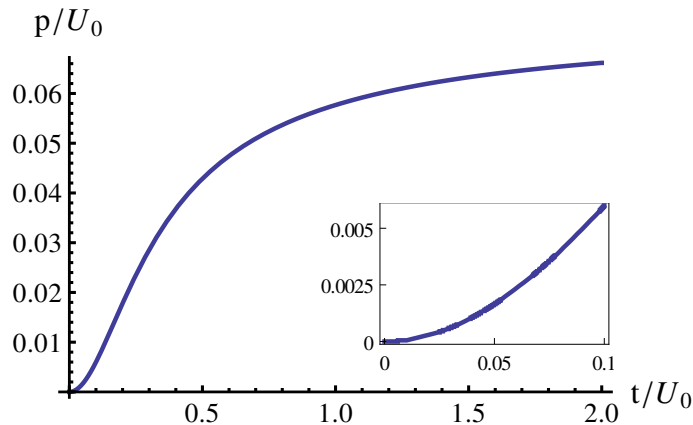
Figure 4.10: Critical magnetic field $p = g\mu_B B$ above which the staircase for two bosons shows a discontinuous behavior signifying spin-flip transitions ($U_2/U_0 = 0.1$).

However, spin non-conserving collisions are negligible over the lifetime of the condensate, and the total magnetization is a conserved quantity on the time scale of the experiment.[1] For a given magnetization the properties of the system are not altered by the linear Zeeman effect, the whole spectrum is merely shifted. Only if one is interested in comparing different magnetizations, the linear Zeeman effect has to be taken into account. In a series of experiments with a given magnetization, it is therefore necessary to include higher-order contributions in the magnetic field. The quadratic Zeeman effect arises because the hyperfine spins characterizing ultracold atoms are mixtures of electron and nuclear spins. Since the magnetic field couples approximately only to the electron spin, the Zeeman effect is nonlinear in the field but can typically be described by a sum of linear and quadratic terms.

For each of the subspaces belonging to different magnetizations S_z^{tot} there is a separate effective Hamiltonian

$$H_q = H_0 + q \sum_{i=L,R} \sum_{\sigma} m_{i\sigma}^2 \hat{n}_{i\sigma} . \qquad (4.13)$$

The magnitude of the quadratic Zeeman shift is given by $q = q_0 B^2$, where e.g. $q_0 = h \times 390$ Hz/G^2 for sodium.[2]

In the case of two bosons the system with magnetization $S_z^{tot} = 0$ possesses the most interesting structure, because the Hilbert space is composed of states with different total spin. For $S_z^{tot} = 2$ the quadratic Zeeman shift does not alter the staircase since it leads to a homogeneous shift of all the energy levels. The staircases at different magnetic fields are shown in Fig. 4.11. For $S_z^{tot} = 0$, the step positions depend in a non-linear way on the magnetic field strength. It is no longer possible to read

---

[1] [Stenger *et al.*(1998), Rodriguez *et al.*(2011)]

[2] [Stenger *et al.*(1998)]
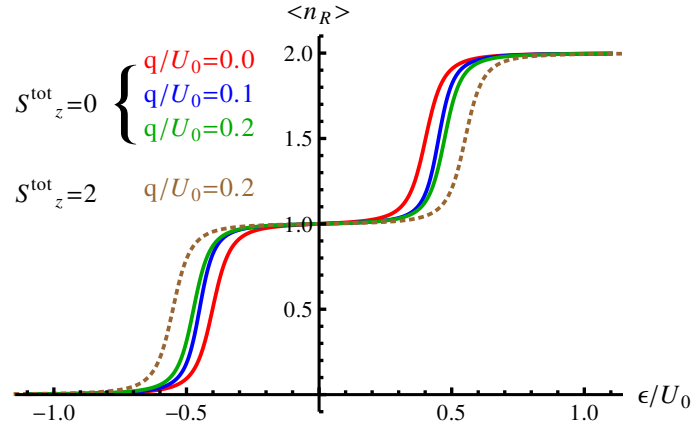
Figure 4.11: Two spin-1 bosons with antiferromagnetic ordering in a double-well potential ($t/U_0 = 0.05$ and $U_2/U_0 = 0.1$). Solid lines: $S_z^{tot} = 0$ for different magnetic fields $q = q_0 B^2$. Dashed line: $S_z^{tot} = 2$. In this case the staircase does not depend on the magnetic field. The difference of this staircase to the ones with $S_z^{tot} = 0$, which is the main manifestation of mesoscopic magnetism, persists in the presence of the quadratic Zeeman effect.

them off in the atomic limit (i.e. $t = 0$), because the existence of the quadratic Zeeman shift leads to additional non-diagonal elements in the Hamiltonian. Note that the quadratic Zeeman effect does not eliminate the difference of the two staircases, which is the main manifestation of mesoscopic magnetism.

Due to the fact that the quadratic Zeeman shift does not commute with the operator of the total spin S^{tot}, the eigenstates of the Hamiltonian given in Eq. (4.13) are no longer eigenstates of S_{tot}. For $B \neq 0$, the ground state of the system is a superposition of different eigenstates of S_{tot}, i.e. states with different S_{tot} hybridize (see Fig. 4.12). For certain values of the energy offset ϵ (e.g. $\epsilon/U_0 = 1$ and $\epsilon/U_0 = -1$ for four bosons) the appearance of a magnetic field changes the ground state strongly. This reflects the specific spin configurations.

The quadratic Zeeman shift changes also the overall spectrum for a given magnetization qualitatively, such that in the case of thermal occupation of the double well the density matrix of the system changes considerably. For $q = 0$ the ground state is nearly degenerate with the first excited state, whereas the gap widens for finite values of q.

Additionally one can include inhomogeneous magnetic fields,

$$H \;=\; H_q + \Delta B \cdot (S_{Lz} - \; S_{Rz}) \;,$$

where ΔB describes the strength of the field gradient. The magnetic field offset ΔB changes the Hamiltonian if $S_{tot_z} \neq 0$. For some configurations, e.g. two bosons in a double well, ΔB leads merely to an overall shift of ϵ i.e., an inhomogeneous magnetic field is equivalent to an energy offset ϵ. In general this is not the case and ΔB is an additional tool to reshape the staircases depending on the spin configuration of the
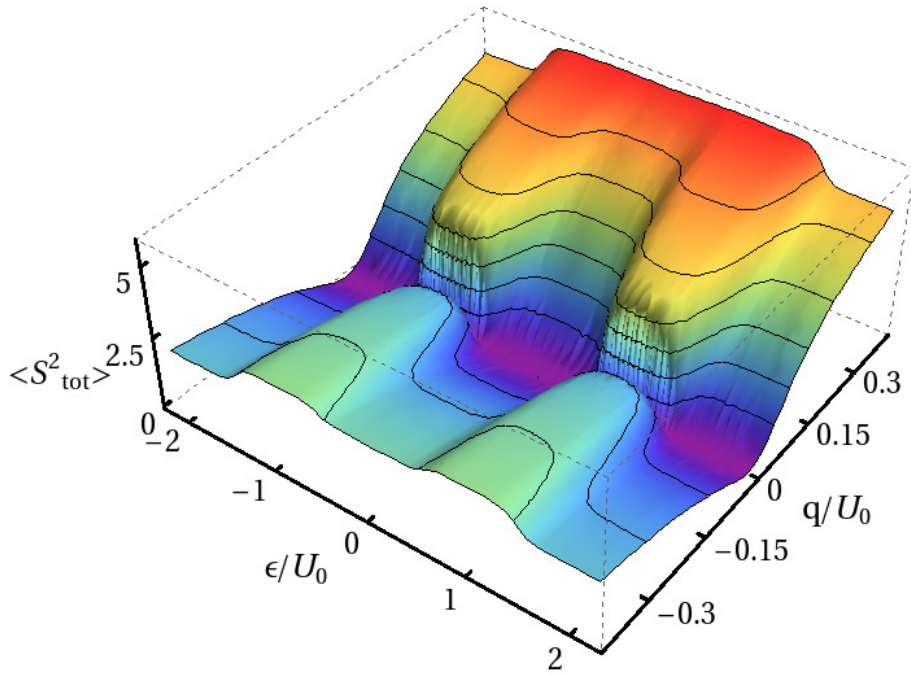
Figure 4.12: Expectation value $\langle S_{tot}^2 \rangle$ of the system for four bosons for different magnetic fields $q = q_0 B^2$ ($S_z^{tot} = 0$, $t/U_0 = 0.05$ and $U_2/U_0 = 0.1$).

system.

4.6 Single Atom Resonances in Superlattices

Adapted from Phys. Rev. A **86**, 023624 (2012).

In this section we go beyond the approximation of isolated double-wells and include the influence of neighboring double wells via a mean-field approximation.

4.6.1 Staircases for Spinless Bosons in Superlattices

Starting from the Hamiltonian (4.3) we can include neighboring double wells via a mean-field ansatz and obtain Eq. (3.38),

$$
\begin{aligned}
\hat{H} \;=\;& \frac{U}{2} \sum_{k=L,R} \hat{n}_k(\hat{n}_k - 1) - t_i(\hat{L}^\dagger \hat{R} + h.c.) + \varepsilon\,(\hat{n}_L - \hat{n}_R) - \mu\,(\hat{n}_L + \hat{n}_R) \\
& - t_e \left(\phi_R \hat{L}^\dagger + \phi_L \hat{R}^\dagger + 2z\phi_R \hat{R}^\dagger + 2z\phi_L \hat{L}^\dagger - \phi_R \phi_L^* - z\phi_R \phi_R^* - z\phi_L^* \phi_L + h.c. \right).
\end{aligned}
\tag{4.14}
$$

The parameters of this Hamiltonian are the intra-well tunneling amplitude t_i, the tunneling amplitude t_e between different double wells (recall that $t_i > t_e$), the on-site interaction strength U, the chemical potential μ and the energy offset within the double wells ε (compare Fig. 3.15). The mean-field order parameters ϕ_L and ϕ_R denote the superfluid density via the relations $n_L^{\text{sf}} = |\langle \hat{L} \rangle|^2$ and $n_R^{\text{sf}} = |\langle \hat{R} \rangle|^2$. When the self consistent values of the order parameters are $\phi_L = \phi_R = 0$ all tunneling between the unit cells of the superlattice is suppressed and the system is called Mott insulating (see Sec. 3.3).

If the offset ε is changed with the other parameters μ, t_i, and t_e fixed, the atom number distribution within the double wells becomes asymmetric. Due to the finite on-site interaction the atom numbers do not change proportionally to ε but in steps, which are called single-atom resonances. In Sec. 4.3 these bosonic staircases were examined for isolated double-well potentials. In the Mott-insulating phase the superlattice decomposes (within mean-field approximation) into an array of isolated double wells (compare Sec. 3.3). Thus, it is possible in this regime to observe the same bosonic staircases as in the case of single double-well potentials.

Figure 4.13 shows the mean atom number in the right well $\langle \hat{n}_R \rangle$ and the standard deviation

$$
\Delta n_R = \sqrt{\langle \hat{n}_R^2 \rangle - \langle \hat{n}_R \rangle^2}
$$

along the dashed line shown in Fig. 3.20. The system is Mott-insulating for a large parameter range ($\mu/U = 1$, $t_i/U = 0.05$, $t_e/U = 0.005$, and $-1.9 \leq \varepsilon/U \leq 1.9$). The inset shows the total number of atoms in the double well $\langle \hat{n} \rangle = \langle \hat{n}_L + \hat{n}_R \rangle$

101
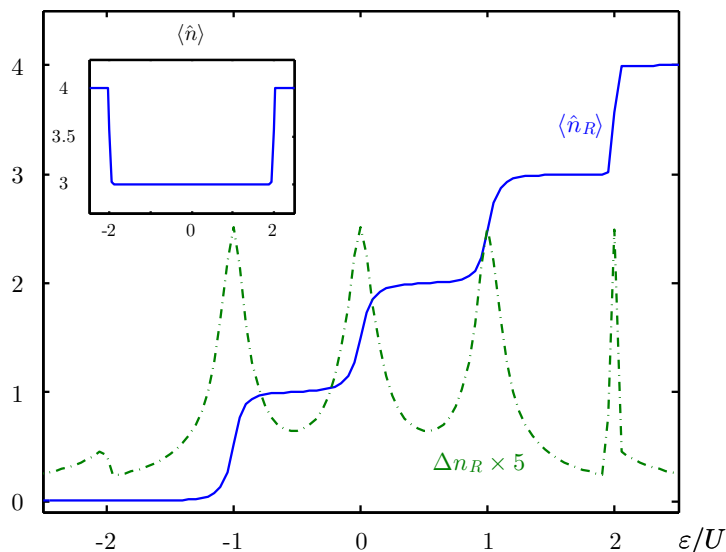
Figure 4.13: Mean particle number in the right well $\langle \hat{n}_R \rangle$ (solid) and standard deviation $\Delta n_R = \sqrt{\langle \hat{n}_R^2 \rangle - \langle \hat{n}_R \rangle^2}$ (dashed) as a function of the energy offset ε for Hamiltonian (4.14) with $\mu/U = 1$ and $t_i/U = 10 t_e/U = 0.05$. The inset shows the mean total particle number in the double well $\langle \hat{n} \rangle = \langle \hat{n}_L + \hat{n}_R \rangle$. The standard deviation is multiplied by 5.

which changes discontinuously at $\varepsilon/U \approx \pm 2$ signaling that the system leaves the Mott-insulating phase. This causes a discontinuity in the function $\langle \hat{n}_R \rangle$. The steps are equidistant since the difference in the on-site interaction between one and two atoms and between two and three atoms (and for higher atom numbers) are the same, namely equal to the on-site interaction U. The spacing between two steps is $\Delta \varepsilon = U$, i.e., the steps occur when the energy offset is large enough to compensate the on-site interaction.

In Fig. 4.14 the expectation value $\langle \hat{n}_R \rangle$ is plotted along a curve with stronger tunneling amplitudes and a shifted chemical potential as compared to Fig. 4.13. Along this curve the system is mostly superfluid. This can be seen from the inset of Fig. 4.14: for $-2U \leq \varepsilon \leq 2U$ the particle number per double well $\langle \hat{n} \rangle$ is not constant anymore. Although the atom staircase looks similar to the one in Fig. 4.13 there are significant differences. The fluctuations in the particle number Δn_R are greatly increased and additional maxima appear. These number fluctuations can be measured in experiments.[1]

Single-atom resonances can also be seen in the density of condensed atoms. The number of condensed atoms per site is connected to the value of the order parameters via the relations, $n_L^{\text{sf}} = |\langle \hat{L} \rangle|^2$ and $n_R^{\text{sf}} = |\langle \hat{R} \rangle|^2$. The ratio of condensed atoms in the

---

[1] [Cheinet *et al.*(2008)]
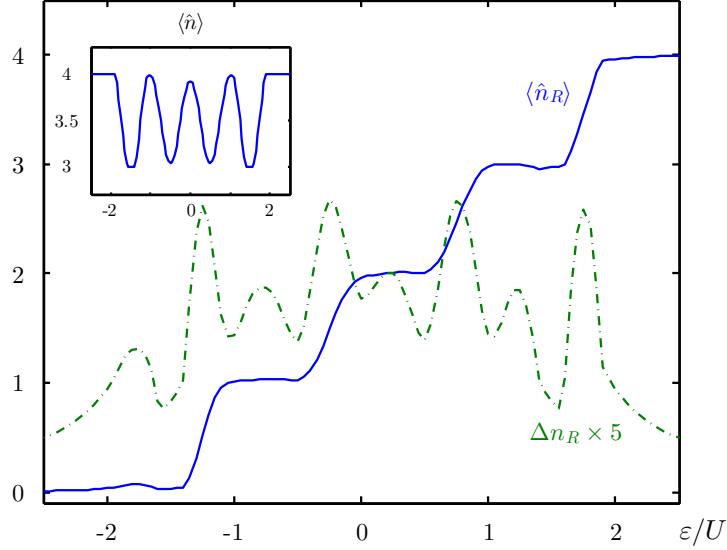
Figure 4.14: Mean particle number in the right well $\langle \hat{n}_R \rangle$ (solid) and standard deviation $\Delta n_R = \sqrt{\langle \hat{n}_R^2 \rangle - \langle \hat{n}_R \rangle^2}$ (dashed) as a function of the energy offset ε for Hamiltonian (4.14) with $\mu/U = 1.2$ and $t_i/U = 10 t_e/U = 0.1$. The inset shows the total particle number in the double well $\langle \hat{n} \rangle = \langle \hat{n}_L + \hat{n}_R \rangle$. The standard deviation is multiplied by 5.

right well to the number of condensed atoms in both wells,

$$\frac{n_R^{\text{sf}}}{n^{\text{sf}}} = \frac{|\langle \hat{R} \rangle|^2}{|\langle \hat{L} \rangle|^2 + |\langle \hat{R} \rangle|^2} \,, \tag{4.15}$$

is plotted in Fig. 4.15 along several paths in parameter space. The solid line corresponds to $t_i = 10 t_e = 0.15U$ and shows steplike behavior. The dotted line shows the total atom number in the right well $\langle \hat{n}_R \rangle$ for the same tunneling amplitudes. Note that the steplike structure is more pronounced for the density of condensed atoms than for the total atom number. For higher tunneling rates the staircase structure disappears (see dashed line with $t_i = 10 t_e = 1U$). In the limit of infinite tunneling amplitudes the ratio $n_{L/R}^{\text{sf}}/n^{\text{sf}}$ does not depend on ε because there is an infinite amount of atoms in the unit cell and changing ε/U by one moves only one atom from one site to the other. This analysis of the asymmetry of the superfluid density also helps to understand the connection between ϕ_L and ϕ_R. The ratio of the two order parameters ϕ_L and ϕ_R does not only depend on the energy offset ε but also on the tunneling amplitudes, the chemical potential, and the on-site interaction.
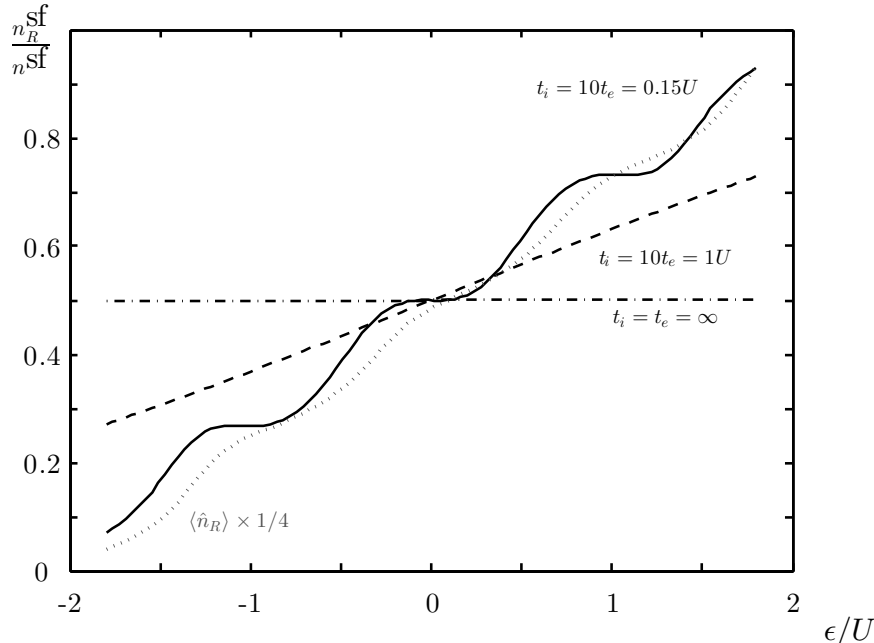
Figure 4.15: Fraction of condensed particles in the right well $n_R^{\mathrm{sf}}/n^{\mathrm{sf}}$ (4.15) for spinless atoms described by the Hamiltonian (4.14). The parameters are chosen such that the system is superfluid over the full range of $\varepsilon/U \in [-1.8, 1.8]$. The chemical potential for all curves is $\mu/U = 1.25$. The solid line corresponds to $t_i/U = 10t_e/U = 0.15$, the dashed line to $t_i/U = 10t_e/U = 1$ and the dashed-dotted line to $t_i = t_e = \infty$. The dotted line shows the atom number in the right well $\langle \hat{n}_R \rangle$ as a function of ε for $t_i/U = 10t_e/U = 0.15$.

4.6.2 Staircases for Spin-1 Bosons in Superlattices

To illustrate the phase diagram and to compare it to the case of spinless bosons we include a bosonic staircase for spin-1 atoms with antiferromagnetic interactions in Fig. 4.16. In this figure the occupation number of the right site of each unit cell $\langle \hat{n}_R \rangle$ is plotted as a function of the energy offset ε. We choose parameters so that the system is Mott-insulating for $-2.5 \leq \varepsilon/U_0 \leq 2.5$. The comparison with Fig. 4.13 shows that antiferromagnetic interactions shift the steps and make them unequally wide. The step corresponding to two atoms in the left site and two atoms in the right site allows the formation of spin singlets ($\langle \hat{\mathbf{S}}^2{}_L \rangle = \langle \hat{\mathbf{S}}^2{}_R \rangle = 0$) in both sites. This is energetically favorable compared to the case of an odd number of atoms on both sites, which form states with $\langle \hat{\mathbf{S}}_L^2 \rangle = \langle \hat{\mathbf{S}}_R^2 \rangle = 2$ (this is analogous to the changed size of the diamonds in Fig. 3.23).
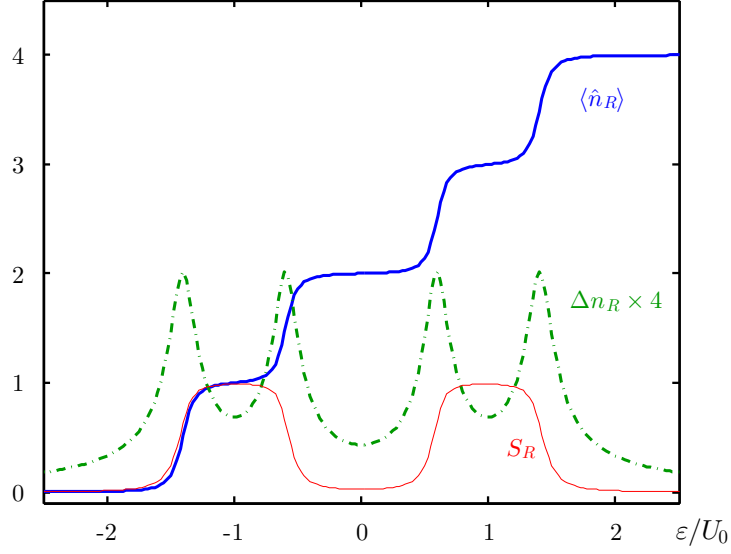
Figure 4.16: Bosonic staircase for spin-1 atoms described by the Hamiltonian (3.41) along the curve $\mu/U_0 = 1.4$, $t_i/U_0 = 0.05$, $t_e/U_0 = 0.005$, $U_2/U_0 = 0.1$ and $\varepsilon/U_0 \in [-2.5, 2.5]$. The thick solid line shows the particle number in the right well $\langle n_R \rangle$ and the dashed line the standard deviation $\Delta n_R = \sqrt{\langle n_R^2 \rangle - \langle n_R \rangle^2}$. The thin solid line shows S_R, the quantum number of the square of the spin in the right well, i.e. $\langle \hat{\mathbf{S}}_R^2 \rangle = S_R(S_R + 1)$. The total particle number $\langle \hat{n}_L + \hat{n}_R \rangle = 4$ over the full shown range of ε. The standard deviation is multiplied by 4.

Chapter 5

Entanglement in Superlattices

Entanglement is a unique feature of quantum mechanical systems. Understanding entanglement deepens our understanding of quantum mechanics and, therefore, is of fundamental interest. Moreover, entanglement is a resource for quantum computation and correlates separated systems stronger than all classical correlations can do.

Pure State Entanglement

In classical mechanics as well as in quantum mechanics we can define pure states. In classical mechanics such a state is a single point in the phase space and in quantum mechanics a complex vector in the Hilbert space. Both times the state is maximally specified and not a probabilistic mixture of distinct pure states. A composite classical system that is in a pure state can be divided and its parts are always pure states. In quantum mechanics this is no longer true: It is possible to prepare a composite systems in a specific pure state, divide it and its parts are not in pure states anymore. Such states are called entangled. Although one has the best possible knowledge of the whole one does not have the best possible knowledge of its parts.[1] When we assume that the two entangled parts are spatially separated there will be some "spooky action over distance": When measuring one part one changes the quantum state of the other part instantaneously.[2]

As an example we examine two entangled qubits, which are in the state

$$|\psi\rangle_{AB} = \frac{1}{\sqrt{2}} \left(|\uparrow_A \downarrow_B\rangle + |\downarrow_A \uparrow_B\rangle \right) , \tag{5.1}$$

where A and B label the qubits. The state (5.1) is a pure state. The von Neumann

---

[1] [Schrödinger(1935)]

[2] [Einstein *et al.*(1935)]

entropy,[1]

$$S = -\mathrm{tr}(\varrho \log_2(\varrho)) \,, \tag{5.2}$$

measures how mixed a density matrix ϱ is; this entropy is zero for the state (5.1).
The entropy has the meaning of a measure of information in the same way as in
statistical physics:[2] A mixed state implies less knowledge of the system than a pure
state. To calculate the quantum state ϱ_1 of the first qubit in the state (5.1) we trace
out the second one,[3]

$$\varrho_A = \langle \uparrow_B |\varrho_{AB}| \uparrow_B \rangle + \langle \downarrow_B |\varrho_{AB}| \downarrow_B \rangle = \begin{pmatrix} 1/2 & 0 \\ 0 & 1/2 \end{pmatrix} \,, \tag{5.3}$$

where $\varrho_{AB} = |\psi\rangle_{AB}\langle\psi|_{AB}$. The density matrix ϱ_A corresponds to a mixed state
and its von Neumann entropy is 1. Note that the von Neumann entropy of a 2×2
matrix cannot be larger than 1; therefore, we call the state (5.3) maximally mixed
and the state (5.1) maximally entangled. In conclusion, although we have maximal
knowledge about the state (5.1) we cannot know less about the state (5.3). Therefore
one says that in entangled states knowledge is stored non-locally.

Whenever we can write a pure state of a composite system as product of pure
states,

$$|\psi\rangle_{AB} = |\psi\rangle_A \otimes |\psi\rangle_B \,,$$

we say that the state is separable. The density matrix of one part, say A, of a
separable state corresponds to a pure state,

$$\varrho_A = \langle \uparrow_B |\varrho_{AB}| \uparrow_B \rangle + \langle \downarrow_B |\varrho_{AB}| \downarrow_B \rangle = |\psi\rangle_A \langle\psi|_A \,,$$

where we assumed (for convenience) a qubit basis (the same is true for higher di-
mensional systems); the density matrix of the composite state is given by $\varrho_{AB} = (|\psi\rangle_A \otimes |\psi\rangle_B)(\langle\psi|_A \otimes \langle\psi|_B)$. Therefore, separable states are not entangled.

In general any pure state $|\psi\rangle$ of a composite system can be written in the Schmidt
decomposition[4]

$$|\psi\rangle = \sum_{i=1}^{D} c_i |\psi_i^A\rangle \otimes |\psi_i^B\rangle \,,$$

where $\{\psi_1^A, \ldots, \psi_D^A\}$ and $\{\psi_1^B, \ldots, \psi_D^B\}$ are complete sets of orthonormal states of
the subsystems A and B, respectively. The coefficients c_i are invariant under local
operations and can therefore be used to quantify the entanglement between A and

---

[1] [Neumann(1955),Nielsen and Chuang(2000)]

[2] [Popescu and Rohrlich(1997)]

[3] [Nielsen and Chuang(2000)]

[4] [Horodecki *et al.*(2009)]

B. The von Neumann entropy of the reduced density matrix of each single qudit is given by[1]

$$E(\psi) = S(\mathrm{Tr}_B|\psi\rangle\langle\psi|) = S(\mathrm{Tr}_A|\psi\rangle\langle\psi|) = -\sum_{i=1}^{D} c_i^2 \log_2 c_i^2, \tag{5.4}$$

where S indicates the entropy. This entanglement measure is called entanglement of formation (EOF). The EOF is the number of Einstein-Podolsky-Rosen pairs asymptotically required to prepare a given state by local operations and classical communication. It ranges from zero to $\log_2 D$. The entanglement of formation of two qudits with $D > 2$ thereby exceeds the entanglement of formation of two qubits, i.e. higher-dimensional objects contain more entanglement and violate all Clauser-Horne-Shimony-Holt-inequalities more strongly than qubits.[2]

Mixed State Entanglement

For a mixed state the von Neumann entropy of a subsystem is not a good entanglement measure anymore because each subsystem can be a mixed state even if there is no entanglement. In general, a mixed state is entangled if it cannot be written as a mixture of unentangled pure states. However, there are infinitely many possibilities to write a mixed state. For example, let us consider two pure two qubit states,

$$|\psi_+\rangle = \frac{1}{\sqrt{2}}\left(|\uparrow\downarrow\rangle + |\downarrow\uparrow\rangle\right) \quad \text{and} \quad |\psi_-\rangle = \frac{1}{\sqrt{2}}\left(|\uparrow\downarrow\rangle - |\downarrow\uparrow\rangle\right), \tag{5.5}$$

where we suppressed the labels of the parts. The mixed state

$$\varrho = \frac{1}{2}\varrho_+ + \frac{1}{2}\varrho_-,$$

(where $\varrho_+ = |\psi_+\rangle\langle\psi_+|$ and $\varrho_- = |\psi_-\rangle\langle\psi_-|$) is a mixture of entangled states. Nevertheless, ϱ can also be written as

$$\varrho = \frac{1}{2}|\uparrow\downarrow\rangle\langle\uparrow\downarrow| + \frac{1}{2}|\downarrow\uparrow\rangle\langle\downarrow\uparrow|,$$

which is mixture of unentangled states. Thus ϱ is not entangled. Therefore, to obtain the amount of entanglement in a given mixed state one must perform a minimization procedure over all pure-state decompositions.

The minimal number of Einstein-Podolsky-Rosen pairs asymptotically required to prepare a given mixed state ϱ is called the entanglement of formation. It is defined as

$$\mathrm{EOF}(\varrho) = \inf \sum_{j=1}^{N} p_j E(\psi_j), \tag{5.6}$$

---

[1] [Dennison and Wootters(2001)]

[2] [Horodecki *et al.*(2009)]

where $E(\psi_j)$ is the pure state entanglement measure given in Eq. (5.4) and the infimum is taken over all pure-state decompositions of ϱ. Note that the pure states ψ_j need to be normalized.

There is a formula to calculate the entanglement of formation for any two qubit state ϱ.[1] It is given by

$$\text{EOF}(\varrho) = h\left(\frac{1 + \sqrt{1 - C(\varrho)^2}}{2}\right),$$

where $h(x) = -x\log_2 x - (1-x)\log_2(1-x)$ and $C(\varrho)$ is the concurrence. The concurrence does not have a direct physical interpretation but can be explicitly calculated for any two qubit state. It is

$$C(\varrho) = \max\{0, \lambda_1 - \lambda_2 - \lambda_3 - \lambda_4\},$$

where the λ_i's are the square roots of the eigenvalues of $\varrho\tilde{\varrho}$ in descending order. Here $\tilde{\varrho}$ is the result of applying a spin-flip operation to ϱ,

$$\tilde{\varrho} = \tilde{\varrho}_{AB} = \left(\sigma_y^A \otimes \sigma_y^B\right)\varrho_{AB}^*\left(\sigma_y^A \otimes \sigma_y^B\right),$$

where ϱ^* denotes the complex conjugate of ϱ, the density matrix is written in the standard basis, which is $\{|\uparrow\uparrow\rangle, |\uparrow\downarrow\rangle, |\downarrow\uparrow\rangle, |\downarrow\downarrow\rangle\}$ and σ_y is the Pauli operator $\left(\begin{smallmatrix} 0 & -i \\ i & 0 \end{smallmatrix}\right)$. The concurrence of a pure state $|\psi_{AB}\rangle$ essentially measures the overlap of the wave function with the wavefunction in which all spins are flipped. The concurrence of $|\psi_{AB}\rangle$ is given by $C(\psi_{AB}) = |\langle\psi_{AB}|\tilde{\psi}_{AB}\rangle|$, where $|\tilde{\psi}_{AB}\rangle = \left(\sigma_y^A \otimes \sigma_y^B\right)|\psi_{AB}^*\rangle$. For example, when we flip the spins in the maximally entangled states (5.5) the states do not change (except for a phase factor) and the concurrence of these states is maximal.

However, there is no closed formula for mixed state entanglement for higher dimensional systems.[2] There are many different entanglement measures for these but none of them is sufficient and able to capture all facets of entanglement.

In the following we will use the negativity of a density matrix as an entanglement measure which is easy to calculate (but fails to detect all entanglement). This measure is based on the notion that any separable density matrix of a bipartite system can be written as

$$\rho = \sum_n w_n\, \rho_n^A \otimes \rho_n^B.$$

If one takes the transpose of only one subsystem, the resulting partial-transpose matrix is still a regular density matrix,

$$\sigma = \sum_n w_n\left(\rho_n^A\right)^T \otimes \rho_n^B,$$

---

[1] [Wootters(1998)]

[2] [Horodecki *et al.*(2009)]

which means that σ has only positive eigenvalues. From this we can follow that whenever the partial transpose of a given density matrix ϱ has negative eigenvalues ϱ is entangled. Note that this is a sufficient but not necessary condition for entanglement.

The entanglement measure negativity is defined as the sum over the negative eigenvalues of the partial transpose of ϱ,[1]

$$\mathcal{N}(\varrho) \equiv \frac{\sum_i |\lambda_i| - \lambda_i}{2} = \frac{||\varrho^{\Gamma_A}||_1 - 1}{2} \, ,$$

where ϱ^{Γ_A} is partial transpose of ϱ with respect to subsystem A, the λ_i's are the eigenvalues of ϱ^{Γ_A} and $||X||_1 = Tr\sqrt{X^\dagger X}$ is the trace norm[2] or the sum of the singular values of the operator X.

5.1 Entanglement in Double-Well Potentials

Adapted from Phys. Rev. A **84**, 063636 (2011).

In the following we calculate the entanglement of formation in superlattices deep in the Mott-insulating quantum phase. In this regime the superlattice decomposes into isolated double-well potentials (within mean-field approximation). Thus, we determine the bipartite entanglement in a double well. We assume ultracold atoms are loaded in a deep double-well potential and describe them with a two-site Bose-Hubbard model

$$\hat{H}_0 = \frac{U_0}{2} \sum_{i=L,R} \hat{n}_i(\hat{n}_i - 1) - t \sum_\sigma (\hat{L}_\sigma^\dagger \hat{R}_\sigma + h.c.) + \varepsilon \left(n_L - n_R \right) + \frac{U_2}{2} \sum_{i=L,R} \left(\vec{S}_i^2 - 2n_i \right) \, ,$$

where the operators are described below Eq. (4.3). At this point, we consider the entanglement mainly as a theoretical characterization of the many-body state of the system.

The entanglement of formation for typical parameters is shown in Fig. 5.1. The maximal entanglement exceeds the maximal entanglement between two qutrits ($\log_2 3 \approx 1.585$). This is due to particle fluctuations. The total amount of entanglement stems from orbital and spin degrees of freedom.

Magnetic fields have a strong effect on the entanglement of formation. Figure 5.2 shows the EOF of four bosons at $S_z^{tot} = 0$ (compare Sec. 2.5). For $q > 0$, the contribution of the spin degrees of freedom to the entanglement of formation is suppressed already by small magnetic fields. This is somewhat surprising, because the system

---

[1] [Vidal and Werner(2002)]

[2] [Golub and Van Loan(1996)]

EOF

2.5

2.0

1.5

1.0

0.5

$<n_R>$

-1.0 -0.5 0.0 0.5 1.0 ϵ/U_0
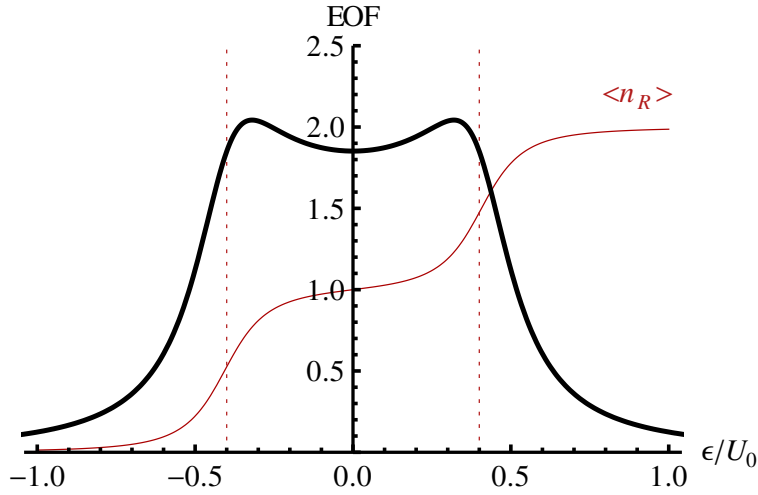
Figure 5.1: Entanglement of formation (EOF) between two wells for two bosons with antiferromagnetic interactions ($t/U_0 = 0.1$ and $U_2/U_0 = 0.1$) for the total spin $S_{tot} = 0$.

is constrained to $S_z^{tot} = 0$, i.e. the state with the strongest spin entanglement of all states with a given total spin. For $q < 0$, this contribution is initially reduced but then remains constant as a function of q.

5.2   Two Spin-1 Bosons

For two bosons and in the case of $S_{tot} = 0$ a possible orthonormal basis is given by

$$\{\psi_1, \psi_2, \psi_3\} = \{|\{2,0\}, \{0,0\}, 0\rangle, |\{1,1\}, \{1,1\}, 0\rangle, |\{0,2\}, \{0,0\}, 0\rangle\}$$

using the notation $|\{n_L, n_R\}, \{S_L, S_R\}, S_{tot}\rangle$. The decomposition

$$|\Psi\rangle = \sum_i^3 c_i |\psi_i\rangle$$

is not a Schmidt decomposition, because the vector $|\psi_2\rangle$ is a superposition of or-thonormal states:

$$|\{1,1\}, \{1,1\}, 0\rangle = -\frac{1}{\sqrt{3}}|1,1,0;1,1,0\rangle + \frac{1}{\sqrt{3}}|1,1,1;1,1,-1\rangle + \frac{1}{\sqrt{3}}|1,1,-1;1,1,1\rangle,$$

using the notation $|n_L, S_L, S_{Lz}; n_R, S_R, S_{Rz}\rangle$. The entanglement of formation of $|\psi_2\rangle$ is given by

$$E(|\psi_2\rangle) = 3\frac{1}{3}\log_2 3 .$$

112
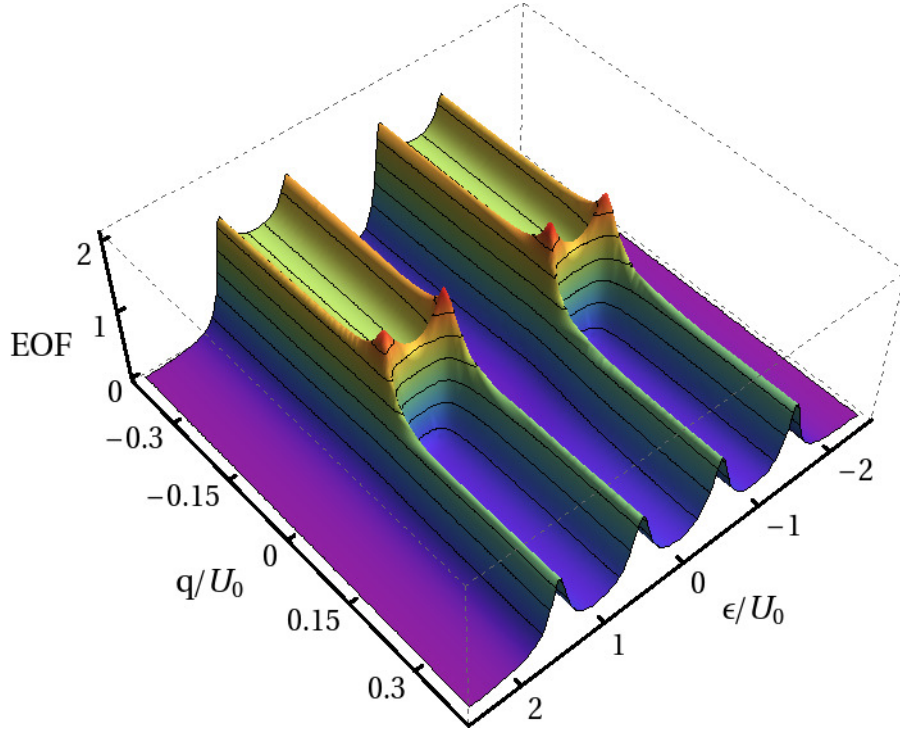
Figure 5.2: EOF between two wells for four particles in the presence of a magnetic field ($S_z^{tot} = 0$, $t/U_0 = 0.05$ and $U_2/U_0 = 0.1$). For $q > 0$, even small fields will eliminate the contribution of the spin degrees of freedom to the entanglement.

The EOF of $|\Psi\rangle$ is given by

$$
\begin{aligned}
E(|\Psi\rangle) &= -c_1^2 \log_2 c_1^2 - c_3^2 \log_2 c_3^2 - 3\left(c_2 \frac{1}{\sqrt{3}}\right)^2 \log_2 \left(c_2 \frac{1}{\sqrt{3}}\right)^2 \\
&= -\sum_i^3 c_i^2 \log_2 c_i^2 + c_2^2 \log_2 3 = -\sum_i^3 c_i^2 \log_2 c_i^2 + \sum_i^3 c_i^2 E(|\psi_i\rangle) \\
&= E_{\text{orbital}} + E_{\text{spin}}. \tag{5.7}
\end{aligned}
$$

The total entanglement between the left and the right well decomposes in an orbital part and a spin part. The orbital part stems from the coefficients which distinguish different orbital wave functions. The spin part originates from the EOF of the individual basis vectors, each weighted with the coefficient c_i^2. The coefficients c_i depend on the tunneling strength t, on the on-site interaction U_0, on the spin-dependent interaction U_2 and the energy offset ε.

In the limit of weak tunneling $t \ll U_0$ the Hamiltonian is diagonal in the basis $\{\psi_1, \psi_2, \psi_3\}$ and the ground state of a symmetric double-well potential (i.e. $\varepsilon = 0$) is given by

$$
|\Psi_0\rangle = |\psi_2\rangle = -\frac{1}{\sqrt{3}}|1,1,0;1,1,0\rangle + \frac{1}{\sqrt{3}}|1,1,1;1,1,-1\rangle + \frac{1}{\sqrt{3}}|1,1,-1;1,1,1\rangle\,, \tag{5.8}
$$
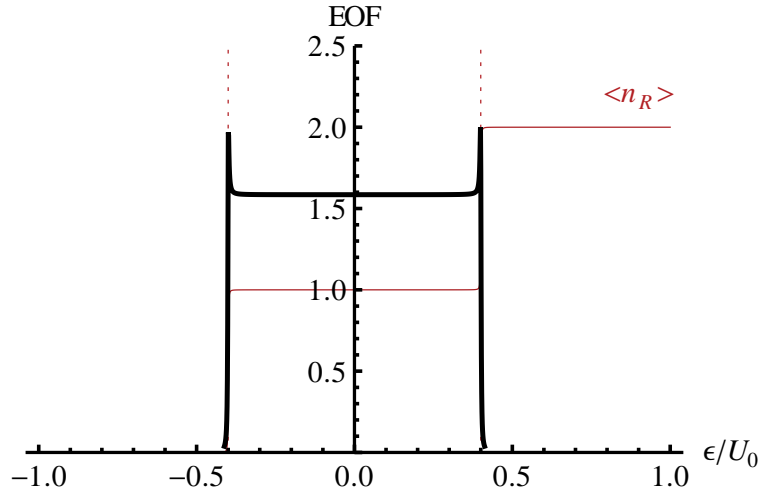
Figure 5.3: EOF between two wells for two bosons for very weak tunneling and antiferromagnetic interactions ($t/U_0 = 0.001$ and $U_2/U_0 = 0.1$) for the total spin $S_{tot} = 0$.

which leads to an entanglement of $E(|\psi_2\rangle) = \log_2 3$, see Fig. 5.3.

In the limit of strong tunneling (i.e. $U_0 \ll t$), the ground state of the system is

$$|\Psi_0\rangle = \frac{1}{2}|\psi_1\rangle + \frac{1}{\sqrt{2}}|\psi_2\rangle + \frac{1}{2}|\psi_3\rangle. \tag{5.9}$$

For this state the orbital entanglement is given by

$$E_{\text{orbital}} = -2\frac{1}{4}\log_2\frac{1}{4} - \frac{1}{2}\log_2\frac{1}{2} = 3/2\,,$$

and the spin entanglement is given by

$$E_{\text{spin}} = \left(\frac{1}{\sqrt{2}}\right)^2 \log_2 3 \approx 0.792\,.$$

The total entanglement is therefore $E(|\Psi_2\rangle) \approx 2.292$. This is not the maximum amount of entanglement that can be obtained for this system (see Fig. 5.4). The maximal entanglement is not the sum of the maximal qutrit entanglement and the maximal orbital entanglement, because the orbital motion leads to particle number fluctuations and reduces the spin entanglement (see Fig. 5.5). The maximal orbital entanglement is realized in the limit of strong tunneling, the maximal spin entanglement corresponds to the maximally localized state, i.e. $|\psi_2\rangle$.

Non-Zero Temperatures

In this section we present some results of the bipartite entanglement for the two-site Bose-Hubbard model for non-zero temperatures. The thermal density matrix

114
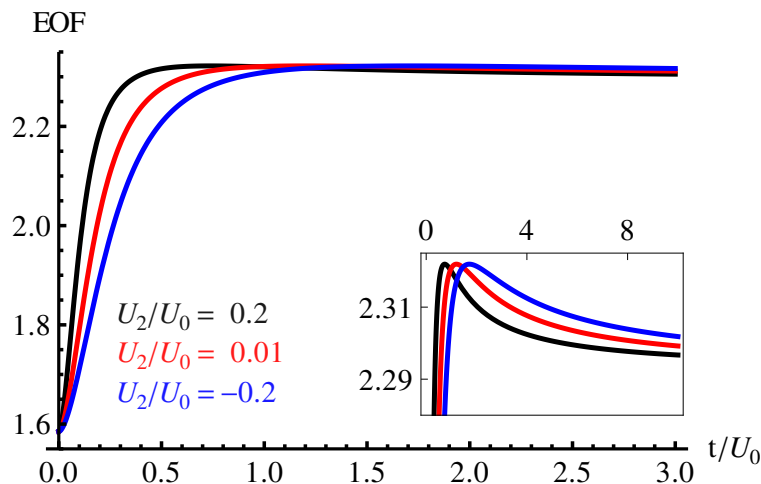
Figure 5.4: EOF between two symmetric wells ($\varepsilon = 0$) for different values of U_2, i.e., different spin interactions.

describing these states is given by

$$\rho(T) = \frac{1}{Z} \sum_i g_i \, e^{-\frac{E_i}{k_B T}} |\psi_i\rangle\langle\psi_i| \,,$$

where Z is the partition function and g_i denotes the degeneracy of the state $|\psi_i\rangle$. In Fig. 5.6 we present the negativity as a function of the energy offset for three temperatures. For small temperatures (blue line in Fig. 5.6, $k_B T = 0.25 U_0$) the negativity resembles main features of the ground state entanglement. Higher temperatures decrease the entanglement and wash out the spikes due to orbital entanglement at $\varepsilon/U_2 = \pm 0.4$.

5.3 Three Spin-1 Bosons

The EOF between the two sites is presented in Fig. 5.7 for $t/U_0 = 0.1$ and in Fig. 5.8 for very weak tunneling. In contrast to the case of two bosons, in the weak-tunneling case the system is not entangled for large intervals of the energy offset ϵ.

To quantify this effect, we analyze the EOF again in detail. The spins $\vec{S}_L$ and $\vec{S}_R$ couple to a total spin, for which three absolute values are possible, $S_{tot} \in \{1, 2, 3\}$.

It is obvious that Eq. (5.7) is applicable for $S_{tot} = 2$ and $S_{tot} = 3$. The interesting case is $S_{tot} = 1$. Each state with the quantum number $S_{tot} = 1$ can be written as

$$|\Psi\rangle = \sum_i^6 c_i |\psi_i\rangle. \tag{5.10}$$

Only two of the basis vectors contain true spin entanglement:
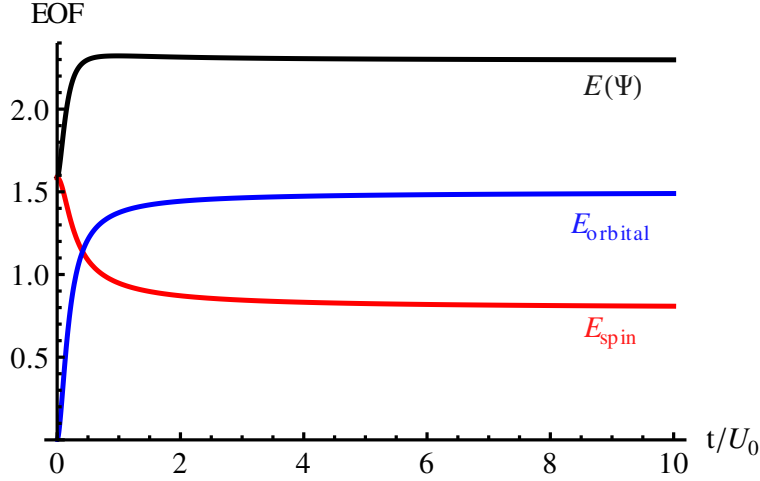
Figure 5.5: EOF, E_{spin} and E_{orbital} between two symmetric wells for $U_2/U_0 = 0.1$.

$$\begin{aligned}
|\psi_2\rangle = |((2,1),(2,1),1)\rangle &= \alpha|2,2,0;1,1,0\rangle + \beta|2,2,1;1,1,-1\rangle + \gamma|2,2,-1;1,1,1\rangle \\
|\psi_4\rangle = |((1,2),(1,2),1)\rangle &= \alpha|1,1,0;2,2,0\rangle + \beta|1,1,1;2,2,-1\rangle + \gamma|1,1,-1;2,2,1\rangle
\end{aligned}$$

with $\alpha = -\sqrt{\frac{2}{5}}$, $\beta = \gamma = \sqrt{\frac{3}{10}}$. Any superposition of $|\psi_2\rangle$ and $|\psi_3\rangle$ can be written as

$$\begin{aligned}
c_2|\psi_2\rangle + c_3|\psi_3\rangle &= \sqrt{c_2^2\alpha^2 + c_3^2}|L\rangle \otimes |1,1,0\rangle_R + c_2\beta|2,2,1;1,1,-1\rangle \\
&+ c_2\gamma|2,2,-1;1,1,1\rangle
\end{aligned} \tag{5.11}$$

where $|L\rangle$ is the normalized function

$$|L\rangle = 1/\sqrt{c_2^2\alpha^2 + c_3^2}\left(c_2\alpha|2,2,0\rangle_L + c_3|2,0,0\rangle_L\right),$$

which is orthogonal to the other vectors appearing in Eqs. (5.11) and (5.10). The decomposition Eq. (5.11) is therefore a Schmidt decomposition and the full entanglement of formation of $|\Psi\rangle$ can be calculated:

$$\begin{aligned}
E(|\Psi\rangle) &= -c_1^2\log_2 c_1^2 - \left(c_2^2\alpha^2 + c_3^2\right)\log_2\left(c_2^2\alpha^2 + c_3^2\right) \\
&- \left(c_2^2\beta^2\right)\log_2\left(c_2^2\beta^2\right) - \left(c_2^2\gamma^2\right)\log_2\left(c_2^2\gamma^2\right) \\
&- \left(c_4^2\alpha^2 + c_5^2\right)\log_2\left(c_4^2\alpha^2 + c_5^2\right) - \left(c_4^2\beta^2\right)\log_2\left(c_4^2\beta^2\right) \\
&- \left(c_4^2\gamma^2\right)\log_2\left(c_4^2\gamma^2\right) - c_6^2\log_2 c_6^2 .
\end{aligned} \tag{5.12}$$

It is possible to decompose the entanglement into different contributions and to generalize the expressions for E_{orbital} and E_{spin} in Eq. (5.7). To calculate the orbital entanglement we construct the orbital wave function and use this to get the EOF of the reduced density matrix. The orbital wave function is

$$|\Psi\rangle_{\mathrm{orbital}} = c_1|3,0\rangle + \sqrt{c_2^2 + c_3^2}|2,1\rangle + \sqrt{c_4^2 + c_5^2}|1,2\rangle + c_6|0,3\rangle,$$

$$N(\rho)$$
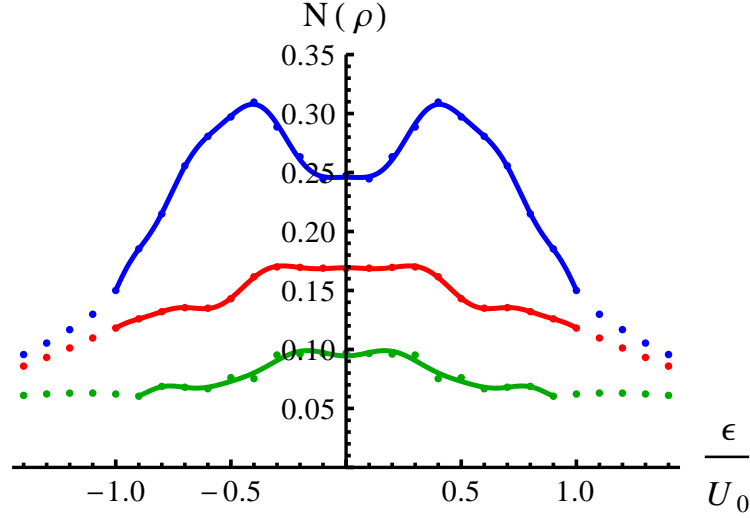
Figure 5.6: Negativity for the two-site Bose-Hubbard model for three different temperatures. The tunneling amplitude is for all temperatures $t/U_0 = 0.1$ and the spin-dependent on-site interaction is $U_2/U_0 = 0.1$. The blue line and the blue dots correspond to $k_B T = 0.25 U_0$, red line and red dots correspond to $k_B T = 0.5 U_0$ and green line and green dots correspond to $k_B T = 0.5 U_0$. Note that due to significant numerical errors the negativity is correct only up to ± 0.025; nevertheless, the accuracy is high enough to obtain the main qualitative features for the different temperatures.

where the quantum numbers refer to $|n_L, n_R\rangle$. So the orbital entanglement of formation between the left and the right well is given by

$$E_{\text{orbital}} = -c_1^2 \log_2 c_1^2 - (c_2^2 + c_3^2) \log_2(c_2^2 + c_3^2) - (c_4^2 + c_5^2) \log_2(c_4^2 + c_5^2) - c_6^2 \log_2 c_6^2 \,. \tag{5.13}$$

The spin wave function is given by

$$|\Psi\rangle_{\text{spin}} = \sqrt{c_1^2 + c_5^2}|\{1,0\},1\rangle + c_2|\{2,1\},1\rangle + \sqrt{c_3^2 + c_6^2}|\{0,1\},1\rangle + c_4|\{1,2\},1\rangle \,, \tag{5.14}$$

where the quantum numbers refer to $|\{S_L, S_R\}, S_{tot}\rangle$. The EOF of these orthonormal basis vectors is

$$E(|\{1,0\},1\rangle) = E(|\{0,1\},1\rangle) = 0$$

and

$$E(|\{2,1\},1\rangle) = E(|\{1,2\},1\rangle) = -\alpha^2 \log_2 \alpha^2 - \beta^2 \log_2 \beta^2 - \gamma^2 \log_2 \gamma^2 \,.$$

The EOF due to spin entanglement is therefore

$$E_{\text{spin}} = c_2^2 E(|\psi_2\rangle) + c_4^2 E(|\psi_4\rangle). \tag{5.15}$$

117
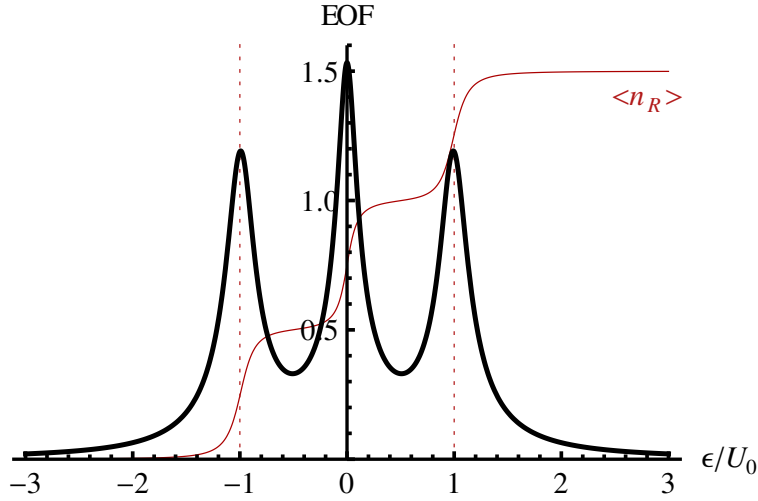
Figure 5.7: EOF between two wells for three bosons with antiferromagnetic interactions ($t/U_0 = 0.1$ and $U_2/U_0 = 0.1$) for the total spin $S_{tot} = 1$.

Note that

$$
\begin{aligned}
\left(c_2^2 \alpha^2 + c_3^2\right) \quad \log_2 \quad & \left(c_2^2 \alpha^2 + c_3^2\right) + \left(c_2^2 \beta^2\right) \log_2 \left(c_2^2 \beta^2\right) + \left(c_2^2 \gamma^2\right) \log_2 \left(c_2^2 \gamma^2\right) \\
\leq \quad & c_3^2 \log_2 \left(c_2^2 + c_3^2\right) + \left(c_2^2\right) \log_2 \left(1 + \frac{c_3^2}{c_2^2}\right) + c_2^2 \log_2 c_2^2 - c_2^2 E(|\psi_2\rangle) \\
= \quad & \left(c_2^2 + c_3^2\right) \log_2 \left(c_2^2 + c_3^2\right) - c_2^2 E(|\psi_2\rangle),
\end{aligned}
\tag{5.16}
$$

where $\log(1 + dz) \leq d\log(1 + z)$ for $d \geq 1$ and $z \geq 0$ has been used. Because of Eq. (5.16) the entanglement of formation is bounded from below,

$$
E(|\Psi\rangle) \geq E_{\text{orbital}} + E_{\text{spin}} .
\tag{5.17}
$$

5.4 Arbitrary Number of Bosons

Let Ψ be a wave function which describes the state of N bosons. This wave function can be written in terms of a basis, which is ordered according to the occupation numbers N_L and N_R, the spin in the left well S_L and in the right well S_R, and the total spin S_{tot};

$$
|\Psi\rangle = \sum_{n=1}^{D} c_n |\phi_n\rangle,
\tag{5.18}
$$
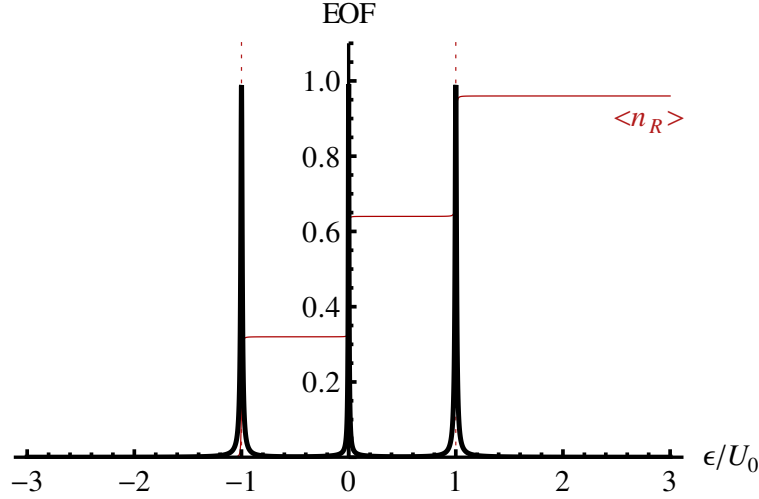
Figure 5.8: EOF between two wells for three bosons with antiferromagnetic interactions ($t/U_0 = 0.005$ and $U_2/U_0 = 0.1$) for the total spin $S_{tot} = 1$.

where $\sum_n c_n^2 = 1$ and $D \geq N$ is the dimension of the basis. We can rearrange this sum by sorting it according to the occupation numbers:

$$|\Psi\rangle = \sum_{m=0}^{N} |\psi_m\rangle,$$

where $|\psi_m\rangle$ is the part of the wave function belonging to $N_L = m$. If $N(m)$ is the number of basis vectors belonging to $N_L = m$, $|\psi_m\rangle$ is given by

$$|\psi_m\rangle = \sum_{i=1}^{N(m)} c(m)_i |\phi(m)_i\rangle, \tag{5.19}$$

where $\sum_{i=1}^{N(m)} c(m)_i^2 \leq 1$ and $c(m)_i$ denote the coefficients c_i which belong to $N_L = m$. Now it is possible to generalize Eqs. (5.13) and (5.15) and to define the orbital EOF

$$E_{\text{orbital}} = -\sum_{m=0}^{N} \sum_{i=1}^{N(m)} c(m)_i^2 \log_2 \sum_{i=1}^{N(m)} c(m)_i^2 \tag{5.20}$$

and the spin EOF

$$E_{\text{spin}} = \sum_{n=1}^{D} c_n^2 E(|\phi_n\rangle). \tag{5.21}$$

It is not necessary to to specify which basis vectors in Eq. (5.18) belong to which angular momentum configuration like in Eq. (5.14), because the total spin entanglement entropy can be written as a sum over all basis vectors.

In this section we prove that Eq. (5.17) is true for any number of bosons in a double well:

$$E(|\Psi\rangle) \geq E_{\text{orbital}} + E_{\text{spin}}. \tag{5.22}$$
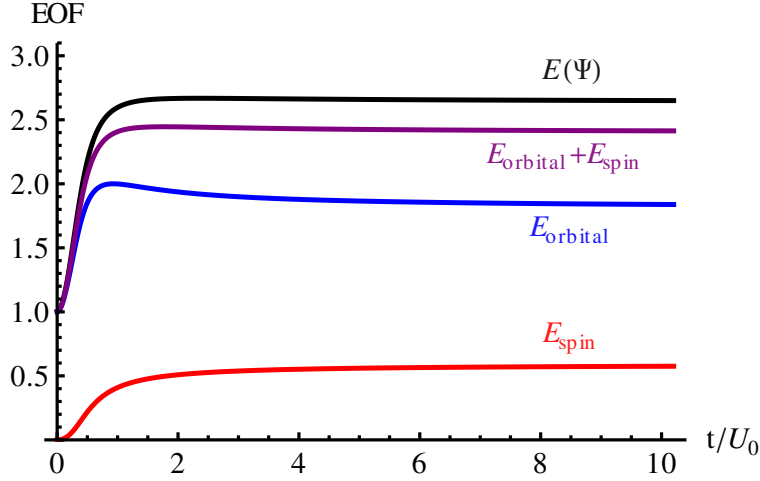
Figure 5.9: EOF, E_{spin}, E_{orbital} and $E_{\text{spin}} + E_{\text{orbital}}$ between two symmetric wells for three bosons with antiferromagnetic interactions ($U_2/U_0 = 0.1$) in a symmetric double-well potential ($\varepsilon/U_0 = 0$).

$E(|\Psi\rangle)$ decomposes in a sum over m: $E(|\Psi\rangle) = \sum_m^N E(|\psi_m\rangle)$. It is possible to write down the EOF for each $|\psi_m\rangle$ in the following way:

$$E(|\psi_m\rangle) = -\sum_j \left(\sum_i \alpha(m)_{ij}^2 c(m)_i^2 \right) \log_2 \left(\sum_i \alpha(m)_{ij}^2 c(m)_i^2 \right),$$

which defines a basis for each vector $\phi(m)_i$:

$$|\phi(m)_i\rangle = \sum_k \sum_l a(m)_{ik} a(m)_{il} |L_k\rangle \otimes |R_l\rangle = \sum_j \alpha(m)_{ij} |L, R\rangle_j \,,$$

where $\sum_j \alpha_{ij}^2 = 1$. To prove Eq. (5.22) for any number of bosons, it is necessary and sufficient to show that Eq. (5.22) is true for each $E(|\psi_m\rangle)$, i.e.,

$$\sum_j \left(\sum_i \alpha_{ij}^2 c_i^2 \right) \log_2 \left(\sum_i \alpha_{ij}^2 c_i^2 \right) \leq \left(\sum_i c_i^2 \right) \log_2 \left(\sum_i c_i^2 \right) + \sum_i c_i^2 \sum_j \alpha_{ij}^2 \log_2 \alpha_{ij}^2 \,.$$

The term on the left-hand side can be rearranged,

$$\begin{aligned}
\sum_j \left(\sum_i \alpha_{ij}^2 c_i^2 \right) \log_2 \left(\sum_i \alpha_{ij}^2 c_i^2 \right) &= \sum_j \sum_i \left(\alpha_{ij}^2 c_i^2 \right) \log_2 \left(\alpha_{ij}^2 c_i^2 \right) \\
&+ \sum_j \sum_i \left(\alpha_{ij}^2 c_i^2 \right) \log_2 \left(\frac{\sum_n \alpha_{nj}^2 c_n^2}{\alpha_{ij}^2 c_i^2} \right) ,
\end{aligned}$$

$$(5.23)$$

as well as the term on the right-hand side,

$$
\left(\sum_i c_i^2 \right) \log_2 \left(\sum_i c_i^2 \right) + \sum_i c_i^2 \sum_j \alpha_{ij}^2 \log_2 \alpha_{ij}^2
$$

$$
= \left(\sum_i c_i^2 \right) \log_2 \left(\sum_i c_i^2 \right) - \sum_i c_i^2 \log_2 c_i^2 + \sum_i \sum_j \left(\alpha_{ij}^2 c_i^2 \right) \log_2 \left(\alpha_{ij}^2 c_i^2 \right) .
$$

Note that due to Jensen's inequality

$$
\sum_j \left(\alpha_{ij}^2 c_i^2 \right) \log_2 \left(\frac{\sum_n \alpha_{nj}^2 c_n^2}{\alpha_{ij}^2 c_i^2} \right) \leq c_i^2 \log_2 \left(\frac{\sum_j \sum_n \alpha_{nj}^2 c_n^2}{c_i^2} \right)
$$

$$
= c_i^2 \log_2 \left(\sum_n c_n^2 \right) - c_i^2 \log_2 c_i^2,
$$

Eq. (5.23) is fulfilled and therefore Eq. (5.22).

Comparison with the Entanglement of Particles

The amount of entanglement shared between two parties might be lowered by super-selection rules.[1] In case two parties share N particles and a particle superselection rule applies, the extractable bipartite entanglement, i.e. the degree of entanglement one can entangle two initially not entangled quantum registers located at A and B, is given by the entanglement of particles[2]

$$
E_P \left(|\Psi_{AB}\rangle \right) \equiv \sum_n P_n \, E \left(|\Psi_{AB}^{(n)}\rangle \right),
$$

where $|\Psi_{AB}^{(n)}\rangle$ is $|\Psi_{AB}\rangle$ projected onto the subspace of fixed local particle number, i.e. n particles for one party and $N - n$ for the other.

The entanglement of particles for two bosons in a double well is given by E_{spin} in Eq. (5.7). For three bosons the case $S_{tot} = 2$ and $S_{tot} = 3$ is trivial, but the case $S_{tot} = 1$ is more interesting and will be examined. To calculate E_P we write down the projection obeying local particle superselection rules. The projections onto $n_L = 3$ and $n_L = 0$ are trivial and do not contribute to E_P. The projection onto $n_L = 2$ leads to Eq. (5.11) with $P_2 = c_2^2 + c_3^2$. The entanglement contained in this state is given by

$$
E \left(|\Psi_{LR}^{(2)}\rangle \right) = -\frac{c_2^2 \alpha^2 + c_3^2}{c_2^2 + c_3^2} \log_2 \frac{c_2^2 \alpha^2 + c_3^2}{c_2^2 + c_3^2} - \frac{c_2^2 \beta^2}{c_2^2 + c_3^2} \log_2 \frac{c_2^2 \beta^2}{c_2^2 + c_3^2} - \frac{c_2^2 \gamma^2}{c_2^2 + c_3^2} \log_2 \frac{c_2^2 \gamma^2}{c_2^2 + c_3^2}
$$

---

[1] [Bartlett and Wiseman(2003)]

[2] [Wiseman and Vaccaro(2003)]

and thereby contributes

$$
\begin{aligned}
P_2 \, E|\Psi_{LR}^{(2)}\rangle &= -\left(c_2^2\alpha^2 + c_3^2\right)\log_2\left(c_2^2\alpha^2 + c_3^2\right) - \left(c_2^2\beta^2\right)\log_2\left(c_2^2\beta^2\right) \\
&\quad - \left(c_2^2\gamma^2\right)\log_2\left(c_2^2\gamma^2\right) + \left(c_2^2 + c_3^2\right)\log_2\left(c_2^2 + c_3^2\right)
\end{aligned}
$$

to E_P. A comparison with Eq. (5.12) shows, that the equation

$$
E(|\Psi\rangle) = E_{\text{orbital}} + E_P \tag{5.24}
$$

holds for three bosons. This equation is also true for higher boson numbers. The contribution of the state (5.19) to E_P is given by

$$
\begin{aligned}
P_m \, E|\Psi_{LR}^{(m)}\rangle &= -\sum_j \left(\sum_i \alpha(m)_{ij}^2 c(m)_i^2\right)\log_2\left(\sum_i \alpha(m)_{ij}^2 c(m)_i^2\right) \\
&\quad + \left(\sum_i c(m)_i^2\right)\log_2\left(\sum_i c(m)_i^2\right) .
\end{aligned}
$$

A comparison with Eq. (5.20) shows that Eq. (5.24) holds indeed for all boson numbers.

The necessity to take a superselection rule into account may arise due to several reasons. In some cases the phase between states with different local particle occupation numbers is not well defined.[1] Consider the bipartite state

$$
|\psi_\theta\rangle_{AB} = \sqrt{\frac{1}{2}}\left(|1,0\rangle + e^{i\phi}|0,1\rangle\right). \tag{5.25}
$$

In case there is no shared reference frame and no tunneling between the two parties the phase is experimentally not accessible and the state is indistinguishable from an incoherent mixture

$$
\rho_{AB} = \frac{1}{2}\left(|1,0\rangle\langle1,0| + |0,1\rangle\langle0,1|\right) . \tag{5.26}
$$

Whenever one is concerned with the occupation number of massive particles, the detailed properties of the system determine which LOCCs (local operations and classical communication) are allowed: if tunneling is forbidden LOCCs will conserve the local particle number. In this case a local particle number super:selection rule must be taken into account. A more trivial example is the case of a superselection rule for the total particle number.[2]

In our model (4.3) the phase is well-defined due to the finite tunneling amplitude. The amount of orbital entanglement E_{orbital} depends directly on the particle fluctuations caused by the tunneling between the sites. In the absence of tunneling, the orbital entanglement vanishes and the superselection rule for the local particle number is effectively enforced.

---

[1] [Dowling *et al.*(2006)]

[2] [Cramer *et al.*(2011)]

Creation of Entanglement Structures

In the case of two spin-1 bosons in a double well the state of total spin zero ($S_{tot} = |\vec{S}_L + \vec{S}_R| = 0$) is singled out. First, it can be separated from the $S_{tot} = 2$ state due to a different particle distribution within the double well in the vicinity of the single-particle tunneling resonance (i.e. $\epsilon/U_0 = 0.5$). Secondly, it represents the two-qutrit singlet state and thereby contains the maximal qutrit entanglement of $\log_2 3$. This distinguishes the qutrit entanglement from qubit entanglement, where the singlet state and the triplet $(S_{tot})_z = 0$ state contain the same amount of entanglement.

This can be used to create specific entanglement structures in 2D optical super-lattices (see Fig. 4.6).

Chapter 6

Conclusions

In this thesis we have analyzed various aspects of spinor condensates in optical superlattices, focusing on possibilities to use them as simulators for mesoscopic magnetism and as devices to create entangled states.

We have analyzed the ground-state phase diagram for spinless and spin-1 atoms in period-2 superlattices. To prepare ourself for this task we reviewed the case of spinless and spin-1 atoms in conventional optical lattices. To study atoms in superlattices we included the dynamics within the unit cells exactly and the tunneling between unit cells in a mean-field approximation. We discussed several methods to treat this mean-field Hamiltonian and concluded that in the spinless case a simple stability analysis is sufficient to determine whether the system is Mott-insulating or superfluid. Using this method, we have calculated the phase diagram for spinless bosons in optical superlattices. In agreement with previous studies we found a contraction of Mott lobes to loops for specific values of the energy offset. We have presented a detailed study of the various Mott phases which emerge when the chemical potential and the energy offset are varied.

In the case of spin-1 atoms in superlattices the mean-field Hamiltonian shows a much richer quantum phase diagram. For antiferromagnetic interactions all Mott lobes are elongated towards higher tunneling amplitudes. Mott lobes with an even number of atoms at each lattice site are especially favored because their atomic spins can couple to form spin singlets. A small, non-vanishing order parameter leads to increased atom number fluctuations and higher spin configurations, and, as a consequence, to higher on-site repulsion. Thus, the ground-state energy for small values of the order parameter is increased. For certain parameter regimes this leads to the appearance of two local minima of the ground state energy functional (one at vanishing order parameter, one at a finite value of the order parameter) separated by an energy barrier. The higher one corresponds to a metastable quantum phase. Thus, the system shows a hysteretic behavior and the phase transitions are of first order, whereas they are strictly of second order for the spinless case. For a realistic value of the spin-dependent interactions for sodium it depends on the parity of the atom number if the phase transition of a specific Mott lobe becomes first order or remains second order. For smaller values of the spin-dependent interactions all Mott

lobes show first-order phase transitions, contrary to the case of spin-1 atoms in usual lattices where the phase transition of the Mott lobe with one atom per site remains second order for all values of the spin interaction. Because of the richer properties of the energy functional in the spin-1 case it is no longer possible to determine the quantum phase of the system with a stability analysis of the Mott phase only. The ground-state energy functional for each point in parameter space has to be analyzed, and we have given a detailed analysis of the size of the various Mott phases in the atomic limit and pointed out the differences to the case of spinless bosons.

We have also discussed the effects of magnetic fields by using an effective Hamiltonian which includes a quadratic Zeeman shift. For antiferromagnetic interactions magnetic fields break the degeneracy between different polar superfluid phases. This leads to new classes of metastable phases and thus an even richer phase diagram. In the ferromagnetic case magnetic fields cause first-order phase transitions and metastable phases. These results apply to spin-1 atoms in superlattices as well as in usual lattices.

Furthermore, we have studied spin-1 atoms deep in the Mott-insulating phase when the superlattice decomposes within mean-field theory into isolated double-well potentials. Ultracold atoms in deep double-well potentials are well described by a two site Bose-Hubbard model. We analyzed the two-site Bose-Hubbard model for spin-1 atoms explicitly for small numbers of bosons. Starting from the explicit form of the Hamiltonian, we have discussed the physics of the bosonic staircases. These bosonic staircases are the result of the finite on-site interaction in the Bose-Hubbard model. Atoms can move from on site to the other when the energy offset is large enough to compensate this on-site interaction; high tunneling amplitudes wash out the staircase structure since the atoms are delocalized in this case. Bosonic staircases of spinless atoms are evenly spaced because the difference in the interaction energy between one and two atoms is the same as between two and three atoms (and for higher atom numbers). This is not the case for spin-1 atoms, and that is the reason why the steps are not regular for spin-1 atoms. The staircases for different total spins establish a correspondence of the spatial motion and the spin configuration making the system a model for mesoscopic magnetism. We have also studied the impact of magnetic fields and found that weak magnetic fields do not destroy this correspondence.

We also generalized the concept of bosonic staircases to extended superlattices. We examined the occupation numbers of single sites and found single-atom resonances. We detected clear fingerprints of single-atom resonances also in the density of condensed bosons. In superlattices, we have also compared the single-atom resonances for spin-1 atoms with the case of spinless atoms and concluded that magnetic ordering changes the occupation numbers of individual lattice sites.

Spinor gases in optical lattices can also be used to engineer strongly correlated states for quantum information processing. We have examined the bipartite entanglement for the two-site Bose-Hubbard model and have constructed states of maximal entanglement. We have shown that spin-1 atoms allow stronger quantum correlations between the wells than spinless bosons. In addition to orbital entangle-

ment, spin-1 atoms allow spinor entanglement. We have analyzed the contribution of orbital and spin degrees of freedom and derived a lower bound of the total entanglement, which is the sum of the orbital entanglement and the spin entanglement. We have examined the quantum correlations between the wells for different values of the energy offset and different ratios of the tunneling strength relative to the on-site interaction. Because the $S_{tot} = 0$ singlet state of two bosons does contain more entanglement than the other eigenstates of the system this correspondence can be used to construct an entanglement witness in the system: in case one detects the typical spatial behavior of the $S_{tot} = 0$ state one can conclude to have its entanglement. With the help of fluorescence imaging it is also possible to depopulate doubly-occupied sites in the lattice and thereby to build a spin filter. At this point, we have consider entanglement mainly as a theoretical characterization of the many-body state of the system. We compared the entanglement of particles and thereby elucidated the meaning of orbital entanglement and of superselection rules for the local particle number.

We have discussed entanglement between the sites, not the entanglement between the individual atoms. Even for an occupancy of one, i.e., one atom per site, these are different quantities, because the bosons are indistinguishable. It was proposed to measure the entanglement between (spinless) bosons in an optical lattice by standard time-of-flight measurements.[1] Such measurements do not preserve the information about the entanglement between the individual sites. There are other possibilities to examine these systems experimentally. First, it is possible to estimate the entanglement by measurements of the atom positions, because these correspond to specific spin configurations, as we have demonstrated. These atom positions can be determined by standard time-of-flight measurements or direct fluorescence detection of individual sites. It is also possible to detect the spin configurations directly in a non-demolishing way with the help of the quantum polarization spectroscopy. Furthermore, it may be possible to relate the entanglement to additional observable experimental quantities, such as magnetization fluctuations in one of the wells, in analogy to what has been discussed for non-interacting particles.[2]

Outlook

Main questions for future works regarding spinor atoms in superlattices will be the the impact of spin-correlations in the Mott phase. It is interesting to generalize the spin-Hamiltonian for usual lattices to superlattices. Two regimes are can be differentiated: When the intra-well tunneling is strong the total spins per double well couples to each other. When the intra-well tunneling is small the total spins per site will couple. Depending on the regime we expect singlet or nematic ordering on sub-lattices and additional points of symmetry breaking and first order phase transitions.

Another future project will be the analysis of spin-2 atoms in superlattices. It

---

[1] [Cramer *et al.*(2011)]

[2] [Song *et al.*(2011)]

turns out that the total spin and its projection on quantization axes do not suffices anymore to describe the state fully. In this case additional quantum numbers determine the magnetic ordering.

In conclusion, we have shown that spinor bosons in optical superlattices show a rich phenomenology of different quantum phases and provide simulators for mesoscopic magnetism due to an unprecedented control of the parameters.

Appendix A

Mean-Field Calculations

A.1 *Mathematica* Code for Sec. 3.1.1

In this section we want to present some calculations done in Chapter 3. The boundaries of the Mott-lobes for spinless bosons in a usual lattice in mean-field approximation (3.12) can be obtained from Eq. (3.18)or Eq. (3.20). To determine the ground state for each parameter tuple (t, U, μ) we use an iterative procedure to calculate the self-consistent value of the order parameter. In this section we use the "Quantum Package" for *Mathematica*.[1]

To treat the problem numerically one has to limit the basis to a finite size and choose an N_{max} such that

$$|\psi\rangle = \sum_{n=0}^{N_{max}} \alpha_n |n\rangle \,. \tag{A.1}$$

In this section we choose $N_{max} = 10$ and create the basis:

```
basis = Table[ |i_n̂⟩, {i, 0, 10}]
```

$$\left\{ |0_{\hat{n}}\rangle, \ |1_{\hat{n}}\rangle, \ |2_{\hat{n}}\rangle, \ |3_{\hat{n}}\rangle, \ |4_{\hat{n}}\rangle, \ |5_{\hat{n}}\rangle, \ |6_{\hat{n}}\rangle, \ |7_{\hat{n}}\rangle, \ |8_{\hat{n}}\rangle, \ |9_{\hat{n}}\rangle, \ |10_{\hat{n}}\rangle \right\}$$

Using the "Quantum Package", we can define operators,

```
DefineOperatorOnKets[ae, { |i_n̂⟩ :→ √(i + 1)  |i + 1_n̂⟩}];
DefineOperatorOnKets[av, { |i_n̂⟩ :→ √i  |(i - 1)_n̂⟩}];
```

Here is `ae` the operator $\hat{b}^\dagger$ in Eq. (3.12) and `av` is $\hat{b}$.

We can now calculate $\hat{b}^\dagger$ and $\hat{b}$ in the given basis:

```
vf[x_, y_] := Expand[(x)† · (av) · y]
ef[x_, y_] := Expand[(x)† · (ae) · y]


v = Expand[Function[{y}, Function[{x}, vf[x, y]] /@ basis] /@ basis];
e = Expand[Function[{y}, Function[{x}, ef[x, y]] /@ basis] /@ basis];
```

The Hamiltonian is given by:

```
h[x_, y_, μ_] := Expand[(x)† · (1/2 (n̂ · (n̂ - 1)) - μ n̂ ) · y]
ham = Expand[Function[{y}, Function[{x}, h[x, y, mu]] /@ basis] /@ basis];


stoerterm[x_, y_] := Expand[(x)† · (av + ae) · y]
stoer = Expand[Function[{y}, Function[{x}, stoerterm[x, y]] /@ basis] /@ basis];


hamiltonian[μ_, t_, φ_] := (ham - t φ stoer) /. {mu → μ}
```

We can use Eq. (3.20) to determine the phase boundary numerically:

```
grenze[μ_] := Block[{eigen},
  eigen = Sort[Thread[Eigensystem[hamiltonian[μ, 0, 0]]]];
  1/ (If[eigen〚2, 1〛 == eigen〚1, 1〛,

      1. × 10^20 , Sum[ (eigen〚n, 2〛.stoer.eigen〚1, 2〛)^2 / (eigen〚n, 1〛 - eigen〚1, 1〛) , {n, 2, dim}]] )]
```

The ground state of the system is determined by an iterative procedure and can be calculated with the following function:

```
gz[μ_, t_, prec_] := Block[{ord, ϕ, grund},
  ϕ = .5;

  grund = Chop[First[Sort[Thread[Eigensystem[hamiltonian[μ, t, ϕ]]]]][[2]], prec];
  ord = grund.v.grund;

  While[Abs[ϕ - ord] > prec,
    ϕ = ord;
    grund = Chop[First[Sort[Thread[Eigensystem[hamiltonian[μ, t, ϕ]]]]][[2]], prec];
    ord = grund.v.grund];
  grund.basis
 ]
```

The function $gz[\mu, t, prec]$ calculates the ground state for any given t/U, μ/U and precision *prec*. The calculation starts with $\phi = 0.5$ and performs as many iteration as needed to obtain the precision $\langle\hat{b}\rangle_{i+1} - \langle\hat{b}\rangle_i < prec$.

For example we obtain for $t/U = 0.15$, $\mu/U = 0.9$ and $prec = 0.001$

```
gz[.9, .15, .001]
```

$0.0937197 \left|0_{\hat{n}}\right\rangle + 0.769862 \left|1_{\hat{n}}\right\rangle + 0.622636 \left|2_{\hat{n}}\right\rangle + 0.103888 \left|3_{\hat{n}}\right\rangle + 0.00779753 \left|4_{\hat{n}}\right\rangle$

At this parameter point the atomic density is given by

```
n[μ_, t_, prec_] := (gz[μ, t, prec])† · (ae · av) · gz[μ, t, prec]
```

```
n[.9, .15, .001]
```

```
1.40066
```

A.2 Matlab Code for Sec. 3.1.1

For most of the calculation in Chapter 3 we used Matlab because it is much more efficient for matrix diagonalizations. The algorithms we use are based on Mathematica algorithms presented in Appendix A.1. To prepare ourself for the more involved calculations in the following we examine the matlab code for the mean-field approximation of the usual Bose-Hubbard model.

To calculate the phase diagram given in Fig. 3.3 we choose our basis according to Eq. (A.1) with $N_{max} = 11$, define the annihilation operators $\hat{b} =$ dest in this basis as well as the identity matrix $\mathbb{1} =$ iden,

```
N = 11;
dest = spdiags(sqrt(0:N-1)',1,N,N);
iden = speye(N,N);

a = dest;
n = a'*a;
```

We can build up the different terms in the Hamiltonian given in Eq. (3.12),

```
Ham_int =  n*(n-iden);
Ham_mu =    n;
Ham_mean = (a+a');
```

and define a function which generates the Hamiltonian for each given μ, t, U and ϕ,

```
function A=ham(mu,t,ph);
global Ham_int; global Ham_mu; global Ham_mean;global iden;
A=(1/2 * Ham_int - mu * Ham_mu - t*ph*Ham_mean +  t *(ph^2)*iden);
```

Note that we had to introduce `global` variables. The iterative procedure to calculate the self-consistent mean-field parameter ϕ can be written like

```
function l=it(mu,t,prec)
  ph=.5;
  [ground,~] = eigs(ham(mu,t,ph),1,'sa');
  global a;
  ord=ground'*a*ground;
  while abs(ph-ord)>prec
     ph=ord;
     [ground,~] = eigs(ham(mu,t,ph),1,'sa');
     ord=ground'*a*ground;
  end;
l=ord;
```

Matlab Code for Sec. 3.2

We write derive the annihilation operators $\hat{b}_1$, $\hat{b}_0$ and $\hat{b}_{-1}$ in the basis with $N_{max} = 10$

```
N = 10;
dest = spdiags(sqrt(0:N-1)',1,N,N);
iden = speye(N,N);

aa1 = kron(kron(dest,iden),iden);
aa0 = kron(kron(iden,dest),iden);
aa1m= kron(kron(iden,iden),dest);
iid = kron(kron(iden,iden),iden);
```

Note that the size of the operators is much bigger than necessary to describe 10 spin-1 atoms. The operators `aa1`, `aa0`, `aa1m` and `iid` have size $N^3 \times N^3$. We sort out all irrelavant entries by introducing a cutoff:

```
cutoff = N;
temp = round(full(diag(aa1'*aa1 +aa0'*aa0+aa1m'*aa1m)));
index = temp<cutoff;

a1 = aa1(index,index);
a0 = aa0(index,index);
a1m = aa1m(index,index);
id = iid(index,index);
```

After this cutoff procedure the size decrease from $N^3 \times N^3 = 1000 \times 1000$ to 220×220. Now we can continue by defining the atom number operator $\hat{n} =$ `n` and the spin-1 matrices according to Eq. (2.33),

```
n = a1'*a1+a0'*a0+a1m'*a1m;
Sx = (a0'*a1 + a1'*a0 + a1m'*a0 + a0'*a1m)/sqrt(2);
Sy = sqrt(-1) * (a0'*a1 - a1'*a0 + a1m'*a0 - a0'*a1m)/sqrt(2);
Sz = (a1'*a1 - a1m'*a1m);
```

and build up the terms of the Hamiltonian (3.24),

```
Ham_int =  n*n-n;
Ham_mu =   n;
Ham_spin = Sx^2 + Sy^2 + Sz^2 -2*n;
```

Similar to the spinless case we introduce a function which generates the Hamiltonian (3.24) for each given t, U, μ and $\vec{\phi}$

```
function A=ham(t,mu,s,ph1,ph0,ph1m)
global a1; global a0; global a1m; global id;
global Ham_int; global Ham_mu; global Ham_spin;

A=(1/2 * Ham_int + s/2* Ham_spin - mu * Ham_mu
 - t*(ph1*(a1+a1')+ph0*(a0+a0')+ph1m*(a1m+a1m'))
 + id*t*(ph1^2+ph0^2+ph1m^2));
```

The iterative procedure can be implemented like in the function `it_spinor`, which is a function of the system parameters and returns the self-consistent value of $\vec{\phi}$,

```
function l=it_spinor(t,mu,s,q,prec,anf1,anf0,anf1m)
ph1 = anf1; ph0 = anf0; ph1m = anf1m;
[ground,~] = eigs(ham(t,mu,s,q,ph1,ph0,ph1m),1,'sa');
global a1; global a0;global a1m;
ord1=ground'*a1*ground;
ord0=ground'*a0*ground;
```

```
ord1m=ground'*a1m*ground;
while (abs(ph1-ord1)+abs(ph0-ord0)+abs(ph1m-ord1m))>prec
    ph1=ord1;ph0=ord0;ph1m=ord1m;
    [ground,energy] = eigs(ham(t,mu,s,q,ph1,ph0,ph1m),1,'sa');
    ord1=ground'*a1*ground;
    ord0=ground'*a0*ground;
    ord1m=ground'*a1m*ground;
end;
l=[ord1,ord0,ord1m];
```

The stable quantum phase of the system can only be determined by an analysis of the ground-state energy functionals since for certain parameter regimes there are several fixed points of the map (3.34). It is straightforward to analyze $E[\phi]$ numerically. When we analyze $E[\phi]$ along one direction, say $\phi_0 = 0$ and $\phi_1 = \phi_{-1} \neq 0$ we can use the following function

```
function A=efph(t,mu,s)
prec = 0.1;
liste(1)= eigs(ham(t,mu,s,0.01,0,0.01),1,'sa');
liste(2)= eigs(ham(t,mu,s,0.05,0,0.05),1,'sa');
sf = liste(1) > liste(2);
if sf == 0
    ph=0:prec:1;
    l=length(ph);
    for ind = 3:l;
        liste(ind) = eigs(ham(t,mu,s,ph(ind),0,ph(ind)),1,'sa');
    end;
    test = diff(diff(liste)>0);
    [a,b]=sort(test,'descend');
    if a(1)==0
        phase = 1;
    elseif  a(1) == 1
        if liste(b(1)) < liste(1)
            phase = 3;
        elseif liste(b(1)) > liste(1)
            phase = 2;
        end;
    end;
else
    phase = 4;
end;
A=phase;
```

For given parameters t, U_0, U_2 and μ the function `efph` returns a number where (1) denotes the Mott phase, (2) the metastable superfluid one, (3) the metastable Mott phase and (4) the superfluid one. Note that this code snippet is insufficient

to calculate the stable quantum phase: for magnetic fields the symmetry betweeen the longitudinal and transversal polar order parameters is broken and one needs to analyze $E[\phi]$ along $\phi_0 \neq 0$ as well.

After performing this numerically efficient method to determine the quantum phase we can use the function `it_spinor` to determine the order parameter of the system. In the superfluid phase we choose a starting point sufficiently far away from zero, say 1; when we know already from the energy-functional analysis that the system is Mott insulating, the order parameter is 0 and we do not need another iterative procedure.

Matlab Code for Sec. 3.3

We start by calculating the relevant operators $\hat{L}$ and $\hat{R}$

```
N = 8;
dest = spdiags(sqrt(0:N-1)',1,N,N);
iden = speye(N,N);

ll = kron(dest,iden);
rr = kron(iden,dest);
iid = kron(iden,iden);
```

We use a cutoff to keep only the basis states belonging to a maximal atom number of N_{max}=8:

```
cutoff = N;
temp = round(full(diag(ll'*ll +rr'*rr )));
index = temp<cutoff;

l = ll(index,index);
r = rr(index,index);
id = iid(index,index);

nl = l'*l;
nr = r'*r;
n=nl+nr;
```

Next we determine the different terms of the Hamiltonian (3.38)

```
Ham_int =  nl*nl-nl+nr*nr-nr;
Ham_mu =   nl+nr;
Ham_eps =   nl-nr;
Ham_ti =  l'*r + r'*l;
```

and define a function which return for each t_i, t_e, U, μ and ε the Hamiltonian (3.38),

```
function A=ham(ti,te,mu,eps,phl,phr)
global l;global r;global id;
global Ham_int; global Ham_mu; global Ham_ti; global Ham_eps;
te_reward = (phr*(l+l')+phl*(r+r')+2*phr*(r+r')+2*phl*(l+l'));
te_punish = 2*(id*phl*phr+id*phl*phl+id*phr*phr);
A = 1/2 * Ham_int - ti * Ham_ti - mu * Ham_mu + eps * Ham_eps
                          - te * te_reward + te * te_punish;
```

We can determine the self-consistent order parameter by an iterative procedure since we deal with spinless bosons. The function performing the iterations is

```
function longit(ti,te,mu,eps,prec,anf)
phl = anf; phr = anf;
[ground,~] = eigs(ham(ti,te,mu,eps,phl,phr),1,'sa');
global l;global r;
ordl=max(ground'*l*ground,0);
ordr=max(ground'*r*ground,0);
ind = 1;
while (abs(phl-ordl)+abs(phr-ordr))>prec% & ind < 100
    if ind > 50
        break;
    else
        phl=ordl;phr=ordr;
        [ground,~] = eigs(ham(ti,te,mu,eps,phl,phr),1,'sa');
        ordl=max(ground'*l*ground,0);
        ordr=max(ground'*r*ground,0);
        ind =ind+1;
    end;
end;
long=[ordl,ordr];
```

In the function `longit` we stop the iterative procedure when the wanted precession `prec` is not reached after 50 iterations. We can use a similar function to determine the ground state and thereby calcualate expectation values such as $\langle \hat{n} \rangle$ for the bosonic staircases in Sec. 4.3.

Matlab Code for Sec. 3.4

In this section we present the matlab code for spin-1 atoms in superlattices without commenting it because the concepts used are the ones used for spin-1 atoms in usual lattices and spinless bosons in superlattices. For the sake of completeness we cite some code snippets.

The basis and relevant operators are defined as follows:

```
N = 7;
cutoff = N;
dest = spdiags(sqrt(0:N-1)',1,N,N);
iden = speye(N,N);


ll1 = kron(kron(kron(kron(kron(dest,iden),iden),iden),iden),iden);
ll0 = kron(kron(kron(kron(kron(iden,dest),iden),iden),iden),iden);
ll1m= kron(kron(kron(kron(kron(iden,iden),dest),iden),iden),iden);

rr1 = kron(kron(kron(kron(kron(iden,iden),iden),dest),iden),iden);
rr0 = kron(kron(kron(kron(kron(iden,iden),iden),iden),dest),iden);
rr1m= kron(kron(kron(kron(kron(iden,iden),iden),iden),iden),dest);

iid = kron(kron(kron(kron(kron(iden,iden),iden),iden),iden),iden);

% Find the relevant entries
temp = round(full(diag(ll1'*ll1 + ll0'*ll0 + ll1m'*ll1m
+ rr1'*rr1 + rr0'*rr0 + rr1m'*rr1m)));
index = temp<cutoff;

% And redefine the operators
global l1;global l0;global l1m;
global r1;global r0;global r1m; global id;

l1 = ll1(index,index);
l0 = ll0(index,index);
l1m = ll1m(index,index);

r1 = rr1(index,index);
r0 = rr0(index,index);
r1m = rr1m(index,index);

id = iid(index,index);

nl = l1'*l1 + l0'*l0 + l1m'*l1m;
nr = r1'*r1 + r0'*r0 + r1m'*r1m;
n=nl+nr;

Sxl = (l0'*l1 + l1'*l0 + l1m'*l0 + l0'*l1m)/sqrt(2);
Syl = sqrt(-1) * (l0'*l1 - l1'*l0 + l1m'*l0 - l0'*l1m)/sqrt(2);
Szl = (l1'*l1 - l1m'*l1m);

Sxr = (r0'*r1 + r1'*r0 + r1m'*r0 + r0'*r1m)/sqrt(2);
Syr = sqrt(-1) * (r0'*r1 - r1'*r0 + r1m'*r0 - r0'*r1m)/sqrt(2);
```

```
Szr = (r1'*r1 - r1m'*r1m);

% Build up the Hamiltonian
global Ham_int; global Ham_mu; global Ham_spin;
global Ham_ti; global Ham_eps; global S; global Slq; global Srq;

Slq = Sxl^2 + Syl^2 + Szl^2;
Srq = Sxr^2 + Syr^2 + Szr^2;
S = Slq + Srq +2*(Sxl*Sxr + Syl*Syr + Szl*Szr);

Ham_int =  nl*nl-nl+nr*nr-nr;
Ham_mu =   nl+nr;
Ham_eps =   nl-nr;
Ham_spin = Slq -2*nl + Srq -2*nr;
Ham_ti =  l1'*r1 + r1'*l1 +l0'*r0 + r0'*l0 +l1m'*r1m + r1m'*l1m ;
```

In the same way as in the previous sections we can use this to define a function generating the Hamiltonian (3.41). The determination of the stable quantum phase is more elaborate than in the other cases but not qualitatively different.

Appendix B

Calculations for Bosonic Staircases

In this section we present the *Mathematica* code for Chapter 4; not all necessary *Mathematica* commands are included but the most relevant.

B.1 Spinless Atoms in a Double-Well Potential

In this section we use the "Quantum Package" for *Mathematica*[1] to calculate the Hamiltonian Eq. (4.1) for different atom numbers per double well. The problem we are solving in this section is fairly easy and it is not necessary to apply this complicated framework, but we can use it as an example for more complicated problems.

Using the "Quantum Package", we can define operators,

```
DefineOperatorOnKets[m1ae, { | i_m̂1̂⟩ ⧴ √i+1̄  | i+1_m̂1̂⟩}];
DefineOperatorOnKets[m1av, { | i_m̂1̂⟩ ⧴ √ī  | (i-1)_m̂1̂⟩}];
DefineOperatorOnKets[m2ae, { | i_m̂2̂⟩ ⧴ √i+1̄  | i+1_m̂2̂⟩}];
DefineOperatorOnKets[m2av, { | i_m̂2̂⟩ ⧴ √ī  | (i-1)_m̂2̂⟩}];
```

Here is `m1ae` the operator $\hat{L}^\dagger$ in Eq. (4.1), `m1av` is $\hat{L}$, `m2ae` is $\hat{R}^\dagger$ and `m2av` is $\hat{R}$. Next we create the basis for five bosons in the double-well potential,

```
bosons = 5;
basis = Table[ | (bosons - i)_m̂1̂ , i_m̂2̂⟩, {i, 0, bosons}]
```

$$\left\{ \; | \; 5_{\hat{m1}} , \; 0_{\hat{m2}} \rangle, \; | \; 4_{\hat{m1}} , \; 1_{\hat{m2}} \rangle, \; | \; 3_{\hat{m1}} , \; 2_{\hat{m2}} \rangle, \; | \; 2_{\hat{m1}} , \; 3_{\hat{m2}} \rangle, \; | \; 1_{\hat{m1}} , \; 4_{\hat{m2}} \rangle, \; | \; 0_{\hat{m1}} , \; 5_{\hat{m2}} \rangle \right\}$$

---

[1]Version 2.3.0 (May 2011) for Mathematica 8 by José Luis Gómez-Muñoz and Francisco Delgado

We can now calculate the Hamiltonian.

```
n1 = m1ae · m1av;
n2 = m2ae · m2av;


tunnelterm = -t (m1ae · m2av + m2ae · m1av);
diagonal = 1 / 2 ( n1 · (n1 - 1) + n2 · (n2 - 1)) - ε (n1 - n2);


h[x_, y_] := (x)† · ( diagonal + tunnelterm) · y


ham =
  Expand[Function[{y}, Function[{x}, h[x, y]] /@ basis] /@ basis];
```

The operator `n1` (`n2`) is the atom number operator of the left (right) well. The function `h[x,y]` takes any two basis vectors and returns their matrix element of Hamiltonian. The variable `ham` is the matrix given in Eq. (4.2). The eigenvalues of this Hamiltonian are given by

```
ew[p_] := Sort[Eigenvalues[ham /. {ε → p, t → .1}]]
```

Fig. 4.2 is a plot of the function `ew[p]`. The bosonic staircase can be calculated in the following way.

```
bas = Table[{bosons - i, i}, {i, 0, bosons}];
nl[p_] := bas〚All, 1〛.(#^2 & /@ First[Sort[Thread[
        Eigensystem[ham /. {ε → p, t → .02}]]]]〚2〛)
int = Table[p, {p, -4, 4, .025}];
n5 = Table[nl[int〚i〛], {i, Length[int]}];
```

The function `nl[p]` calculates the expectation value of the operator $\hat{n}_L$ in the ground state of the system when the energy off-set has the value p. Fig. 4.3 is a `ListPlot` of the table `n5`. We have used the `Table` function instead of the `Plot` command in order to superimpose the bosonic staircases belonging to different boson numbers (see right panel of Fig. 4.3).

B.2   Spin-1 Atoms in a Double-Well Potential

In this section we develop the *Mathematica* code for Sec. 4.2. We include in the code of Sec. B.1 the additional aspects of the spin-1 case. We want to find the ground state properties of the Hamiltonian Eq. (4.3). The basis we choose to treat this Hamiltonian is still a Fock basis, but we need to specify more quantum numbers (see Sec. 4.2), such as the total spin and the spin in the left and right site. To generate the basis given in Eq. (4.5) we use the function

```
basisb[x_] := Table[Table[Table[{{x - n, n}, {i, j}, k}, {k, Abs[i + j],
        Abs[i - j], -1}],
    {i, x - n, 0, -2}, {j, n, 0, -2}], {n, 0, x}] // Flatten[#, 3] & ;
```

We rewrite this basis in terms of the spins of the left and right site and their z-projections, whereby we can use the usual Clebsch-Gordan coefficients. Thus, we relate two equivalent choices for the basis spanning the Hilbert space,

$$|\{n_L, n_R\}, \{S_L, S_R\}, S_{tot}\rangle \quad \Leftrightarrow \quad |n_L, S_L, S_L^z, n_R, S_R, S_R^z\rangle. \tag{B.1}$$

The following function `secondquant[x,sz]` does this.

```
secondquant[x_, sz_] :=
 Table[ClebschGordan[{x[[2, 1]], l}, {x[[2, 2]], m}, {x[[3]], sz}]
     state[x[[1, 1]], x[[2, 1]], l, x[[1, 2]], x[[2, 2]], m],
    {l, x[[2, 1]], -x[[2, 1]], -1},
    {m, x[[2, 2]], -x[[2, 2]], -1}] // Flatten // Plus @@ # &
```

To illustrate the function `secondquant` we give an example.

```
test = basisb[2][[4]]
```

```
{{1, 1}, {1, 1}, 1}
```

```
secondquant[test, 0]
```

$$-\frac{\text{state}[1, 1, -1, 1, 1, 1]}{\sqrt{2}} + \frac{\text{state}[1, 1, 1, 1, 1, -1]}{\sqrt{2}}$$

The variable `test` is the basis vector E_4 in Eq. (4.5) and is translated into an expression containing the function `state` which has as functions parameters $n_L, S_L, S_L^z, n_R, S_R, S_R^z$. To calculate the function `state` we need to know how the spins of the atoms in each single site couple.

We define annihilation and creation operators for the left site,

```
DefineOperatorOnKets[m1ae1, { | i_⎵m1n1̂ ⟩ ⤇ √(i + 1)  | i + 1_m1n1̂ ⟩}];

DefineOperatorOnKets[m1ae0, { | j_⎵m1n0̂ ⟩ ⤇ √(j + 1)  | (j + 1)_m1n0̂ ⟩}];

DefineOperatorOnKets[m1ae1m, { | k_⎵m1n1m̂ ⟩ ⤇ √(k + 1)  | (k + 1)_m1n1m̂ ⟩}];

DefineOperatorOnKets[m1av1, { | i_⎵m1n1̂ ⟩ ⤇ √i  | (i - 1)_m1n1̂ ⟩}];

DefineOperatorOnKets[m1av0, { | j_⎵m1n0̂ ⟩ ⤇ √j  | (j - 1)_m1n0̂ ⟩}];

DefineOperatorOnKets[m1av1m, { | k_⎵m1n1m̂ ⟩ ⤇ √k  | (k - 1)_m1n1m̂ ⟩}];
```

The annihilation and creation operators for the right well are introduced analogously. Now we are able to express all relevant spin operators such as S_L, S_L^2, S_{tot}^2 etc. (see Eq. (2.33)) in terms of annihilation and creation operators.

```
sz = {{1, 0, 0}, {0, 0, 0}, {0, 0, -1}};
sp = √2 {{0, 1, 0}, {0, 0, 1}, {0, 0, 0}};
sm = √2 {{0, 0, 0}, {1, 0, 0}, {0, 1, 0}};


avvm1 = {m1av1, m1av0, m1av1m};
aevm1 = {m1ae1, m1ae0, m1ae1m};


sm2qm1 = Table[aevm1〚i〛 · (sm.avvm1)〚i〛, {i, 3}] // Plus @@ # &;
sp2qm1 = Table[aevm1〚i〛 · (sp.avvm1)〚i〛, {i, 3}] // Plus @@ # &;
sz2qm1 = Table[aevm1〚i〛 · (sz.avvm1)〚i〛, {i, 3}] // Plus @@ # &;


squadm1 = sp2qm1 · sm2qm1 - sz2qm1 + sz2qm1 · sz2qm1 // Expand;
```

Here S_L^- is given by sm2qm1 and S_L^+ by sm2qm1. The operator S_L^2 is given by squadm1.

We are now able to calculate the Clebsch-Gordan coefficients for any number of spin-1 bosons. For example, for 3 bosons in the same site the operator S^2 (can equal to S_L^2 or S_R^2) takes the form `test`:

```
num = 3;
basis = Table[Table[ | i_{m1n1}, j_{m1n0}, (num - i - j)_{m1n1m}), {j, 0, num - i}],
     {i, 0, num}] // Flatten;
l = Length[basis];

test = Table[Table[(basis[[i]])† · squadm1 · basis[[n]], {i, l}], {n, l}];
test // MatrixForm
```

$$
\begin{pmatrix}
12 & 0 & 0 & 0 & 0 & 0 & 0 & 0 & 0 & 0 \\
0 & 12 & 0 & 0 & 0 & 0 & 0 & 0 & 0 & 0 \\
0 & 0 & 10 & 0 & 4 & 0 & 0 & 0 & 0 & 0 \\
0 & 0 & 0 & 6 & 0 & 2\sqrt{6} & 0 & 0 & 0 & 0 \\
0 & 0 & 4 & 0 & 4 & 0 & 0 & 0 & 0 & 0 \\
0 & 0 & 0 & 2\sqrt{6} & 0 & 8 & 0 & 0 & 0 & 0 \\
0 & 0 & 0 & 0 & 0 & 0 & 10 & 4 & 0 & 0 \\
0 & 0 & 0 & 0 & 0 & 0 & 4 & 4 & 0 & 0 \\
0 & 0 & 0 & 0 & 0 & 0 & 0 & 0 & 12 & 0 \\
0 & 0 & 0 & 0 & 0 & 0 & 0 & 0 & 0 & 12
\end{pmatrix}
$$

We can diagonalize the matrix `test` to obtain the eigenstates of S^2 in terms of annihilation and creation operators.

```
table[3] = Table[{(1 / Norm[eigen[[i, 2]]] eigen[[i, 2]].basis)† · squadm1 · (
          1 / Norm[eigen[[i, 2]]] eigen[[i, 2]]).basis //
      Function[x, l /. Solve[l² + l == x, l] // Flatten // Sort // Last],
     (1 / Norm[eigen[[i, 2]]] eigen[[i, 2]].basis)† · sz2qm1 ·
      (1 / Norm[eigen[[i, 2]]] eigen[[i, 2]]).basis,
     (1 / Norm[eigen[[i, 2]]] eigen[[i, 2]]).basis}, {i, l}] // Simplify;
```

`table[3] // MatrixForm`

$$\begin{pmatrix}
3 & 3 & \left| 0_{m\hat{1}n0},\ 3_{m\hat{1}n1},\ 0_{m1\hat{n}1m} \right\rangle \\[4pt]
3 & 2 & \left| 1_{m\hat{1}n0},\ 2_{m\hat{1}n1},\ 0_{m1\hat{n}1m} \right\rangle \\[4pt]
3 & 1 & \frac{\left| 0_{m\hat{1}n0},2_{m\hat{1}n1},1_{m1\hat{n}1m} \right\rangle + 2\left| 2_{m\hat{1}n0},1_{m\hat{1}n1},0_{m1\hat{n}1m} \right\rangle}{\sqrt{5}} \\[8pt]
3 & 0 & \sqrt{\frac{3}{5}}\ \left| 1_{m\hat{1}n0},\ 1_{m\hat{1}n1},\ 1_{m1\hat{n}1m} \right\rangle + \sqrt{\frac{2}{5}}\ \left| 3_{m\hat{1}n0},\ 0_{m\hat{1}n1},\ 0_{m1\hat{n}1m} \right\rangle \\[8pt]
3 & -1 & \frac{\left| 0_{m\hat{1}n0},1_{m\hat{1}n1},2_{m1\hat{n}1m} \right\rangle + 2\left| 2_{m\hat{1}n0},0_{m\hat{1}n1},1_{m1\hat{n}1m} \right\rangle}{\sqrt{5}} \\[8pt]
3 & -2 & \left| 1_{m\hat{1}n0},\ 0_{m\hat{1}n1},\ 2_{m1\hat{n}1m} \right\rangle \\[4pt]
3 & -3 & \left| 0_{m\hat{1}n0},\ 0_{m\hat{1}n1},\ 3_{m1\hat{n}1m} \right\rangle \\[4pt]
1 & 1 & \frac{2\left| 0_{m\hat{1}n0},2_{m\hat{1}n1},1_{m1\hat{n}1m} \right\rangle - \left| 2_{m\hat{1}n0},1_{m\hat{1}n1},0_{m1\hat{n}1m} \right\rangle}{\sqrt{5}} \\[8pt]
1 & 0 & \sqrt{\frac{2}{5}}\ \left| 1_{m\hat{1}n0},\ 1_{m\hat{1}n1},\ 1_{m1\hat{n}1m} \right\rangle - \sqrt{\frac{3}{5}}\ \left| 3_{m\hat{1}n0},\ 0_{m\hat{1}n1},\ 0_{m1\hat{n}1m} \right\rangle \\[8pt]
1 & -1 & \frac{2\left| 0_{m\hat{1}n0},1_{m\hat{1}n1},2_{m1\hat{n}1m} \right\rangle - \left| 2_{m\hat{1}n0},0_{m\hat{1}n1},1_{m1\hat{n}1m} \right\rangle}{\sqrt{5}}
\end{pmatrix}$$

The table `table[3]` contains for each total spin quantum number and each z-projection S_z the state in the basis $|n_1, n_0, n_{-1}\rangle$, where n_σ denotes the number of atoms in the hyperfine state $\sigma \in \{1, 0, -1\}$.

To calculate the Hamiltonian Eq. (4.3) for eg. 4 bosons we need to build the `table[n]` for up to `n=4`. Having these eigenfunctions of S^2 we derived an expression for the function `state`

```
state[n1_, s1_, sz1_, n2_, s2_, sz2_] :=
 (Select[table[n1], #[[1]] == s1 && #[[2]] == sz1 &] // Flatten // #[[3]] &) ⊗
   (Select[table[n2], #[[1]] == s2 && #[[2]] == sz2 &] // Flatten // #[[3]] &) //
  Expand
```

The function `state[n1,sl,slz,nr,sr,srz]` returns the wavefunction of the atoms in the double well when the quantum numbers $n_L, S_L, S_L^z, n_R, S_R$ and S_R^z are given. As an example we look at the wavefunction of the system, when three atom are placed in the left site and the right site is empty. Their spin configuration is such that they couple to the total spin 1 and the z-projection is -1.

`state[3, 1, -1, 0, 0, 0]`

$$\frac{2 \; \left| \; 0_{m1\hat{n}0} , \; 1_{m1\hat{n}1} , \; 2_{m1\hat{n}1m} , \; 0_{m2\hat{n}0} , \; 0_{m2\hat{n}1} , \; 0_{m2\hat{n}1m} \right\rangle}{\sqrt{5}} - \frac{\left| \; 2_{m1\hat{n}0} , \; 0_{m1\hat{n}1} , \; 1_{m1\hat{n}1m} , \; 0_{m2\hat{n}0} , \; 0_{m2\hat{n}1} , \; 0_{m2\hat{n}1m} \right\rangle}{\sqrt{5}}$$

We can now use the function `secondquant` to express the basis given in Eq. (4.5) in second quantisation

`secondquant[basisb[2]⟦4⟧, 0]`

$$-\frac{\left| \; 0_{m1\hat{n}0} , \; 0_{m1\hat{n}1} , \; 1_{m1\hat{n}1m} , \; 0_{m2\hat{n}0} , \; 1_{m2\hat{n}1} , \; 0_{m2\hat{n}1m} \right\rangle}{\sqrt{2}} + \frac{\left| \; 0_{m1\hat{n}0} , \; 1_{m1\hat{n}1} , \; 0_{m1\hat{n}1m} , \; 0_{m2\hat{n}0} , \; 0_{m2\hat{n}1} , \; 1_{m2\hat{n}1m} \right\rangle}{\sqrt{2}}$$

To calculate the Hamiltonian we define a function `h` which calculates the matrix elements of the Hamiltonian.

```
tunnelterm = (m1ae1 · m2av1 + m2ae1 · m1av1 +
    m1ae0 · m2av0 + m2ae0 · m1av0 + m1ae1m · m2av1m + m2ae1m · m1av1m );

h[x_, y_, ϵ_, u2_, tu_] := (erzeinzeln[x, 0])† ·
  (( u0 / 2 (x⟦1, 1⟧² - x⟦1, 1⟧ + x⟦1, 2⟧² - x⟦1, 2⟧) + ϵ (x⟦1, 1⟧ - x⟦1, 2⟧) +
      u2 / 2 (x⟦2, 1⟧ (x⟦2, 1⟧ + 1) - 2 x⟦1, 1⟧ + x⟦2, 2⟧ (x⟦2, 2⟧ + 1) - 2 x⟦1, 2⟧ ) )
    · erzeinzeln[y, 0])
+ (erzeinzeln[x, 0])† · (-tu tunnelterm · erzeinzeln[y, 0])
```

This function can be used in the same way as in Sec. B.1 to generate the Hamiltonian.

Bibliography

[Abraham and Shaw(1992)] Abraham, R. H. and Shaw, C. D., *Dynamics-the geometry of behavior*, Addison-Wesley (1992).

[Abramowitz and Stegun(1964)] Abramowitz, I. and Stegun, I. A., *Handbook of Mathematical Functions*, National Bureau of Standards (1964).

[Alet *et al.*(2006)] Alet, F., Walczak, A. M., and Fisher, M. P., *Exotic quantum phases and phase transitions in correlated matter*, Physica A: Statistical Mechanics and its Applications **369**, 122 (2006).

[Altman *et al.*(2004)] Altman, E., Demler, E., and Lukin, M. D., *Probing many-body states of ultracold atoms via noise correlations*, Phys. Rev. A **70**, 013603 (2004).

[Anderlini *et al.*(2007)] Anderlini, M., Lee, P. J., Brown, B. L., Sebby-Strabley, J., Phillips, W. D., and Porto, J. V., *Controlled exchange interaction between pairs of neutral atoms in an optical lattice*, Nature **448**, 452 (2007).

[Anderson *et al.*(1995)] Anderson, M. H., Ensher, J. R., Matthews, M. R., Wieman, C. E., and Cornell, E. A., *Observation of Bose-Einstein condensation in a dilute atomic vapor*, Science **269**, 198 (1995).

[Averin *et al.*(2008)] Averin, D. V., Bergeman, T., Hosur, P. R., and Bruder, C., *Single-atom box: Bosonic staircase and effects of parity*, Phys. Rev. A **78**, 031601 (2008).

[Averin *et al.*(1985)] Averin, D. V., Zorin, A. B., and Likharev, K. K., Sov. Phys. JETP **61**, 407 (1985).

[Bakr *et al.*(2010)] Bakr, W. S., Peng, A., Tai, M. E., Ma, R., Simon, J., Gillen, J. I., Fölling, S., Pollet, L., and Greiner, M., *Probing the superfluid-to-Mott insulator transition at the single-atom level*, Science **329**, 547 (2010).

[Barnett and P.M. Radmore(2002)] Barnett, S. and P.M. Radmore. *Methods in Theoretical Quantum Optics*, Oxford University Press (2002).

[Barrett *et al.*(2001)] Barrett, M. D., Sauer, J. A., and Chapman, M. S., *All-optical formation of an atomic Bose-Einstein condensate*, Phys. Rev. Lett. **87**, 010404 (2001).

[Bartlett and Wiseman(2003)] Bartlett, S. D. and Wiseman, H. M., *Entanglement constrained by superselection rules*, Phys. Rev. Lett. **91**, 097903 (2003).

[Batrouni *et al.*(2002)] Batrouni, G. G., Rousseau, V., Scalettar, R. T., Rigol, M., Muramatsu, A., Denteneer, P. J. H., and Troyer, M., *Mott domains of bosons confined on optical lattices*, Phys. Rev. Lett. **89**, 117203 (2002).

[Batrouni *et al.*(2009)] Batrouni, G. G., Rousseau, V. G., and Scalettar, R. T., *Magnetic and superfluid transitions in the one-dimensional spin-1 boson Hubbard model*, Phys. Rev. Lett. **102**, 140402 (2009).

[Batrouni *et al.*(1990)] Batrouni, G. G., Scalettar, R. T., and Zimanyi, G. T., *Quantum critical phenomena in one-dimensional Bose systems*, Phys. Rev. Lett. **65**, 1765 (1990).

[Bergeman *et al.*(1987)] Bergeman, T., Erez, G., and Metcalf, H. J., *Magnetostatic trapping fields for neutral atoms*, Phys. Rev. A **35**, 1535 (1987).

[Black *et al.*(2007)] Black, A. T., Gomez, E., Turner, L. D., Jung, S., and Lett, P. D., *Spinor dynamics in an antiferromagnetic spin-1 condensate*, Phys. Rev. Lett. **99**, 070403 (2007).

[Blakie and Clark(2004)] Blakie, P. B. and Clark, C. W., *Wannier states and Bose-Hubbard parameters for 2D optical lattices*, Journal of Physics B: Atomic, Molecular and Optical Physics **37**, 1391 (2004).

[Bloch *et al.*(2012)] Bloch, I., Dalibard, J., and Nascimbène, S., *Quantum simulations with ultracold quantum gases*, Nature Physics **8**, 267 (2012).

[Bloch *et al.*(2008)] Bloch, I., Dalibard, J., and Zwerger, W., *Many-body physics with ultracold gases*, Rev. Mod. Phys. **80**, 885 (2008).

[Bloch *et al.*(2000)] Bloch, I., Hansch, T. W., and Esslinger, T., *Measurement of the spatial coherence of a trapped Bose gas at the phase*, Nature **403**, 166 (2000).

[Bogoliubov(1947)] Bogoliubov, N., *On the theory of superfluidity*, J. Phys. (USSR) **11**, 23 (1947).

[Bookjans *et al.*(2011)] Bookjans, E. M., Hamley, C. D., and Chapman, M. S., *Strong quantum spin correlations observed in atomic spin mixing*, Phys. Rev. Lett. **107**, 210406 (2011).

[Bose(1924)] Bose, S. N., *Plancks Gesetz und Lichtquantenhypothese*, Zeitschrift für Physik **26**, 178 (1924).

[Bradley *et al.*(1995)] Bradley, C. C., Sackett, C. A., Tollett, J. J. and Hulet, R. G., *Evidence of Bose-Einstein Condensation in an Atomic Gas with Attractive Interactions*, Phys. Rev. Lett. **75**, 1687 (1995).

[Breit and Rabi(1931)] Breit, G. and Rabi, I. I., Measurement of nuclear spin. Phys. Rev. **38**, 2082 (1931).

[Bruder *et al.*(1993)] Bruder, C., Fazio, R., and Schön, G., *Superconductor - Mott-insulator transition in Bose systems with finite-range interactions*, Phys. Rev. B **47**, 342 (1993).

[Bruus and Flensberg(2004)] Bruus, H. and Flensberg, K., *Many-body Quantum Theory In Condensed Matter Physics*, Oxford University Press (2004).

[Büchler *et al.*(2003)] Büchler, H. P., Blatter, G., and Zwerger, W., *Commensurate-incommensurate transition of cold atoms in an optical lattice*, Phys. Rev. Lett. **90**, 130401 (2003).

[Buluta and Nori(2009)] Buluta, I. and Nori, F.. *Quantum simulators*, Science **326**, 108 (2009).

[Buonsante *et al.*(2005)] Buonsante, P., Penna, V., and Vezzani, A., *Analytical mean-field approach to the phase diagram of ultracold bosons in optical super-lattices*, Laser Physics **15**, 361 (2005).

[Buonsante and Vezzani(2004)] Buonsante, P. and Vezzani, A., *Phase diagram for ultracold bosons in optical lattices and superlattices*, Phys. Rev. A **70**, 033608 (2004).

[Burger *et al.*(2001)] Burger, S., Cataliotti, F. S., Fort, C., Minardi, F., Inguscio, M., Chiofalo, M. L., and Tosi, M. P., *Superfluid and dissipative dynamics of a Bose-Einstein condensate in a periodic optical potential*, Phys. Rev. Lett. **86**, 4447 (2001).

[Burke *et al.*(1998)] Burke, J. P., Greene, C. H., and Bohn, J. L., *Multichannel cold collisions: Simple dependences on energy and magnetic field*, Phys. Rev. Lett. **81**, 3355 (1998).

[Capogrosso-Sansone *et al.*(2007)] Capogrosso-Sansone, B., Prokof'ev, N. V., and Svistunov, B. V., *Phase diagram and thermodynamics of the three-dimensional Bose-Hubbard model*, Phys. Rev. B **75**, 134302 (2007).

[Chang *et al.*(2004)] Chang, M.-S., Hamley, C. D., Barrett, M. D., Sauer, J. A., Fortier, K. M., Zhang, W., You, L., and Chapman, M. S., *Observation of spinor dynamics in optically trapped ^{87}Rb Bose-Einstein condensates*, Phys. Rev. Lett. **92**, 140403 (2004).

[Chang *et al.*(2005)] Chang, M.-S., Qin, Q., Zhang, W., You, L., and Chapman, M. S., *Coherent spinor dynamics in a spin-1 Bose condensate*, Nature Physics **1**, 111 (2005).

[Cheinet *et al.*(2008)] Cheinet, P., Trotzky, S., Feld, M., Schnorrberger, U., Moreno-Cardoner, M., Fölling, S., and Bloch, I., *Counting atoms using interaction blockade in an optical superlattice*, Phys. Rev. Lett. **101**, 090404 (2008).

[Chen *et al.*(2010)] Chen, B.-L., Kou, S.-P., Zhang, Y., and Chen, S., *Quantum phases of the Bose-Hubbard model in optical superlattices*, Phys. Rev. A **81**, 053608 (2010).

[Chu(1991)] Chu, S., *Laser manipulation of atoms and particles*, Science **253**, 861 (1991).

[Chu *et al.*(1986)] Chu, S., Bjorkholm, J. E., Ashkin, A., and Cable, A., *Experimental observation of optically trapped atoms*, Phys. Rev. Lett. **57**, 314 (1986).

[Chung and Yip(2009)] Chung, M.-C. and Yip, S., *Phase diagrams for spin-1 bosons in an optical lattice*, Phys. Rev. A **80**, 053615 (2009).

[Clément *et al.*(2009)] Clément, D., Fabbri, N., Fallani, L., Fort, C., and Inguscio, M., *Exploring correlated 1D Bose gases from the superfluid to the Mott-insulator state by inelastic light scattering*, Phys. Rev. Lett. **102**, 155301 (2009).

[Clément *et al.*(2010)] Clément, D., Fabbri, N., Fallani, L., Fort, C., and Inguscio, M., *Bragg spectroscopy of strongly correlated bosons in optical lattices*, Journal of Low Temperature Physics **158**, 5 (2010).

[Cohen-Tannoudji *et al.*(1992)] Cohen-Tannoudji, C., Diu, B., and Laloe, F., *Quantum Mechanics*, Wiley-Interscience (1992).

[Cramer *et al.*(2011)] Cramer, M., Plenio, M. B., and Wunderlich, H., *Measuring entanglement in condensed matter systems*, Phys. Rev. Lett. **106**, 020401 (2011).

[Dahan *et al.*(1996)] Dahan, M., Peik, E., Reichel, J., Castin, Y., and Salomon, C., *Bloch oscillations of atoms in an optical potential*, Phys. Rev. Lett. **76**, 4508 (1996).

[Dalibard(1998)] Dalibard, J., Collisional dynamics of ultra-cold atomic gases. *Proceedings of the International School of Physics Enrico Fermi, Course CXL: Bose-Einstein condensation in gases* (1998).

[Davis *et al.*(1995)] Davis, K. B., Mewes, M. O., Andrews, M. R., van Druten, N. J., Durfee, D. S., Kurn, D. M., and Ketterle, W., *Bose-Einstein condensation in a gas of sodium atoms*, Phys. Rev. Lett. **75**, 3969 (1995).

[De Chiara *et al.*(2008)] De Chiara, G., Calarco, T., Anderlini, M., Montangero, S., Lee, P. J., Brown, B. L., Phillips, W. D., and Porto, J. V., *Optimal control of atom transport for quantum gates in optical lattices*, Phys. Rev. A **77**, 052333 (2008).

[De Chiara *et al.*(2011)] De Chiara, G., Lewenstein, M., and Sanpera, A., *Bilinear-biquadratic spin-1 chain undergoing quadratic zeeman effect*, Phys. Rev. B **84**, 054451 (2011).

[De Chiara and Sanpera(2011)] De Chiara, G. and Sanpera, A., *Detection of entanglement in ultracold lattice gases*, Journal of Low Temperature Physics **165**, 292 (2011).

[Dell'Anna(2012)] Dell'Anna, L., *Analytical approach to the two-site Bose-Hubbard model: From Fock states to Schrödinger cat states and entanglement entropy*, Phys. Rev. A **85**, 053608 (2012).

[Demler and Zhou(2002)] Demler, E. and Zhou, F., *Spinor bosonic atoms in optical lattices: Symmetry breaking and fractionalization*, Phys. Rev. Lett. **88**, 163001 (2002).

[Dennison and Wootters(2001)] Dennison, K. A. and Wootters, W. K., *Entanglement sharing among quantum particles with more than two orthogonal states*, Phys. Rev. A **65**, 010301 (2001).

[DePue *et al.*(1999)] DePue, M. T., McCormick, C., Winoto, S. L., Oliver, S., and Weiss, D. S., *Unity occupation of sites in a 3D optical lattice*, Phys. Rev. Lett. **82**, 2262 (1999).

[dos Santos and Pelster(2009)] dos Santos, F. E. A. and Pelster, A., *Quantum phase diagram of bosons in optical lattices*, Phys. Rev. A **79**, 013614 (2009).

[Dowling *et al.*(2006)] Dowling, M. R., Doherty, A. C., and Wiseman, H. M., *Entanglement of indistinguishable particles in condensed-matter physics*, Phys. Rev. A **73** 052323 (2006).

[Eckert *et al.*(2008)] Eckert, K., Romero-Isart, O., Rodriguez, M., Lewenstein, M., Polzik, E. S., and Sanpera, A., *Quantum non-demolition detection of strongly correlated systems*, Nature Physics **4**, 50 (2008).

[Einstein(1925)] Einstein, A., *Quantentheorie des einatomigen idealen Gases*, Sitzungsberichte der Preussischen Akademie der Wissenschaften, **1**, 3 (1925).

[Einstein *et al.*(1935)] Einstein, A., Podolsky, B., and Rosen, N., *Can quantum-mechanical description of physical reality be considered complete?* Phys. Rev. **47**, 777 (1935).

[Elstner and Monien(1999)] Elstner, N. and Monien, H., *Dynamics and thermodynamics of the Bose-Hubbard model*, Phys. Rev. B **59**, 12184 (1999).

[Fabbri *et al.*(2009)] Fabbri, N., Clément, D., Fallani, L., Fort, C., Modugno, M., van der Stam, K. M. R., and Inguscio, M., *Excitations of Bose-Einstein condensates in a one-dimensional periodic potential*, Phys. Rev. A **79**, 043623 (2009).

[Ferrini *et al.*(2008)] Ferrini, G., Minguzzi, A., and Hekking, F. W. J., *Number squeezing, quantum fluctuations, and oscillations in mesoscopic Bose Josephson junctions*, Phys. Rev. A **78**, 023606 (2008).

[Fetter(1998)] Fetter, A. L., *Theory of a dilute low-temperature trapped Bose condensate*, Four lectures from International School of Physics"Enrico Fermi" on Bose-Einstein Condensation in Atomic Gases, Varenna (1998).

[Feynman(1982)] Feynman, R., *Simulating physics with computers*, International Journal of Theoretical Physics **21**, 467 (1982).

[Fisher *et al.*(1989)] Fisher, M. P. A., Weichman, P. B., Grinstein, G., and Fisher, D. S., *Boson localization and the superfluid-insulator transition*, Phys. Rev. B **40**, 546 (1989).

[Fölling *et al.*(2005)] Fölling, S., Gerbier, F., Widera, A., Mandel, O., Gericke, T., and Bloch, I., *Spatial quantum noise interferometry in expanding ultracold atom clouds*, Nature **434**, 481 (2005).

[Fölling *et al.*(2007)] Fölling, S., Trotzky, S., Cheinet, P., Feld, M., Saers, R., Widera, A., Müller, T., and Bloch, I., *Direct observation of second-order atom tunnelling*, Nature **448**, 1029 (2007).

[Foot(2010)] Foot, C. J., Atomic physics, Oxford University Press (2010).

[Freericks and Monien(1996)] Freericks, J. K. and Monien, H., *Strong-coupling expansions for the pure and disordered Bose-Hubbard model*, Phys. Rev. B **53**, 2691 (1996).

[García-Ripoll *et al.*(2004)] García-Ripoll, J. J., Martin-Delgado, M. A., and Cirac, J. I., *Implementation of spin Hamiltonians in optical lattices*, Phys. Rev. Lett. **93**, 250405 (2004).

[Gati and Oberthaler(2007)] Gati, R. and Oberthaler, M. K., *A bosonic Josephson junction*, Journal of Physics B: Atomic, Molecular and Optical Physics **40**, 61 (2007).

[Gemelke *et al.*(2009)] Gemelke, N., Zhang, X., Hung, C.-L., and Chin, C., *In situ observation of incompressible Mott-insulating domains in ultracold atomic gases*, Nature **460**, 995 (2009).

[Gerbier *et al.*(2008)] Gerbier, F., Trotzky, S., Fölling, S., Schnorrberger, U., Thompson, J. D., Widera, A., Bloch, I., Pollet, L., Troyer, M., Capogrosso-Sansone, B., Prokof'ev, N. V., and Svistunov, B. V., *Expansion of a quantum gas released from an optical lattice*, Phys. Rev. Lett. **101**, 155303 (2008).

[Gerlach and Stern(1924)] Gerlach, W. and Stern, O., *Über die Richtungsquantelung im Magnetfeld*, Ann.Phys.-Berlin **74**, 673 (1924).

[Golub and Van Loan(1996)] Golub, G. H. and Van Loan, C. F., *Matrix Computations (3rd ed.)*, Johns Hopkins (1996).

[Greif *et al.*(2011)] Greif, D., Tarruell, L., Uehlinger, T., Jördens, R., and Esslinger, T., *Probing nearest-neighbor correlations of ultracold fermions in an optical lattice*, Phys. Rev. Lett. **106**, 145302 (2011).

[Greiner *et al.*(2001)] Greiner, M., Bloch, I., Mandel, O., Hänsch, T. W., and Esslinger, T., *Exploring phase coherence in a 2D lattice of Bose-Einstein condensates*, Phys. Rev. Lett. **87**, 160405 (2001).

[Greiner *et al.*(2002)a] Greiner, M., Mandel, O., Esslinger, T., Hänsch, T., and Bloch, I., *Quantum phase transition from a superfluid to a Mott insulator in a gas of ultracold atoms*, Nature **415**, 39 (2002).

[Greiner *et al.*(2002)b] Greiner, M., Mandel, O., Hansch, T. W., and Bloch, I., *Collapse and revival of the matter wave field of a Bose-Einstein condensate*, Nature **419**, 51 (2002).

[Greiner *et al.*(2005)] Greiner, M., Regal, C. A., Stewart, J. T., and Jin, D. S., *Probing pair-correlated fermionic atoms through correlations in atom shot noise*, Phys. Rev. Lett. **94**, 110401 (2005).

[Gribakin and Flambaum(1993)] Gribakin, G. F. and Flambaum, V. V., *Calculation of the scattering length in atomic collisions using the semiclassical approximation*, Phys. Rev. A **48**, 546 (1993).

[Grimm *et al.*(2000)] Grimm, R., Weidemueller, M., and Ovchinnikov, Y. B., *Optical dipole traps for neutral atoms*, Advances In Atomic, Molecular, and Optical Physics, Volume **42**, 95 (2000).

[Gross *et al.*(2011)] Gross, C., Strobel, H., Nicklas, E., Zibold, T., Bar-Gill, N., Kurizki, G., and Oberthaler, M. K., *Atomic homodyne detection of continuous-variable entangled twin-atom states*, Nature **480**, 219 (2011).

[Grynberg *et al.*(1993)] Grynberg, G., Lounis, B., Verkerk, P., Courtois, J.-Y., and Salomon, C., *Quantized motion of cold Cesium atoms in two- and three-dimensional optical potentials*, Phys. Rev. Lett. **70**, 2249 (1993).

[Gutzwiller(1963)] Gutzwiller, M. C., *Effect of correlation on the ferromagnetism of transition metals*, Phys. Rev. Lett. **10**, 159 (1963).

[Guzman *et al.*(2011)] Guzman, J., Jo, G.-B., Wenz, A. N., Murch, K. W., Thomas, C. K., and Stamper-Kurn, D. M., *Long-time-scale dynamics of spin textures in a degenerate $f = 1$ ^{87}RB spinor Bose gas*, Phys. Rev. A **84**, 063625 (2011).

[Hall *et al.*(1998)a] Hall, D. S., Matthews, M. R., Ensher, J. R., Wieman, C. E., and Cornell, E. A., Dynamics of component separation in a binary mixture of Bose-Einstein condensates. Phys. Rev. Lett. **81**, 1539 (1998).

[Hall *et al.*(1998)b] Hall, D. S., Matthews, M. R., Wieman, C. E., and Cornell, E. A., *Measurements of relative phase in two-component Bose-Einstein condensates.* Phys. Rev. Lett. **81**, 1543 (1998).

[Hamley *et al.*(2012)] Hamley, C. D., Gerving, C. S., Hoang, T. M., Bookjans, E. M., and Chapman, M. S., *Spin-nematic squeezed vacuum in a quantum gas*, Nature Physics **8**, 305 (2012).

[Hammerer *et al.*(2010)] Hammerer, K., Sørensen, A. S., and Polzik, E. S., *Quantum interface between light and atomic ensembles*, Rev. Mod. Phys. **82**, 1041 (2010).

[Hemmerich *et al.*(1995)] Hemmerich, A., Weidemüller, M., Esslinger, T., Zimmermann, C., and Hänsch, T., *Trapping atoms in a dark optical lattice*, Phys. Rev. Lett. **75**, 37 (1995).

[Ho(1998)] Ho, T.-L., *Spinor Bose condensates in optical traps*, Phys. Rev. Lett. **81**, 742 (1998).

[Horodecki *et al.*(2009)] Horodecki, R., Horodecki, P., Horodecki, M., and Horodecki, K., *Quantum entanglement*, Reviews of Modern Physics **81**, 865 (2009).

[Huang(1987)] Huang, K., *Statistical Mechanics, 2. Edition*, John Wiley & Sons (1987).

[Hubbard(1963)] Hubbard, J., *Electron correlations in narrow energy bands*, Proc. R. Soc. **276**, 238 (1963).

[Hugenholtz and Pines(1959)] Hugenholtz, N. M. and Pines, D., *Ground-state energy and excitation spectrum of a system of interacting bosons*, Phys. Rev. **116**, 489 (1959).

[Hung *et al.*(2010)] Hung, C.-L., Zhang, X., Gemelke, N. and Chin, C., *Slow Mass Transport and Statistical Evolution of an Atomic Gas across the Superfluid-Mott-Insulator Transition*, Phys. Rev. Lett. **104**, 160403 (2010).

[Imambekov *et al.*(2003)] Imambekov, A., Lukin, M., and Demler, E., *Spin-exchange interactions of spin-one bosons in optical lattices: Singlet, nematic, and dimerized phases*, Phys. Rev. A **68**, 063602 (2003).

[Imambekov *et al.*(2004)] Imambekov, A., Lukin, M., and Demler, E., *Magnetization plateaus for spin-one bosons in optical lattices: Stern-Gerlach experiments with strongly correlated atoms*, Phys. Rev. Lett. **93**, 120405 (2004).

[Isacsson and Girvin(2005)] Isacsson, A. and Girvin, S. M., *Multiflavor bosonic Hubbard models in the first excited Bloch band of an optical lattice*, Phys. Rev. A **72**, 053604 (2005).

[Jaksch *et al.*(1998)] Jaksch, D., Bruder, C., Cirac, J. I., Gardiner, C. W., and Zoller, P., *Cold bosonic atoms in optical lattices*, Phys. Rev. Lett. **81**, 3108 (1998).

[Jaksch and Zoller(2005)] Jaksch, D. and Zoller, P., *The cold atom Hubbard toolbox*, Annals of Physics **315**, 52 (2005).

[Jessen and Deutsch(1996)] Jessen, P. and Deutsch, I. H., *Optical lattices*, Adv. Atm. Mol. Opt. Phys. **37**, 95 (1996).

[Julsgaard(2003)] Julsgaard, B., *Entanglement and Quantum Interactions with Macroscopic Gas Samples*, Ph.D. Thesis, University of Aarhus (2003).

[Kashurnikov *et al.*(1996)] Kashurnikov, V., Krasavin, A., and Svistunov, B., JETP Lett. **64**, 99 (1996).

[Kashurnikov *et al.*(2002)] Kashurnikov, V. A., Prokof'ev, N. V., and Svistunov, B. V., *Revealing the superfluid - Mott-insulator transition in an optical lattice*, Phys. Rev. A **66**, 031601 (2002).

[Ketterle(2002)] Ketterle, W., Nobel lecture: *When atoms behave as waves: Bose-Einstein condensation and the atom laser*, Rev. Mod. Phys. **74**, 1131 (2002).

[Kimura *et al.*(2005)] Kimura, T., Tsuchiya, S., and Kurihara, S., *Possibility of a first-order superfluid-Mott-insulator transition of spinor bosons in an optical lattice*, Phys. Rev. Lett. **94**, 110403 (2005).

[Kleinert *et al.*(2012)] Kleinert, H., Narzikulov, Z., and Rakhimov, A., *Quantum phase transitions in optical lattices beyond the Bogoliubov approximation*, Phys. Rev. A **85**, 063602 (2012).

[Köhl *et al.*(2005)] Köhl, M., Moritz, H., Stöferle, T., Schori, C., and Esslinger, T., *Superfluid to Mott insulator transition in one, two, and three dimensions*, Journal of Low Temperature Physics **138**, 635 (2005).

[Kohn(1959)] Kohn, W., *Analytic properties of Bloch waves and Wannier functions*, Phys. Rev. **115**, 809 (1959).

[Kosterlitz and Thouless(1973)] Kosterlitz, J. M. and Thouless, D. J., *Ordering, metastability and phase transitions in two-dimensional systems*, Journal of Physics C: Solid State Physics **6**, 1181 (1973).

[Krauth *et al.*(1992)] Krauth, W., Caffarel, M., and Bouchaud, J.-P., *Gutzwiller wave function for a model of strongly interacting bosons*, Phys. Rev. B **45**, 3137 (1992).

[Krutitsky and Graham(2004)] Krutitsky, K. V. and Graham, R., *Spin-1 bosons with coupled ground states in optical lattices*, Phys. Rev. A **70**, 063610 (2004).

[Krutitsky *et al.*(2005)] Krutitsky, K. V., Timmer, M., and Graham, R., *First-and second-order superfluid-Mott-insulator phase transitions of spin-1 bosons with coupled ground states in optical lattices*, Phys. Rev. A **71**, 033623 (2005).

[Kühner and Monien(1998)] Kühner, T. D. and Monien, H., *Phases of the one-dimensional Bose-Hubbard model*, Phys. Rev. B **58**, 14741 (1998).

[Kühner *et al.*(2000)] Kühner, T. D., White, S. R., and Monien, H., *One-dimensional Bose-Hubbard model with nearest-neighbor interaction*, Phys. Rev. B **61**, 12474 (2000).

[Kupferschmidt and Müller(2010)] Kupferschmidt, Joern N. and Mueller, Erich J., *Role of interactions in time-of-flight expansion of atomic clouds from optical lattices*, Phys. Rev. A **82**, 023618 (2010).

[Kuwamoto *et al.*(2004)] Kuwamoto, T., Araki, K., Eno, T., and Hirano, T., *Magnetic field dependence of the dynamics of* ^{87}Rb *spin-2 Bose-Einstein condensates*, Phys. Rev. A **69**, 063604 (2004).

[Lafarge *et al.*(1993)] Lafarge, P., Joyez, P., Esteve, D., Urbina, C., and Devoret, M. H., Nature **365**, 422 (1993).

[Lafarge *et al.*(1991)] Lafarge, P., Pothier, H., Williams, E. R., Esteve, D., Urbina, C., and Devoret, M. H., Z. Phys. B: Condens. Matter **85**, 327 (1991).

[Lee *et al.*(2007)] Lee, P. J., Anderlini, M., Brown, B. L., Sebby-Strabley, J., Phillips, W. D., and Porto, J. V., *Sublattice addressing and spin-dependent motion of atoms in a double-well lattice*, Phys. Rev. Lett. **99**, 020402 (2007).

[Leggett(2001)] Leggett, A. J., *Bose-Einstein condensation in the alkali gases: Some fundamental concepts*, Rev. Mod. Phys. **73**, 307 (2001).

[Leggio *et al.*(2011)] Leggio, B., Napoli, A., and Messina, A., *Quantum phase transitions and heat capacity in a two-atoms Bose-Hubbard model*, arXiv quant-ph: 1107.1611 (2011).

[Lewenstein *et al.*(2012)] Lewenstein, M., Sanpera, A., and Ahufinger, V., *Ultracold atoms in Optical Lattices: simulating quantum many body physics*, Oxford University Press, Oxford (2012).

[Lewenstein *et al.*(2007)] Lewenstein, M., Sanpera, A., Ahufinger, V., Damski, B., De, A. S., and Sen, U., *Ultracold atomic gases in optical lattices: mimicking condensed matter physics and beyond*, Adv. Phys. **56**, 243 (2007).

[Liu *et al.*(2009)] Liu, Y., Jung, S., Maxwell, S. E., Turner, L. D., Tiesinga, E., and Lett, P. D., *Quantum phase transitions and continuous observation of spinor dynamics in an antiferromagnetic condensate*, Phys. Rev. Lett. **102**, 125301 (2009).

[Lücke *et al.*(2011)] Lücke, B., Scherer, M., Kruse, J., Pezzé, L., Deuretzbacher, F., Hyllus, P., Topic, O., Peise, J., Ertmer, W., Arlt, J., Santos, L., Smerzi, A., and Klempt, C., *Twin matter waves for interferometry beyond the classical limit*, Science **334**, 773 (2011).

[Mandel *et al.*(2003)] Mandel, O., Greiner, M., Widera, A., Rom, T., Hänsch, T. W., and Bloch, I., *Controlled collisions for multi-particle entanglement of optically trapped atoms*, Nature **425**, 937 (2003).

[Marzari and Vanderbilt(1997)] Marzari, N. and Vanderbilt, D., *Maximally localized generalized Wannier functions for composite energy bands*, Phys. Rev. B **56**, 12847 (1997).

[Matthews *et al.*(1998)] Matthews, M. R., Hall, D. S., Jin, D. S., Ensher, J. R., Wieman, C. E., Cornell, E. A., Dalfovo, F., Minniti, C., and Stringari, S., *Dynamical response of a Bose-Einstein condensate to a discontinuous change in internal state*, Phys. Rev. Lett. **81**, 243 (1998).

[Mazzarella *et al.*(2011)] Mazzarella, G., Salasnich, L., Parola, A., and Toigo, F., *Coherence and entanglement in the ground state of a bosonic Josephson junction: From macroscopic Schrödinger cat states to separable Fock states*, Phys. Rev. A **83**, 053607 (2011).

[Metcalf and der Straten(1999)] Metcalf, H. J. and der Straten, P. V., *Laser Cooling and Trapping*, Springer (1999).

[Migdall *et al.*(1985)] Migdall, A. L., Prodan, J. V., Phillips, W. D., Bergeman, T. H., and Metcalf, H. J., *First observation of magnetically trapped neutral atoms*, Phys. Rev. Lett. **54**, 2596 (1985).

[Modugno and Pettini(2012)] Modugno, M. and Pettini, G., *Maximally localized Wannier functions for ultracold atoms in one-dimensional double-well periodic potentials*, New Journal of Physics **14**, 055004 (2012).

[Myatt *et al.*(1997)] Myatt, C. J., Burt, E. A., Ghrist, R. W., Cornell, E. A., and Wieman, C. E., *Production of two overlapping Bose-Einstein condensates by sympathetic cooling*, Phys. Rev. Lett. **78**, 586 (1997).

[Nelson *et al.*(2007)] Nelson, K. D., Li, X., and Weiss, D. S., *Imaging single atoms in a three-dimensional array*, Nature Physics **3**, 556 (2007).

[Neumann(1955)] Neumann, J. V., *Mathematische Grundlagen der Quantenmechanik*, Springer, Berlin (1955).

[Nielsen and Chuang(2000)] Nielsen, M. A. and Chuang, I. L., *Quantum Computation and Quantum Information*, Cambridge Univ. Press, Cambridge (2000).

[Ohmi and Machida(1998)] Ohmi, T. and Machida, K., *Bose-Einstein condensation with internal degrees of freedom in alkali atom gases*, Journal of the Physical Society of Japan **67**, 1822 (1998).

[Orús and Vidal(2008)] Orús, R. and Vidal, G., *Infinite time-evolving block decimation algorithm beyond unitary evolution*, Phys. Rev. B **78**, 155117 (2008).

[Osterloh(2008)] Osterloh, A., *Entanglement and its facets in condensed matter systems*, arXiv 0810.1240 (2008).

[Osterloh and Hyllus(2009)] Osterloh, A. and Hyllus, P., *Estimating multipartite entanglement measures*, arXiv quant-ph: 0908.3467 (2009).

[Pai *et al.*(2008)] Pai, R. V., Sheshadri, K., and Pandit, R., *Phases and transitions in the spin-1 Bose-Hubbard model: Systematics of a mean-field theory*, Phys. Rev. B **77**, 014503 (2008).

[Partridge *et al.*(2006)] Partridge, G. B., Li, W., Kamar, R. I., Liao, Y.-a., and Hulet, R. G., *Pairing and phase separation in a polarized fermi gas*, Science **311**, 503 (2006).

[Pedri *et al.*(2001)] Pedri, P., Pitaevskii, L., Stringari, S., Fort, C., Burger, S., Cataliotti, F. S., Maddaloni, P., Minardi, F., and Inguscio, M., *Expansion of a coherent array of Bose-Einstein condensates*, Phys. Rev. Lett. **87**, 220401 (2001).

[Pethick and Smith(2008)] Pethick, C. J. and Smith, H., *Bose-Einstein Condensation in Dilute Gases*, Cambridge University Press; 2 edition (2008).

[Phillips(1998)] Phillips, W. D., Nobel lecture: *Laser cooling and trapping of neutral atoms*, Rev. Mod. Phys. **70**, 721 (1998).

[Pino *et al.*(2012)] Pino, M., Prior, J., Somoza, A. M., Jaksch, D., and Clark, S. R., *Re-entrance and entanglement in the one-dimensional Bose-Hubbard model*, arXiv 1206.0222 (2012).

[Popescu and Rohrlich(1997)] Popescu, S. and Rohrlich, D., *Thermodynamics and the measure of entanglement*, Phys. Rev. A **56**, 3319 (1997).

[Pritchard *et al.*(1986)] Pritchard, D. E., Raab, E. L., Bagnato, V., Wieman, C. E., and Watts, R. N., *Light traps using spontaneous forces*, Phys. Rev. Lett. **57**, 310 (1986).

[Prokof'ev *et al.*(1998)] Prokof'ev, N., Svistunov, B., and Tupitsyn, I., *Worm algorithm in quantum monte carlo simulations*, Physics Letters A **238**, 253 (1998).

[Raab *et al.*(1987)] Raab, E. L., Prentiss, M., Cable, A., Chu, S., and Pritchard, D. E., *Trapping of neutral sodium atoms with radiation pressure*, Phys. Rev. Lett. **59**, 2631 (1987).

[Rey(2004)] Rey, A. M., *Ultra-cold bosonic atoms in optical lattices*, PhD thesis, University of Maryland at College Park (2004).

[Rey *et al.*(2005)] Rey, A. M., Blakie, P. B., Pupillo, G., Williams, C. J., and Clark, C. W., *Bragg spectroscopy of ultracold atoms loaded in an optical lattice*, Phys. Rev. A **72**, 023407 (2005).

[Rey *et al.*(2007)] Rey, A. M., Gritsev, V., Bloch, I., Demler, E., and Lukin, M. D., *Preparation and detection of magnetic quantum phases in optical superlattices*, Phys. Rev. Lett. **99**, 140601 (2007).

[Rinck and Bruder(2011)] Rinck, M. and Bruder, C., *Effects of a single fermion in a Bose Josephson junction*, Phys. Rev. A **83**, 023608 (2011).

[Rizzi *et al.*(2005)] Rizzi, M., Rossini, D., De Chiara, G., Montangero, S., and Fazio, R., *Phase diagram of spin-1 bosons on one-dimensional lattices*, Phys. Rev. Lett. **95**, 240404 (2005).

[Rodriguez *et al.*(2011)] Rodriguez, K., Argüelles, A., Kolezhuk, A. K., Santos, L., and Vekua, T., *Field-induced phase transitions of repulsive spin-1 bosons in optical lattices*, Phys. Rev. Lett. **106**, 105302 (2011).

[Rokhsar and Kotliar(1991)] Rokhsar, D. S. and Kotliar, B. G., *Gutzwiller projection for bosons*, Phys. Rev. B **44**, 10328 (1991).

[Rom *et al.*(2006)] Rom, T., Best, T., van Oosten, D., Schneider, U., Fölling, S., Paredes, B., and Bloch, I., *Free fermion antibunching in a degenerate atomic fermi gas released from an optical lattice*, Nature **444**, 733 (2006).

[Rommer and Östlund(1997)] Rommer, S. and Östlund, S., *Class of ansatz wave functions for one-dimensional spin systems and their relation to the density matrix renormalization group*, Phys. Rev. B **55**, 2164 (1997).

[Roscilde *et al.*(2009)] Roscilde, T., Rodriguez, M., Eckert, K., Romero-Isart, O., Lewenstein, M., Polzik, E., and Sanpera, A., *Quantum polarization spectroscopy of correlations in attractive fermionic gases*, New Journal of Physics **11** (5), 055041 (2009).

[Roth and Burnett(2003)] Roth, R. and Burnett, K., *Superfluidity and interference pattern of ultracold bosons in optical lattices*, Phys. Rev. A **67**, 031602 (2003).

[Sachdev(2001)] Sachdev, S., *Quantum Phase Transitions*, Cambridge Univ. Press, Cambridge (2001).

[Scalettar *et al.*(1991)] Scalettar, R. T., Batrouni, G. G., and Zimanyi, G. T., *Localization in interacting, disordered, Bose systems*, Phys. Rev. Lett. **66**, 3144 (1991).

[Schmaljohann *et al.*(2004)] Schmaljohann, H., Erhard, M., Kronjäger, J., Kottke, M., van Staa, S., Cacciapuoti, L., Arlt, J. J., Bongs, K., and Sengstock, K., *Dynamics of f = 2 spinor Bose-Einstein condensates*, Phys. Rev. Lett. **92**, 040402 (2004).

[Schrödinger(1935)] Schrödinger, E., *Die gegenwärtige Situation in der Quantenmechanik*, Naturwissenschaften **23** (48), 807 (1935).

[Sebby-Strabley *et al.*(2006)] Sebby-Strabley, J., Anderlini, M., Jessen, P. S., and Porto, J. V., *Lattice of double wells for manipulating pairs of cold atoms*, Phys. Rev. A **73**, 033605 (2006).

[Sherson *et al.*(2010)] Sherson, J. F., Weitenberg, C., Endres, M., Cheneau, M., Bloch, I., and Kuhr, S., *Single-atom-resolved fluorescence imaging of an atomic Mott insulator*, Nature **467**, 68 (2010).

[Sheshadri *et al.*(1993)] Sheshadri, K., Krishnamurthy, H. R., Pandit, R., and Ramakrishnan, T. V., *Superfluid and insulating phases in an interacting-boson model: Mean-field theory and the RPA*, EPL (Europhysics Letters) **22**, 257 (1993).

[Shin *et al.*(2006)] Shin, Y., Zwierlein, M. W., Schunck, C. H., Schirotzek, A., and Ketterle, W., *Observation of phase separation in a strongly interacting imbalanced fermi gas*, Phys. Rev. Lett. **97**, 030401 (2006).

[Song *et al.*(2011)] Song, H. F., Flindt, C., Rachel, S., Klich, I., and Le Hur, K., *Entanglement entropy from charge statistics: Exact relations for noninteracting many-body systems*, Phys. Rev. B **83**, 161408 (2011).

[Spielman *et al.*(2007)] Spielman, I. B., Phillips, W. D., and Porto, J. V., *Mott-insulator transition in a two-dimensional atomic Bose gas*, Phys. Rev. Lett. **98**, 080404 (2007).

[Stamper-Kurn and Ketterle(2000)] Stamper-Kurn, D. and Ketterle, W., *Spinor condensates and light scattering from Bose-Einstein condensates*, arXiv cond-mat.soft: 0005001 (2000).

[Stamper-Kurn *et al.*(1998)] Stamper-Kurn, D. M., Andrews, M. R., Chikkatur, A. P., Inouye, S., Miesner, H.-J., Stenger, J., and Ketterle, W., *Optical confinement of a Bose-Einstein condensate*, Phys. Rev. Lett. **80**, 2027 (1998).

[Stamper-Kurn and Ueda(2012)] Stamper-Kurn, D. M. and Ueda, M., *Spinor Bose gases: Explorations of symmetries, magnetism and quantum dynamics*, arXiv 1205.1888 (2012).

[Stenger *et al.*(1998)] Stenger, J., Inouye, S., Stamper-Kurn, D. M., Miesner, H.-J., Chikkatur, A. P., and Ketterle, W., *Spin domains in ground-state Bose-Einstein condensates*, Nature **396**, 345 (1998).

[Stöferle *et al.*(2004)] Stöferle, T., Moritz, H., Schori, C., Köhl, M., and Esslinger, T., *Transition from a strongly interacting 1D superfluid to a Mott insulator*, Phys. Rev. Lett. **92**, 130403 (2004).

[Stoof *et al.*(2009)] Stoof, H. T. C., Gubbels, K. B., and Dickerscheid, D. B. M., *Ultracold Quantum Fields*, Springer (2009).

[Svidzinsky and Chui(2003)] Svidzinsky, A. A. and Chui, S. T., *Insulator-superfluid transition of spin-1 bosons in an optical lattice in magnetic field*, Phys. Rev. A **68**, 043612 (2003).

[Toth *et al.*(2008)] Toth, E., Rey, A. M., and Blakie, P. B., *Theory of correlations between ultracold bosons released from an optical lattice*, Phys. Rev. A **78**, 013627 (2008).

[Trefzger and Sengupta(2011)] Trefzger, C. and Sengupta, K., *Nonequilibrium dynamics of the Bose-Hubbard model: A projection-operator approach*, Phys. Rev. Lett. **106**, 095702 (2011).

[Trotzky *et al.*(2008)] Trotzky, S., Cheinet, P., Fölling, S., Feld, M., Schnorrberger, U., Rey, A. M., Polkovnikov, A., Demler, E. A., Lukin, M. D., and Bloch, I., *Time-resolved observation and control of superexchange interactions with ultracold atoms in optical lattices*, Science **319**, 295 (2008).

[Trotzky *et al.*(2010)] Trotzky, S., Pollet, L., Gerbier, F., Schnorrberger, U., Bloch, I., Prokof/' ev, N. V., Svistunov, B., and Troyer, M., *Suppression of the critical temperature for superfluidity near the Mott transition*, Nature Physics **6**, 998 (2010).

[Tsuchiya *et al.*(2004)] Tsuchiya, S., Kurihara, S., and Kimura, T., *Superfluid-Mott insulator transition of spin-1 bosons in an optical lattice*, Phys. Rev. A **70**, 043628 (2004).

[Ueda and Kawaguchi(2010)] Ueda, M. and Kawaguchi, Y., *Spinor Bose-Einstein condensates*, arXiv cond-mat.quant-gas: 1001.2072 (2010).

[van Oosten *et al.*(2001)] van Oosten, D., van der Straten, P., and Stoof, H. T. C., *Quantum phases in an optical lattice*, Phys. Rev. A **63**, 053601 (2001).

[Vaucher *et al.*(2008)] Vaucher, B., Nunnenkamp, A., and Jaksch, D., *Creation of resilient entangled states and a resource for measurement-based quantum computation with optical superlattices*, New Journal of Physics **10**, 023005 (2008).

[Vengalattore *et al.*(2010)] Vengalattore, M., Guzman, J., Leslie, S. R., Serwane, F., and Stamper-Kurn, D. M., *Periodic spin textures in a degenerate $f = 1$ ^{87}Rb spinor Bose gas*, Phys. Rev. A **81**, 053612 (2010).

[Vengalattore *et al.*(2008)] Vengalattore, M., Leslie, S. R., Guzman, J., and Stamper-Kurn, D. M., *Spontaneously modulated spin textures in a dipolar spinor Bose-Einstein condensate*, Phys. Rev. Lett. **100**, 170403 (2008).

[Vidal and Werner(2002)] Vidal, G. and Werner, R. F., *Computable measure of entanglement*, Phys. Rev. A **65**, 032314 (2002).

[Wagner *et al.*(2011)] Wagner, A., Bruder, C., and Demler, E., *Spin-1 atoms in optical superlattices: Single-atom tunneling and entanglement*, Phys. Rev. A **84**, 063636 (2011).

[Wagner *et al.*(2012)] Wagner, A., Nunnenkamp, A., and Bruder, C., *Mean-field analysis of spinor bosons in optical superlattices*, Phys. Rev. A **86**, 023624 (2012).

[Weitenberg *et al.*(2011)] Weitenberg, C., Endres, M., Sherson, J. F., Cheneau, M., Schauss, P., Fukuhara, T., Bloch, I., and Kuhr, S., *Single-spin addressing in an atomic Mott insulator*, Nature **471**, 319 (2011).

[White(1992)] White, S. R., *Density matrix formulation for quantum renormalization groups*, Phys. Rev. Lett. **69**, 2863 (1992).

[Widera *et al.*(2005)] Widera, A., Gerbier, F., Fölling, S., Gericke, T., Mandel, O., and Bloch, I., *Coherent collisional spin dynamics in optical lattices*, Phys. Rev. Lett. **95**, 190405 (2005).

[Wiseman and Vaccaro(2003)] Wiseman, H. M. and Vaccaro, J. A., *Entanglement of indistinguishable particles shared between two parties*, Phys. Rev. Lett. **91**, 097902 (2003).

[Wootters(1998)] Wootters, W. K., *Entanglement of formation of an arbitrary state of two qubits*, Phys. Rev. Lett. **80**, 2245 (1998).

[Yukalov(2009)] Yukalov, V., *Cold bosons in optical lattices*, Laser Physics **19**, 1 (2009).

[Zimmermann *et al.*(2011)] Zimmermann, B., Müller, T., Meineke, J., Esslinger, T., and Moritz, H., *High-resolution imaging of ultracold fermions in microscopically tailored optical potentials*, New Journal of Physics **13**, 043007 (2011).

[Zwerger(2003)] Zwerger, W., *Mott-Hubbard transition of cold atoms in optical lattices*, Journal of Optics B: Quantum and Semiclassical Optics **5**, 9 (2003).

Appendix C

Lebenslauf von Andreas Wagner

Geboren am 27.7.1980 in Scherzingen (CH).

Anschrift:	Andreas Wagner
	Winkelweg 12
	CH-9470 Buchs SG
	Switzerland
Telefon:	+41 76 72 47 443
E-Mail:	wagner-email@gmx.de
Nationalität:	Deutsch

Oktober 2008	Beginn eines Promotionsstudiums an der Universität Basel in der Arbeitsgruppe von Prof. Christoph Bruder.
September 2008	Abschluss des Studiums der Physik mit dem Nebenfach Mathematik als Diplom-Physiker. Note: "sehr gut" Diplomarbeit: "Mittlere Zustandsdichte von Andreev-Graphen", Betreuer: Prof. Felix von Oppen, PhD; Dr. Sven Gnutzmann.
April 2005 - 2007	Unterbrechung des Studiums aufgrund einer schweren infektionsbedingten Herz-Kreislauf Erkrankung. Fortsetzung des Studiums nach vollständiger Genesung.
2005	Beginn der Diplomarbeit
2003- 2004	Teilnahme an den Master of Mathematics Kursen der University of York als Erasmus Student. MMath Project: "Bosonic String Theory and D-Branes", (Noten: $2 \times B$, $10 \times A$).
2000- 2003	Grund- und Hauptstudium an der Freien Universität Berlin
2000	Abitur (Note 1.2) am Heinrich-Suso Gymnasium Konstanz